

3-D RESERVOIR AND STOCHASTIC FRACTURE NETWORK MODELING FOR  
ENHANCED OIL RECOVERY, CIRCLE RIDGE PHOSPHORIA/TENSLEEP  
RESERVOIR, WIND RIVER RESERVATION, ARAPAHO AND SHOSHONE TRIBES,  
WYOMING

Final Technical Report – May 1, 2000 through October 31, 2002

Paul La Pointe<sup>1</sup>  
Jan Hermanson<sup>1</sup>  
Robert Parney<sup>1</sup>  
Thorsten Eiben<sup>1</sup>  
Mike Dunleavy<sup>2</sup>  
Ken Steele<sup>2</sup>  
John Whitney<sup>3</sup>  
Darrell Eubanks<sup>3</sup>  
Roger Straub<sup>4</sup>

Report Date: February 7, 2003

DOE Award Number: DE-FG26-00BC15190

<sup>1</sup>Golder Associates Inc.  
18300 NE Union Hill Road, Suite 200  
Redmond, WA 98052

<sup>2</sup>Marathon Oil Company  
Rocky Mountain Region  
1501 Stampede Ave.  
Cody, WY 82414

<sup>3</sup>Marathon Oil Company  
5555 San Felipe  
Houston, TX 77056

<sup>4</sup>GeoData Services  
P. O. Box 1123  
Coos Bay, OR 97420

“This report was prepared as an account of work sponsored by an agency of the United States Government. Neither the United States Government nor any agency thereof, nor any of their employees, make any warranty, express or implied, or assumes any legal liability or responsibility for the accuracy, completeness, or usefulness of any information, apparatus, product, or process disclosed, or represents that its use would not infringe privately owned rights. Reference herein to any specific commercial product, process, or service by trade name, trademark, manufacturer, or otherwise does not necessarily constitute or imply its endorsement, recommendation, or favoring by the United States Government or any agency thereof. The views and opinions of authors expressed herein do not necessarily state or reflect those of the United States Government or any agency thereof”

## **ABSTRACT**

This report describes the results made in fulfillment of contract DE-FG26-00BC15190, “3-D Reservoir and Stochastic Fracture Network Modeling for Enhanced Oil Recovery, Circle Ridge Phosphoria/Tensleep Reservoir, Wind River Reservation, Arapaho and Shoshone Tribes, Wyoming”. The goal of this project is to improve the recovery of oil from the Tensleep and Phosphoria Formations in Circle Ridge Oilfield, located on the Wind River Reservation in Wyoming, through an innovative integration of matrix characterization, structural reconstruction, and the characterization of the fracturing in the reservoir through the use of discrete fracture network models.

Fields in which natural fractures dominate reservoir permeability, such as the Circle Ridge Field, often experience sub-optimal recovery when recovery processes are designed and implemented that do not take advantage of the fracture systems. For example, a conventional waterflood in a main structural block of the Field was implemented and later suspended due to unattractive results. It is estimated that somewhere less than 20% of the OOIP in the Circle Ridge Field have been recovered after more than 50 years’ production.

Marathon Oil Company identified the Circle Ridge Field as an attractive candidate for several advanced IOR processes that explicitly take advantage of the natural fracture system. These processes require knowledge of the distribution of matrix porosity, permeability and oil saturations; and understanding of where fracturing is likely to be well-developed or poorly developed; how the fracturing may compartmentalize the reservoir; and how smaller, relatively untested subthrust fault blocks may be connected to the main overthrust block.

For this reason, the project focused on improving knowledge of the matrix properties, the fault block architecture and to develop a model that could be used to predict fracture intensity, orientation and fluid flow/connectivity properties. Knowledge of matrix properties was greatly extended by calibrating wireline logs from 113 wells with incomplete or older-vintage logging suites to wells with a full suite of modern logs. The model for the fault block architecture was derived by 3D palinspastic reconstruction. This involved field work to construct three new cross-sections at key areas in the Field; creation of horizon and fault surface maps from well penetrations and tops; and numerical modeling to derive the geometry, chronology, fault movement and folding history of the Field through a 3D restoration of the reservoir units to their original undeformed state. The methodology for predicting fracture intensity and orientation variations throughout the Field was accomplished by gathering outcrop and subsurface image log fracture data, and comparing it to the strain field produced by the various folding and faulting events determined through the 3D palinspastic reconstruction. It was found that the strains produced during the initial folding of the Tensleep and Phosphoria Formations corresponded well without both the orientations and relative fracture intensity measured in outcrop and in the subsurface. The results have led to a 15% to 20% increase in estimated matrix pore volume, and to the plan to drill two horizontal drain holes located and oriented based on the modeling results. Marathon Oil is also evaluating alternative tertiary recovery processes based on the quantitative 3D integrated reservoir model..

## Table of Contents

1	<u>INTRODUCTION</u> .....	1
1.1	<u>Overview of the Issues at Circle Ridge</u> .....	1
1.2	<u>Geological Background of the Circle Ridge Field</u> .....	6
1.1.1	<u>Regional Geology and Tectonic History of the Wind River Basin</u> .....	6
1.1.2	<u>Stratigraphy</u> .....	8
1.3	<u>Strategies for Building the 3D Comprehensive Reservoir Model</u> .....	14
1.3.1	<u>Matrix properties</u> .....	14
1.3.2	<u>Fault block architecture</u> .....	14
1.3.3	<u>Reservoir-scale fracture model</u> .....	15
1.3.4	<u>Integrated 3D reservoir model</u> .....	19
1.4	<u>Strategy for Model Validation</u> .....	21
1.5	<u>Strategy for Model Utilization</u> .....	21
2	<u>Experimental Work</u> .....	23
2.1	<u>Overview</u> .....	23
2.2	<u>Petrophysical Analysis to Expand Matrix Property Coverage</u> .....	23
2.2.1	<u>Overview</u> .....	23
2.2.2	<u>MULTIMIN Analysis</u> .....	24
2.2.3	<u>Porosity Crossplots</u> .....	29
2.2.4	<u>Density Log Only</u> .....	29
2.2.5	<u>Gamma Ray Neutron (GRN) Porosity</u> .....	39
2.3	<u>Field Data Collection</u> .....	39
2.3.1	<u>Geological Reconnaissance &amp; Cross-section data gathering</u> .....	39
2.3.2	<u>Experimental Techniques for Calculating Fracture Orientations, Intensity and Size from Outcrop Data</u> .....	45
2.3.3	<u>Statistical analysis techniques</u> .....	48
2.4	<u>Construction of Balanced Cross-Sections</u> .....	53
2.5	<u>Construction of Balanced Cross-Sections and Validation of Cross-Sections Using Retrodeformation Software</u> .....	59
2.5.1	<u>Overview</u> .....	59
2.5.2	<u>Analysis techniques</u> .....	60
2.5.3	<u>Available Technology for 3D Reconstructions</u> .....	60
2.5.4	<u>Restoring thrusts and faults</u> .....	61
2.5.5	<u>Restoring folds</u> .....	64
2.5.6	<u>Strain Analysis Measures</u> .....	71
2.6	<u>Experimental Techniques for Analysis of Subsurface Well Data</u> .....	76
2.6.1	<u>Fracture Image logs</u> .....	76
2.6.2	<u>Dynamic flow logs</u> .....	78
2.6.3	<u>Single well pressure build-up or fall off tests</u> .....	78
2.6.4	<u>Falloff and Multi-well Interference Testing:</u> .....	79
2.6.5	<u>Injected tracer studies</u> .....	80
2.6.6	<u>Analysis of well tests using DFN models</u> .....	83
2.7	<u>Experimental Techniques for Comparison of Strain Values Calculated from 3D Palinspastic Reconstruction with Fracture Orientations and Intensity in Outcrop</u> .....	84

2.8	<a href="#">Experimental Techniques For Validation of DFN Model Geometry and Connectivity Using Subsurface Fracture Geometry and Flow Data</a>	87
2.9	<a href="#">Integration of the Matrix and Fault Block Architecture Into a Single Numerical Reservoir Model</a>	88
2.10	<a href="#">Assessment of Compartmentalization/Tributary Drainage in Fracture Networks</a>	89
2.11	<a href="#">Calculation of Effective Reservoir Properties</a>	92
2.11.1	<a href="#">Calculation of parameters for the DFN model</a>	92
2.11.2	<a href="#">Generation of the DFN models</a>	97
2.11.3	<a href="#">calculation of effective reservoir properties</a>	101
2.12	<a href="#">Integration of the Matrix and Fault Block Architecture Into a Single Numerical Reservoir Model</a>	103
3	<a href="#">RESULTS</a>	105
3.1	<a href="#">Overview</a>	105
3.2	<a href="#">Matrix Property Calculations</a>	106
3.3	<a href="#">Fault Block Reconstructions</a>	108
3.4	<a href="#">Validation of Cross Sections Using Retrodeformation Software</a>	120
3.4.1	<a href="#">Overview</a>	120
3.4.2	<a href="#">Implications of restoring the geological model</a>	121
3.4.3	<a href="#">Creation of polygonal volumes</a>	122
3.4.4	<a href="#">Restoring faults and thrusts</a>	123
3.4.5	<a href="#">Restoring the initial fold structure</a>	123
3.5	<a href="#">Geological Controls on Fracture Development in the Reservoir</a>	127
3.5.1	<a href="#">Field Data Collection &amp; Analysis</a>	127
3.5.2	<a href="#">Comparison of outcrop &amp; subsurface fracture orientations and intensity with structural history</a>	139
3.5.3	<a href="#">Evolution of fracture fairways due to development of structural hinges</a>	155
3.6	<a href="#">Development of the Reservoir Scale Fracture Model</a>	173
3.6.1	<a href="#">Conductive fracture intensity</a>	173
3.6.2	<a href="#">Derivation of fracture flow parameter values from well tests</a>	178
3.6.3	<a href="#">DFN Model parameter summary</a>	193
3.7	<a href="#">Calculation of Reservoir Engineering Parameters</a>	195
3.8	<a href="#">3D Integrated Reservoir Model</a>	197
3.9	<a href="#">Evaluation of Reservoir Management Strategies</a>	200
3.10	<a href="#">Technology Transfer</a>	203
3.10.1	<a href="#">Meetings and workshops</a>	203
3.10.2	<a href="#">Publications/Conference presentations</a>	203
3.10.3	<a href="#">Project Web Site</a>	205
4	<a href="#">CONCLUSIONS</a>	208
4.1	<a href="#">Overview</a>	208
4.2	<a href="#">Improvements in Reservoir Understanding</a>	208
4.2.1	<a href="#">Fault Block architecture</a>	208
4.2.2	<a href="#">Matrix properties</a>	210
4.2.3	<a href="#">Reservoir scale fracturing</a>	211
4.2.4	<a href="#">Reservoir visualization</a>	211
4.3	<a href="#">Development of Reservoir Management Strategies</a>	213

4.3.1	<u>Calculation of effective fracture properties for numerical reservoir simulation.....</u>	213
4.3.2	<u>Use of project results for enhanced recovery process selection and design</u> 214	
5	<u>REFERENCES.....</u>	216
6	<u>APPENDIX.....</u>	220

**List of Graphical Materials**

[Figure 1-1. Impact of fracture knowledge on recovery, Tract 17, Yates Field, TX](#) ..... 1

[Figure 1-2. The first step to improved oil recovery is to admit that you have a fracture problem. Typified by this photograph of a crack in the pavement opposite an outcrop of Tensleep Sandstone in the Wind River Canyon, engineers sometimes try to “pave over” fractures and hope that the problems will go away. However, as the photograph above shows, the fracture opens up each Spring no matter how much “paving over” takes place. The fracture in the pavement actually is part of a very large \(over 40 m high\) fracture that is obvious in the vertical outcrop. There is little hope that putting tar into the fracture each summer will ever stop fluids from moving through the large fracture and disrupting the pavement.](#)..... 2

[Figure 1-3. Outcrop of Tensleep Formation, Wind River Canyon, Wyoming, illustrating roles of matrix as storage and natural fractures as permeability.](#)..... 3

[Figure 1-4. Location map of the Circle Ridge Field.](#)..... 4

[Figure 1-5. Index map showing the Circle Ridge Field and surrounding positive and negative structural elements that define the primary basin and uplift pattern in Wyoming.](#)..... 7

[Figure 1-6 Schematic strain ellipsoid with  \$\sigma\_1\$  oriented parallel to the anticlinal axis of Circle Ridge \(modified from Reading, 1980\). Contractional structures, like reverse faults and anticlinal folds, are oriented parallel to  \$\sigma\_1\$ . Extensional structures, like normal faults, are oriented perpendicular to  \$\sigma\_1\$ . Oblique faults, indicated with arrows in the slip direction, are oriented  \$30^\circ\$  to  \$\sigma\_3\$ .](#)..... 7

[Figure 1-7. False-color satellite photo of the Circle Ridge Field. The Field formed due to compression and thrusting from the northeast. Note the increased shortening in the northwestern end of the Field. The increased shortening was accommodated through tighter folding and imbricate faulting.](#)..... 8

[Figure 1-8 Stratigraphic column for the Circle Ridge Formation \(from Smith 2000\).](#)..... 9

[Figure 1-9. Geologic map \(from Smith, 2000\). Geological symbols used in map are referenced in Figure 1-8.](#)..... 10

[Figure 1-10. Relation between principal stress directions and resultant fracture orientations \(Riedel, 1929\).  \$\sigma\_1\$  and  \$\sigma\_3\$  are the maximum and minimum principal stresses, respectively. “T” is the extension \(Mode I\) joint set. “R” and “R” are the primary and secondary Riedel shears, which are active in compression, typically when the deformation occurs deep in the crust, pore pressures are low and the angle between  \$\sigma\_1\$  and the reference fault plane is large. At shallow depths, low confining pressures, high pore pressures or when the master fault subparallels  \$\sigma\_1\$ , the “P”, “X” and “T” sets are favored.](#)..... 17

[Figure 1-11. Illustration of release \(b-c\) and extension \(a-c\) joints in relation to fold geometry.](#)..... 18

[Figure 1-12. Schematic diagram of Stearns model of fracture orientations related to folding. The red line in the Type I fracture group is a joint or extension fracture, while the orange lines show the orientations of Type I conjugate “shear” fractures. The yellow line shows the orientation of the Type II joint or extension fracture, while the cyan lines show the orientations of the Type II conjugate “shear” fractures. The complete Stearns model contains other fractures not shown in the schematic above.](#)..... 19

<a href="#">Figure 1-13. Steoplots illustrating the characteristic relations of the Type I and Type II extension joint sets with respect to bedding.....</a>	20
<a href="#">Figure 2-1. Phosphoria MULTIMIN display.....</a>	25
<a href="#">Figure 2-2. Picket Plot for Shoshone 66-49, Phosphoria Formation.....</a>	27
<a href="#">Figure 2-3. Phosphoria MULTIMIN predicted and real logs .....</a>	28
<a href="#">Figure 2-4. Tensleep MULTIMIN display .....</a>	30
<a href="#">Figure 2-5. Pickett Plot for well 66-49, Tensleep Formation.....</a>	31
<a href="#">Figure 2-6. Tensleep MULTIMIN predicted and actual logs .....</a>	32
<a href="#">Figure 2-7. Crossplot of rhob and nphi in Shoshone 66-49, Phosphoria Formation.....</a>	33
<a href="#">Figure 2-8. Crossplot of rhob and nphi in Shoshone 66-49, Tensleep Formation.....</a>	34
<a href="#">Figure 2-9. Comparison of crossplot porosity (X-axis) to MULTIMIN porosity (PHIT – Y-axis) in the Phosphoria Formation for 46 wells. ....</a>	35
<a href="#">Figure 2-10. Comparison of crossplot porosity (X-axis) to MULTIMIN porosity (PHIT – Y-axis) in the Tensleep Formation for 46 wells.....</a>	36
<a href="#">Figure 2-11. Porosity determination from density log, Shoshone 66-49, Phosphoria Formation. ....</a>	37
<a href="#">Figure 2-12. Porosity determination from density log, Shoshone 66-49, Tensleep Formation. ....</a>	38
<a href="#">Figure 2-13. GRN log, Shoshone 66-15, Tensleep Formation.....</a>	40
<a href="#">Figure 2-14. GRN log, Shoshone 66-45, Phosphoria Formation.....</a>	41
<a href="#">Figure 2-15. GRN log, Shoshone 66-45, Tensleep Formation.....</a>	42
<a href="#">Figure 2-16. Frequency plot of GRN count rate (NEU), Shoshone 66-34.....</a>	43
<a href="#">Figure 2-17. Rescale module with representative settings for the GRN count rate (NEU) to porosity (PHIT_NEU), Shoshone 66-34.....</a>	44
<a href="#">Figure 2-18. Picture showing the topography of Circle Ridge. The spectrum corresponds to elevation where red is the highest and green represents the lower parts. The fault traces of the Red Gully and Green Valley faults cross cut the whole field. Orange Canyon and Blue Draw are also shown in the NW part of the field. The cross-sections are shown as hatched lines. The P, T and Z sections were produced by Anderson and O’Connell (1993) and H01, H02 and H03 are the new cross-sections from the June field campaign.....</a>	45
<a href="#">Figure 2-19. Scanline affixed to Triassic Red Peak Member.....</a>	46
<a href="#">Figure 2-20. Detail of scanline measurements. The photo illustrates the measurement of fracture trace length for a specific fracture crossing the scanline.....</a>	47
<a href="#">Figure 2-21. Example of data recorded for each scanline.....</a>	47
<a href="#">Figure 2-22. Analysis of fracture orientations, including rotation into bedding plane.....</a>	48
<a href="#">Figure 2-23. Example of possible interpretation of fracture orientations relative to bedding orientation.....</a>	49
<a href="#">Figure 2-24. Methodology for calculating intensity scaling parameters. ....</a>	50
<a href="#">Figure 2-25. Example of a plot to determine the intensity scaling characteristics of fracture data collected along a scanline.....</a>	51
<a href="#">Figure 2-26. Illustration of the structural restoration process.....</a>	53
<a href="#">Figure 2-27. Perspective view of the Anderson and O’Connell (1993) P, T ad Z sections as they appear in the 3D model. ....</a>	55
<a href="#">Figure 2-28. Cross-sections H01, H02 and H03 performed by the project team during the June 2000 field campaign.....</a>	56

<a href="#">Figure 2-29. Geological map of Circle Ridge modified after Anderson and O’Connell (1993) and Smith (2000).</a>	56
<a href="#">Figure 2-30. Competent sandstone horizons in the Sundance Formation forms vertical walls of rock in the southern part of Circle Ridge.</a>	57
<a href="#">Figure 2-31 Overthrust block at Circle Ridge after Smith (2000).</a>	58
<a href="#">Figure 2-32. 3D Model of the major faults in the field; The Red Gully (red) and Green Valley (green) Faults and the Blue Draw Fault (blue), Gray Wash Fault (gray), Purple Sage Fault (behind), and Yellow Flats Fault (behind) together with the Phosphoria (gray) and Tensleep (orange) formations.</a>	59
<a href="#">Figure 2-33 Illustration of a cross-section of the calculated flow path along a fault surface (from Midland Valley, 2000).</a>	62
<a href="#">Figure 2-34 Slip slider menu in 3DMove to perform movement by slip value (from Midland Valley, 2000)</a>	62
<a href="#">Figure 2-35 Shear calculation using fault parallel flow (from Midland Valley, 2000)</a>	63
<a href="#">Figure 2-36 Slip along flowlines using the restore to surfaces movement mode (from Midland Valley, 2000)</a>	64
<a href="#">Figure 2-37 Implications of the Restore-to-Surface movement method (from Midland Valley, 2000)</a>	64
<a href="#">Figure 2-38 Cross-section through a hanging wall fold (from Midland Valley, 2000)</a>	65
<a href="#">Figure 2-39 Cross-section through the restored hanging wall fold (from Midland Valley, 2000)</a>	66
<a href="#">Figure 2-40 The concept of vertical shear and the restored length (l) (from Midland Valley, 2000)</a>	66
<a href="#">Figure 2-41 Illustration of the flexural slip unfolding algorithm (from Midland Valley, 2000)</a>	68
<a href="#">Figure 2-42 Orientation of the pin plane/surface and strain plane. Red arrow indicates the unfolding direction (from Midland Valley, 2000)</a>	69
<a href="#">Figure 2-43 Maintaining sinuous line length with a vertical pin (from Midland Valley, 2000)</a>	69
<a href="#">Figure 2-44 Illustration of the bed linkage and the slip system for each vertex in the deformed formation (from Midland Valley, 2000)</a>	70
<a href="#">Figure 2-45 Flexurally unfolded template and passive horizons (from Midland Valley, 2000)</a>	70
<a href="#">Figure 2-46 Strained tetrahedron with strain ellipsoid. The XYZ axes are eigenvectors of the strain field, and are the principal strain axes.</a>	72
<a href="#">Figure 2-47 Example of the calculation of current dilatation (from Midland Valley, 2000)</a>	73
<a href="#">Figure 2-48 Example of absolute and RMS dilation calculations (from Midland Valley, 2000)</a>	73
<a href="#">Figure 2-49 Flinn diagram showing the nature of the strain; plane, constrictional or flattening strain ellipsoid.</a>	75
<a href="#">Figure 2-50. Location of wells in which fracture image log and spinner survey data was collected for the project. Shoshone 66-07 and Shoshone 66-14 are in the Overthrust block.</a>	77
<a href="#">Figure 2-51. Location of wells in which single-well buildup or fall-off test data was obtained for the project.</a>	79

<a href="#">Figure 2-52. Location of wells used in multiwell interference testing.</a>	80
<a href="#">Figure 2-53. Location of wells in which Bottom Hole Pressures (BHP) were monitored during the Nitrogen Injection experiment. Shoshone 65-02 was the injector.</a>	81
<a href="#">Figure 2-54. Location of injection well (Shoshone 65-20 – colored red) and monitoring wells (colored cyan and purple) used for bromide tracer test in the subthrust Phosphoria.</a>	82
<a href="#">Figure 2-55. Scanline used to measured fractures. Outcrop is of the Triassic Red Peak Member of the Chugwater Formation.</a>	85
<a href="#">Figure 2-56. DFN model for subthrust block 6, showing fracture compartments formed due to variation in intensity related to folding. The diagram on the left shows all fractures and three vertical well locations. The diagram on the right shows the fracture compartments.</a>	90
<a href="#">Figure 2-57. Hypothetical example of how strain maps and subsurface tracer data can be related to understand compartmentalization and tributary drainage. Green circle represent wells that appear to have strong pressure or flow connection in a tracer test, while white-shaded circle represent wells that appear disconnected. The contour colors denote the magnitude of strain, while the blue arrows indicate the trend of the dominant extensional fracture set predicted from the strain tensor.</a>	91
<a href="#">Figure 2-58. Example of fractures of identical orientations belonging to different sets.</a>	93
<a href="#">Figure 2-59. Example of data being entered into FRED for generation of a fracture set.</a>	98
<a href="#">Figure 2-60. Generation of one fracture set in a DFN model. The block shown is Block 6, Tensleep Formation, viewed from east to west. The grid shown is the tetrahedral grid containing extensional strain values and orientations produced in the palinspastic reconstruction of the field.</a>	99
<a href="#">Figure 2-61. Example of fracture set clipped against upper and lower boundaries of Tensleep Formation, Block 6.</a>	99
<a href="#">Figure 2-62. Final DFN model for Tensleep Formation, Block 6, including both major fracture sets clipped against the upper and lower boundaries of the Tensleep Formation.</a>	100
<a href="#">Figure 2-63. DFN model of structural blocks 6, 8 and 9 for both Tensleep and Phosphoria Formations. Also shown are the Green Valley, Yellow Flats and Blue Wash Faults.</a>	100
<a href="#">Figure 2-64. Example of a grid (cyan) generated between the upper (red) and lower (green) Tensleep boundaries for Block 6.</a>	102
<a href="#">Figure 2-65. Values of vertical permeability calculated for grid shown in Figure 2-64. Values are in mD.</a>	102
<a href="#">Figure 2-66. Data flow from project tasks into the integrated reservoir model.</a>	104
<a href="#">Figure 3-1. Expansion of matrix property data through re-calibration of older logs. Photograph on left shows wells (red circles) where modern logs had previously made it possible to calculate matrix porosity and oil saturation. Photograph on right shows wells (yellow circles) in which re-calibrated logs were used to estimate matrix properties.</a>	106
<a href="#">Figure 3-2. Use of project website to download interpreted well log data, including matrix porosity and saturations.</a>	107
<a href="#">Figure 3-3. Determining fault block geometry through a 3D balanced reconstruction.</a>	108

<a href="#"><u>Figure 3-4. The field mapping team for the cross-section and fracture data collection. From left to right: Paul La Pointe (Golder); Jan Hermanson (Golder); Sherry Blackburn (enrolled member of the Northern Arapaho Tribe &amp; Marathon Oil intern).</u></a>	109
<a href="#"><u>Figure 3-5. The cross sections were mapped using GPS locations of contacts. The sections were anchored to benchmarks (like the one shown in the photo) and routed through or very near to wells in key areas of the fields.</u></a>	109
<a href="#"><u>Figure 3-6 Example of minor normal and strike slip faults in the northeastern corner of the field. Gypsum Springs is offset in several sections by less than 20 ft.</u></a>	110
<a href="#"><u>Figure 3-7 Photograph showing the Green Valley Fault offset in the Gypsum Springs and the Popo Agie where finger is pointing. The Red Gully Fault runs through the larger gap in the Popo Agie member below the hand.</u></a>	111
<a href="#"><u>Figure 3-8 View down the Orange Canyon with Red Peak shales and sands to the left and Gypsum Springs to the right.</u></a>	112
<a href="#"><u>Figure 3-9 Top view of the location of major fault blocks in the Phosphoria formation.</u></a>	113
<a href="#"><u>Figure 3-10 Illustration of the undulating extension of the top of the Phosphoria formation. The undulation of the surface is controlled by well top information from the Anderson and O'Connell database.</u></a>	113
<a href="#"><u>Figure 3-11 3D Illustration of the extension of the Red Gully Fault and the Green Valley Fault based on the well tops and the surface geology. The intersection between the two shows that the Green Valley Fault needs to be steeper than the Red Gully Fault in order to honor the well top data.</u></a>	114
<a href="#"><u>Figure 3-12 Illustration of the original extension of the Orange Canyon Fault in a bow shape below the Circle Ridge structure. This extension has no basis in well top information and has been excluded in the restoration process. The red line on the fault surface indicates where the new interpretation ends. Cross-sections are shown for a better 3D understanding of the extension of the fault.</u></a>	115
<a href="#"><u>Figure 3-13 The location of the Anderson and O'Connell cross-sections (P-P', T-T' and Z-Z') and the new cross-sections assembled during the 2000 summer field campaign (H01 to H03). The black lines represent the main fault traces of the Red Gully, Green Valley, Orange Canyon and Blue Draw faults.</u></a>	116
<a href="#"><u>Figure 3-14 Cross-section P to P' after Anderson and O'Connell (1993)</u></a>	117
<a href="#"><u>Figure 3-15 Cross-section T to T' after Anderson and O'Connell (1993).</u></a>	117
<a href="#"><u>Figure 3-16 The H01-H01' cross-section</u></a>	118
<a href="#"><u>Figure 3-17 The H02-H02' cross-section</u></a>	118
<a href="#"><u>Figure 3-18 The H03-H03' cross-section</u></a>	119
<a href="#"><u>Figure 3-19. Fault reconstructions for the Circle Ridge Field.</u></a>	120
<a href="#"><u>Figure 3-20 The Phosphoria, Tensleep and Amsden formation top surfaces</u></a>	120
<a href="#"><u>Figure 3-21 Close-up of the polygons of fault blocks 6 and 9 on the Phosphoria surface as defined by Smith (2000).</u></a>	121
<a href="#"><u>Figure 3-22 Phosphoria and Tensleep volume elements</u></a>	122
<a href="#"><u>Figure 3-23 Illustration of the unfaulted Tensleep formation showing fault blocks 1, 6, 8, 9, 11 and 14 in green color as part of the overthrust and the top of the anticline.</u></a>	124
<a href="#"><u>Figure 3-24 Completely restored Tensleep formation using Flexural Slip Unfolding. The color map reflect the amount of accumulated strain throughout the restoration process where blue colors are lowest recorded strains and the red are the highest.</u></a>	125

<a href="#">Figure 3-25 Vertical Shear Unfolding of the unfaulted Tensleep formation (top view). The color map shows the accumulated strain, with blue colors showing the lowest recorded strains and the red colors the highest.</a>	126
<a href="#">Figure 3-26 Vertical Shear Unfolding of the unfaulted Phosphoria formation (top view). The color map shows the accumulated strain, with blue colors showing the lowest recorded strains and the red colors the highest.</a>	126
<a href="#">Figure 3-27 Vertical Shear Unfolding of the unfaulted Amsden formation (top view). The color map shows the accumulated strain, with blue colors showing the lowest recorded strains and the red colors the highest.</a>	127
<a href="#">Figure 3-28. Stereoplot for Scanline 1, rotated relative to bedding plane.</a>	129
<a href="#">Figure 3-29. Stereoplot for Scanline 2, rotated relative to bedding plane.</a>	129
<a href="#">Figure 3-30. Stereoplot for Scanline 3, rotated relative to bedding plane.</a>	130
<a href="#">Figure 3-31. Stereoplot for Scanline 4, rotated relative to bedding plane.</a>	130
<a href="#">Figure 3-32. Stereoplot for Scanline 5, rotated relative to bedding plane.</a>	131
<a href="#">Figure 3-33. Stereoplot for Scanline 6, rotated relative to bedding plane.</a>	131
<a href="#">Figure 3-34. Stereoplot for Scanline 7, rotated relative to bedding plane.</a>	132
<a href="#">Figure 3-35. Stereoplot for Scanline 5, rotated relative to bedding plane.</a>	132
<a href="#">Figure 3-36. Stereoplot for Scanline 9, rotated relative to bedding plane.</a>	133
<a href="#">Figure 3-37. Stereoplot for Scanline 11, rotated relative to bedding plane.</a>	133
<a href="#">Figure 3-38. Mass dimension calculations for the 11 scanline sites. Plots a through k are, in order, for scanlines 1 through 11.</a>	135
<a href="#">Figure 3-39. Composite plot of mass dimension calculations for all 11 scanlines.</a>	138
<a href="#">Figure 3-40. Map of principal extensional strain magnitude produced by folding. The contour map shows the approximate horizontal limits of the fault blocks used in the reconstruction. The location of the eleven scanline sites are shown on the map. The strains shown have been mapped on the present-day structural configuration of the Circle Ridge Field, and represent deformation in the Tensleep Formation.</a>	139
<a href="#">Figure 3-41. Fracture orientations measured at scanlines 6 (red circle) and 5 (black circle). Black lines indicate trend of principal extension. Lines lengths are proportional to the magnitude of extension.</a>	140
<a href="#">Figure 3-42. Plunge of principal direction of extension (contours) and trend of maximum extension direction. Plunge at Scanline 6 (red circle) is about 50° to the northeast. Plunge at Scanline 5 (black circle) is similar. Black lines indicate trend of principal extension. Lines lengths are proportional to the magnitude of extension.</a>	141
<a href="#">Figure 3-43. Comparison of extensional strain and fracture orientations measured at scanlines 7 (yellow circle), 8 (red circle) and 9 (violet circle). Black lines indicate trend of principal extension. Lines lengths are proportional to the magnitude of extension.</a>	142
<a href="#">Figure 3-44. Plunge of principal direction of extension (contours) and trend of maximum extension direction. Green shading indicates very shallow plunges. The three scanlines generally are in the vicinity of very shallow plunges, varying from -30° to +30°. This is consistent with the steep dips shown by all of the major joint sets in Scanlines 7, 8 and 9. Black lines indicate trend of principal extension. Lines lengths are proportional to the magnitude of extension.</a>	142
<a href="#">Figure 3-45. Orientation of joints and principal extensional strain for Scanline 10 (Red Peak). The direction of strain is perpendicular to the dominant northeasterly-striking</a>	

joint set. Black lines indicate trend of principal extension. Lines lengths are proportional to the magnitude of extension.....	143
Figure 3-46. Plunge of principal direction of extension (contours) and trend of maximum extension direction. The contours show the amount of plunge of the principal direction of extension. Green shading indicates very shallow plunges. Black lines indicate trend of principal extension. Lines lengths are proportional to the magnitude of extension.....	144
Figure 3-47. Orientation of joints and principal extensional strain for Scanline 11 (Red Peak). The direction of strain is perpendicular to the dominant northeasterly-striking joint set. Black lines indicate trend of principal extension. Lines lengths are proportional to the magnitude of extension.....	145
Figure 3-48. Plunge of principal direction of extension (contours) and trend of maximum extension direction around Scanline 11. The contours show the amount of plunge of the principal direction of extension. Light blue shading indicates shallow plunges. Black lines indicate trend of principal extension. Lines lengths are proportional to the magnitude of extension.....	145
Figure 3-49. Orientation of joints and principal extensional strain for Scanlines 1 and 2 (pink circle), Scanline 3 (red circle) and Scanline 4 (black circle). Black lines indicate trend of principal extension. Lines lengths are proportional to the magnitude of extension.....	147
Figure 3-50. Plunge of principal direction of extension (contours) and trend of maximum extension direction around Scanlines 1, 2 (pink circle) 3 (red circle) and 4 (black circle). The contours show the amount of plunge of the principal direction of extension. Dark blue and orange/red shading indicates steep plunges. Black lines indicate trend of principal extension. Lines lengths are proportional to the magnitude of extension.....	147
Figure 3-51. Comparison of fracture orientations in outcrop and in the subsurface for Shoshone 66-14.....	148
Figure 3-52. Comparison of fracture orientations in outcrop and in the subsurface for Shoshone 66-07.....	149
Figure 3-53. Comparison of fracture orientations in Shoshone 65-37 with direction of maximum extension.....	151
Figure 3-54. Comparison of fracture orientations in Shoshone 66-14 with direction of maximum extension.....	151
Figure 3-55. Comparison of fracture orientations in Shoshone 66-07 with direction of maximum extension.....	152
Figure 3-56. Graph of fracture intensity vs. extensional strain magnitude.....	153
Figure 3-57. Comparison of strain magnitude and fracture intensity in outcrop near the northwest nose of the anticline.....	154
Figure 3-58. 3D view of imbricate blocks 6, 8 and 9 from the north looking south. The orange and blue dashed lines correspond to high strain corridors that separate the rock into panels that have more or less constant dip.....	155
Figure 3-59. 3D view of imbricate blocks and illustration of two horizontal “hinges” or flexure zones (orange dashed lines) formed during the initial folding of the field....	156
Figure 3-60. Example of a horizontal flexure zone. Most rock does not deform in a continuous curve (cyan-colored line), but rather as panels with more or less constant	

<u>curvature that deform in zones of higher intensity fracturing or faulting between panels (red lines). The more highly fractured nature of these hinge zones typically leads to greater erosion on the surface.</u> .....	157
<u>Figure 3-61. Example of a dip-parallel flexural hinge zone. The lower photo shows approximate bedding orientation for two blocks of Crow Mountain in the eastern portion of the Field. The difference in strike is over 18°, although the perspective of the photo makes this less obvious. The black arrow indicates the location of the flexural hinge, and as seen in both the top photo and the lower photo, this zone is much more highly fractured and eroded than the adjacent rock blocks. The top photo is taken at the top of the flexural hinge gully looking downward in the direction of the arrow in the lower photo.</u> .....	158
<u>Figure 3-62. Structural blocks involved in the Bromide Tracer experiment in the Phosphoria Formation. Blocks 6, 8 and 9 are the uppermost imbricate fault blocks.</u> .....	159
<u>Figure 3-63. Time vs. bromide concentration for the bromide tracer test monitoring wells.</u> .....	161
<u>Figure 3-64. Bromide tracer test breakthrough pattern. The bromide was injected into Shoshone 65-20 (colored red). Large and nearly instantaneous breakthrough was seen in Shoshone 65-53; other strong breakthroughs were seen in Shoshone 65-37 (4 days) and in Shoshone 65-73 (20 hours). These wells are colored orange. The other wells (purple indicates a Tensleep completion with no Phosphoria completion; blue a Phosphoria completion) were monitored, but no large breakthroughs were seen. ....</u>	163
<u>Figure 3-65. Large-scale fracturing in the upper Tensleep Formation at Zeisman dome. Upper photo shows large joints that extend from the top of the dune sequence to the bottom of the dune sequence, but consistently terminate at the boundaries of the dune sequence (lower photo).</u> .....	164
<u>Figure 3-66. Fracture strikes inferred from strain field. Black lines indicate strike of dominant extensional fracture set, while length of line and color of contour indicates the magnitude of extensional strain. Wells are color-coded according to result and completion interval: black = injector; purple = Tensleep but no Phosphoria completion; blue = Phosphoria completion but no response; orange = Phosphoria completion and breakthrough observed.</u> .....	165
<u>Figure 3-67. Bottom-hole pressures measured during nitrogen injection test.</u> .....	166
<u>Figure 3-68. Surface pressures measured during the nitrogen injection test.</u> .....	167
<u>Figure 3-69. Overview of Nitrogen Injection tests results. The Overthrust Block is viewed looking from southeast to northwest. Contours indicate extensional strain magnitude, red lines indicate strike of fractures in response to extensional strain field. Wells where nitrogen breakthrough was indicated are shown; size of yellow circle at well top indicates the time of breakthrough (large circle indicate slow response; small circles indicate rapid response). Nitrogen test took place in upper portion of the structure where the reservoir tends to flatten.</u> .....	168
<u>Figure 3-70. Pressure magnitudes and possible migration pathways for the nitrogen injection test. View is looking down on the structure from the southwest to the northeast. Size of circles indicates magnitude of pressure response. The largest responses were seen in two wells on flexure corridors close to the injector. Most of the responding wells are either in the cyan-colored pod above and left (northwest) of</u>	

<a href="#"><u>the injector, or along the downdip flexure corridor to the right (southeast) of the injector.....</u></a>	169
<a href="#"><u>Figure 3-71. Time to breakthrough for only the wells in which a breakthrough response was observed. Radius of circle is proportional to time of breakthrough, so large circle indicate a longer time to breakthrough than small circles. Note that the responding wells tend to be in the high strain regions around the injector, and that the time to breakthrough is relatively short for the 5 wells in the center of the diagram nearest the injector, and increases along the red-dashed fracture corridors as indicated in the figure. ....</u></a>	170
<a href="#"><u>Figure 3-72. Delineation of strain pods. Most of the responding wells are in one of two strain “pods”. Non-responding wells are typically not in these pods. They tend to be in low strain zones or in pods separated from the pods connected to the injector pods by areas of low strain. White dashed line indicates a dip-parallel flexure zone. ....</u></a>	171
<a href="#"><u>Figure 3-73. Strain pattern and the development of dip-parallel and strike parallel hinge zones.....</u></a>	172
<a href="#"><u>Figure 3-74. Orientation of fractures and bedding in Shoshone 66-14 interpreted from image logs. The top of the Tensleep Formation is shown by the solid blue line. ....</u></a>	174
<a href="#"><u>Figure 3-75. Cumulative fracture count for Shoshone 66-14 for fractures interpreted from image log. Red solid lines indicate alternating zones of higher and lower fracture intensity. Dashed blue line indicates the approximate top of the Tensleep Formation. ....</u></a>	175
<a href="#"><u>Figure 3-76. Correspondence of bedding intensity and fracture intensity. Intensity is calculated over 15 ft (4.572 m) non-overlapping windows. ....</u></a>	176
<a href="#"><u>Figure 3-77. Cumulative production profile for Shoshone 66-14.....</u></a>	177
<a href="#"><u>Figure 3-78. Comparison of cumulative fracture intensity and cumulative production from Shoshone 66-14. The red line is the % production from the spinner survey data. The blue line is the cumulative percent of fractures starting at a depth of 835 ft. (there were not enough 4-pad fractures to plot this component separately). ....</u></a>	178
<a href="#"><u>Figure 3-79. Key well locations for nitrogen injection test. ....</u></a>	179
<a href="#"><u>Figure 3-80. Local scale DFN model for Shoshone 65-02.....</u></a>	181
<a href="#"><u>Figure 3-81. Pressure snap shot at 100 hours. Color indicates change from initial reservoir conditions in red.....</u></a>	181
<a href="#"><u>Figure 3-82. Build up test simulations for average fracture permeabilities of 1 to 1000 mD .....</u></a>	182
<a href="#"><u>Figure 3-83. Permeability thickness values based on late-time derivative curves.....</u></a>	182
<a href="#"><u>Figure 3-84. Strain grid for development of regional scale model.....</u></a>	183
<a href="#"><u>Figure 3-85. Regional scale DFN model populated by strain perpendicular and strain parallel fracture sets. ....</u></a>	184
<a href="#"><u>Figure 3-86. Fracture intensity values (<math>P_{32}</math>) resulting from an average <math>P_{32}</math> value of 0.08</u></a>	185
<a href="#"><u>Figure 3-87. Pressure snapshot of injection in regional model with permeability ratio Set1:S .....</u></a>	187
<a href="#"><u>Figure 3-88. Pressure snapshot of injection in regional model permeability ratio Set1:Set2 = 10. This simulation shows earlier pressure breakthrough to the north-west and south-east rather than to the north-east set2 = 1.....</u></a>	187
<a href="#"><u>Figure 3-89. Permeability ratio Set1:Set2 = 0.1.....</u></a>	188

<a href="#">Figure 3-90. Change in pressure for wells 52, 49 and 68. Pressure response is quicker for Shoshone 66-68 because it is closer to the injection in Shoshone 65-2.....</a>	188
<a href="#">Figure 3-91. Change in pressure for wells 65-52, 66-49 and 66-68. Pressure response is quicker for Shoshone 66-49 although Shoshone 66-68 is closer to the injection in Shoshone 65-2.....</a>	189
<a href="#">Figure 3-92. Breakthrough curves for all wells for varying the ratio of the fracture intensities between the T and L sets.....</a>	189
<a href="#">Figure 3-93. Relative breakthrough curves as a function of fracture length.....</a>	190
<a href="#">Figure 3-94. High-resolution spinner profile for Shoshone 65-37.....</a>	192
<a href="#">Figure 3-95. Fall-off curve for Shoshone 65-20.....</a>	193
<a href="#">Figure 3-96. Outcrop of Tensleep Sandstone in the Wind River Canyon.....</a>	194
<a href="#">Figure 3-97. Example of the DFN model for imbricate blocks 8 and 9. The major faults (Red Gully, Yellow Flats, Green Valley and Blue Draw are also shown.....</a>	195
<a href="#">Figure 3-98. Examples of the calculation of effective reservoir properties for Block 6... </a>	196
<a href="#">Figure 3-99. Matrix porosity distributed from well data in the Overthrust Block. The colors represent the value of the porosity. The wells used to create the model are also shown, and the colors in these wells indicate the value of matrix porosity calculated from the wireline log suite. The subvertical surfaces shown are not faults, but rather fence displays of the matrix porosity to help visualize the three-dimensional distribution of the data.....</a>	197
<a href="#">Figure 3-100. Distribution of fracture porosity in the Overthrust Block.....</a>	198
<a href="#">Figure 3-101. Distribution of fracture intensity in the Overthrust Block.....</a>	198
<a href="#">Figure 3-102. Distribution of effective fracture <math>K_{xx}</math> values in the Overthrust Block.....</a>	199
<a href="#">Figure 3-103. Distribution of effective fracture <math>K_{yy}</math> values in the Overthrust Block.....</a>	199
<a href="#">Figure 3-104. Distribution of effective fracture <math>K_{zz}</math> values in the Overthrust Block.....</a>	200
<a href="#">Figure 3-105. Example of fracture model for use in drainhole planning.....</a>	202
<a href="#">Figure 3-106. Overview of home page for Circle Ridge Project.....</a>	205
<a href="#">Figure 3-107. Screen grab showing new interface for <i>Workflow</i> module.....</a>	206
<a href="#">Figure 3-108. Web site activity, August 17, 2000 through July 31, 2002.....</a>	207
<a href="#">Figure 4-1. Two of three structural cross-sections prepared by Anderson and O'Connell for the Circle Ridge Field.....</a>	208
<a href="#">Figure 4-2. 3D visualization of the faults as reconstructed in this project.....</a>	209
<a href="#">Figure 4-3. Visualization of fault surfaces prior to this project.....</a>	209
<a href="#">Figure 4-4. Expansion of matrix property knowledge through calibration of older wireline logs.....</a>	210
<a href="#">Figure 4-5. Satellite image of Field with perceived regional northeasterly striking fracture set superimposed on photo.....</a>	212
<a href="#">Figure 4-6. Rosette of Terzaghi-corrected fracture strikes at the eleven scanline sites.....</a>	212
<a href="#">Figure 4-7. Example of 3D visualization of reservoir parameter values and well control.....</a>	213
<a href="#">Figure 4-8. Water and oil rates for the Circle Ridge Field, 1978 – present.....</a>	214

## List of Tables

<a href="#">Table 2-1. Data sources for palinspastic reconstruction of Circle Ridge Field.</a> .....	54
<a href="#">Table 2-2. Coverage information for fracture image logs.</a> .....	77
<a href="#">Table 2-3. Coverage information for spinner and temperature logs.</a> .....	78
<a href="#">Table 3-1. Summary of mass dimensions for all 11 scanlines. Orange shading indicates Red Peak Member, while light blue shading indicates Crow Mountain Member.</a> ....	138
<a href="#">Table 3-2. Fracture intensity vs. extensional strain.</a> .....	153
<a href="#">Table 3-3. Raw data obtained in injection and monitoring wells during the bromide tracer experiment.</a> .....	160
<a href="#">Table 3-4. Summary of time to maximum measured bromide concentration. Values for wells shaded yellow represent maximum measured concentrations, but do not correspond to obvious breakthroughs, and may be more due to random fluctuations in bromide levels, measurement precision, minor breakthroughs, or some combination of these factors.</a> .....	161
<a href="#">Table 3-5. Injection rate data for nitrogen injection test.</a> .....	166
<a href="#">Table 3-6. Geometric inputs for local DFN model.</a> .....	180
<a href="#">Table 3-7. Input parameters for varying fracture intensities in T and L sets.</a> .....	190
<a href="#">Table 3-8. Input parameters for breakthrough test with variable fracture length.</a> .....	190
<a href="#">Table 3-9. Table of parameters for DFN models.</a> .....	194

# 1 INTRODUCTION

## 1.1 Overview of the Issues at Circle Ridge

Optimizing recovery in fracture-dominated reservoirs requires knowledge of both the spatial variation in matrix properties, the fault block architecture that may impact pressure and fluid communication between blocks, and how the variations in intensity and orientation of joints and small faults detract or enhance recovery.

Many fields have been produced as if the fractures were not present. Often the failure to appreciate the impact that natural fracturing can have on the effectiveness of recovery processes has led to continual decline. On the other hand, the attempt to better understand the fracturing and to tailor the recovery process to exploit the natural fracture system has led to increased recovery (Figure 1-1 and Figure 1-2).

Produced via depletion until; 1970.

In 1976, gas injection pressure maintenance program initiated to retard water invasion.

1979: water flooding commenced.

1983-1989: Polymer flooding

1985 – 1991: CO<sub>2</sub> injection

1992: Decision made to “Stop fighting fractures and take advantage of them”

1992: Detailed study of natural fracture system commences

1992 – 1994 : Nearly 400 well with poorly developed fracturing are shut in. Oil production rates remain stable.

1993 – 1994 : Nearly 30 short radius horizontal wells drilled, increasing production

1995 – present: Recognition of gravity drainage leads to implementation of a double-displacement production mechanism that leads to a 20% increase in production.

1997 – present: TAGS process exploits fractures to further enhance production through a combined steam injection-gravity drainage mechanism.

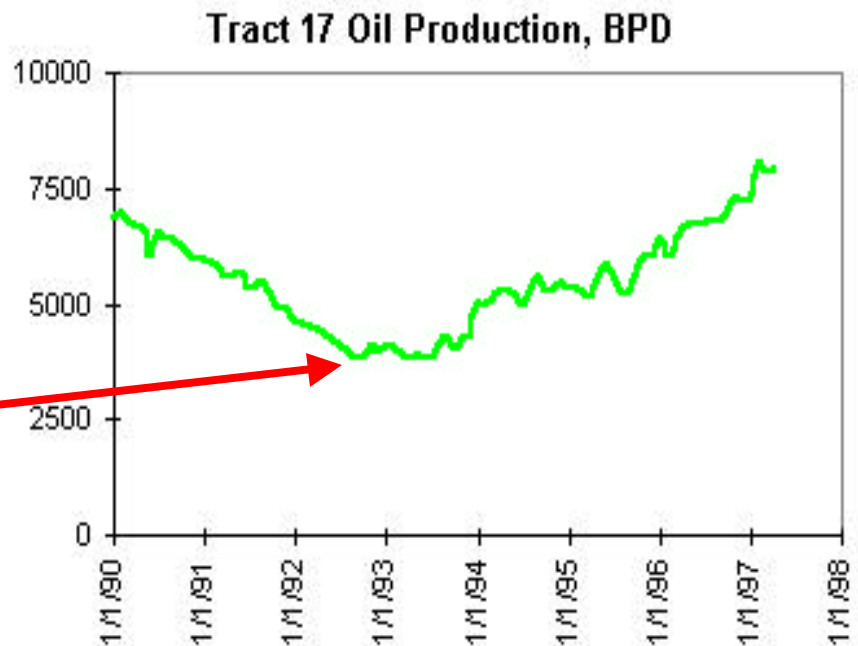
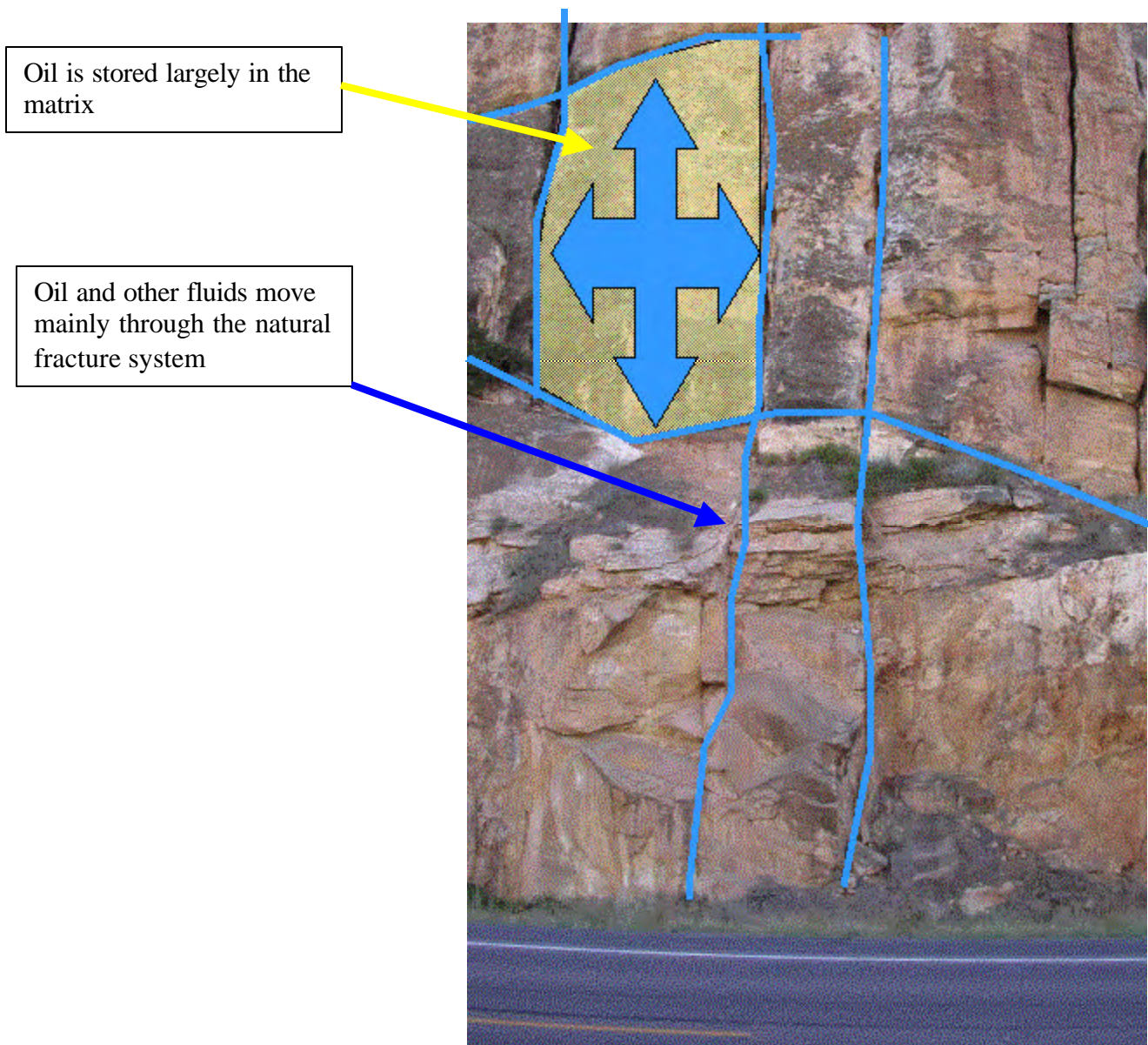


Figure 1-1. Impact of fracture knowledge on recovery, Tract 17, Yates Field, TX



**Figure 1-2. The first step to improved oil recovery is to admit that you have a fracture problem. Typified by this photograph of a crack in the pavement opposite an outcrop of Tensleep Sandstone in the Wind River Canyon, engineers sometimes try to “pave over” fractures and hope that the problems will go away. However, as the photograph above shows, the fracture opens up each Spring no matter how much “paving over” takes place. The fracture in the pavement actually is part of a very large (over 40 m high) fracture that is obvious in the vertical outcrop. There is little hope that putting tar into the fracture each summer will ever stop fluids from moving through the large fracture and disrupting the pavement.**

The production history of the Circle Ridge Field illustrates the opportunities that better knowledge of fracturing and matrix properties can have for increasing recovery and improving oil rates. This field has been under production for more than 50 years. However, to date less than 20% of the OOIP is estimated to have been recovered. A waterflood implemented in the largest reservoir block has been suspended. The reason that the Circle Ridge Field has had low recoveries is related to the impact of fractures as the primary conduits for fluid movement (Figure 1-3). In order to produce oil from the matrix, it is necessary that it move through the fracture system. If the wells do not adequately connect to the fracture system, then the injection efficiency or the tributary



**Figure 1-3. Outcrop of Tensleep Formation, Wind River Canyon, Wyoming, illustrating roles of matrix as storage and natural fractures as permeability.**

drainage for the well will be sub-optimal.

In keeping with their successful application of innovative reservoir management practices based on the characterization and exploitation of the fracture system (Figure 1-1) at Yates and elsewhere, Marathon Oil Company has identified the Circle Ridge Field as a promising candidate for improved recovery through gas injection.

The Circle Ridge Field is located on the Wind River Reservation in west central Wyoming (Figure 1-4). The Field is owned by the Northern Arapaho and Eastern Shoshone Tribes, and is operated by Marathon Oil Company.

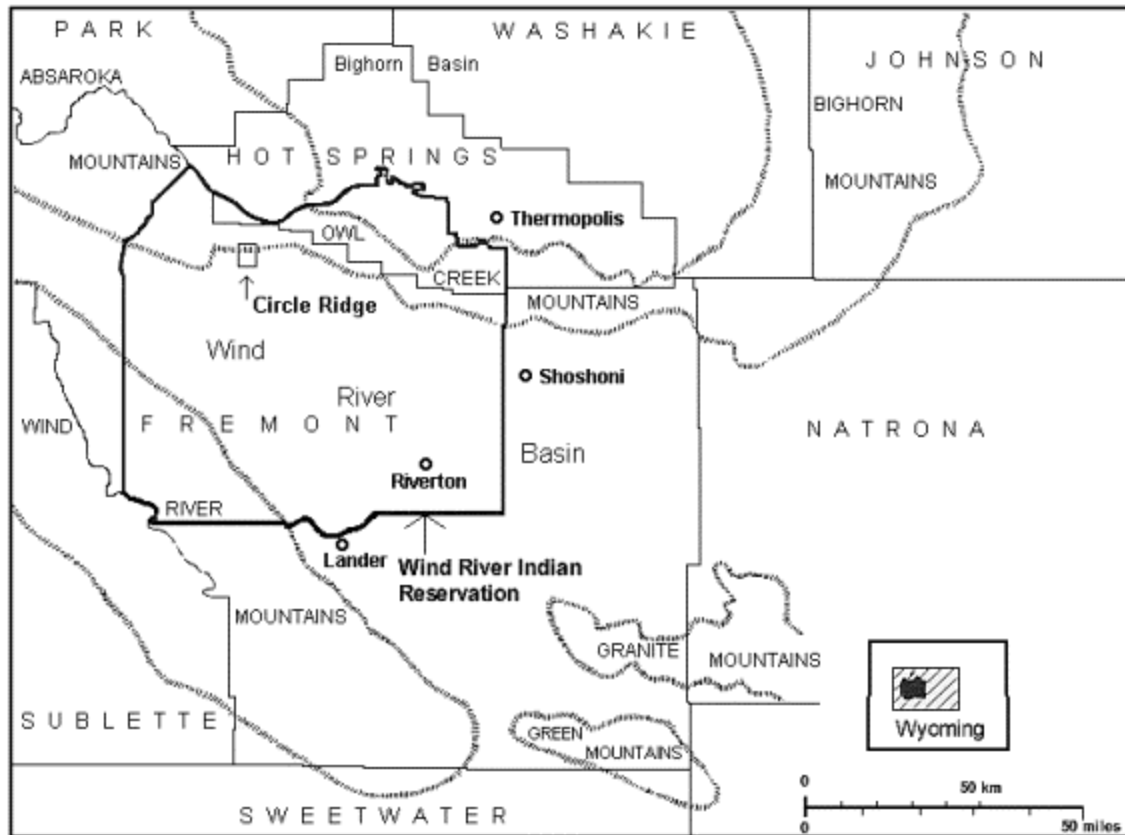


Figure 1-4. Location map of the Circle Ridge Field.

Due to the highly fractured nature of the Phosphoria and Tensleep Formations in Circle Ridge, water flooding for secondary recovery operations has proved only marginally effective. As mentioned previously, Tensleep and Phosphoria water flooding has been suspended in the overthrust block, the major remaining reserve target for the field. In dual porosity fields like Circle Ridge, filling the fractures with gas and driving the fracture gas-liquid contact down structure can improve the drainage rates of oil from the matrix. This gas-oil gravity drainage mobilization process is described by the Richardson and Blackwell (1971) equation:

$$\frac{(\Delta Z)_{S_o}}{\Delta t} = \frac{4.4 \times 10^{-5} K_v \Delta \rho dK_{r_o}}{u_o q dS_o} \quad \text{Equation 1-1}$$

where:  $K_{r_o}$  = relative permeability to oil

$K_v$  = matrix vertical permeability, in millidarcies

$S_o$  = oil saturation, fraction of pore volume

$\Delta t$  = change in time in days

$\Delta \rho$  = difference in density between draining liquid and injected gas, in  $\text{lb}_m/\text{ft}^3$

$u_o$  = oil viscosity, in centipoises  
 $q$  = porosity, fraction of bulk rock volume  
 $(\Delta Z)_{s_o}$  = vertical distance oil saturation moves in ft

As indicated by this equation, in order to predict the process, matrix permeability and porosity, as well as current oil saturations, must be known.

Equally as important is an understanding of the fracturing in the field. Knowledge of fracture porosity, in conjunction with the oil drainage rates and reservoir pressures, allows for the projection of gas requirements for gas-oil gravity drainage projects. This gas injection forecast is critical to the design and economics of the project. Additionally, Marathon's experience with gas injection projects has indicated the importance of fracture understanding in maximizing oil capture efficiency and in limiting the production of gas. Gas production is very undesirable, as it must be recompressed for reinjection or replaced by increased extraneous gas injection. Both of these cases result in higher costs for the project and a lowering of economic viability. The optimum placement of completions within highly productive fractures helps maximize the production of oil per completion, while limiting the potential for gas coning and production. An improved picture of fracture intensity and compartmentalization also aids in the placement of gas injectors. Ideal placement of injectors can help limit the number of injectors required and ensure that unnecessarily high completion pressure drops are not encountered.

In addition to studying the viability of gas injection at Circle Ridge, Marathon would like to evaluate the potential for dewatering the fracture system through increased withdrawals. This dewatering can create dual porosity gas-oil gravity drainage even with little or no additional gas injection. In conjunction with this dewatering, Marathon plans to investigate the use of horizontal drain holes to aid in the efficient capture of oil. Information from this project will aid the placement of the horizontal drain holes at or directly below the oil-water contact in the fracture system. The orientation of the boreholes will be guided by the desire to intersect fractures and to produce areas of undrained oil-filled fractures.

The improved reconstruction and visualization of the major faults in the Field should also aid future recompletion attempts. This visualization will also help quantify the potential for expanding any improved oil recovery process into the smaller fault blocks.

Thus, there have been three focuses of this project:

1. Improved spatial knowledge of matrix porosity, permeability and oil saturation;
2. More realistic models of the major faults and fault blocks; and
3. Development of a model to predict the fracture intensity and orientation throughout the reservoir, along with fracture-related engineering properties such as directional fracture permeability and fracture porosity.

## 1.2 Geological Background of the Circle Ridge Field

### 1.1.1 REGIONAL GEOLOGY AND TECTONIC HISTORY OF THE WIND RIVER BASIN

The tectonic history of the area around Circle Ridge began with an early Precambrian or Archeozoic orogenic deformation phase. Contractional mountain building, dike intrusion, and the development of several regional fracture systems subdivided the basement rocks in the area into a mosaic of blocks (Fanshawe, 1952). Post-orogenic crustal stability was achieved during the Late Precambrian as long periods of active erosion produced a lowland among the earlier-formed mountain ranges (Fanshawe, 1952).

From the Paleozoic Era until Late Cretaceous, central Wyoming was part of the continental shelf along the eastern side of the Cordillera (Keefer, 1969). Paleozoic and lower Mesozoic strata were deposited mainly in shallow seas, with the exception of Silurian units which were either deposited and eroded before the Devonian or were never deposited (Keefer, 1969). Widespread facies changes and unconformities commonly associated with fluctuations in sea level or low-amplitude tectonic movements created a spectacular, multi-colored stratigraphy. Some areas were periodically raised above sea level and eroded while surrounding areas remained submerged thus creating formations with widespread thickness variations (Keefer, 1969).

Deformation related to the subduction of the oceanic Farallon Plate underneath the continental North American Plate began roughly 80 million years ago (Coney, 1978; Stock and Molnar, 1988; and Brown, 1993). This tectonic event, known as the Laramide Orogeny, continued intermittently with increasing intensity through the Paleocene and ceased by the end of the Early Eocene. Structural deformation during the Laramide Orogeny is characterized by crustal shortening to produce giant fault-bounded, basement-involved uplifts along the perimeter of basins (Figure 1-5). Precambrian-cored uplifts separate basins that are filled with sediments accumulated during deformation. Brown (1993) characterized the Laramide Orogeny as a tectonic “front” that swept eastward across the Wyoming Foreland, creating crustal deformation sequences that grow progressively younger from west to east. Plate convergence during the Laramide Orogeny created structural deformation in a primary stress direction of N 40° to 50° E (Brown, 1988). Primary structures across the Wyoming Foreland, including Circle Ridge, trend northwest, perpendicular to the inferred direction of maximum principal stress (Figure 1-6 and Figure 1-7). Northwest trending structures are generally thrusts, fold-thrusts, thrust-folds, and uplifted basement blocks (Brown, 1988; 1993).

Beginning in Late Cretaceous time, the seaways shifted east as Laramide deformation began downwarping the Wind River Basin and uplifting of the peripheral areas including the Owl Creek Mountains. The Wind River Basin is bounded by faulted and folded Paleozoic and Mesozoic sediments, but the basin is overlain by nearly flat-lying Eocene deposits that accumulated as a result of erosion of the surrounding areas since Laramide

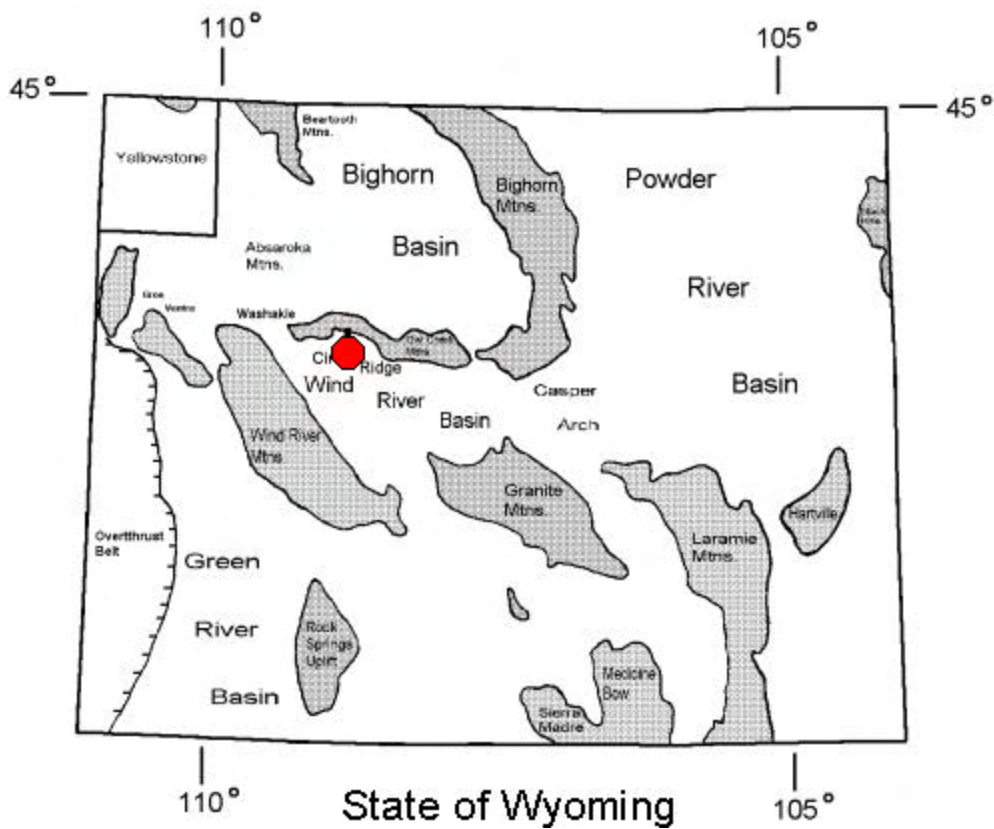


Figure 1-5. Index map showing the Circle Ridge Field and surrounding positive and negative structural elements that define the primary basin and uplift pattern in Wyoming.

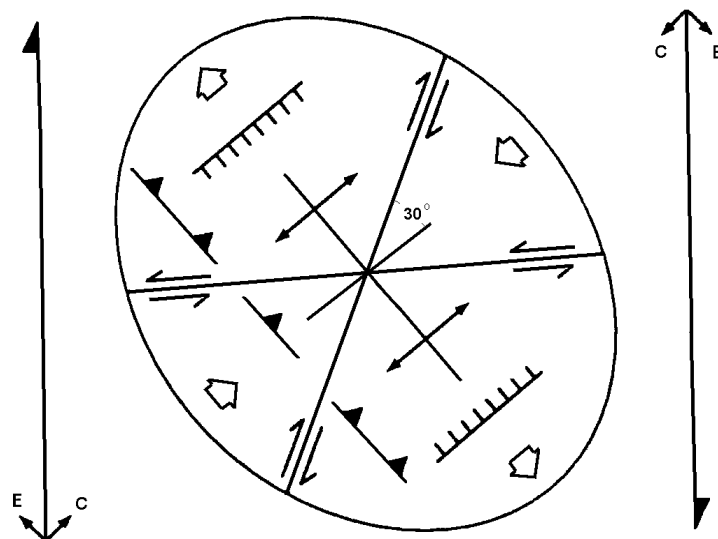


Figure 1-6 Schematic strain ellipsoid with  $s_1$  oriented parallel to the anticlinal axis of Circle Ridge (modified from Reading, 1980). Contractural structures, like reverse faults and anticlinal folds, are oriented parallel to  $s_1$ . Extensional structures, like normal faults, are oriented perpendicular to  $s_1$ . Oblique faults, indicated with arrows in the slip direction, are oriented  $30^\circ$  to  $s_3$ .



**Figure 1-7. False-color satellite photo of the Circle Ridge Field. The Field formed due to compression and thrusting from the northeast. Note the increased shortening in the northwestern end of the Field. The increased shortening was accommodated through tighter folding and imbricate faulting.**

time. The arcuate-shaped basin encompasses approximately 13,600 km<sup>2</sup> with a length over 216 km and a width of as much as 56 km. The Owl Creek Mountains are an east-west trending uplift thrust over the northern margin of the Wind River Basin. The Wind River cuts through this uplift, forming the Wind River Canyon.

### 1.1.2 STRATIGRAPHY

Exposed stratigraphic units at Circle Ridge range from the Permian Phosphoria Formation to the Cretaceous Mowry Formation. Subsurface formations include all units from Precambrian basement to the Pennsylvanian Tensleep Formation (Figure 1-8).

#### 1.2.1.1 *Madison Limestone*

The Madison Limestone is a Lower Mississippian assemblage of carbonates that rests unconformably above the older Devonian Darby Formation. The Madison Limestone is in general a massive limestone and dolomite unit deposited on the Wyoming shelf (Gower, 1978). In the Wind River Basin, the thickness varies from 68 m to 240 m, reflecting minor tectonic movements (Gower, 1978). In addition, karsted zones in the upper part of the Madison Limestone may be former evaporitic zones that were leached either during or after Mississippian time, also accounting for thickness variations (Keefer, 1965). At Circle Ridge, the Madison Limestone measures about 210 m and is known

Era	Period	Unit	Symbol	
Mesozoic	Cretaceous	Mowry Shale		
		Undifferentiated Thermopolis Shale	Ku	
	Jurassic	Cloverly Formation	Kcv	
		Morrison Formation	Jm	
		Sundance Formation	Js	
		Gypsum Springs Formation	Jgs	
		Nugget Sandstone	Jn	
	Triassic	Popo Agie Member	TRpa	
		Chugwater Formation	Crow Mountain Member	TRcm
			Red Peak Shale	TRrp
		Dinwoody Formation	TRd	
Paleozoic	Permian	Phosphoria Formation	Pp	
	Pennsylvanian	Tensleep Sandstone		
		Amsden Formation		
	Mississippian	Madison Limestone		
	Devonian	Darby Formation		
	Ordovician	Bighorn Dolomite		
	Cambrian	Gallatin Limestone		
		Gros Ventre Shale		
Flathead Sandstone				
PRECAMBRIAN				

Rock Units Exposed in Outcrop in the Circle Ridge Field

Primary Reservoir Units

**Figure 1-8 Stratigraphic column for the Circle Ridge Formation (from Smith 2000)**

only in the subsurface (Olson, 1948). These shelf carbonates are generally homogenous in lithology with several porosity zones containing commercial petroleum accumulations (Stipp, 1952). Currently, the Madison Limestone is the deepest drilled reservoir at Circle Ridge. As of June of 1992, the Madison Limestone had produced 1.317 MMBO (Anderson and O’Connell, 1993).

### 1.1.2.1 Amsden Formation

The Amsden Formation is Late Mississippian to Early Pennsylvanian in age, and occupies the interval between the underlying Madison Limestone and the overlying Tensleep Formation. The contact of the Amsden Formation with the underlying Madison Limestone is an erosional unconformity, while the contact of the Amsden Formation with the overlying Tensleep Formation is conformable (Love, 1939). The Amsden Formation

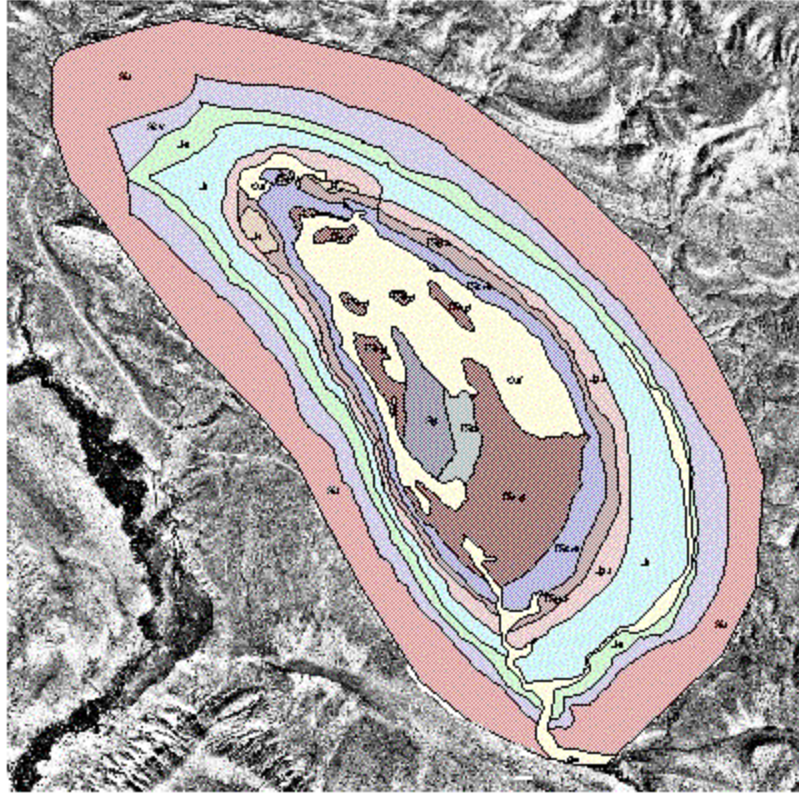


**Figure 1-9. Geologic map (from Smith, 2000). Geological symbols used in map are referenced in Figure 1-8.**

is a heterogeneous series of sandstone, shale, and limestone that was deposited under marine conditions (Keefer, 1965). It is separated into three members beginning with the Darwin Sandstone, which is a basal sandstone that fills the underlying karsted Madison (Olson, 1948). The middle member is the Horseshoe Shale. The upper member, the Ranchester Limestone, is a cherty carbonate. Within the Wind River Basin, the Amsden Formation varies in thickness from 60 m to 120 m (Gower, 1978). They are known only in the subsurface (Olson, 1948). Anderson and O'Connell (1993) reported that 3.522 MMBO had been produced from all of the productive units within the Amsden Formation as of June of 1992.

#### *1.1.2.2 Tensleep Formation*

A conformable contact separates the Tensleep Formation and the Amsden Formations, indicating no significant withdrawal of the sea at the close of Amsden time (Love, 1939). The lower unit of the Pennsylvanian Tensleep Formation is dolomite and limestone (Agaston, 1952). Shales and fine- to medium-grained, cross-bedded sands make-up the upper clastic unit. The abundant medium-scale cross-beds, frosted quartz grains, and limestone cement were used to interpret the depositional environment as a beach (Agaston, 1952). The Tensleep is capped with an unconformity separating it from the overlying Phosphoria Formation. The Tensleep Formation is widespread in Wyoming and has a highly variable thickness, with a range of 65 m to 183 m in the Wind River

Basin (Gower, 1978). At Circle Ridge, the Tensleep measures 90 m (Olsen, 1948). The thickness variance is due to the loss of the upper sand, which was removed prior to deposition of the overlying Permian Phosphoria Formation (Pedry, 1975). The Tensleep Formation became exposed as the seas migrated eastward and the upper sand eroded (Keefer, 1965).

The Tensleep Formation is the most productive reservoir at Circle Ridge. Anderson and O'Connell (1993) reported the Tensleep Formation had produced 16.313 MMBO as of June of 1992.

#### *1.1.2.3 Phosphoria Formation.*

An erosional unconformity separates the Pennsylvanian Tensleep Formation from the Permian Phosphoria Formation. A progressive withdrawal of the Paleozoic seas occurred between Late Pennsylvanian and Early Permian (Agaston, 1952). A new marine transgression deposited the Phosphoria. The Phosphoria Formation averages 64 m thick at Circle Ridge, although within the Wind River Basin, the Phosphoria Formation can measure up to 396 m in thickness (Andrews, 1944).

The Phosphoria Formation is the oldest formation exposed at the surface in the center of Circle Ridge, and can be subdivided into two units. The basal unit is primarily a cherty dolomite and thin, hard, brown limestone that was deposited in a shallow marine environment (Mills, 1956). The upper unit, as seen on the surface at Circle Ridge, contains red, phosphatic shales and sandstones that weather to a dark brown. The upper unit accumulated within an arid climate and shallow marine environment (Frielinghausen, 1952). The Phosphoria Formation is the second most prolific oil-producing unit at Circle Ridge. Anderson and O'Connell (1993) reported the Phosphoria Formation had produced 7.867 MMBO as of June of 1992.

#### *1.1.2.4 Dinwoody Formation*

The basal Triassic unit is the Dinwoody Formation. The contact between the Dinwoody Formation and the Phosphoria Formation appears continuous and conformable as it crops out in the central hill of Circle Ridge. The Dinwoody is composed of silts and sandy, anhydritic shale with a few interbedded gray dolomites and limestone. It has a unique white to yellow color. The 43 m thick Dinwoody Formation was deposited in semi-restricted marine or supratidal environment (Kinsman, 1969).

#### *1.1.2.5 Chugwater Formation*

Overlying the Dinwoody is one of Wyoming's thickest and most distinctive formations, the Triassic Chugwater Formation. The Chugwater Formation is separated into three members—Red Peak, Crow Mountain, and Popo Agie. The basal Red Peak Shale is the thickest at 314 m (Anderson and O'Connell, 1993). It contains a blood-red, interbedded siltstone and sandstone that accumulated within a paralic and nearshore marine complex (Picard, 1978). The upper portion of the Red Peak weathers into shades of tan, gray, red

and purple. The Crow Mountain is 64 m thick of purple, very fine-grained sandstone, and gray to red siltstone (Anderson and O'Connell, 1993). The main depositional environment for the Crow Mountain Member was probably a tidal flat complex (Picard, 1978). The upper Chugwater member, the Popo Agie, is dark red to purple on the base, and weathers to a dark rust color or ochre color. The upper portion is a bright tan siltstone with sharp brittle edges. It sounds like glass when walked upon. The difference in color is probably from different amounts of iron oxides present. The Popo Agie Member represents dominantly fluvial conditions, whereas the ochre-colored unit was deposited in a lacustrine environment on a deltaic plain (Picard, 1978). At Circle Ridge, the Popo Agie Member measures 52 m in thickness (Anderson and O'Connell, 1993).

#### *1.1.2.6 Nugget Sandstone*

Unconformably overlying the Popo Agie Member is the Lower Jurassic Nugget Sandstone. This formation is only present along the northwest corner of Circle Ridge and can be up to 15 m thick when present. The base of the Nugget is a fine- to very fine-grained, tan to buff sandstone with interbedded red siltstone beds. Above the basal unit is a red sandstone of the same texture. Large- and small-scale cross-bedding structures were found that might indicate eolian deposition. Much controversy exists today concerning the discontinuous surface exposure of the Jurassic Nugget Formation in the Wind River Basin. Picard (1978) has suggested that regional and local tectonism may have contributed to the observed thickness variations.

#### *1.1.2.7 Gypsum Springs Formation*

The lower and upper contacts of the Gypsum Springs are unconformities (Anderson and O'Connell, 1993). The basal portion of the Gypsum Springs Formation at Circle Ridge is a 29 m thick massive layer of gypsum (Anderson and O'Connell, 1993). The upper portion contains a pink to red gypsiferous siltstone with interbedded shale measuring 32 m thick (Anderson and O'Connell, 1993). The gypsum weathers to a dark, puffy texture similar to heads of broccoli. The abundance of gypsum with the interbedded siltstone and shale beds would represent deposits that accumulated on the continental platform with intervals of isolation from the main sea. Kinsman (1969) interpreted the depositional environment as a semi-restricted basin with sabka and tidal mudflat conditions.

#### *1.1.2.8 Sundance Formation*

The Sundance Formation and overlying Morrison Formation are the two Upper Jurassic units at Circle Ridge. A distinctive strip of grass is seen at the contact between the Sundance Formation and the Gypsum Springs Formation. At Circle Ridge, a series of shale, sandstone, and limestone beds compose the 96 m thick Sundance Formation (Anderson and O'Connell, 1993). Colors range from gray to light brown to green. The fine-grained sands and shale can be highly glauconitic with sedimentary characteristics that include thin cross-beds, ripples, and planar beds. An abundance of *Gryphea* was found loosely atop the soils of the Sundance and cemented within beds. The combination

of characteristics and different bed compositions lead to the interpretation that the Sundance represents a variety of marine depositional environments—open marine platform, lagoon, and barrier bar (Peterson, 1954; Keefer, 1965).

#### *1.1.2.9 Morrison Formation*

Overlying the Sundance Formation, and separated by a conformable contact, is the Morrison Formation. Along the northeast flank of Circle Ridge, a cherty conglomerate bed of the Morrison Formation marks the contact above the Sundance Formation. In the study area, the Morrison is 61 m thick and comprised of white, fine-grained sandstones and tan shale (Anderson and O'Connell, 1993). It was deposited in a non-marine environment as intermixed lacustrine, swamp, flood plain, and river deposits (Downs, 1952). The Morrison Formation is a regionally extensive unit found throughout Colorado, Idaho, Utah, and Wyoming. Dinosaur bones have been found in this formation, most notably at Dinosaur National Park, Colorado.

#### *1.1.2.10 Cloverly Formation*

The types of environments and conditions in which the Morrison Formation was deposited are largely repeated within the Cretaceous Cloverly Formation. The basal fluvial unit is a distinctive light gray, pebbly conglomerate. Above the conglomerate unit is a cross-bedded, gray to dark brown sandstone with interbedded bentonitic shales, silts, and clays. The upper part of the Cloverly Formation is composed mostly of rust-colored silts and sandstones that are called the Rusty Bed Member. Structures include ripples and cross-beds. The sandstone is fluvial in origin and was probably deposited in stream channels cut into the underlying lacustrine deposits (Curry, 1962). At Circle Ridge, the Cloverly Formation is 87 m thick (Andrews, 1944).

#### *1.1.2.11 Cretaceous Undifferentiated*

The dark, bentonitic shales that form a gradational contact above the Cloverly belong to the Thermopolis Formation. The Thermopolis Shale and Mowry Shale have been mapped together in this study to form the Cretaceous Undifferentiated. The Thermopolis marine shale layer coincides with the transgression of the Early Cretaceous seas into the Wind River Basin (Burtner and Warner, 1984). The bentonitic shales are dark gray to black in color, and contain thin layers of sandy and silty claystone. About 14 m from the top of the Thermopolis Formation rests the Muddy Sandstone Member of the Thermopolis Formation. The Muddy Sandstone Member contains a white to buff, fine- to medium-grained sandstone, which is sharply distinctive from surface exposure with the Thermopolis Formation. The sandstone in the Muddy Sandstone Member represents overlapping marine and non-marine sandstone facies and therefore indicates a brief regression in the Cretaceous sea (Curry, 1962).

The other formation in the Cretaceous Undifferentiated (Ku) in this study is the Mowry Formation. The contact between the Thermopolis Shale and the Mowry Shale is often difficult to locate. Generally, the base of the Mowry Shale is recognized as porcelaneous

shale that conformably overlies the Muddy Sandstone Member. This hard shale is gray, fissile, organic-rich, and locally sandy. Numerous bentonite beds within the Mowry and the other Cretaceous formations indicate episodic volcanic activity at the same time from the northwest corner of Wyoming (Downs, 1952). The Mowry is 195 m thick at Circle Ridge, and is a structurally incompetent unit that slumps frequently, producing uneven topography (Andrews, 1944).

### **1.3 Strategies for Building the 3D Comprehensive Reservoir Model**

#### **1.3.1 MATRIX PROPERTIES**

Many of the wells in the Circle Ridge Field are old, and modern logging suites were not run in them. The information contained in the logs that were run is not sufficient on its own to calculate the necessary matrix parameters. However, there are a number of wells in the Circle Ridge Field that do have modern logging suites that do allow the required matrix properties to be calculated.

The strategy to calculate matrix properties from the older logs was to calibrate these logs to the modern suites. This added step of calibration made it possible to calculate matrix properties in 113 additional wells. Details of the calibration methodology are presented in Section 2.2 of this report.

#### **1.3.2 FAULT BLOCK ARCHITECTURE**

There is no seismic data in the Circle Ridge Field that can be used to determine the geometry and location of the major faults. Data on fault locations comes from well penetrations and from surface geological mapping.

Prior to this project, Anderson and O'Connell (1993) constructed the only cross-sections through the Field and interpreted the tectonic evolution of the Field based on these reconstructions. Later Smith (2000) remapped the surface geology of the Circle Ridge Field. He combined these maps with Anderson and O'Connell's cross-sections to create a model that was used for computing reservoir volumes, and to look for untested fault blocks. The model was not balanced three-dimensionally and has obvious kinematic problems.

The strategy adopted in this project was to create a fully 3D model of the major faults and reservoir horizons, and then to undertake a complete 3D palinspastic reconstruction of the Field using 3D balancing constraints. The existing cross-sections of Anderson and O'Connell (1993) were not sufficient for this purpose, so additional cross-sections were constructed. These cross-sections were based upon field measurements along transects chosen to pass through wells where there was additional subsurface control on the formation tops and faults. Two additional cross-sections were constructed in the structurally complex northwestern end of the Field, and one cross-section was constructed in the southeastern end of the Field.

These cross-sections together with Anderson and O'Connell (1993) cross sections were combined with the structural contour maps constructed from well penetrations. A 3D palinspastic reconstruction program was then used to restore the Tensleep and Phosphoria Formations to their original unfaulted and unfolded state.

### 1.3.3 RESERVOIR-SCALE FRACTURE MODEL

The reservoir scale fracture model consists of those joints and faults that do not delineate major structural blocks. These fractures are probably on the order of a few meters in radius up to a few hundred meters in radius. They are large enough and permeable enough to strongly impact reservoir flow, but small enough that they cannot be correlated from well to well or to outcrop on the surface, as the case with the larger block-defining faults.

Data on reservoir scale fracturing can come from both direct and indirect sources. Direct sources include outcrops, core, fracture image logs, and spinner logs. Indirect sources include seismic attributes or structural surrogates like bedding thickness or bedding curvature.

No seismic data was available at Circle Ridge, so the only data available potentially comes from downhole logs, core and outcrop.

Downhole data has the advantage that it pertains directly to the target reservoir units. It also has many disadvantages: cost, coverage and directionality being the three most important. Because of the cost, it would be prohibitively expensive to obtain fracture image log data in a large number of wells. Moreover, not all wells can be logged. For example, only those that are not cased in the reservoir intervals could potentially be logged. The cost and the subset of wells with suitable open-hole completions reduce substantially the number and location where direct subsurface data can be obtained through logs. In addition, wells are essentially unidirectional samples of the three-dimensional fracturing in the reservoir. Fractures that are oriented orthogonal to the wellbore will more likely be intersected, and hence imaged and recorded, than fractures that are subparallel to the wellbore axis. This implies that subvertical fractures may be rarely intersected by a vertical well, or entirely missed if the image log only covers a small interval. As the wells in the Circle Ridge Field are vertical or subvertical, and outcrops of the Tensleep and Phosphoria Formations elsewhere in the Wind River and Bighorn Basins show that important fractures form in a subvertical orientation orthogonal to bedding, there will be some incompleteness in the fracture data obtained through well logs.

While outcrop data does not have the problems with cost or spatial coverage that wellbore log data has, its relevance to the fracture pattern developed in the subsurface reservoir units must be established before it can be used. There are always issues regarding whether the stress relief near the surface has created or enhanced some fracture

sets, and whether the deformation of the younger, mechanically different outcrop formations has been similar to the reservoir formations.

At Circle Ridge, the formations exposed at the surface immediately overlay the reservoir formations, so there is a reasonable chance that the outcrop formations might have experienced very similar deformation processes to the reservoir formations, and thus might be useful for learning about what structural or other types of geological controls might be useful for predicting fracture patterns in the subsurface.

The strategy for building the reservoir-scale fracture model thus relied upon both subsurface and surface fracture data. However, it was not assumed that the outcrop data would necessarily be related to the subsurface fracture data. Rather, the overlying rock units exposed in outcrop in the Field were studied to find any evidence of detachment or decoupling from the subsurface reservoir units. Moreover, as subsurface image log data was acquired, it was compared to outcrop fracture data in the immediate vicinity of the well, to assess how closely the outcrop fracturing corresponded to the subsurface fracture data.

Analysis of the subsurface and surface fracture data makes it possible to assemble a database of fracture intensity and orientation in many different structural positions throughout the Field. However, it does not in and of itself provide all that is needed to predict fracture orientations and intensity where there are no wells or outcrops. The issue of how to interpolate or extrapolate beyond well control is central to building the reservoir fracture model. This was done in the next stage.

The second stage in building the reservoir-scale fracture model was to determine what geological factors produced the observed fracturing. Since the Circle Ridge Field is a highly deformed assemblage of rocks, it is likely that the fractures arose during the folding and faulting that transformed the flat lying reservoir rocks into their present geometrical configuration.

The strategy for determining just how the deformation may have led to the fracturing was to compare the strain pattern produced by each folding and faulting event to the fracture pattern measured downhole and in outcrop. The strain pattern can be calculated from the 3D palinspastic reconstruction (Section 1.3.2) by starting with the flat-lying reservoir units, and then computing the geometrical strain after each folding or faulting event deduced in the reconstruction.

Rock mechanics research has shown that there is a geometrical relationship between the principal directions of stress and strain and the orientation of fractures (e.g. Billings, 1972; Jaeger and Cook, 1976). Extension fractures (sometimes termed Mode I fractures in fracture mechanics literature) form a surface orthogonal to the direction of minimum principal stress, which is also the direction on maximum extensional strain. Faults or Mode II fractures, in which slippage occurs parallel to the fracture surface, form from 30° to 45° from the direction of maximum compression or contraction (Figure 1-10).

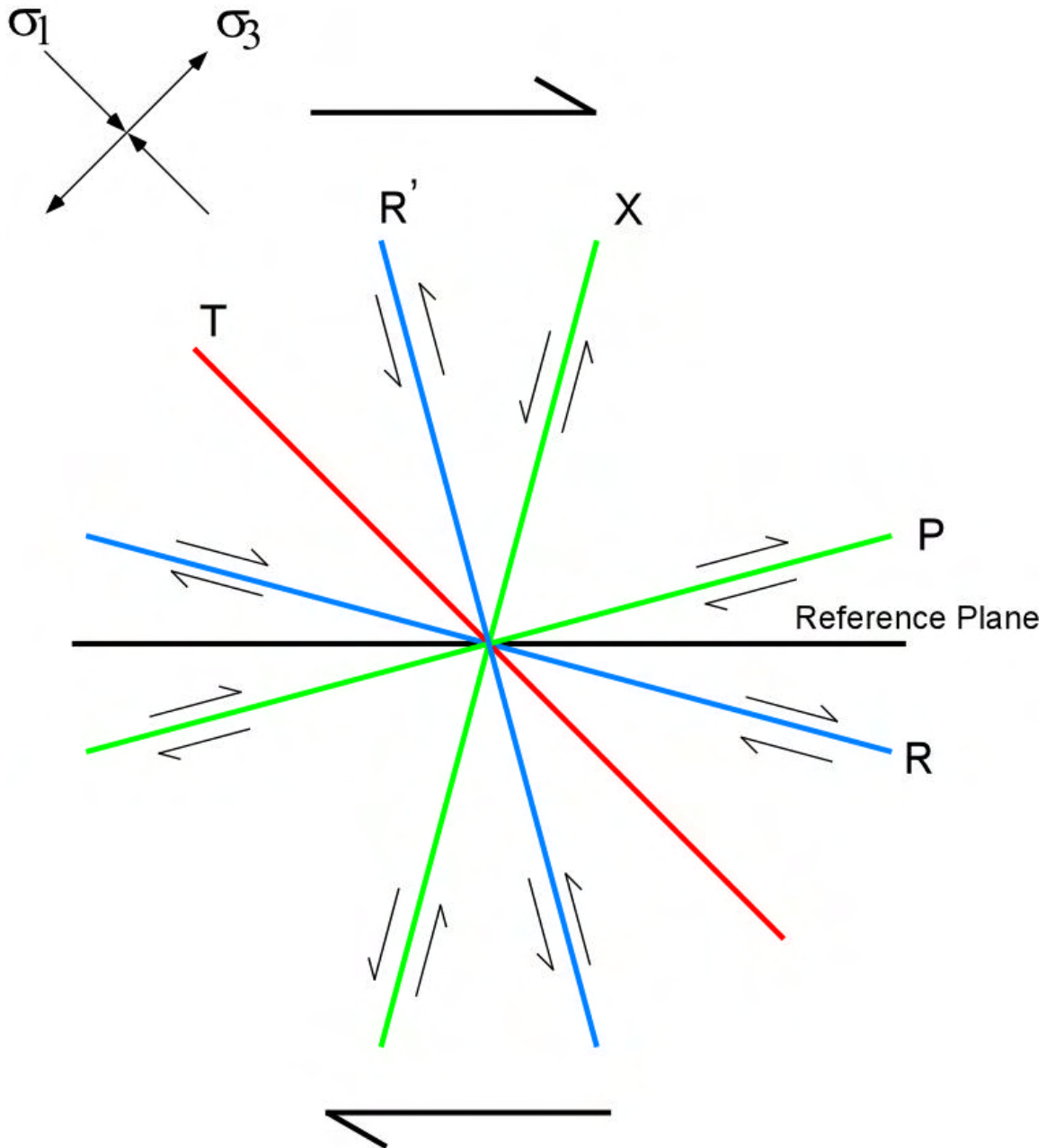
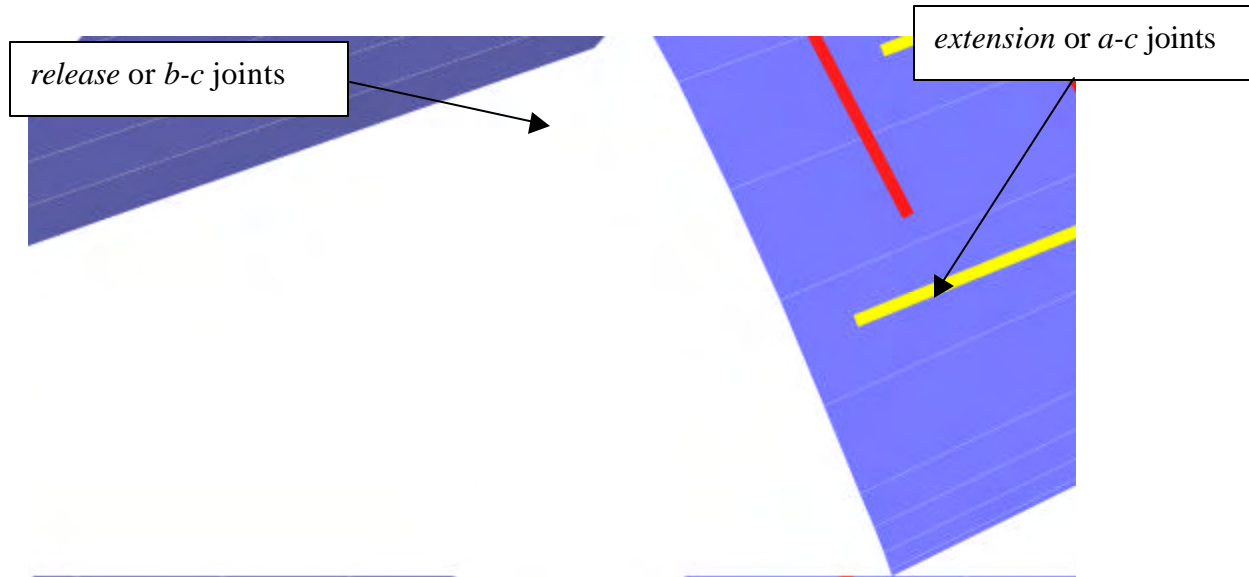


Figure 1-10. Relation between principal stress directions and resultant fracture orientations (Riedel, 1929).  $\sigma_1$  and  $\sigma_3$  are the maximum and minimum principal stresses, respectively. “T” is the extension (Mode I) joint set. “R” and “R'” are the primary and secondary Riedel shears, which are active in compression, typically when the deformation occurs deep in the crust, pore pressures are low and the angle between  $\sigma_1$  and the reference fault plane is large. At shallow depths, low confining pressures, high pore pressures or when the master fault subparallels  $\sigma_1$ , the “P”, “X” and “T” sets are favored.

The classic Riedel model illustrated in Figure 1-10 is primarily a model for secondary fractures associated with faults. Many other models for fracturing related to folding have

also been proposed. The two most common are the plate-bending model (Billings, 1972) and the Stearns model (Stearns and Friedman, 1972).

The plate-bending model predicts the formation of two Mode I or extension fracture sets, referred to as *extension* or *a-c* joints; and *release* or *b-c* joints (Figure 1-11).



**Figure 1-11. Illustration of release (b-c) and extension (a-c) joints in relation to fold geometry.**

A related, though more complex model, was proposed by Stearns and Friedman (1972). Figure 1-12 shows the Type I and Type II fracture orientations in this model. The conjugate “shear” fractures typically make an angle of 30° to 45° with their associated extension fracture set. It is rare that all of the orientations are present, or that the conjugate fractures sets are present in equal intensities. Occasionally, one of the conjugate orientations is entirely absent.

The extension fractures in either of the models depicted in Figure 1-11 or Figure 1-12 have characteristic orientations with respect to bedding that is obvious in stereoplots of bedding and fractures (Figure 1-13). These two stereoplots show how the Type I extension fracture parallels the bedding dip, and how the Type II extension fracture is vertical and parallels bedding strike. The contours shown in the figure are concentrations of fracture poles. Those labeled Type I in the unrotated stereoplot are on the edges of the stereoplot and are at an azimuthal angle of 30° from north. The poles labeled Type II in the unrotated diagram represent a fracture with a 30° strike and a 60° dip to the northwest. Bedding (shown by the red line in the lefthand plot) strikes 30° and dips 30° to the southeast. The fact that the poles for the Type II set plot on the great circle representing bedding indicates that the Type II set is orthogonal to bedding. The stereoplot on the right shows how the fracture orientations look when the data are rotated

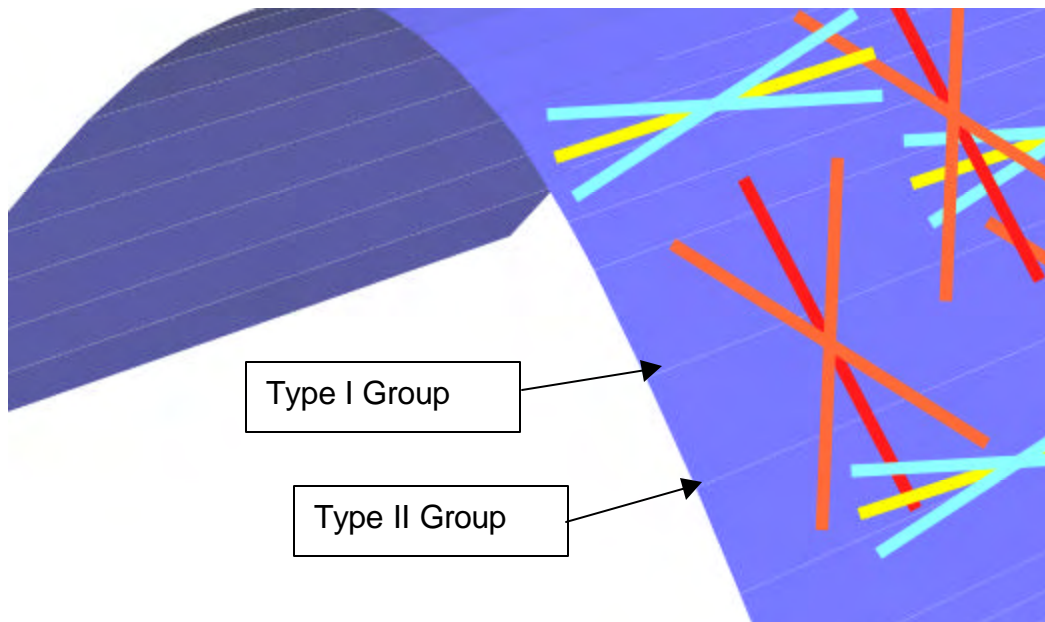


**Figure 1-12. Schematic diagram of Stearns model of fracture orientations related to folding. The red line in the Type I fracture group is a joint or extension fracture, while the orange lines show the orientations of Type I conjugate “shear” fractures. The yellow line shows the orientation of the Type II joint or extension fracture, while the cyan lines show the orientations of the Type II conjugate “shear” fractures. The complete Stearns model contains other fractures not shown in the schematic above.**

into the plane of bedding. In this rotated stereoplot, the bedding strikes north-south and is horizontal. The fracture poles in this rotated orientation cluster at the four compass positions shown.

The strategy was to examine the fracture data, and determine whether it showed any of these characteristic relations to faulting or folding.

These comparisons were carried out in two different ways. The first series of comparisons focused strictly on the relation of the fracture orientations with local bedding orientation. The second series of comparisons examined the local strain field during the structural evolution of the Circle Ridge Field, to determine if any of the orientations characteristic of the Riedel model (Figure 1-10) were present.

#### 1.3.4 INTEGRATED 3D RESERVOIR MODEL

An important aspect of this project was the creation of an integrated matrix/fault block/fracture numerical model. This model allows the visualization of the fractures in 3-D and their relation with other parameters, and provides the numerical parameter values

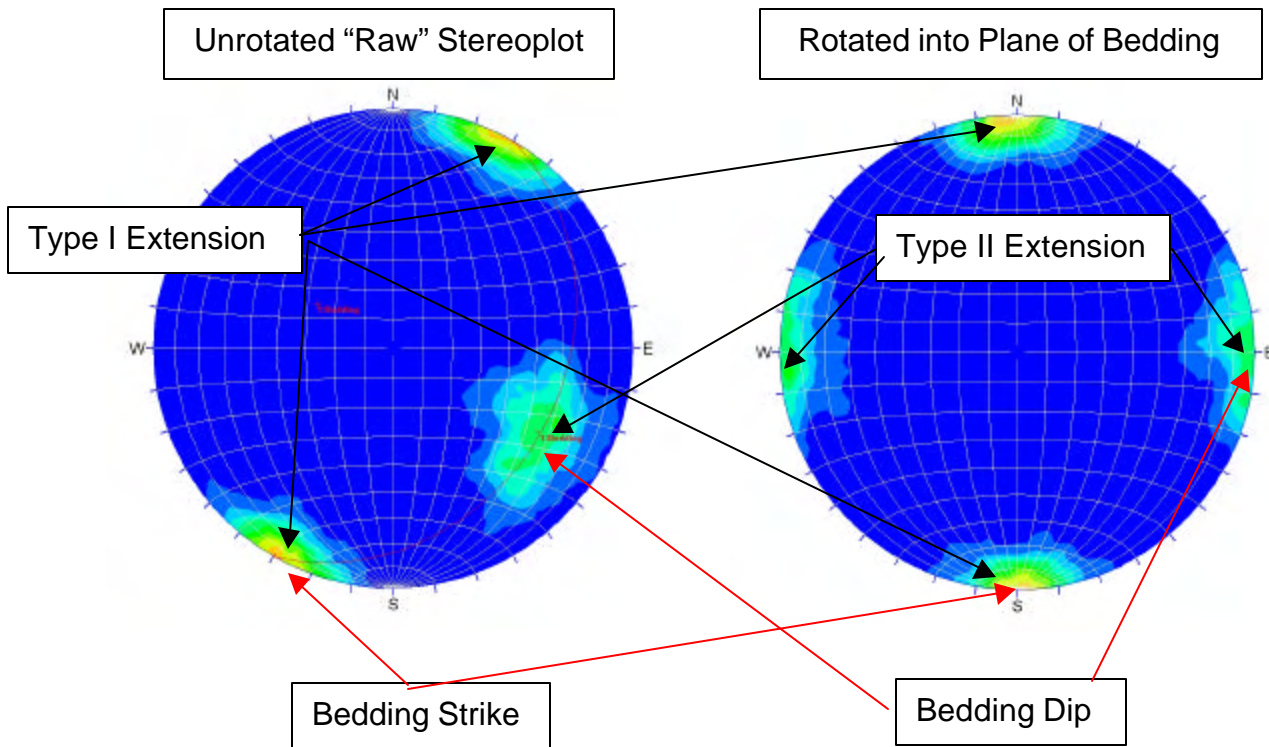


**Figure 1-13. Stereoplots illustrating the characteristic relations of the Type I and Type II extension joint sets with respect to bedding.**

to reservoir simulations or other calculations to design and evaluate options to enhance production.

The Circle Ridge Field is encompassed within a complex structural setting. The basic structure that defines the field is an anticline. The complexity enters due to the faulting of the anticline structure. This complexity is not just due to the number of the faults observed and modeled, but also the type of faulting in the Field. Many faults intersect other faults, cross other faults, or die out. The Circle Ridge Field has not only nearly vertical faulting which is fairly simple to model, but also shallowly dipping faults and in particular, shallowly dipping reverse faults. This last type of fault is difficult to incorporate in many 3D modeling software systems.

Of the modeling software packages that can handle the complex types of faulting that occur at Circle Ridge, further classification of the software can be made in their ability to upscale the geo-cellular model to reservoir simulation models. This process of upscaling has been addressed in some of the software so that directly readable grid files are written that can be read by the reservoir simulation software. This becomes important in order to allow the operator of the field a method of evaluating the best economic methods of extracting the most reserves from the field. The ability of geo-cellular models to easily output simulation modeling grids is an important point to consider in picking the geologic modeling software.

Initial experiments with importing the data into Roxar's RMS™ software showed that the current release of RMS could not handle reverse faults without breaking the model into

several pieces, which is cumbersome for use in later simulation or other types of calculation. Additional evaluations of Technoguide's Petrel™ and Gocad™ were also carried out to determine the best piece of software to be used. Eventually, Gocad™ was selected due to considerations of technical capabilities, cost and ease of integration with Marathon's existing reservoir software.

#### **1.4 Strategy for Model Validation**

Model validation is an important, if not essential, part of developing a reservoir model that engineers can use for planning and development. For the Circle Ridge model, validation consisted of testing and evaluating two complementary aspects of the model:

1. How well did the fracture orientations and intensity variations in the fracture model correspond to measured data?
2. How well did the model reproduce reservoir-scale flow behavior?

The first validation was not carried out as a separate validation task, in that it was inherent in developing the original reservoir-scale fracture model. The strategy for validating the geometrical aspects of the fracture model consisted of comparing the strain data at various stages in the palinspastic reconstruction, and the fracture pattern likely to have been generated by it, to measured surface and subsurface fracture orientations and intensity variations. The development of the fracture model based upon the strain history constitutes a preliminary validation of the geometry of the fracture model.

A more comprehensive validation of the model was carried out by using the preliminary reservoir-scale fracture model to simulate transient well tests and to compare its connectivity to the connectivity and compartmentalization of the reservoir as indicated by two tracer tests. In order to more thoroughly test the model, one test was carried out in the Tensleep Formation in the overthrust block, while a second test was carried out predominantly in the Phosphoria Formation in some of the underlying imbricate blocks. The actual tracer tests were not simulated numerically, but rather the fracture model was assessed in terms of the breakthrough patterns observed in monitoring wells. This validation tests whether the reservoir-scale connective geometry, essentially the geometry of the highly conductive fracture conduits or corridors, matches the local interwell corridor geometry inferred from the tracer tests. This is important, because it is the location and orientation of these corridors, and an understanding of why they occur where and in what orientation, that is key for improving field development in the ways indicated in Section 1.1.

#### **1.5 Strategy for Model Utilization**

Section 1.1 reviewed the importance of knowing how matrix properties, reservoir-scale fracture and fracture network properties, and fault block architecture vary throughout the field for designing and implementing advanced recovery processes and siting and completing new wells.

The utilization of the model to enhance recovery was not part of the scope of this project, although it has and is being used for those purposes. As described in Section 1.1, the results from this project will be used in a number of different ways. The overall strategy has been to combine all of the reservoir data – matrix, fracture and fault – into a single numerical model that can be interrogated, viewed and used as input for other software or engineering calculations. For example, it may be necessary to derive input parameter values for a reservoir simulation in order to assess the feasibility and economic sense of implementing a particular tertiary recovery scheme. In this instance, the integrated model is used to produce *input values*. Another use is through interrogation or visualization. As will be discussed in a later section of this report, the reservoir-scale fracture information has been used to orient a proposed lateral from an existing vertical well. The re-orientation of the lateral was based upon the dominant direction of fracturing in the 3D model, and in the fracture intensity patterns contained in the model. This is an example of how the *visualization* or *interrogation* of the model can be used to enhance recovery.

## **2 Experimental Work**

### **2.1 Overview**

This section describes the experimental procedures used in carrying out the project. They are divided into procedures for recalibrating wireline logs from older wells in order to extend knowledge of matrix properties; acquisition and interpretation of subsurface data; acquisition and interpretation of outcrop data; techniques used in creating the 3D fault block architecture; techniques used in carrying out the 3D palinspastic reconstruction; and methods for deriving reservoir properties and incorporating them into the final 3D reservoir model.

### **2.2 Petrophysical Analysis to Expand Matrix Property Coverage**

#### **2.2.1 OVERVIEW**

The purpose of the petrophysical work at Circle Ridge was to determine as accurately as possible the distribution of oil in the Phosphoria and Tensleep Formations, the primary reservoir units for the reasons discussed in Section 1.1. Two of the critical parameters that can be derived from log are matrix porosity and matrix oil saturation. The results of this analysis were integrated into the 3D reservoir model and interpolated between well control using a spatial interpolation algorithm. The data covered the overthrust area and a number of downthrown blocks that make up the subthrust part of the field in the northwest area of the field. Not all wells could be analyzed using the same approach due to differences in available log types and quality. As a result, several different analysis approaches were used.

The primary and most accurate analysis approach utilized the MULTIMIN program, which is an optional module to the Paradigm Geophysical Corporation's (<http://www.paradigmgeo.com>) GeoLog6® log interpretation program. The MULTIMIN program provides for a simultaneous solution for minerals, porosity, and fluids. The analysis requires density, neutron, shallow and deep resistivity logs as a minimum suite for analysis. The algorithms embodied in the software represent the current state-of-the-method available for determining porosity and fluid saturation from logs. Fifty wells had the required measurements to run this type of analysis. Thirty-nine of these were in the overthrust and eleven were in the subthrust blocks. Six of the wells contained section from both the overthrust and subthrust, so the total number of wells analyzed was forty-four.

The second most accurate method to assess porosity was to plot density and compensated neutron logs when both were available. This procedure was used when resistivity measurements were lacking, and the MULTIMIN analysis could not be carried out as a result. An accurate porosity can be obtained; however the Phosphoria did require a minor adjustment as will be discussed later. A total of twelve wells fell into this category, four

in the overthrust and eight in the subthrust. Two of the wells contained section from both the overthrust and subthrust so the total number of wells analyzed was ten.

The third most accurate porosity was determined when the only porosity measurement available was the density. It is extremely difficult to determine an accurate porosity with only one measurement. To make some use of this data, a method was developed that derived the best guess porosity and is shown in Section 2.2.4 of this report. Thirty-three wells contained only a density log; twenty-three in the overthrust and ten in the subthrust. Two of the wells contained section from both the overthrust and subthrust, so the total number of wells analyzed was thirty-one.

The last measurement to be addressed is the gamma ray neutron (GRN). The method of getting porosity was determined from the only two wells that contained both the GRN and some other measurement. In these two wells the other measurement was the density. It was important to utilize the GRN wells due to the shear number that only had this measurement. A total of forty-eight wells are involved, thirty-nine in the overthrust and nine in the subthrust. By including these wells, additional information was gained in areas that would not have any porosity coverage at all. It is understood that the accuracy of the GRN porosity is certainly suspect when used alone with no calibrated reference to compare to.

The next sections describe in greater detail the results of each of these four types of analyses.

## 2.2.2 MULTIMIN ANALYSIS

Figure 2-1 shows the results of the Phosphoria model that was generated over the first ten to twenty wells that were worked on. These wells were used as a calibration set to allow processing of the remaining wells. MULTIMIN operates on a "model" concept where all parameters for a given formation are saved in a model file. There is a Phosphoria model file and a Tensleep model file.

Another feature of MULTIMIN concerns the oil API and gas specific gravity parameters. These and all other fluid and tool parameters are corrected to reservoir conditions (for example, temperature, pressure, or hole size). Currently MULTIMIN will only handle oil or gas, not a combination of both.

### 2.2.2.1 *Phosphoria Analysis*

The Phosphoria model has the following characteristics:

- The gamma ray was not utilized in determining minerals. The effect of the Uranium mineral on the gamma ray response in the Phosphoria is well known.

- Track 1 - MULTIMIN minerals and total volume display
- Track 2 - depth in feet
- Track 3 - total porosity and fluid content. Area shaded green is percentage of porosity that is unmoved oil, area shaded yellow is percentage of moved oil in the invaded zone. The clear area is percent water saturation in the undisturbed formation.
- Track 4 - water saturation
- Track 5 - measured hole diameter and density correction

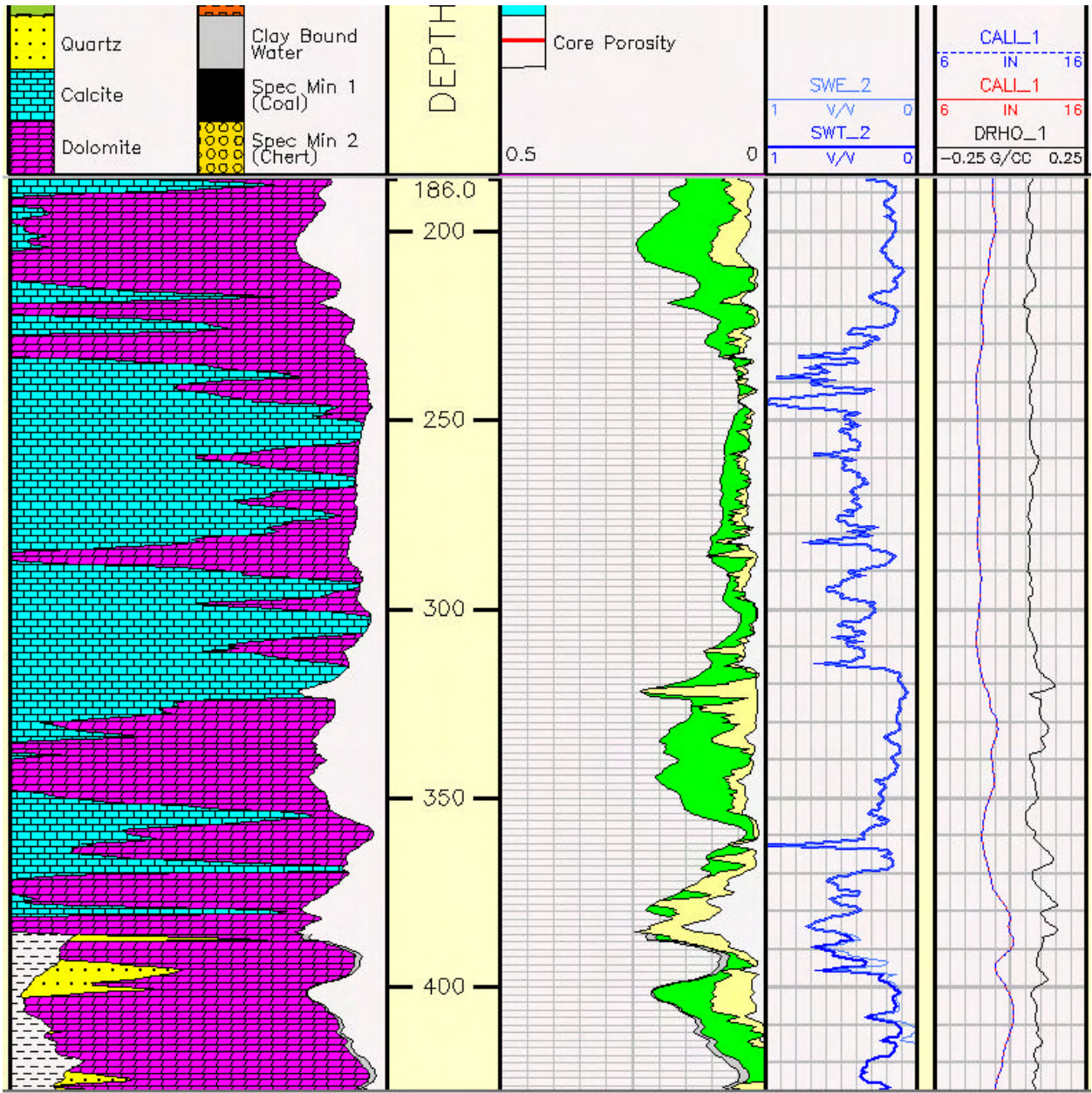


Figure 2-1. Phosphoria MULTIMIN display

- Only calcite and dolomite were chosen for mineral determination. The Phosphoria is usually found to be a clean carbonate.
- The water resistivity for the Phosphoria was adjusted during model determination. By utilizing the Pickett plot (Asquith and Gibson, 1982) during generation of the model, it soon became apparent that these values (shown below) applied across the Circle Ridge field. So, from the Pickett plot:

Rw: 1 ohmm at 80 degrees F (water resistivity)  
a: 1  
m: 1.8 (cementation exponent for porosity)  
n: 2 (water saturation exponent)

Figure 2-2 shows the Pickett plot for the Phosphoria in well 66-49.

Figure 2-3 presents (in black) the original logs used by MULTIMIN to create the mineral percentages, porosity, and fluid saturations. Also presented (in red) are the reconstructed logs generated by MULTIMIN, which shows how well the model predicts the original data.

As previously mentioned, the gamma ray log was not used in the Phosphoria model to determine the results. Thus there is no predicted gamma ray log in Track 1. However, the gamma ray log was used in the Tensleep model, and Figure 2-3 shows the match over this formation. Figure 2-3 covers the same interval as is shown in Figure 2-1.

#### 2.2.2.2 Tensleep Analysis

Figure 2-4 shows the results of the Tensleep model that was generated. The Tensleep model has the following characteristics:

- The gamma ray log was utilized for determining minerals.
  - Quartz, dolomite, and illite clay were chosen for mineral determination. The Tensleep also contains traces of heavy mineral, such as pyrite. Since there were an insufficient number of measurements to solve for pyrite, the end point for zero porosity was adjusted upwards from 2.65 to 2.67 in the model for the density to compensate.
- The water resistivity for the Tensleep, like the Phosphoria, was adjusted during model determination in a similar manner (Pickett plot).

Figure 2-5 shows the Pickett Plot for the Tensleep Formation.

The following values that worked well for the Phosphoria Formation also worked well for the Tensleep:

Track 1 - black: logged GR red: MULTIMIN predicted gr  
 Track 2 - black: logged nphi red: MULTIMIN predicted nphi  
 Track 3 - black: logged rhob red: MULTIMIN predicted rhob  
 Track 4 - intervals shown  
 Track 5 - black: logged dt red: MULTIMIN predicted dt -- no logs shown  
 Track 6 - black: logged x conductivity red: MULTIMIN predicted x conductivity  
 Track 7 - black: logged t conductivity red: MULTIMIN predicted t conductivity

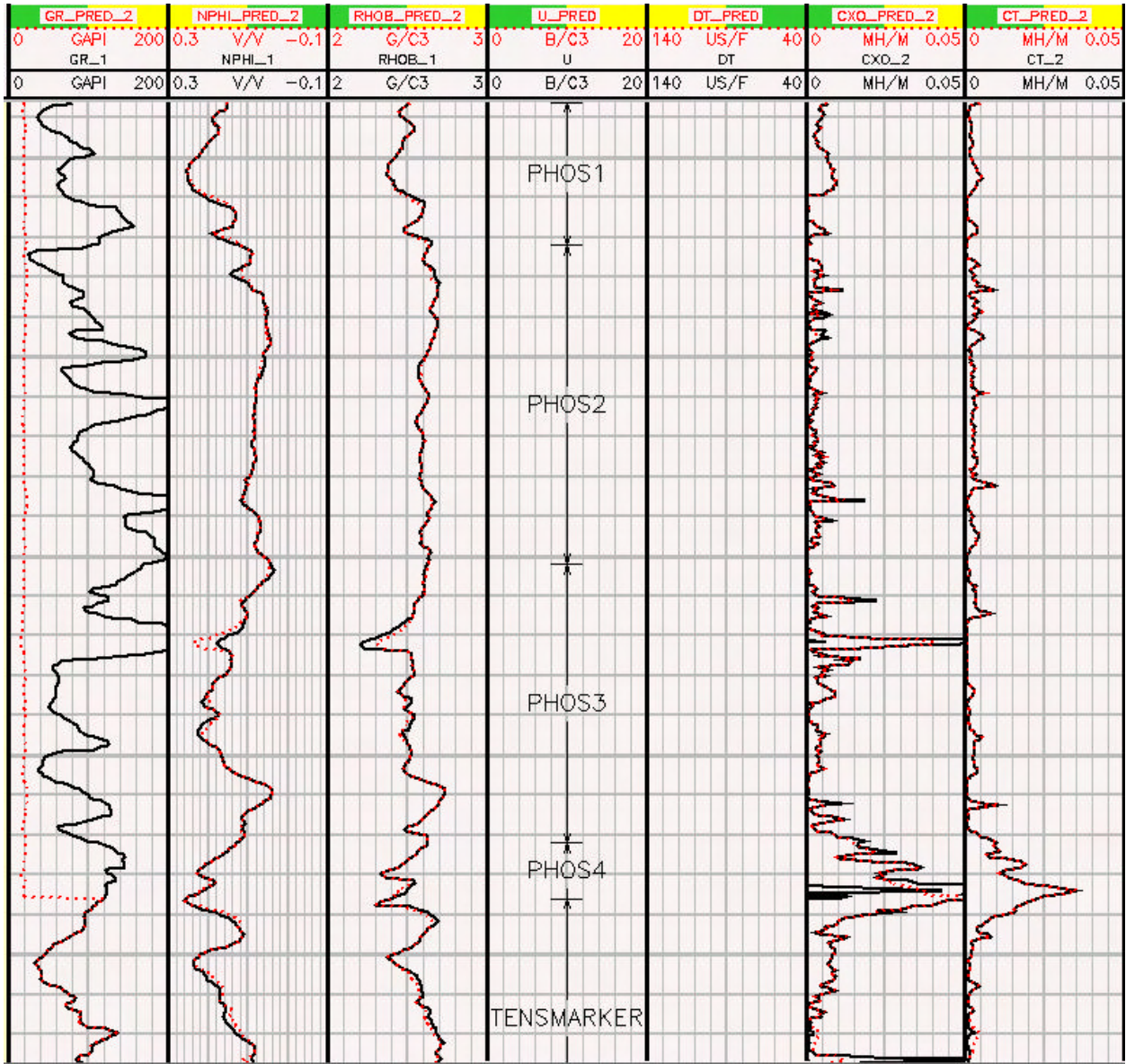


Figure 2-2. Picket Plot for Shoshone 66-49, Phosphoria Formation

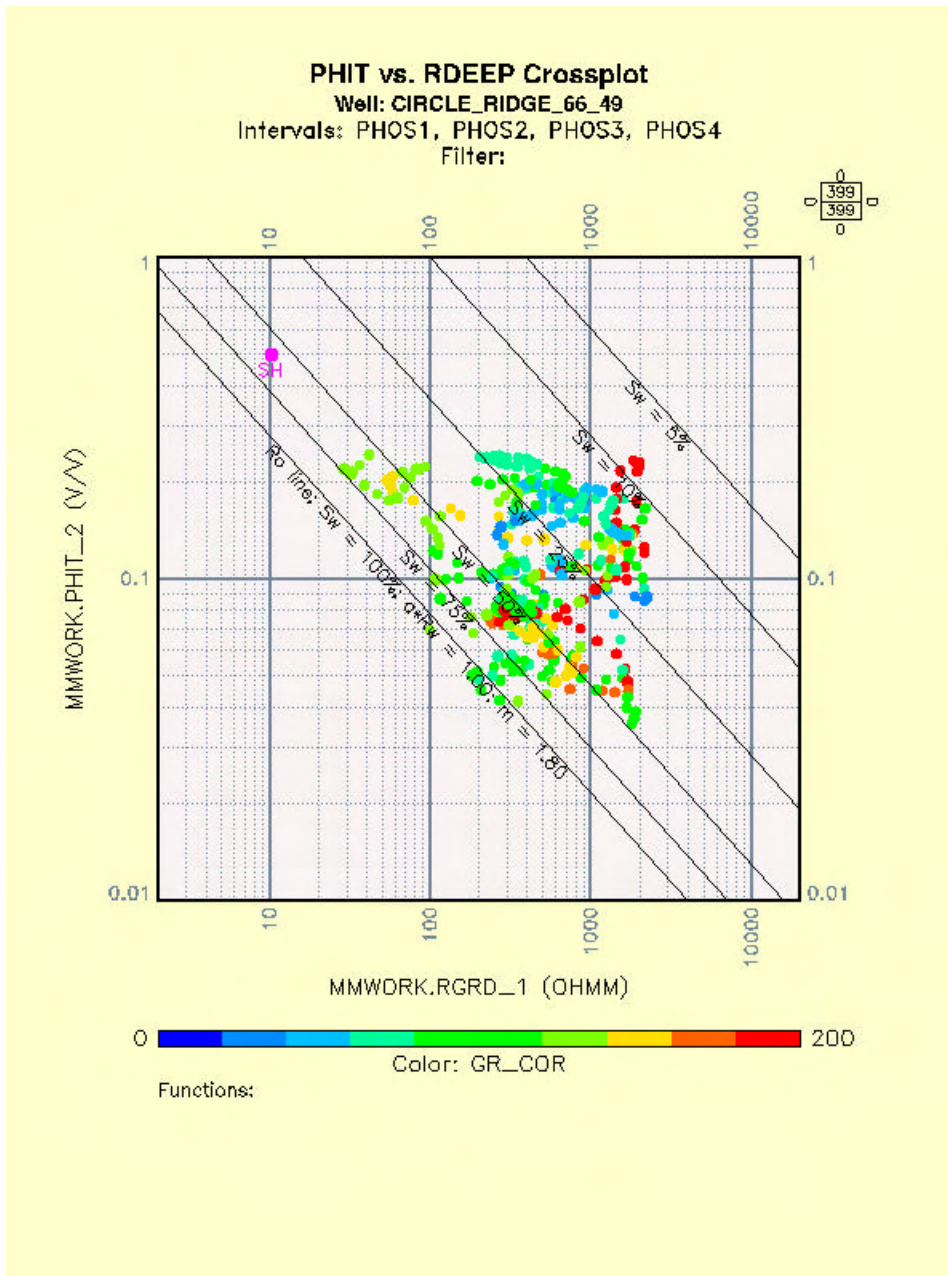


Figure 2-3. Phosphoria MULTIMIN predicted and real logs

Rw: 1 ohmm at 80 degrees F (water resistivity)  
a: 1  
m: 1.8 (cementation exponent for porosity)  
n: 2 (water saturation exponent)

Figure 2-6 presents the reconstructed logs generated by MULTIMIN. The Figure shows that there is a good fit between the predicted logs and the originals. Figure 2-6 covers the same interval as Figure 2-4.

### 2.2.3 POROSITY CROSSPLOTS

This section addresses the methodology used in wells in which the density and compensated neutron logs are the only porosity logs available.

Figure 2-7 demonstrates the "cp1b" function that allows determination of porosity and apparent matrix density from the density and compensated neutron logs in the Phosphoria Formation. Figure 2-8 shows an analogous plot for the Tensleep Formation.

Figure 2-9 shows a comparison of the crossplot porosity in forty-six wells that contain the MULTIMIN porosity for the Phosphoria. A quadratic regression (the blue curve) was performed that corrected crossplot porosity to more closely match the PHIT MULTIMIN porosity. This was used on the ten wells that fit the crossplot criteria.

Figure 2-10 is the corresponding plot to Figure 2-9 for the Tensleep Formation. This plot shows that little correction to the crossplot porosity is required to closely match the MULTIMIN porosity in the Tensleep.

This process was performed on four wells in the overthrust and eight in the subthrust portions of the Circle Ridge Field.

### 2.2.4 DENSITY LOG ONLY

In some wells, density logs are the only porosity logs available, making accurate determination of total porosity more difficult. The method relies upon use of the gamma ray log in concert with the density log to first determine rock type, and then to compute porosity based upon relations and parameter values for the rock type. A solution for each formation was generated, and a LOGLAN (GeoLog® programming language) program was built to handle both the Phosphoria and Tensleep at once. The annotated LOGLAN program is presented in Appendix 1.

Figure 2-11 shows the results of the program on well 66-49 Phosphoria Formation. There is reasonable agreement with the MULTIMIN porosity. Figure 2-12 shows the results on the same well in the Tensleep Formation.

This analysis was carried out on twenty-three wells in the overthrust and ten wells in the subthrust. No single well of this type contained both overthrust and subthrust sections.

- Track 1 - MULTIMIN minerals and total volume display
- Track 2 - depth in feet
- Track 3 - total porosity and fluid content. Area shaded green is percentage of porosity that is unmoved oil, area shaded yellow is percentage of moved oil in the invaded zone. The clear area is percent water saturation in the undisturbed formation. The red asterisks are core porosity.
- Track 4 - water saturation
- Track 5 - measured hole diameter and density correction

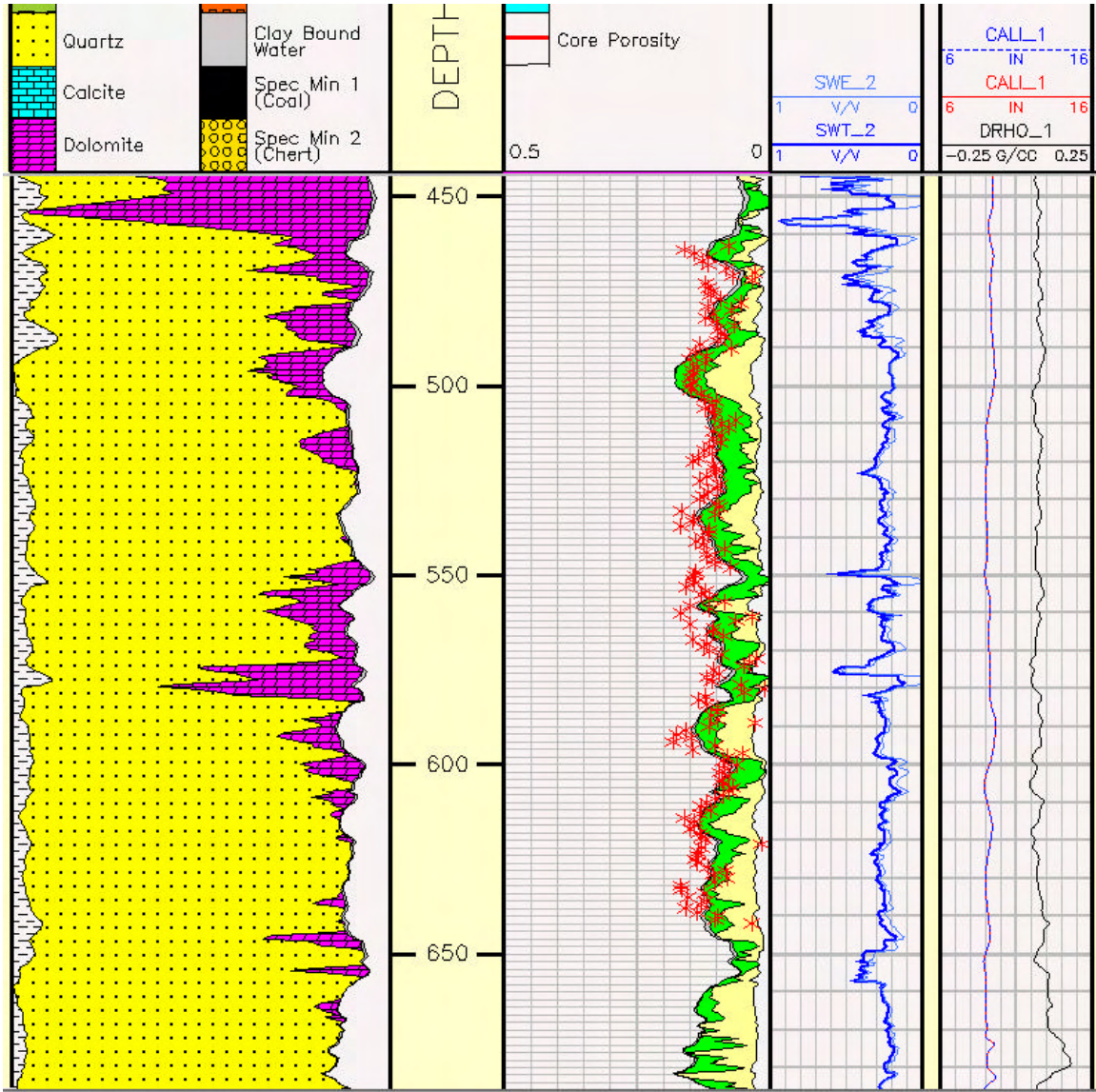


Figure 2-4. Tensleep MULTIMIN display

Track 1 - black: logged GR    red: MULTIMIN predicted gr  
 Track 2 - black: logged nphi    red: MULTIMIN predicted nphi  
 Track 3 - black: logged rhob    red: MULTIMIN predicted rhob  
 Track 4 - intervals shown  
 Track 5 - black: logged dt    red: MULTIMIN predicted dt -- no logs shown  
 Track 6 - black: logged x conductivity    red: MULTIMIN predicted x conductivity  
 Track 7 - black: logged t conductivity    red: MULTIMIN predicted t conductivity

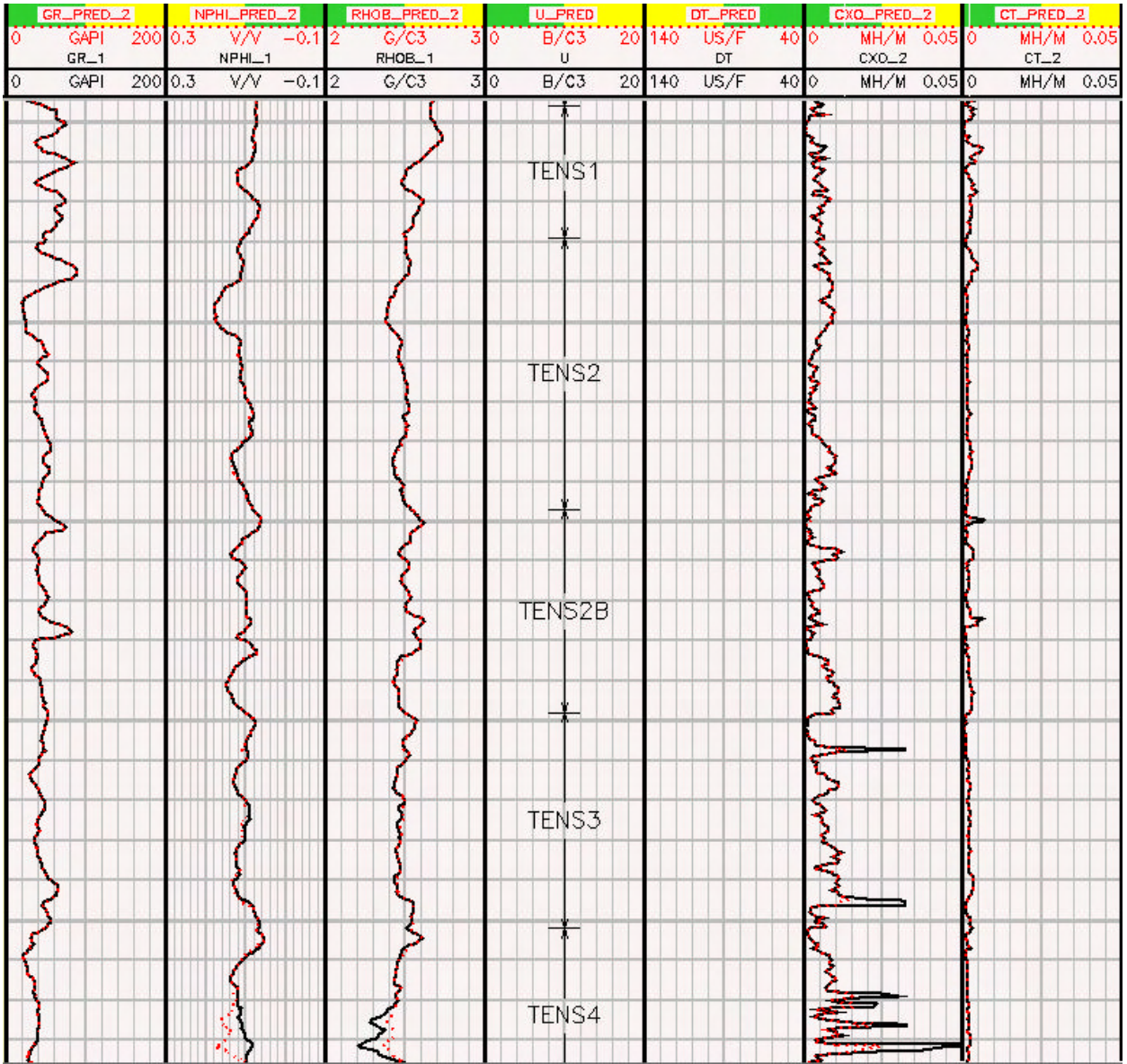


Figure 2-5. Pickett Plot for well 66-49, Tensleep Formation

**PHIT vs. RDEEP Crossplot**  
**Well: CIRCLE\_RIDGE\_66\_49**  
**Intervals: TENSMARKER, TENS1, TENS2, TENS2B, TENS3, TENS4, TENS5**  
**Filter:**

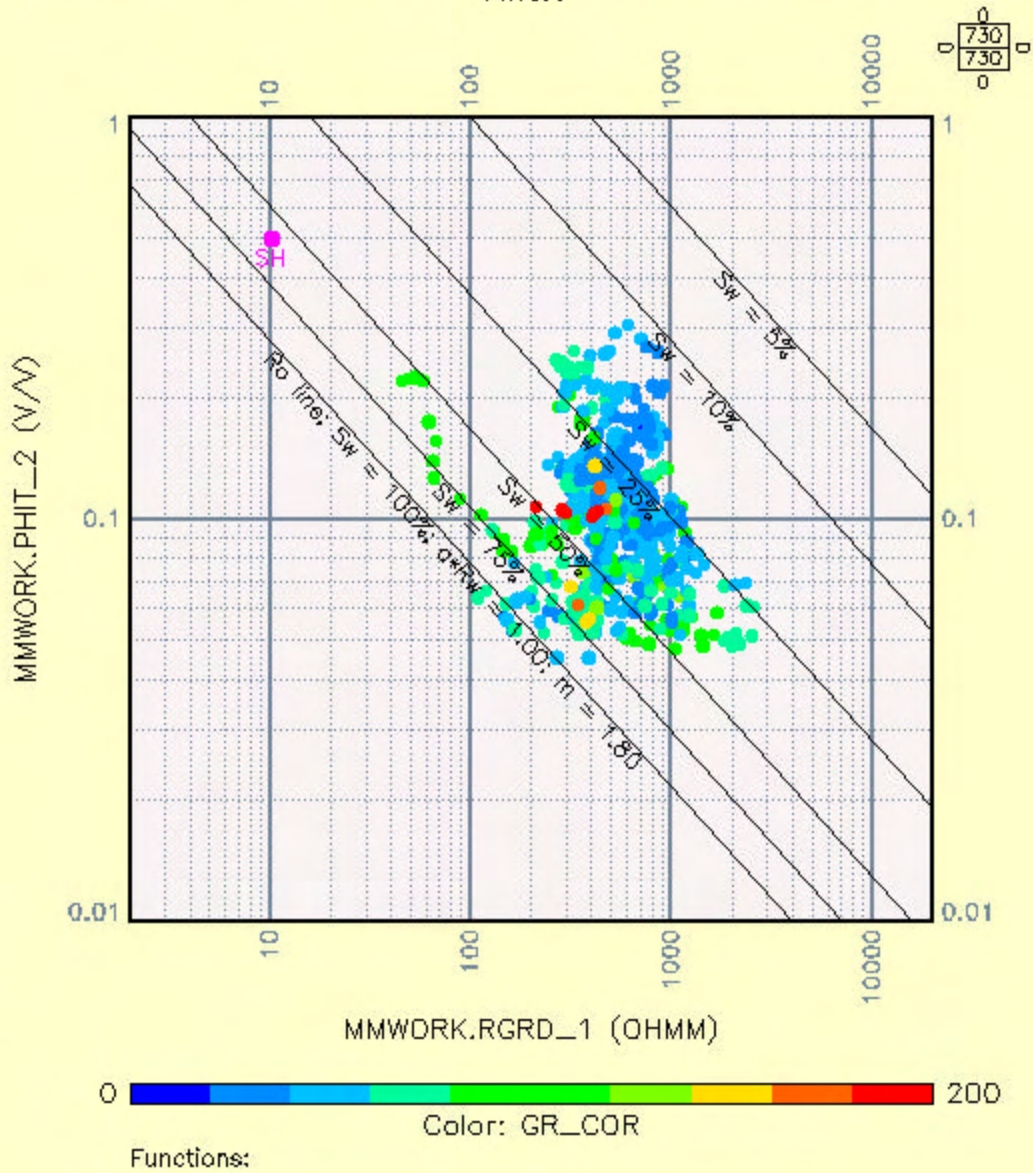


Figure 2-6. Tensleep MULTIMIN predicted and actual logs

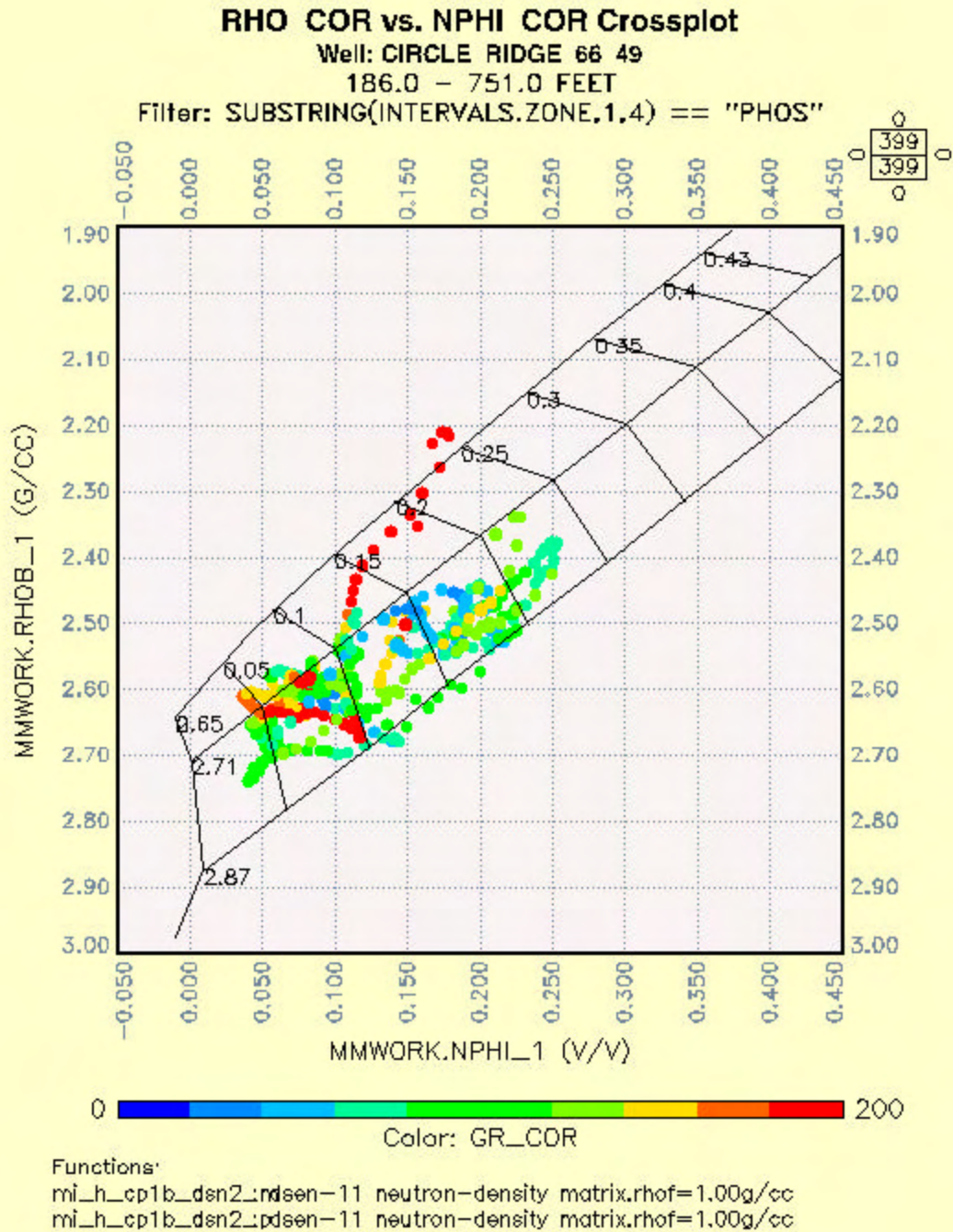


Figure 2-7. Crossplot of rhob and nphi in Shoshone 66-49, Phosphoria Formation

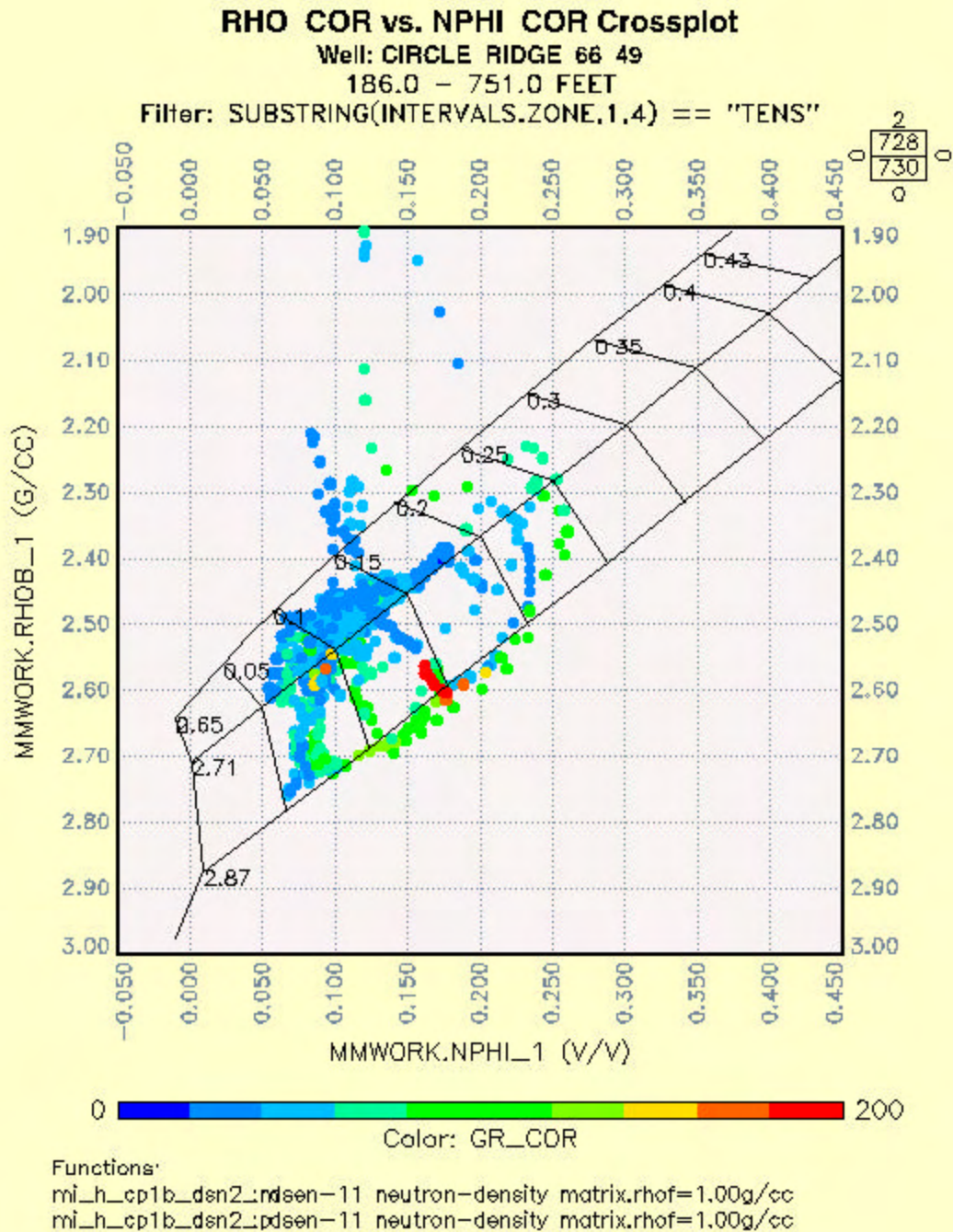


Figure 2-8. Crossplot of rhob and nphi in Shoshone 66-49, Tensleep Formation

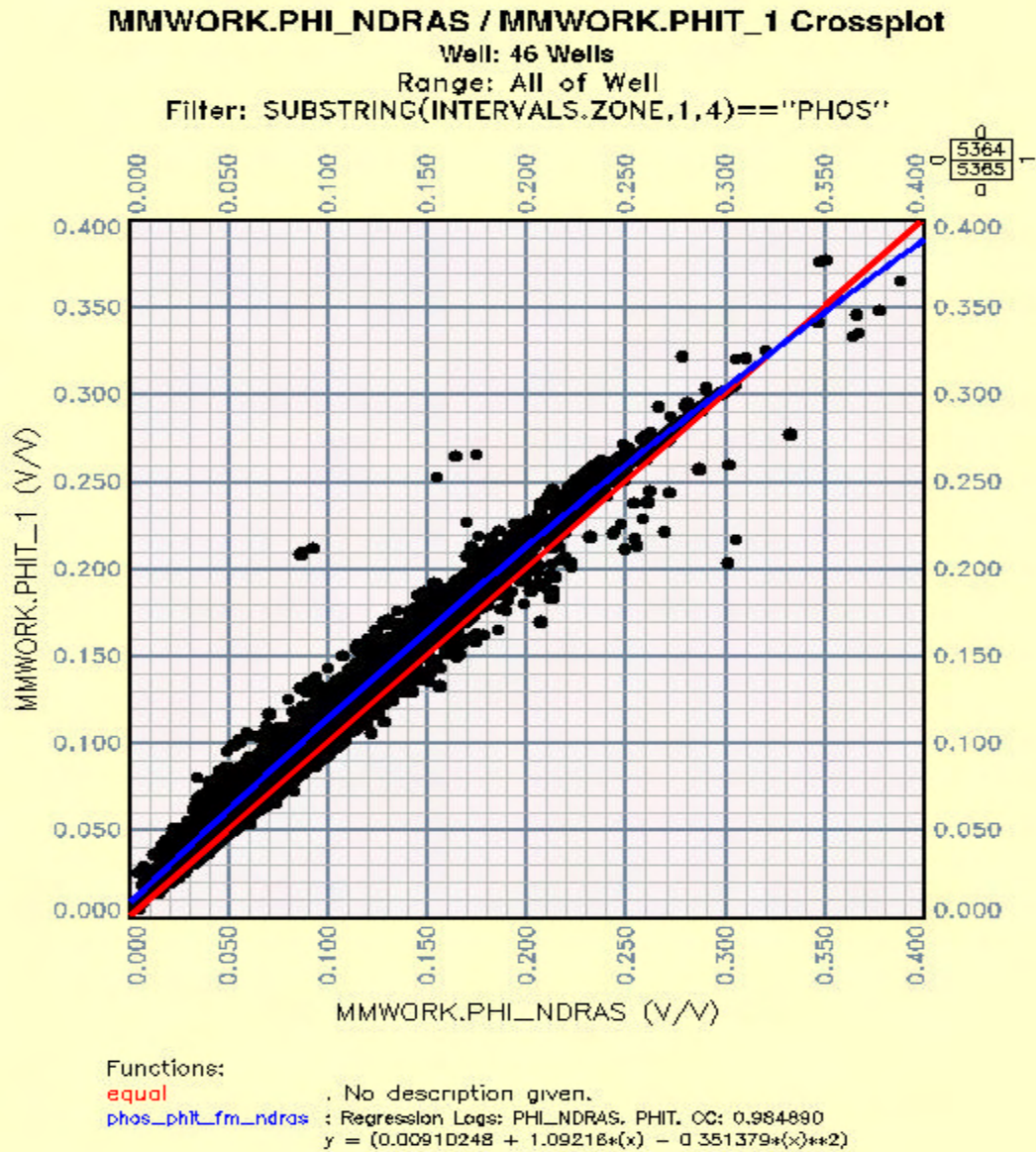


Figure 2-9. Comparison of crossplot porosity (X-axis) to MULTIMIN porosity (PHIT – Y-axis) in the Phosphoria Formation for 46 wells.

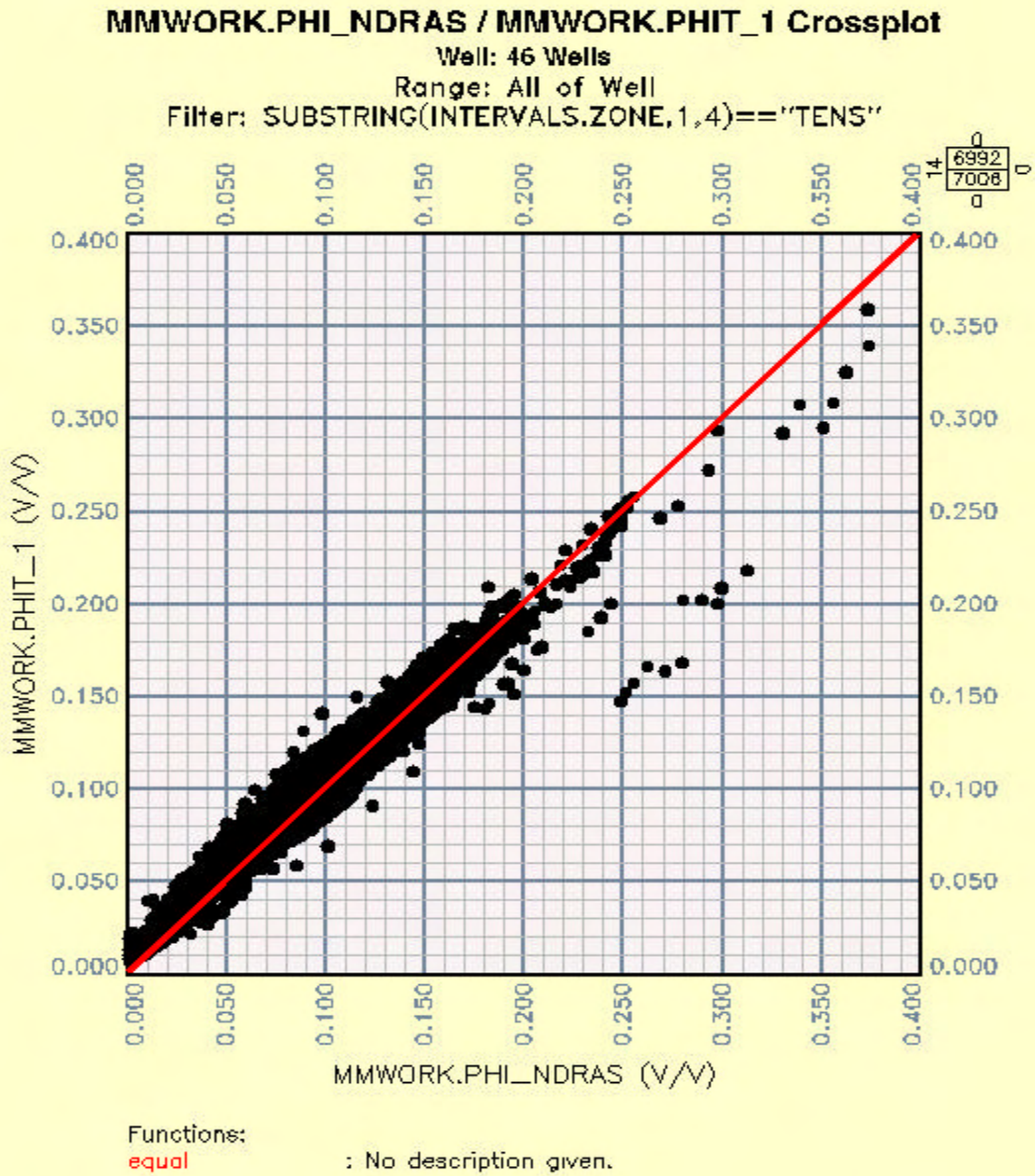


Figure 2-10. Comparison of crossplot porosity (X-axis) to MULTIMIN porosity (PHIT – Y-axis) in the Tensleep Formation for 46 wells.

Track 1: blue - calculated water saturation    black - gr

Track 2: depth in feet

Track 3: black - density porosity    magenta - MULTIMIN porosity    blue - density log

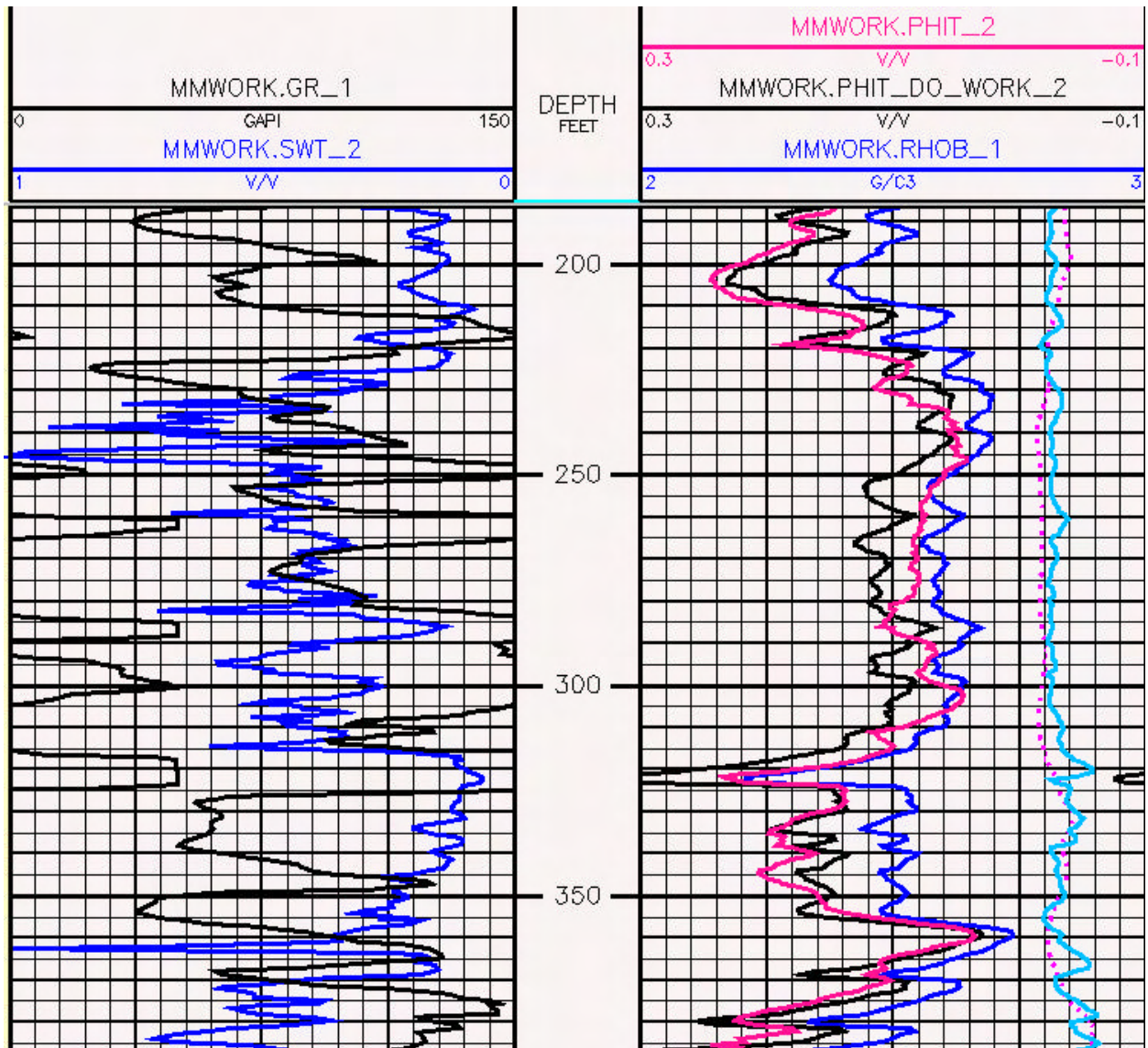


Figure 2-11. Porosity determination from density log, Shoshone 66-49, Phosphoria Formation.

Track 1: blue - calculated water saturation black - gr  
 Track 2: depth in feet  
 Track 3: black - density porosity magenta - MULTIMIN porosity blue - density log

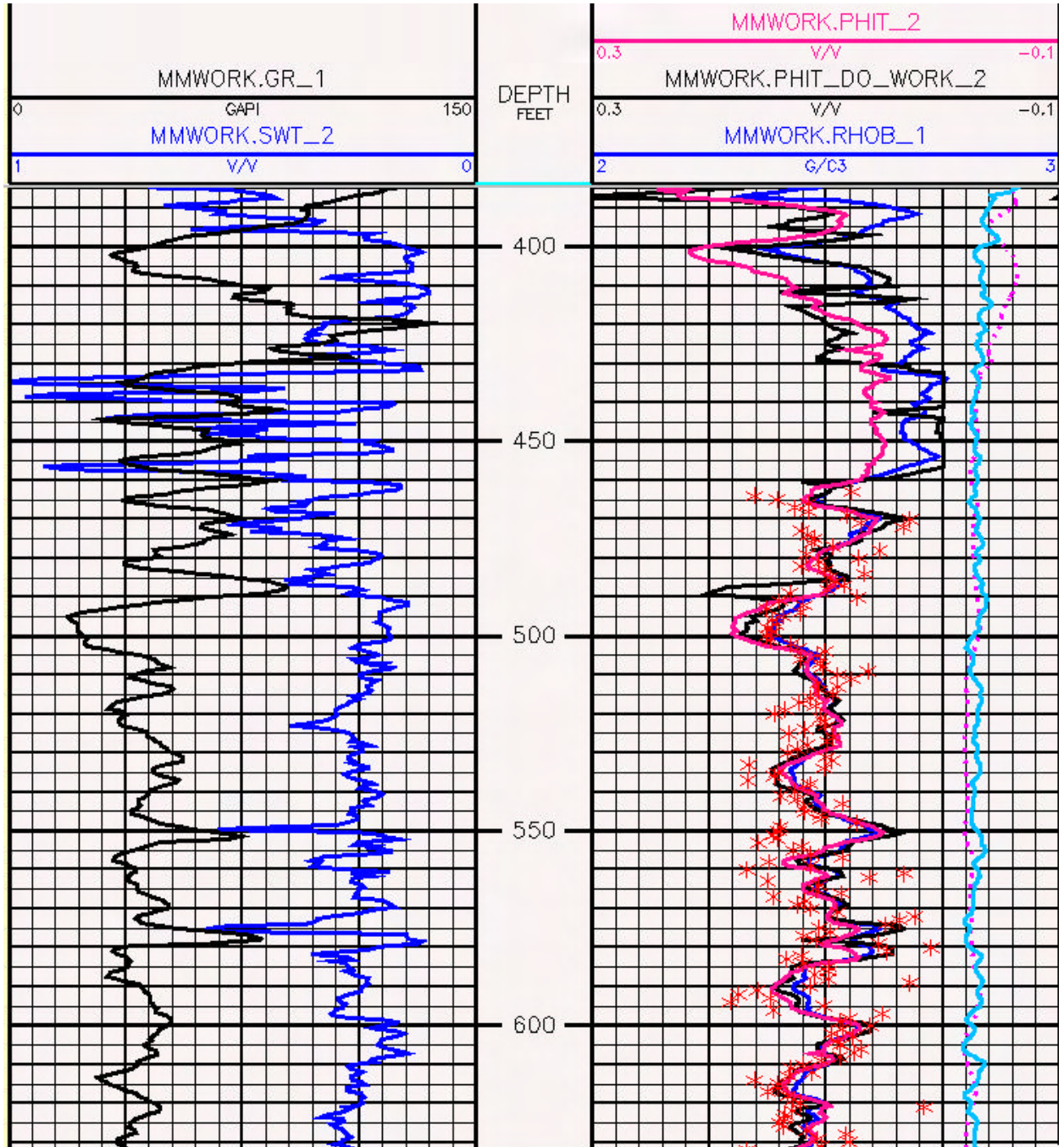


Figure 2-12. Porosity determination from density log, Shoshone 66-49, Tensleep Formation.

## 2.2.5 GAMMA RAY NEUTRON (GRN) POROSITY

The method used for these wells relies on an old technique of log analysis (Asquith and Gibson, 1982). The wells in the Circle Ridge Field that have only the GRN logs were drilled in the 1950's and 1960's. Of all of these wells, two also contained density logs, which proved very useful for calibration.

Figure 2-13 through 2-15 show the calibration of the GRN using the control provided by the density log for the Tensleep Formation in two wells and for the Phosphoria Formation in one well. The logs for these two wells suggest that it may be possible to estimate porosity from GRN count rate. Near the bottom of the Phosphoria there are anhydrite layers, which produce a low GRN porosity point (or high GRN count rate). The Phosphoria layers "PHOS1" and "PHOS2" shown on the figure generally have higher porosity points (or lower GRN count rates). These observations can be used to estimate porosity in the following manner by re-scaling the transforming a linear count rate (NEU) to a logarithmic porosity value (PHIT\_NEU).

First, a GRN count rate frequency histogram was computed for the two formations. Figure 2-16 shows this histogram for Well 66-34. This is one of the oldest wells, where the count rate is extremely low. The minimum and maximum values from this histogram are used to define the limits of the input log, in this case, the GRN count (Figure 2-17). In order to map the GRN count rate to the same scale as the porosity, and because of the inverse relation between porosity and GRN count rate, the old minimum value of 1.8 is mapped to 30% porosity, while the old maximum GRN count rate value of 13.2 is mapped to 1% porosity.

## 2.3 Field Data Collection

Several weeks of fieldwork took place in June and July, 2000 to gather geological transect data for building cross-sections through the field, and to garner detailed fracture attribute information for key formations and structural positions in order to relate the structural evolution to fracture development.

### 2.3.1 GEOLOGICAL RECONNAISSANCE & CROSS-SECTION DATA GATHERING

Several days of geological reconnaissance were undertaken prior to siting cross-sections and scanlines in order to determine the most useful locations. The starting point for the reconnaissance was the geological map prepared by Smith (2000). The goal was to field check the mapped geology and structure, to update existing or map new faults and folds exposed at the surface, and to determine which formation or formations had fracture patterns that would be most similar to those developed in the reservoir formations, had exposures in several different structural positions, had good fracture development, and also were accessible.

Track 1: black - gr log    blue - calculated water saturation (SWT) from density porosity  
 Track 2: depth  
 Track 3: formation tops  
 Track 4: magenta - density porosity    black - GRN porosity    blue - density correction

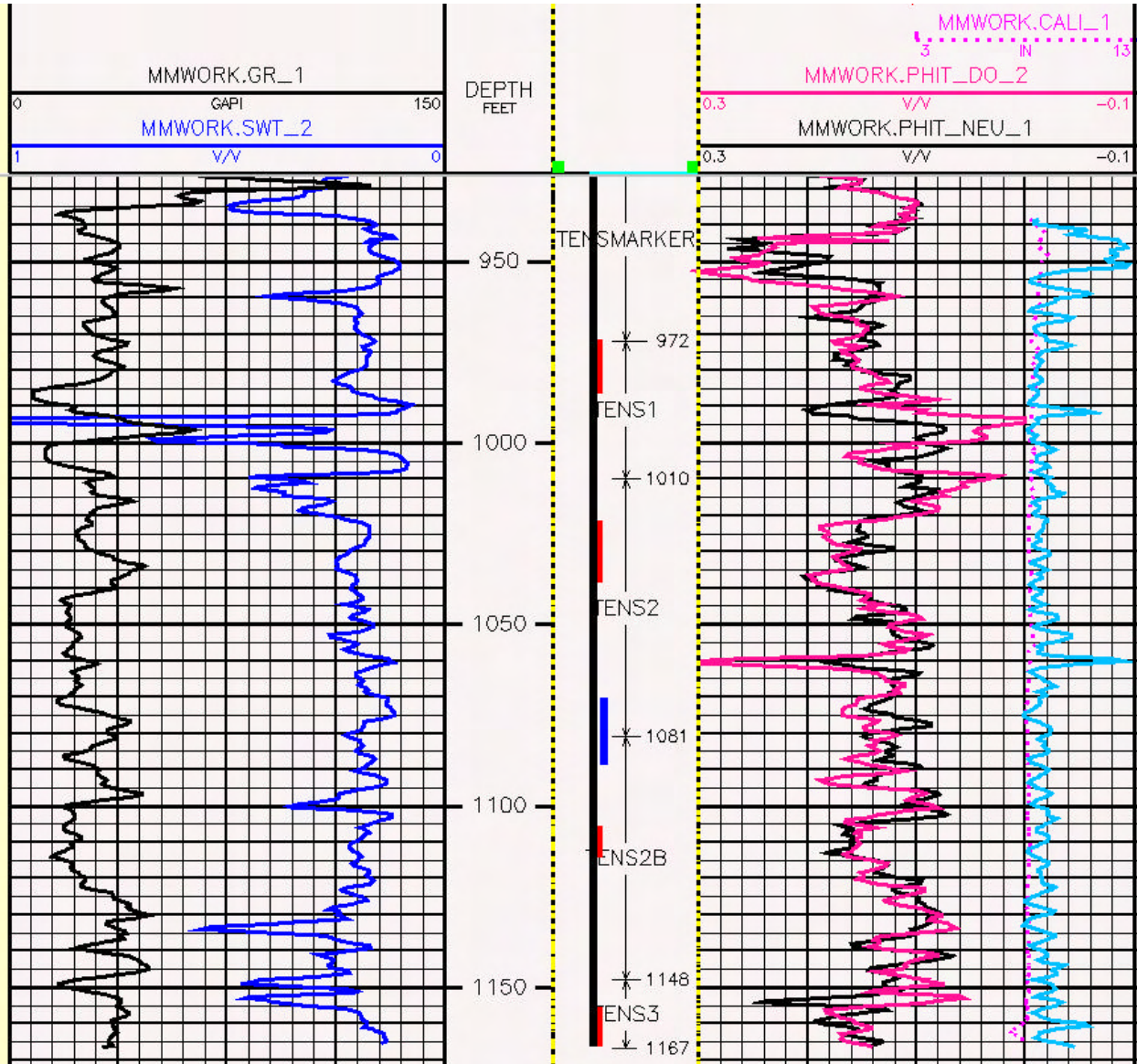


Figure 2-13. GRN log, Shoshone 66-15, Tensleep Formation

Track 1: black - gr log    blue - calculated water saturation (SWT) from density porosity  
 Track 2: depth  
 Track 3: formation tops  
 Track 4: magenta - density porosity    black - GRN porosity    blue - density correction

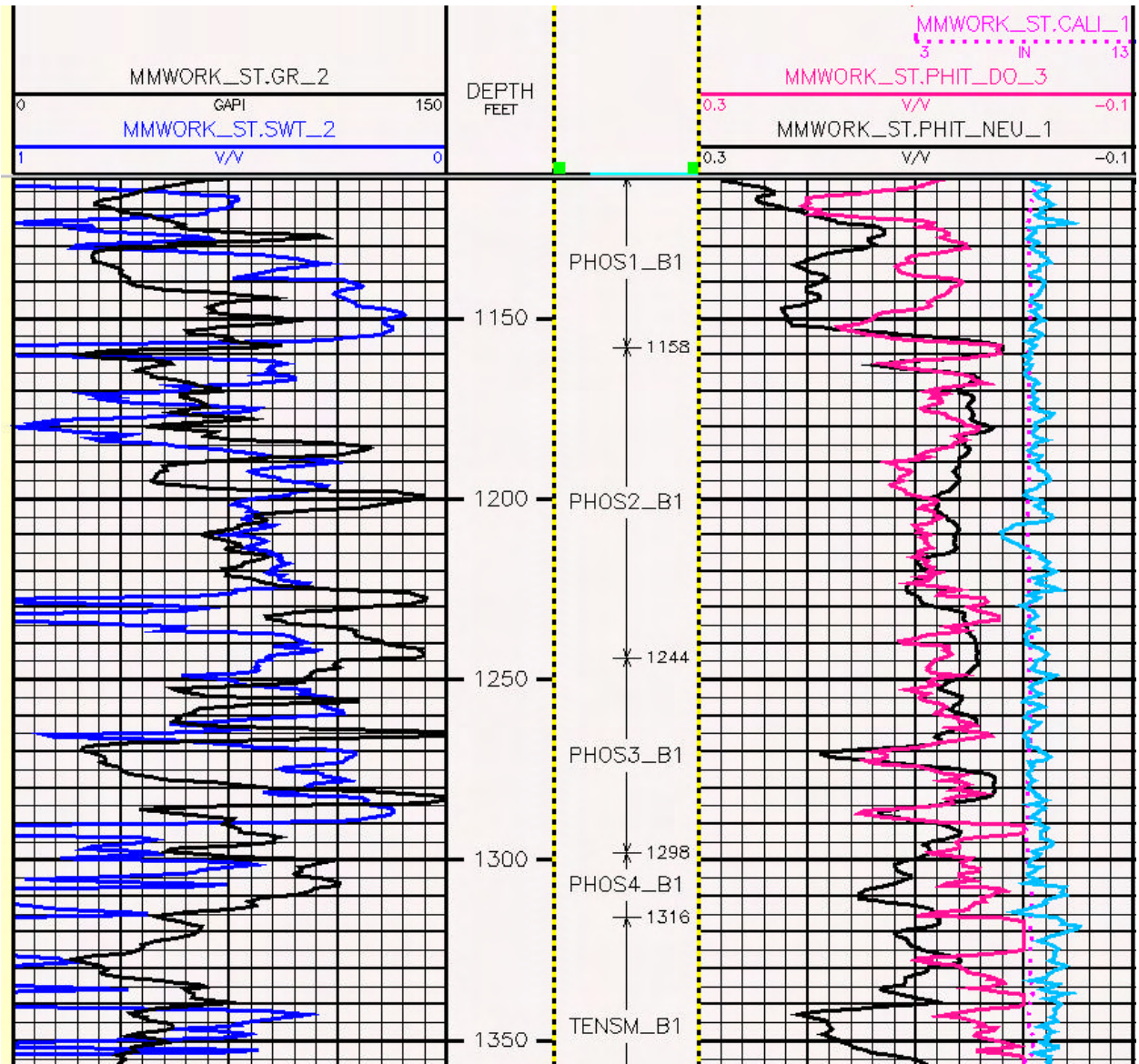


Figure 2-14. GRN log, Shoshone 66-45, Phosphoria Formation

Track 1: black - gr log    blue - calculated water saturation (SWT) from density porosity  
 Track 2: depth  
 Track 3: formation tops  
 Track 4: magenta - density porosity    black - GRN porosity    blue - density correction

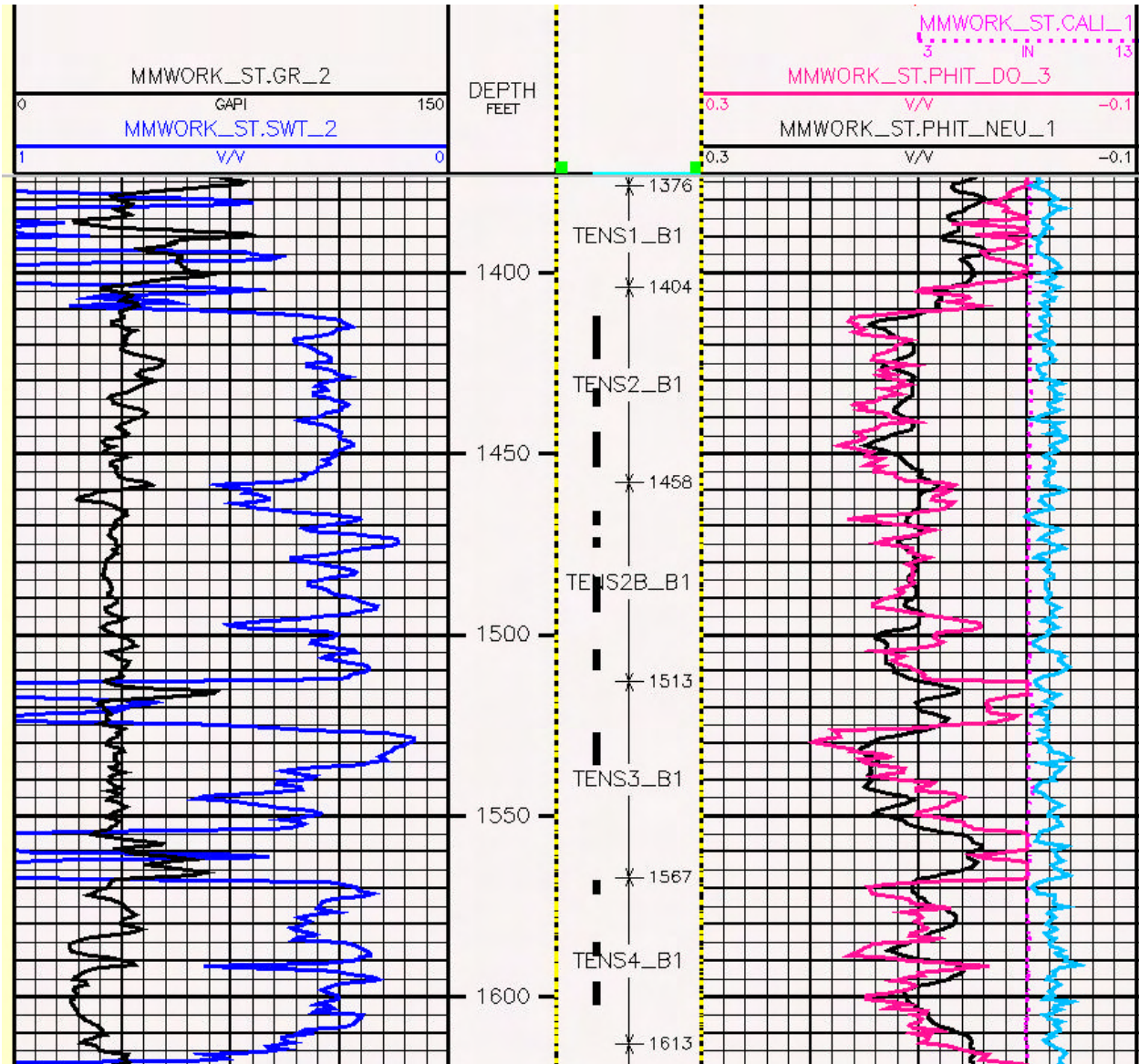
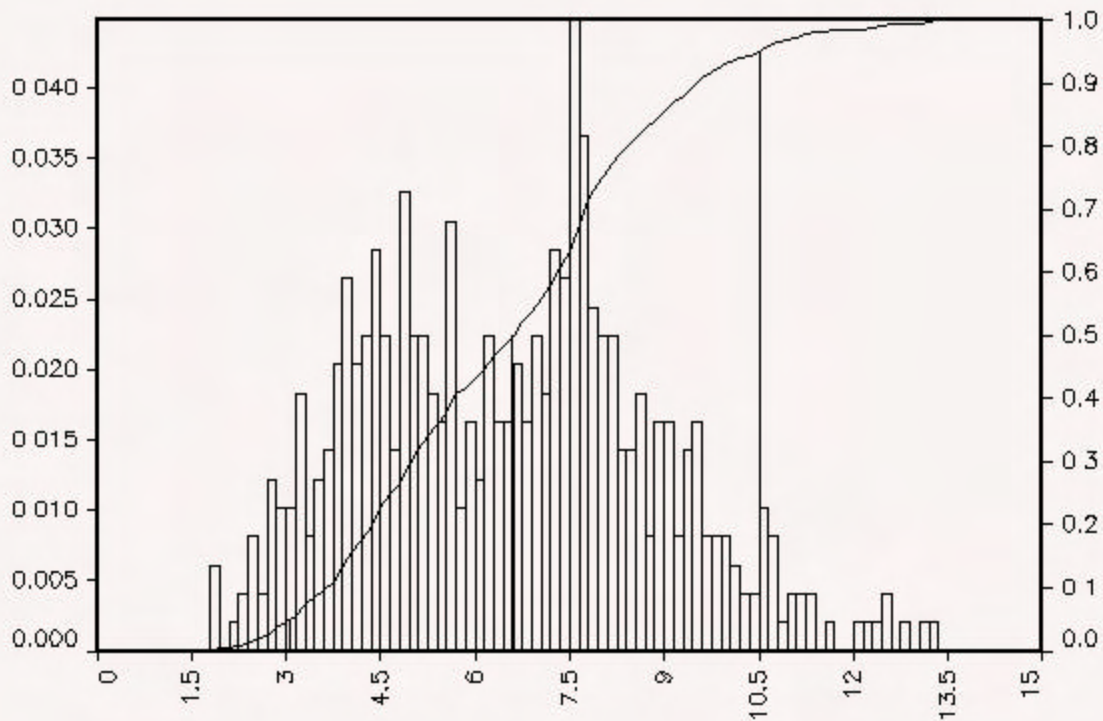


Figure 2-15. GRN log, Shoshone 66-45, Tensleep Formation

Frequency Histogram of MMWORK.NEU\_1  
 Well: CIRCLE\_RIDGE\_66\_34  
 695.0 - 940.0 FEET  
 Filter:



Statistics:

Possible values	491
Missing values	0
Minimum value	1.84618
Maximum value	13.21988
Range	11.37370
Mean	6.52962
Geometric Mean	6.10429
Harmonic Mean	5.65372
Variance	5.23578
Standard Deviation	2.28818
Skewness	0.27143
Kurtosis	2.55963
Median	6.58125
Mode	7.57500

Figure 2-16. Frequency plot of GRN count rate (NEU), Shoshone 66-34

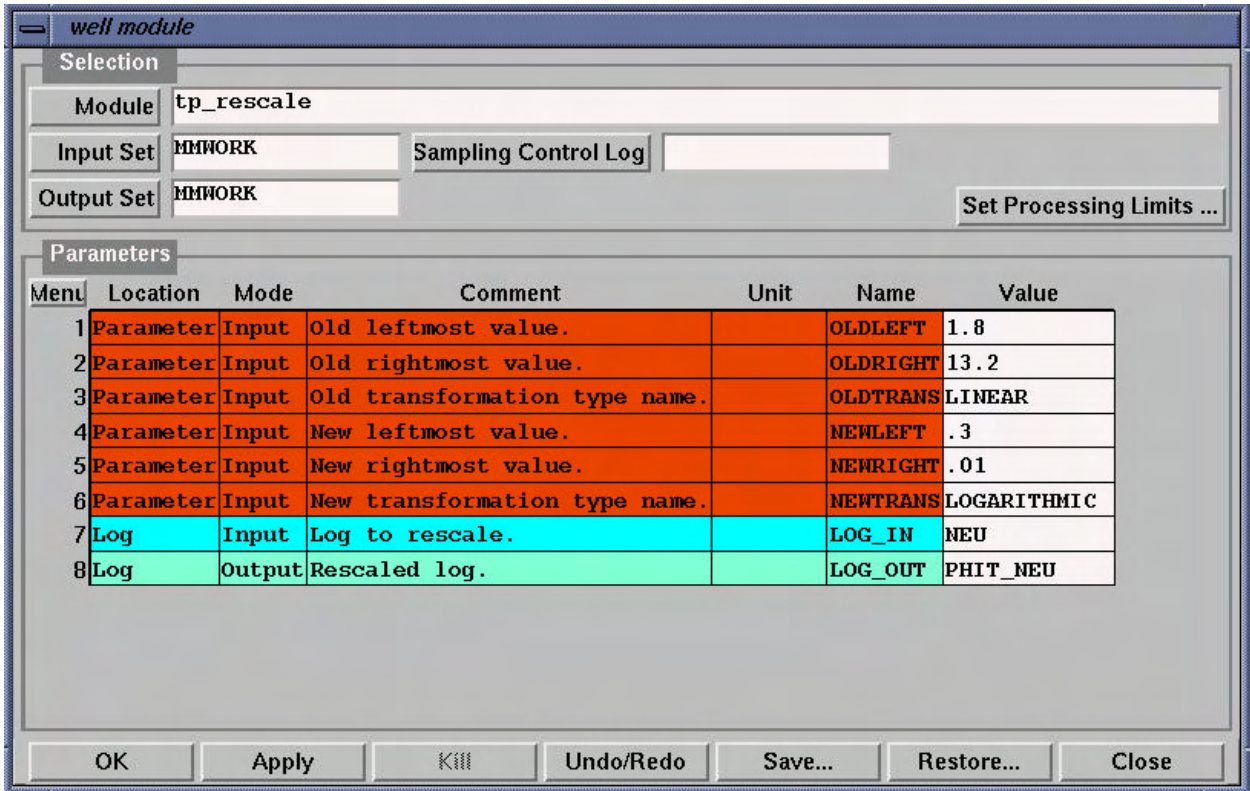


Figure 2-17. Rescale module with representative settings for the GRN count rate (NEU) to porosity (PHIT\_NEU), Shoshone 66-34.

Field reconnaissance showed that there were areas in the field that required greater structural detail and control. To accomplish this, three new cross-sections were sited. Their locations are shown in Figure 2-18. The cross-sections were located so that they would pass through or very close to wells where there was subsurface data on formation tops and faults.

Two of the new cross-sections were located in the northwestern end of the Field. This is an area of considerable structural complexity where there are several major faults and the hinge of the fold changes azimuth.

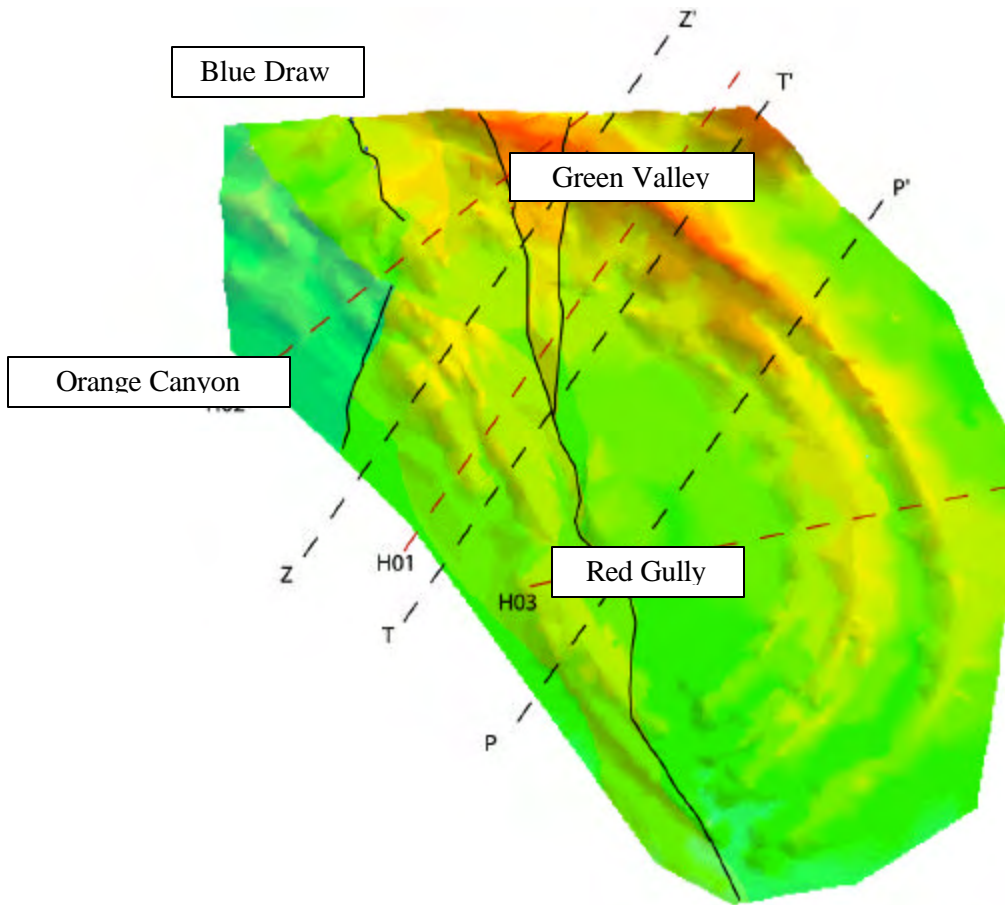


Figure 2-18. Picture showing the topography of Circle Ridge. The spectrum corresponds to elevation where red is the highest and green represents the lower parts. The fault traces of the Red Gully and Green Valley faults cross cut the whole field. Orange Canyon and Blue Draw are also shown in the NW part of the field. The cross-sections are shown as hatched lines. The P, T and Z sections were produced by Anderson and O’Connell (1993) and H01, H02 and H03 are the new cross-sections from the June field campaign.

### 2.3.2 EXPERIMENTAL TECHNIQUES FOR CALCULATING FRACTURE ORIENTATIONS, INTENSITY AND SIZE FROM OUTCROP DATA

#### 2.3.2.1 Overview

The analysis of fracture orientations, intensity and size is important for two different aspects of this project:

1. determination of how finite strain may control fracture development; and
2. development of statistical models for these quantities in order to create DFN models.

In the Circle Ridge Field, fracture information is very sparse in the subsurface, coming from unoriented core and a few image logs. Since the methodology adopted in this

project requires the comparison of the strain field in various structural positions relative to the fracture orientations, intensity and size, subsurface data is not adequate as spatial coverage is very low and there is no direct information on fracture size. On the other hand, the top of the Field is only a few hundred meters below the surface near the crest, so that the abundant outcrops above the Field should reflect a similar deformation history, at least in those units below the detachment zone afforded by the Gypsum Springs Formation. Thus the fracture parameters necessary for ascertaining the structural controls on fracturing and developing input statistical distributions has been based upon studies of fracturing in outcrop (Figure 2-19).

### 2.3.2.2 Scanline Sampling



**Figure 2-19. Scanline affixed to Triassic Red Peak Member.**

Figure 2-20 shows the measurement of the trace length for one specific fracture crossing the scanline, while Figure 2-21 summarizes the data collected and the form it was collected in. Note that orientation information about each scanline, as well as the prevailing bedding orientation, was collected in addition to the fracture data. This information was collected primarily in order to compensate for biases that result from scanline sampling of fractures (La Pointe and Hudson, 1985). All orientations were collected without adjustment for magnetic declination. Corrections for declination were made during the processing of the data. A complete database consisting of all of the scanline data can be found in the project webpage, <http://www.fracturedreservoirs.com>.



Figure 2-20. Detail of scanline measurements. The photo illustrates the measurement of fracture trace length for a specific fracture crossing the scanline.

**Name: SCANLINE\_8**                      **Date: 070600**

---

GPS points along the scan line

Waypoint	Altitude (ft)	Scanline dist. (ft)	Leg	Orientation
134	7218	0		
135	7226	21	1	180 -5
136	7225	36	2	165 2

Rocktype                      Read Peak  
 Stratigraphic thickness                        
 Bedding orientation                      N6W, 11N

---

Scanline length ft (decimal)	Leg	Orientation		Trace length		Terminations		Movement	Comments
		Strike	Dip	ft	in	upper	lower		
0.5	1	N85W	78S	2	7	T	U		
0.8	1	N86W	80S	0	9	T	A		
0.9	1	N84W	82S	0	7	B	B		
1.5	1	N89E	85S	1	8	B	B		
1.1	1	N58W	90S	3	8	A	U		
2.5	1	N80E	90S	10	0	U	U		CaCO3 filled
2.7	1	N71W	74N	2	0	B	A		
3.1	1	N76W	86N	4	0	A	U		
3.4	1	N85E	85N	1	5	B	U		
3.8	1	N70E	90S	5	4	A	U		
3.2	1	N76W	74N	5	7	A	U		
4.4	1	N90W	66S	1	3	A	B		
4.9	1	N89W	67N	7	10	U	U		
5.2	1	N79W	88N	2	0	A	U		
5.5	1	N65E	66N	1	3	H	T		
6.6	1	N72W	68S	1	4	T	B		
6.4	1	N24W	81S	4	2	T	T		

Figure 2-21. Example of data recorded for each scanline.

### 2.3.3 STATISTICAL ANALYSIS TECHNIQUES

#### 2.3.3.1 Fracture Orientations

The method adopted in this project for characterizing fracture orientations consisted of plotting all geologically similar fractures on a stereoplot, correcting for magnetic declination, and then correcting for orientation biases using the Terzaghi correction (Terzaghi, 1965). Additionally, all fractures were rotated relative to bedding in such a way that measured bedding strike was rotated about the Z-axis so that it was north-south. Then the fractures were rotated about the north-south axis until bedding dips were horizontal. These rotations make it possible to compare fracture orientations with bedding orientation, to assess whether there is a consistent pattern as would be expected if fractures were formed due to folding (Figure 1-13). These steps are shown in Figure 2-22.

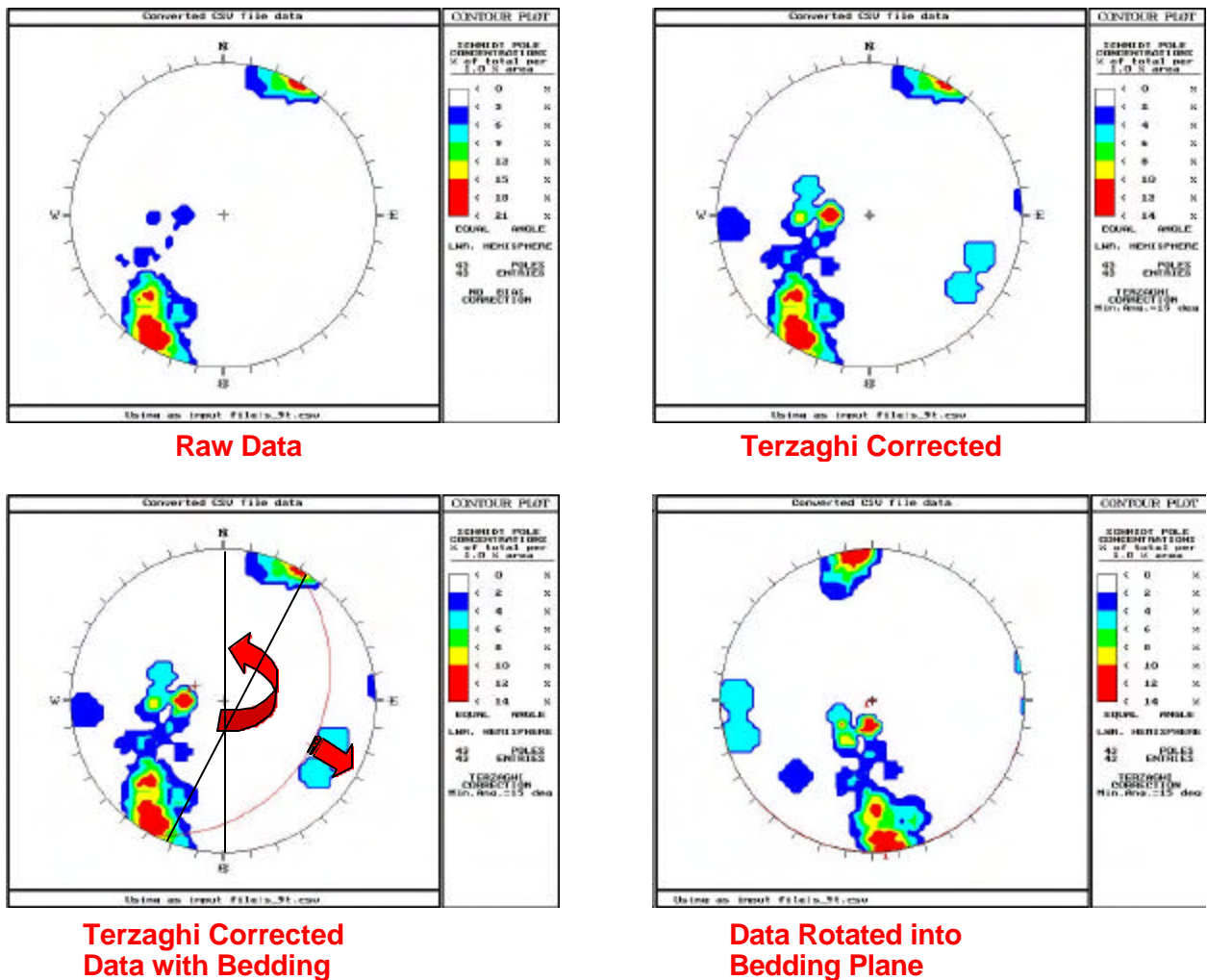


Figure 2-22. Analysis of fracture orientations, including rotation into bedding plane.

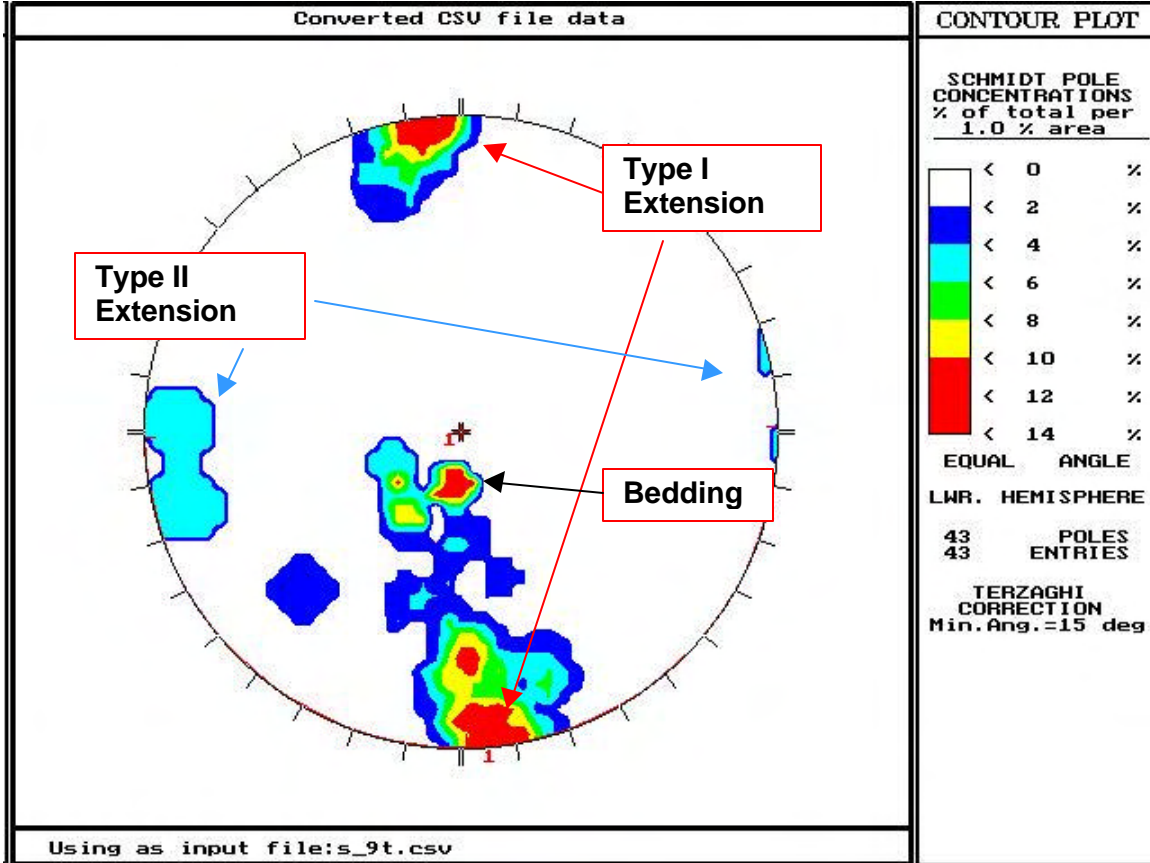


Figure 2-23. Example of possible interpretation of fracture orientations relative to bedding orientation.

Figure 2-23 shows how the fracture orientations may be interpreted once they have been rotated into the bedding plane. In this example, there are three concentrations of poles to fractures. The greatest concentration (the red contours) occurs near the top and bottom of the equal-area stereoplot. This indicates a modal fracture orientation that strikes parallel to the dip direction of bedding and is also orthogonal to bedding. This orientation is sometimes referred to as a Type I extension fracture (Stearns and Friedman, 1972). Another major concentration occurs near the center of the diagram. This concentration of fracture poles indicates an orientation nearly parallel to bedding. A third, much weaker, concentration is shown by the cyan contours near the left and right edges of the stereoplot. This concentration of fracture poles indicates an orientation orthogonal to bedding and in a strike direction parallel to bedding strike. This orientation is often referred to as a Type II extension fracture set (Stearns and Friedman, 1972). Thus, the orientations shown in this diagram, taken from Scanline #9, show two sets of fractures that are in orientations that are commonly predicted to occur during folding of rock (the Type I and Type II extension sets), while a third set is subparallel to bedding.

### 2.3.3.2 Fracture Intensity

Fracture intensity has been defined in many different ways for different purposes. In this project, the nomenclature of Dershowitz and Herda (1992) has been adopted.

In order to generate a DFN model, it is necessary to know the value of the volumetric fracture intensity,  $P_{32}$ , which is defined as the fracture surface area per unit volume of rock for the rock volume in which fractures are to be generated. This cannot be directly measured in the field, but instead, is calculated from  $P_{10}$  (number of fractures per unit length) or  $P_{21}$  (total fracture trace length per unit area of rock surface). For scanline data, the natural measure of fracture intensity is  $P_{10}$ .

Many studies have shown that fracture intensity, including  $P_{10}$ , often varies with the scale of measurement (Barton and La Pointe, 1995). Since the scale of the scanline (tens of meters) differs from the scale of the reservoir (hundreds or thousands of meters), it is essential to quantify the intensity scaling behavior of fracture intensity so that the scanline calculations can be correctly upscaled to the reservoir.

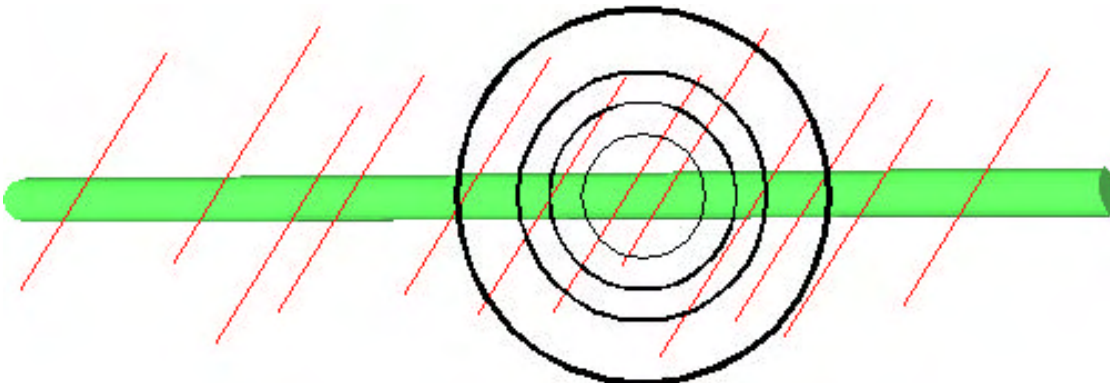
**Figure 2-24. Methodology for calculating intensity scaling parameters.**

Figure 2-24 shows how the intensity scaling parameters are calculated for scanline or wellbore data. A series of nested circles of different radii are centered on each fracture intersecting the scanline or wellbore. The number of fractures within each circle is counted. This series of calculations is repeated for every fracture intersecting the scanline, and the results for each specific radius value are averaged over all fractures. The results are plotted on doubly logarithmic axes, with the number of fractures plotted on the vertical axis and the radius on the horizontal axis. This type of plot can be used to test whether the scaling of intensity follows a fractal or a Poissonian process, because both can be represented as a power law of the form:

$$N(R) = rR^D \quad \text{Equation 2-1}$$

where  $R$  = the radius of the circle,  
 $N(R)$  = the mean number of fractures in a circle of radius  $R$ ,  
 $r$  = a constant, and  
 $D$  = the scaling exponent.

In the above equation,  $D$  is often referred to as the *mass dimension* (Mandelbrot, 1983).



For a scanline,  $D$  typically varies between 0.0 and 1.0. If  $D$  is not equal to 1.0, the scaling law is a fractal or power law relation. If  $D = 1.0$ , then the scaling law is Poissonian. The importance of Poissonian vs. fractal scaling behavior is significant when the intensity of fracturing is being estimated at a scale different than the one over which the data was collected. This can be seen by deriving the expression for  $P_{10}$  from Equation 2-12:

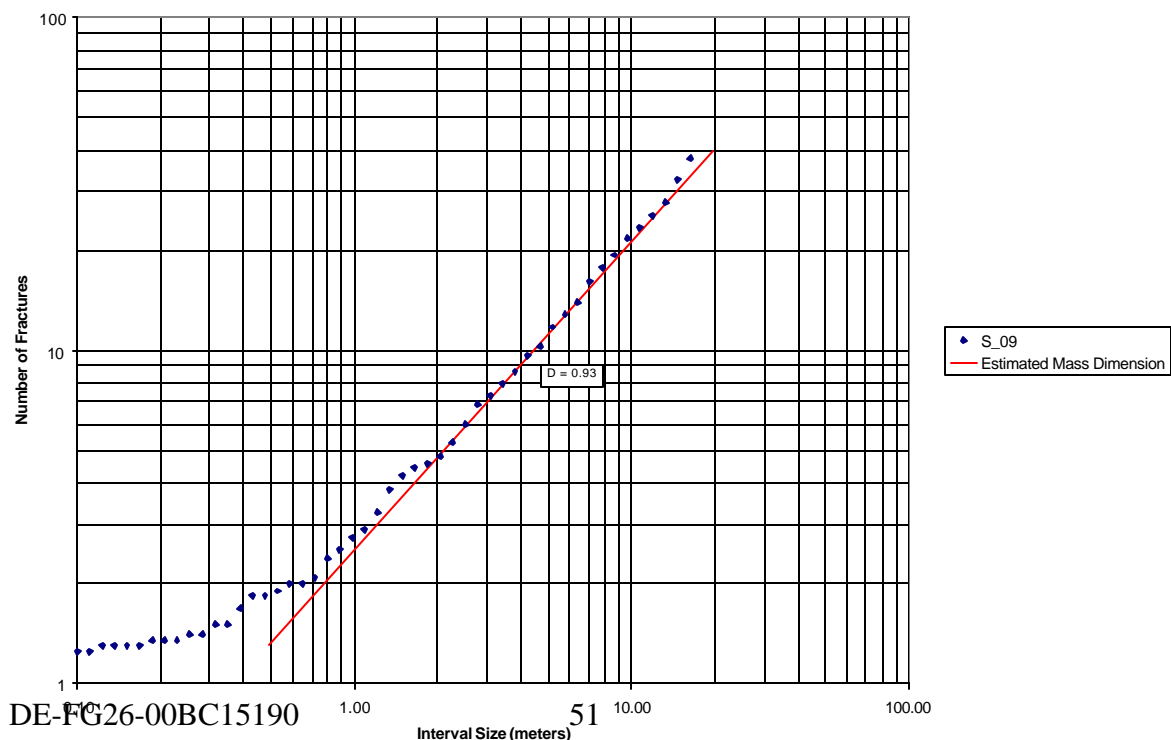
$$P_{10}(R) = \frac{N(R)}{2R} \propto R^{D-1} \quad \text{Equation 2-2}$$

**Figure 2-25. Example of a plot to determine the intensity scaling characteristics of fracture data collected along a scanline.**

This equation shows that the value of  $P_{10}$  depends upon scale, except when  $D = 1.0$ . In this case, the  $P_{10}$  intensity is scale-independent.

Figure 2-25 shows an example of plotting the average number of fractures as a function of circle radius from scanline data. The departure from linearity at small circles (radii less than about 1 m) is due to the circle size approaching the minimum fracture spacing. This represents the lower limit of fractal scaling behavior, and so is not considered when fitting a straight line to the data. The figure shows a straight line fit through non-linear regression to the data for circles larger than the minimum fracture spacing. In this example, the data are well approximated by a straight line. The slope of this line is the scaling exponent or mass fractal dimension.

This type of scaling calculation was carried out for every scanline.



### 2.3.3.3 Fracture Trace Length

In order to generate a DFN model, it is necessary to specify the size distribution for each fracture set. This is done by specifying a radius distribution for the fractures, and specifying a fracture shape.

Size or fracture radius are not directly measured in outcrop fracture data; only fracture trace lengths can be measured. The trace length distribution differs from the radius distribution. Fortunately, the radius distribution can be derived from the trace length distribution either through analytical equations or by simulation.

An important and related issue is to compare size distribution information among different scanline sites. This is necessary for two purposes:

1. To assess whether there are differences in size distributions that can be related to strain or other geological factors; and
2. To determine a size distribution for the fractures that represents fractures at a larger size than encountered in the scanline data sets.

The process for evaluating this issue is to examine the number of fractures greater than or equal to a specific size based on all of the data from the different sources. Since each data set may pertain to a scanline with a different length, the number of fractures must be normalized for the scanline length.

The common way for carrying out this normalization is to divide the number of fractures by the length of the scanline. This type of length normalization is essentially Euclidean, since it assumes that if the scanline length were doubled, the numbers of fractures would also double. A Poissonian spatial model, typified by  $D = 1.0$ , is the only power law model for which the Euclidean length renormalization is correct. For other values of  $D$ , a different type of length renormalization is required, one that uses Equation 2-12 .

Fracture trace lengths often follow a relation given by:

$$N(X > x) = \left( \frac{x_0}{x} \right)^{D_l} \quad \text{Equation 2-3}$$

where  $x_0$  = the minimum trace length considered,

$x$  = a trace length of size greater than  $x_0$ ,

$N(X > x)$  = the number of fractures with a trace length greater than a specific length  $x$ , and

$D_l$  = the trace length scaling exponent.

The trace length scaling exponent in Equation 2-14 is not related to the intensity scaling exponent in Equation 2-12.

The procedure to commensurate fracture trace length data from different scanline sites is to renormalize them to a common length. For example, if there are 50 fractures found on a 100 meter scanline, then the number of fractures for a 200 meter scanline would be calculated by using Equation 2-12. The values of  $N(X>x)$  in Equation 2-14 would then be scaled by this ratio, rather than by a simple (Euclidean) doubling of the number.

## 2.4 Construction of Balanced Cross-Sections

The construction of the balanced cross-sections was a critical first step in carrying out the 3D palinspastic reconstruction that was subsequently used to construct the 3D fault block model for the Field, and to determine the strain history of the field as it related to reservoir-scale fracture orientations and intensity variations.

To understand where fractures form in a geologically complex environment, rock units can be unfolded and restored back to their original unfolded and unfaulted flat lying depositional position. Forward restoration from this initial configuration makes it possible to estimate the strains developed during the process. By using the 2D or preferably 3D strains from a successful restoration process across the field, fractures can be generated in accordance with the matching strain model. Moreover, restoration provides better geometrical definition of the fault block architecture of the reservoir which is crucial for maximizing cost-effective and technically efficient recovery.

The geological development of an oilfield often involves several deformation mechanisms such as compressional folding, thrusting, fault propagation folds, and so on. Each type of deformation requires a specific type of restoration mechanism such as flexural slip, fault parallel flow or shear strain, often in combination with each other. In order to unravel the complex deformation history, it is necessary to understand the current geological situation well. In the case of the Circle Ridge Field, this requires a good 3D geological model over the field before any attempt to perform any restoration process begins.

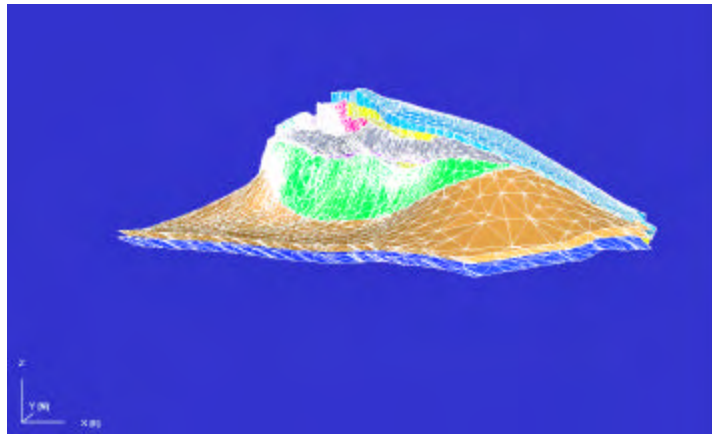
Table 2-1 shows the input data used for constructing a 3D geological model over the Circle Ridge field. Additional information was taken from Anderson and O'Connell (1993) and from Marathon Oil geologists Brendan Curran and Ken Steele, and engineers Mike Dunleavy and Jim Baker.

**Figure 2-26. Illustration of the structural restoration process.**

3D Structural reconstruction is figuring out how to go from this...



to this...



Input data	Description	Performed by
Field data	Field data with explicit mapping of faults and fractures.	Performed by the project team in June 2000.
Cross-sections	3 sections across the field in approximately NE-SW direction (P-P', T-T' and Z-Z')	Anderson and O'Connell (1993)
	3 additional sections, two in NE-SW direction and on E-W (H01, H02, H03)	Performed by the project team in June 2000
Well data	Formation tops from 206 wells drilled across the field	Marathon Oil
	115 reanalyzed wells with reinterpreted formation tops	Performed by the project team in August 2000
Geological model	3D EarthVision model over the field	Smith (2000) as part of a BSc degree at The Baylor University, Texas

**Table 2-1. Data sources for palinspastic reconstruction of Circle Ridge Field.**

The geological model follows the well formation top data from the two separate data sets available (see Table 2-1). The formation tops interpreted by the recent analysis by Straub (GeoData Services; see Section 2.2) prevails when differences occur between the two

data sets. The cross-sections performed by Anderson and O'Connell (1993; Figure 2-18 and Figure 2-27) have been used to control the shape and the offset of faults and horizons. However, these cross-sections are traced from published papers and do not contain relevant coordinate data which excludes them for being a direct part of the 3D geological model. On the other hand, the newly acquired cross-sections H01, H02 and H03, shown in Figure 2-28, are included in the 3D model and provides good control of the extension of the formations up to the surface. Note that the locations of the recently acquired cross-sections have been recorded with GPS measurements which is essential when incorporating the data into a 3D model. Finally, the model has been conditioned to the geological outcrop map presented by Anderson and O'Connell (1993) and Smith (2000; see Figure 2-29) Circle Ridge's structure is well expressed in the surface topography as seen in Figure 2-18. Prominent cuestas clearly define the "kidney-shaped" structure from air photos and are therefore excellent markers for field mapping. The Circle Ridge anticline has been erosionally breached, and thus forms a topographic basin in the center. The main anticline axis trends N 15°-20° W, nearly perpendicular to the N 40°-50° E stress direction inferred as the principle direction of horizontal compression during the Laramide Orogeny. The fold is overturned, with the steepest beds on the southwestern flank. Resistant limestone beds of the Jurassic Sundance Formation form vertical standing walls, such as the one shown in Figure 2-30.

**Figure 2-27. Perspective view of the Anderson and O'Connell (1993) P, T and Z sections as they appear in the 3D model.**



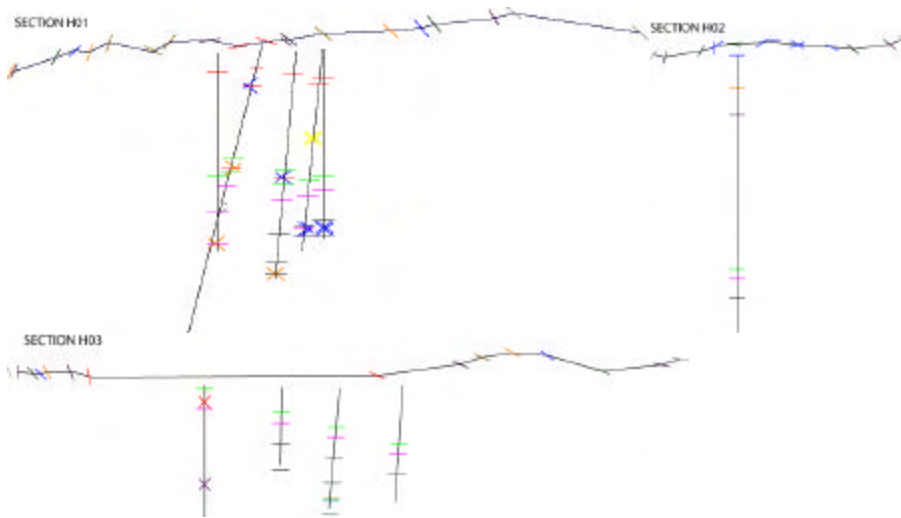


Figure 2-28. Cross-sections H01, H02 and H03 performed by the project team during the June 2000 field campaign.

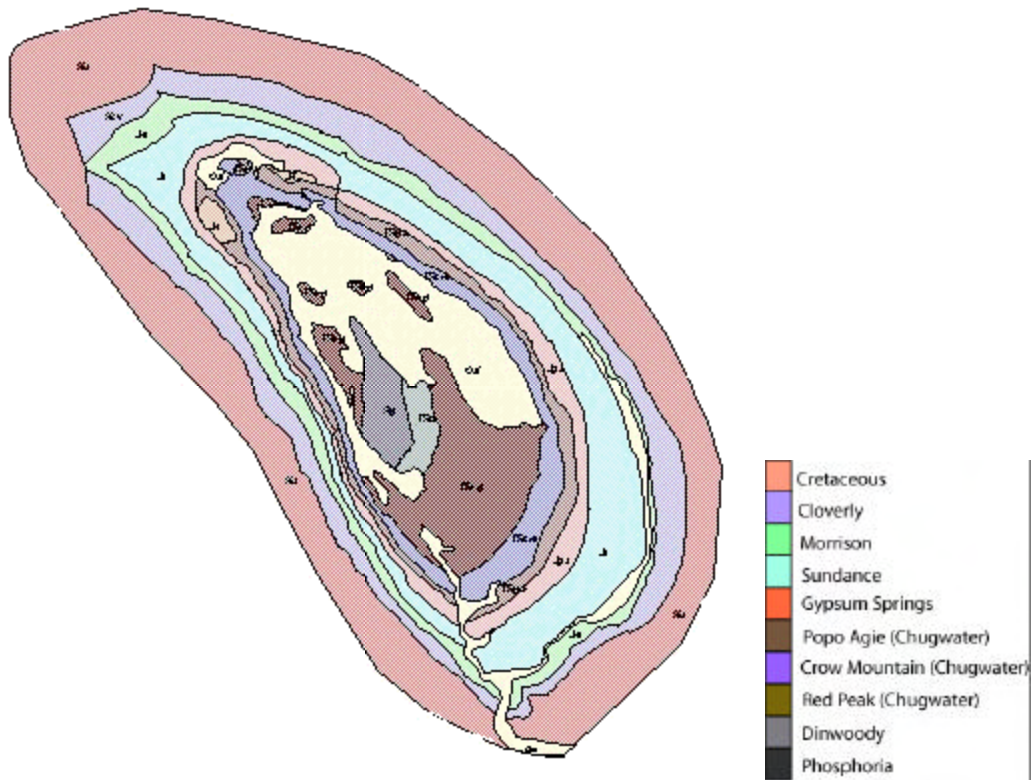
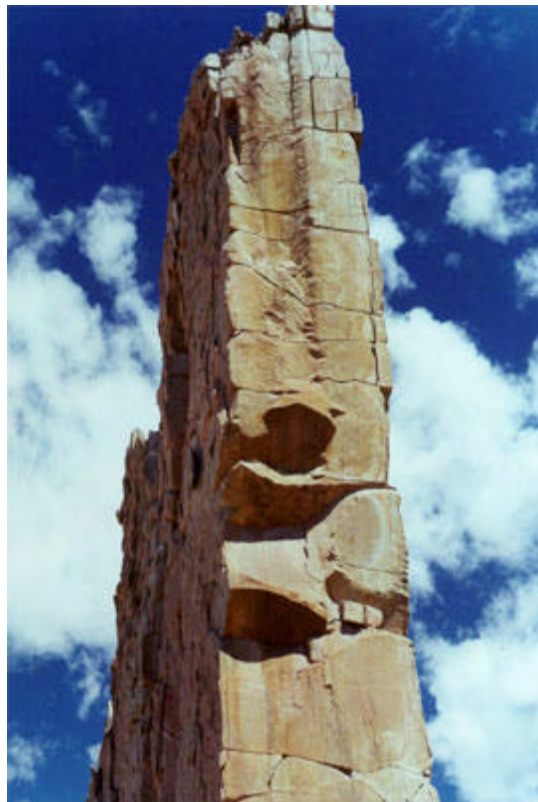


Figure 2-29. Geological map of Circle Ridge modified after Anderson and O'Connell (1993) and Smith (2000).

A fault-propagation fold is the best interpretation for the overall structure of Circle Ridge (Anderson and O'Connell, 1993). Fault-propagation folds form when a master propagating thrust fault loses slip and terminates upsection. Observations supporting a fault-propagation interpretation at Circle Ridge include the fold asymmetry and the southwestern overturned limb. However, the controlling reverse fault has not yet been identified, presumably because it lies beneath any current well penetrations. Seismic data in the area are too poor in quality to identify such a fault with any confidence.

Several smaller, northeast dipping, thrust faults imbricate the crest of the structure. The number of reverse fault imbrications, as identified from borehole data, increases in the northwestern part of the field. The Red Gully Fault (RGF), the fault with greatest amount



**Figure 2-30. Competent sandstone horizons in the Sundance Formation forms vertical walls of rock in the southern part of Circle Ridge.**

of displacement at Circle Ridge, cuts the field into two blocks termed the overthrust block (Figure 2-31) and the subthrust block. The subthrust block (footwall block of the Red Gully Fault) actually consists of several sub-blocks divided by the Blue Draw Fault (BDF), Gray Wash Fault (GWF), Purple Sage Fault (PSF), and Yellow Flats Fault (YFF) that compartmentalize the reservoirs (Figure 2-32). The Blue Draw Fault, like the Red Gully Fault, has surface exposure while the others are recognized only from well data. One of the major concerns of the geological model is the extension of these faults in the subthrust block. Several imbrications possibly exist between the Green Valley Fault and the Red Gully fault making the northeasterly part of the field extremely complex.

The palinspastic reconstruction is performed in 3D space restoring key formations back to the undeformed state. As the collected fracture data comes mainly from the Red Peak and the Crow Mountain formations they will be used as controlling horizons and will be the main focus for strain together with the producing units Phosphoria and Tensleep. The complete geological model contains data for all horizons down to the Darby formation and are listed in Figure 2-31 and also shown in Figure 1-8.

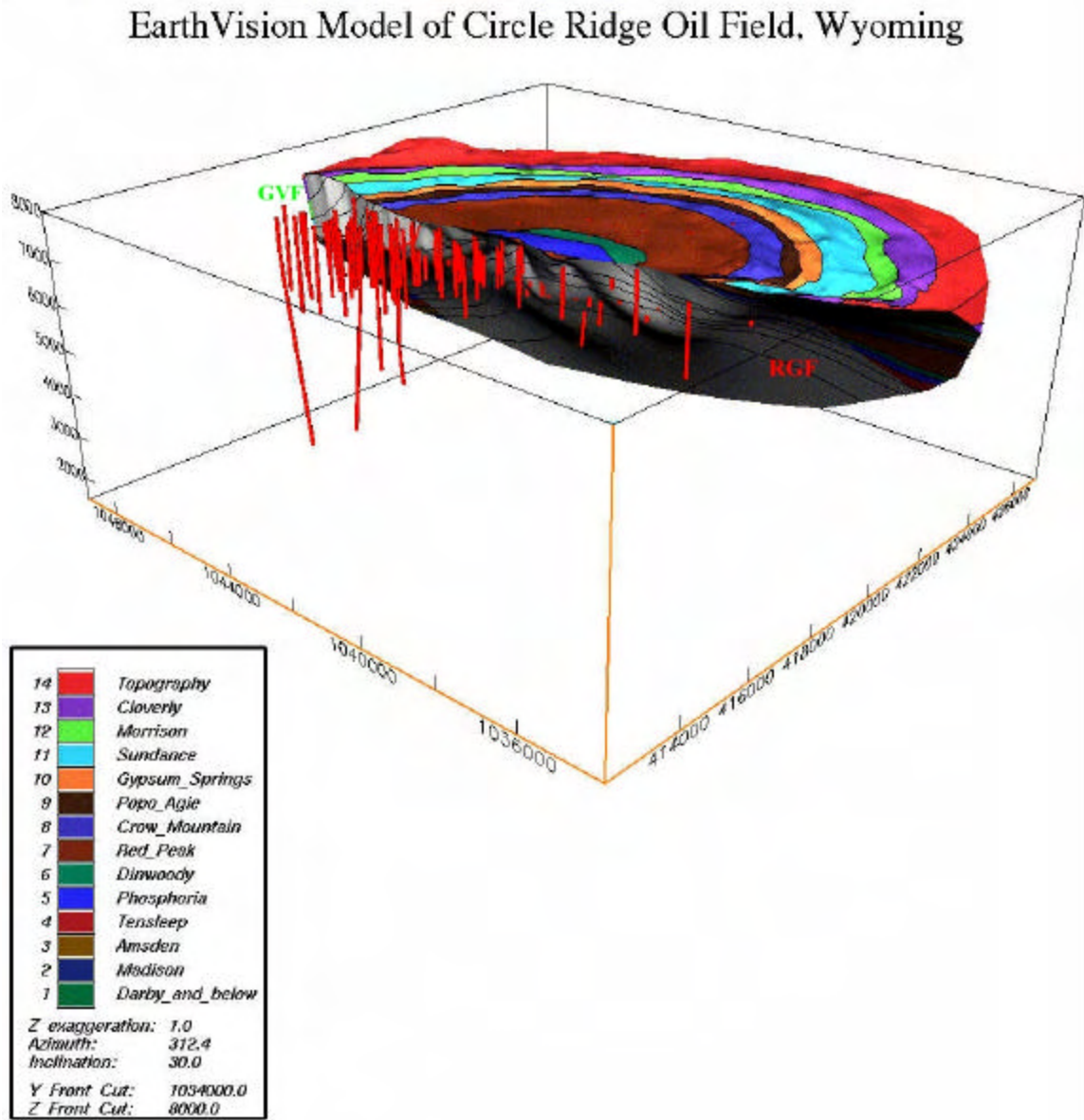
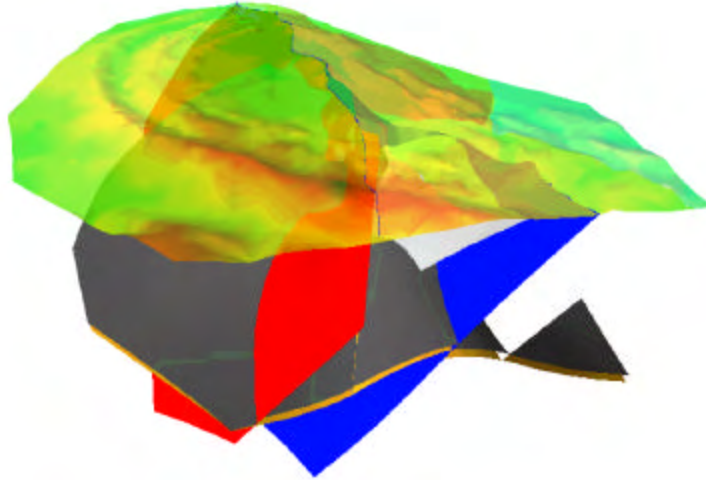


Figure 2-31 Overthrust block at Circle Ridge after Smith (2000).



**Figure 2-32. 3D Model of the major faults in the field; The Red Gully (red) and Green Valley (green) Faults and the Blue Draw Fault (blue), Gray Wash Fault (gray), Purple Sage Fault (behind), and Yellow Flats Fault (behind) together with the Phosphoria (gray) and Tensleep (orange) formations.**

The dominating strain mechanism to restore Circle Ridge is interpreted to be fault parallel flow along the main Red Gully thrust. However, the smaller fault blocks in the northern part of the field may well be better explained by other restoration mechanisms such as parallel shear and flexural slip.

The restoration process was completed in the Spring of 2001.

## **2.5 Construction of Balanced Cross-Sections and Validation of Cross-Sections Using Retrodeformation Software**

### **2.5.1 OVERVIEW**

The construction of the balanced cross sections is an iterative process in which different algorithms are applied to unfold and unfaul the reservoir. Unless the order of the various folding and faulting events is approximately correct, and the folding and faulting mechanisms are approximately correct, it will not be possible to restore the formations to their originally fault-lying state, or to do so in such a manner that they “balance”. After a balanced model is attained, the strain field is calculated from the successful palinspastic reconstruction and compared with the fracture geometry measured in outcrop in the subsurface, in order to determine how the strain field relates to fracture pattern

development, as well as to the parameter values necessary to utilize strain information for developing the discrete fracture network (DFN) model.

### 2.5.2 ANALYSIS TECHNIQUES

Palinspastic reconstructions of folded and faulted stratigraphy have been widely used for the last 20 years. The reconstructions have mainly been based on 2D cross-sections and several different theoretical methods for various types of fold and fault related deformations have been established by a number of authors( Suppe, 1983, 1985, 1989; Suppe et al , 1990; Medwedeff, 1989; and Mitra, 1986, 1990).

In contrast to 2D reconstructions, the complexity of restoring surfaces and volumes of rock requires the use of computers. The methodology to restore folded and faulted formations are essentially the same as has been used for 2D problems, but has been expanded to allow for movement in all three dimensions. The amount of geometric calculations and thus the need for fast computers has until recently limited full reservoir reconstructions. Due to the increase in computer power over the past few years, 3D palinspastic reconstructions are now possible.

### 2.5.3 AVAILABLE TECHNOLOGY FOR 3D RECONSTRUCTIONS

There are presently two commercial forward and reverse geological modeling packages available at the open market today: 3DMove by Midland Valley Ltd. and Geosec3D by Paradigm. There also exist a number of 2D and pseudo-3D restoration packages that can handle specific types of restoration techniques. For this study 3DMove has been chosen for its ability to simulate inclined shear, fault parallel flow, flexural slip unfolding and many other reconstruction techniques truly in three dimensions. 3DMove provides all the techniques listed below, which are required for the Circle Ridge restoration:

- Full 3D restoration and forward modeling capability
- Applicable to strike slip, extension, thrusting, salt tectonics and inversion
- Fast restore-to-target-horizon approach for quick look analysis
- Move on fault capability for full kinematical analysis
- Inclined shear and flexural slip capability
- 3D Model building and visualization
- 2D and 3D data as input
- Wells and seismic display
- Fault construction tools
- Displacement analysis
- Cut-off mapping in 3D and through time
- Contour and 2D sectioning of the 3D model
- Strain visualization
- Interactive freehand model editing
- Full 3D volume representation and attribute filling

## 2.5.4 RESTORING THRUSTS AND FAULTS

The primary method for restoring faults and thrusts in Circle Ridge has been the Fault Parallel Flow algorithm. Below follows a description of the used method and its implications.

### 2.5.4.1 *Fault Parallel Flow*

Fault parallel flow is a kinematic restoration method allowing hanging wall surfaces to be moved across faults in such a way that the hanging wall vertices move parallel to the fault segments over which they are flowing.

Fault Parallel Flow involves a two-stage process:

1. Define the hanging walls and faults, specify the transport direction and calculate the flow model.
2. Once the flow model has been calculated, the hanging walls can be moved using a number of different techniques as described later in this section.

The fault parallel flow method in 3DMove calculates a flow path for every hanging wall vertex. The general procedure is as follows:

For every hanging wall vertex;

- Create a vertical slice through the faults along the specified transport direction. This produces a fault line over which the hanging wall vertex would move.
- Generate the bisectors for the line.
- Calculate and store the flow path of the hanging wall vertex through the bisectors.

An example fault line and flow path are shown in Figure 2-33. The bisectors merge as they intersect with one another, allowing the delineation of dip domains. Each dip domain has a corresponding fault segment. The hanging wall vertex will pass through the bisectors, moving parallel to the fault segment for any given dip domain.

Once this flow path is generated, the hanging wall vertex can be easily moved along it. It is also possible to apply shear to the hanging wall, by applying an additional slip value to the vertices relative to their height above the fault.

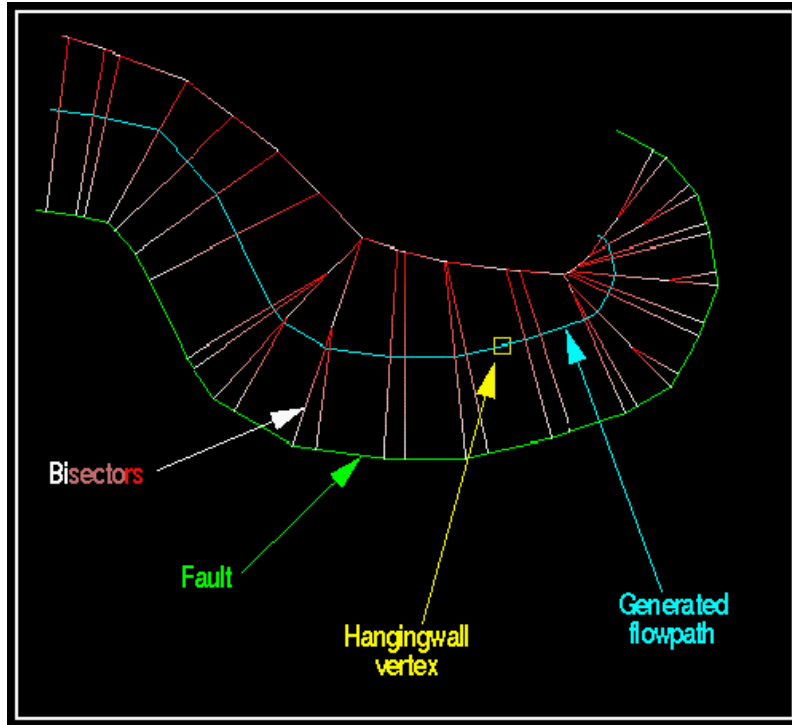


Figure 2-33 Illustration of a cross-section of the calculated flow path along a fault surface (from Midland Valley, 2000)

There are three options for moving the flow model in 3DMove:

1. Movement by Slip value
2. Movement using Heave bands
3. Restore-to-Surface movement

A slip slider bar is used to change the slip across the whole model (Figure 2-34). A constant slip value is applied to every hanging wall vertex.

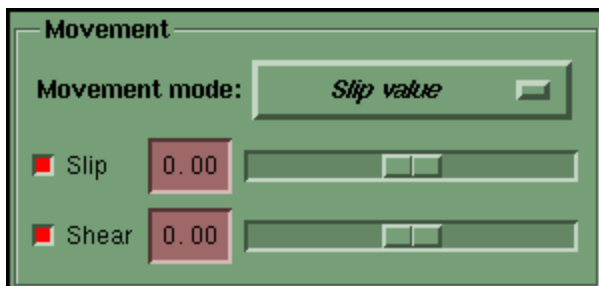


Figure 2-34 Slip slider menu in 3DMove to perform movement by slip value (from Midland Valley, 2000)

The shear slider is used to change the shear across the model. Using the shear slider applies an additional slip value (on top of the specified slip) relative to the hanging wall vertex's height above the fault. This is illustrated in Figure 2-35.

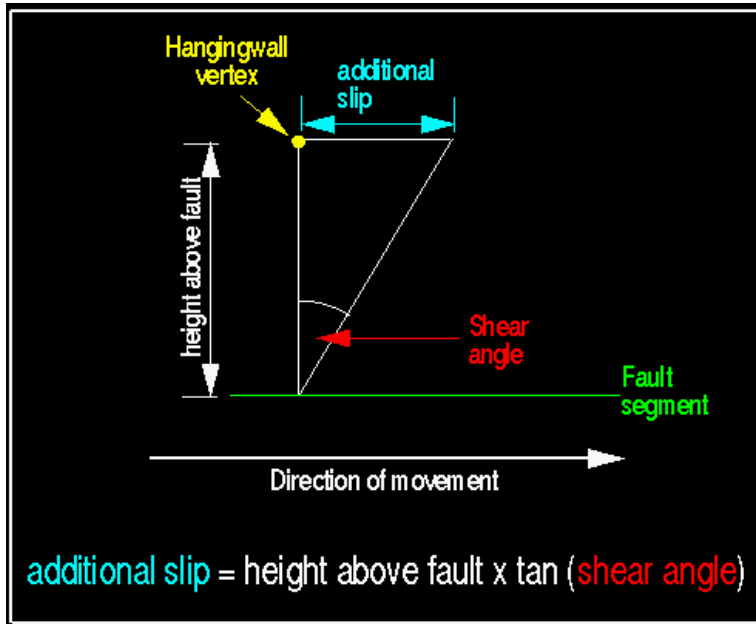


Figure 2-35 Shear calculation using fault parallel flow (from Midland Valley, 2000)

Heave bands movement mode allows the change of slip profile across the fault. Heave bands are usually used to enable different amounts of slip on different sections of the hanging wall formation to match the opposing side of the formation (on the footwall side). This method is desirable when observations show that in order to match the surfaces, variable movements along the fault need to be applied.

The shear slider is also available in this mode, and allows you to independently vary the shear applied to the hanging wall vertices.

The Restore-to-Surface movement mode applies a unique slip value to every hanging wall vertex.

This is done by matching two surfaces on different sides of the fault with each other. 3D Move will calculate - for every flow path in the flow model - the slip distance between the deformed surface and the undeformed surface as shown in Figure 2-36. However, this technique works well only if the fault is relatively steep. If the hanging wall is almost in plane with the fault, the slip lines increase in length back down the fault, as shown in Figure 2-37.

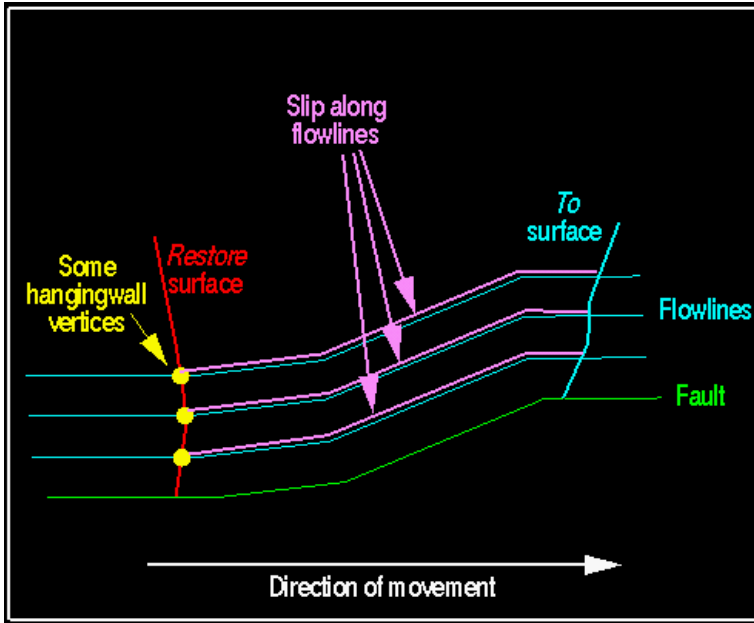


Figure 2-36 Slip along flowlines using the restore to surfaces movement mode (from Midland Valley, 2000)

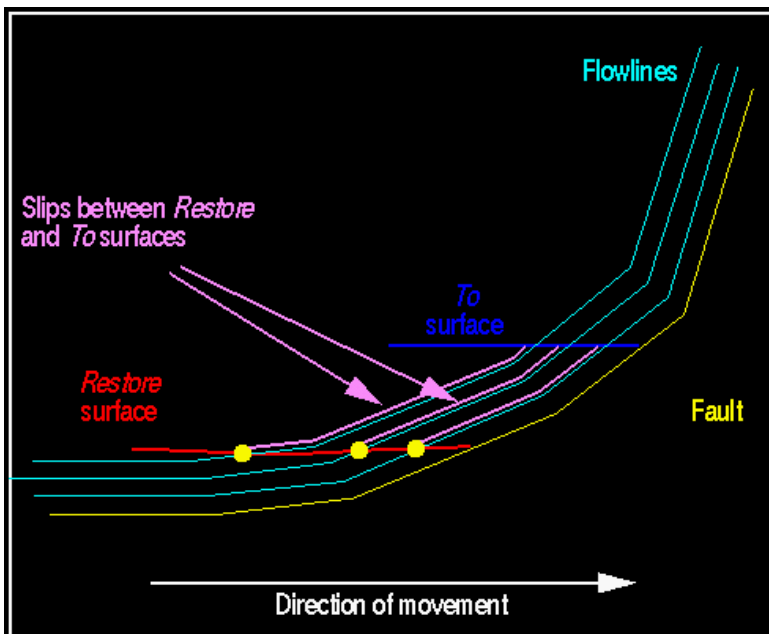


Figure 2-37 Implications of the Restore-to-Surface movement method (from Midland Valley, 2000)

### 2.5.5 RESTORING FOLDS

Two techniques have been utilized to restore folded strata;

1. Vertical and inclined shear unfolding, and
2. Flexural slip unfolding.

A short explanation of the implications of each restoration technique is presented in the next sections.

### 2.5.5.1 Vertical and inclined shear unfolding

Vertical and inclined shear balancing preserves the volume of the restored formation. Figure 2-38 shows a black and red surface, which represent a cross-section through a hanging wall fold. The black surface is shown unfolded back to a datum, which represents the pre-deformation geometry (horizontal dotted green line). This datum can be set at any Z depth or elevation.

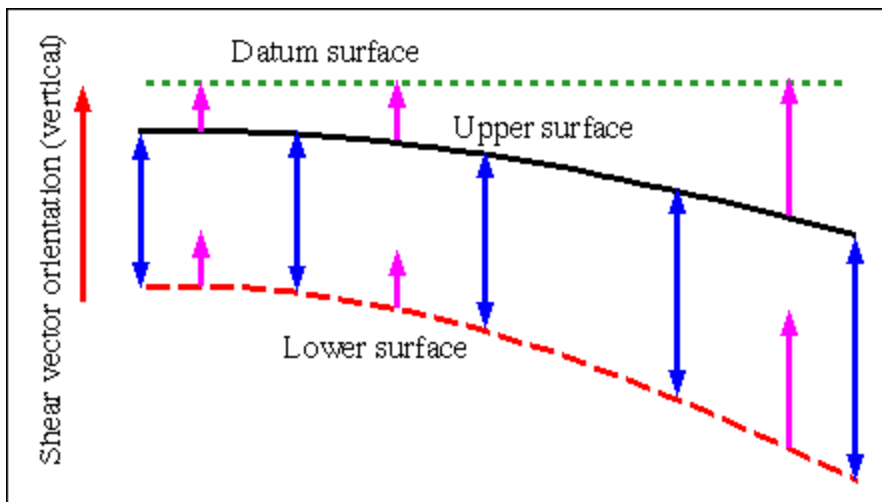


Figure 2-38 Cross-section through a hanging wall fold (from Midland Valley, 2000)

The black and red surfaces are unfolded along a chosen shear vector, in this case a vertical shear vector, represented by the thick, red arrow.

To retro-deform the fold, the black bed is translated vertically to the green datum, with the vertical translation distance varying across the section. The pink arrows represent this distance. The lower red bed is translated the same vertical distance as the black bed that enables volumes to be preserved within the model.

The vertical distance between the black and the red beds is maintained in the orientation of the shear vector. The blue, double-headed arrows in Figure 2-39 represent this distance.

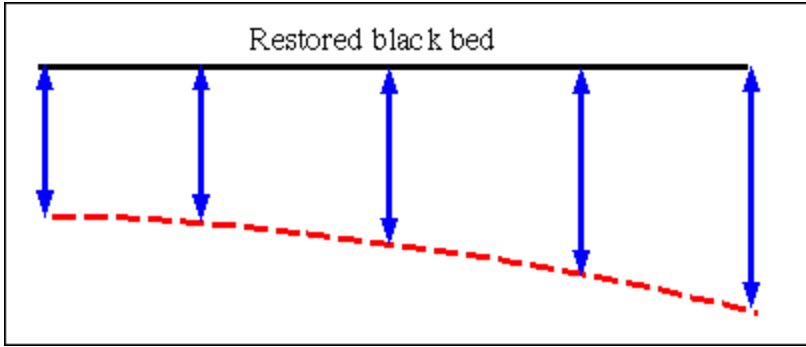


Figure 2-39 Cross-section through the restored hanging wall fold (from Midland Valley, 2000)

Figure 2-39 illustrates how the line length and therefore the surface area of the black surface will change as it is unfolded.

For a constant dip surface using vertical shear, the restored length is shorter than the original length, as shown in Equation 2-1 and Figure 2-40:

$$l = l_o \cos(\mathbf{q}) \quad \text{Equation 2-4}$$

where  $\mathbf{q}$  is the bed dip,  
 $l$  is the restored length, and  
 $l_o$  is the original length.

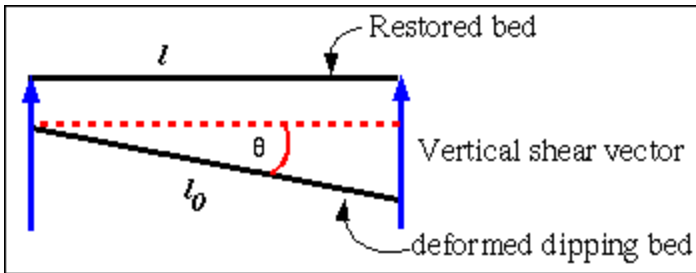


Figure 2-40 The concept of vertical shear and the restored length (l) (from Midland Valley, 2000)

Figure 2-40 illustrates the new area of the restored surface and its relationship with the angle between the restored bed and the deformed dipping bed:

$$A = A_o \cos(\mathbf{q}) \quad \text{Equation 2-5}$$

where  $A_o$  is the original area of the surface, and  
 $A$  is the new area.

The area change ( $\mathbf{DA}$ ) is given by:

$$\Delta A = A_o - A = A_o (1 - \cos(\mathbf{q})) \quad \text{Equation 2-6}$$

This means that the more steeply dipping the surface is, the greater will be the area change of the restored surface. For a smooth, curved surface, such as a fold, the area change is a complex function, with increasing area change as bedding dip increases.

The key point to note, regarding this technique, is that volume is preserved, but surface area will change. The surface area only remains constant for vertical shear. The map view "footprint" of the surface remains the same.

#### 2.5.5.2 *Flexural slip unfolding*

The flexural slip unfolding algorithm allows unfolding to occur such that the unfolded model:

- maintains the line length of the template surface in the direction of unfolding;
- maintains the orthogonal bed thickness between the template surface and other passive objects;
- maintains volume of the fold and the model;
- maintains surface area for cylindrical folds with the pin surface coincident with the axial plane; and
- line length and surface area is not maintained in the passive surface (surface area is not maintained in non-cylindrical folds).

For layer-parallel beds, flexural slip unfolding represents flexural slip during fold formation.

The flexural slip unfolding method can be used to validate complex thrust deformations and the cover rocks surrounding intrusive salt structures. As with the inclined shear unfolding mechanism, the methodology of using the flexural slip unfolding algorithm is to unfold the rocks and then to translate the unfolded components to their pre-deformation positions. The structural model is validated if the unfolded rocks can be reassembled to form a coherent geometry.

Analogous to the inclined shear methodology previously described, the shear vector orientation determines the unfolding direction. For example with vertical shear, the beds are unfolded onto a datum (usually horizontal) with the volume of the fold being preserved. However, the surface area of the fold is not preserved between the folded and unfolded stages. In contrast, the flexural slip unfolding algorithm preserves the line length (Length L shown below in Figure 2-41) in the direction of unfolding and also the surface area.

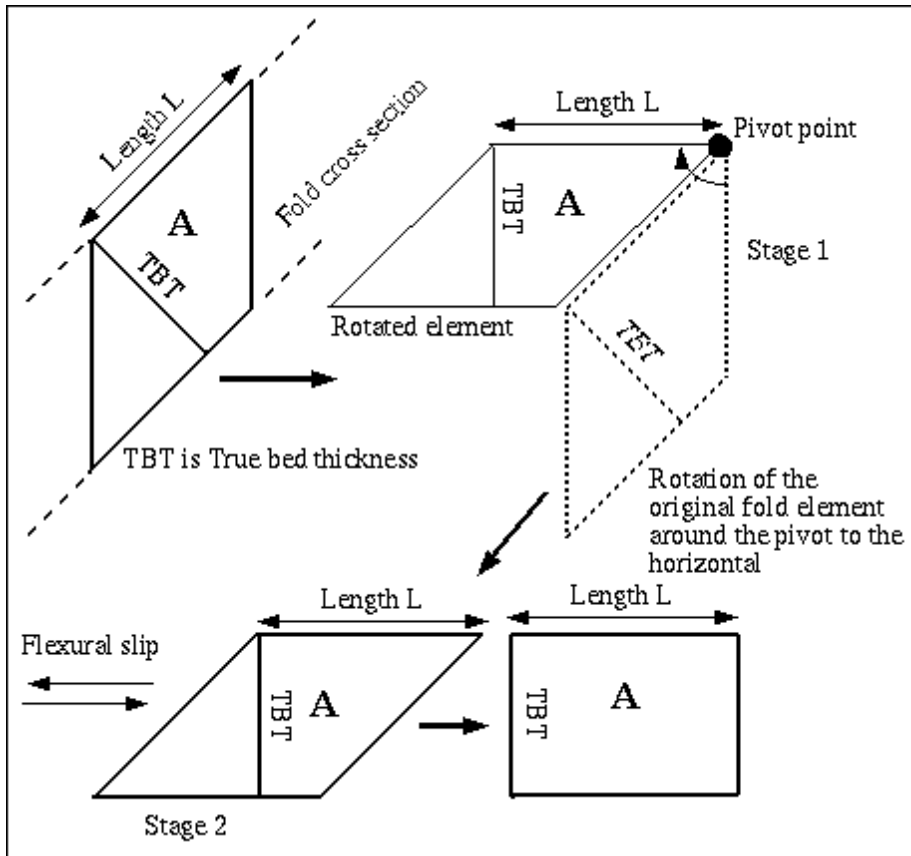


Figure 2-41 Illustration of the flexural slip unfolding algorithm (from Midland Valley, 2000)

Figure 2-41 shows part of a fold as seen in a cross-section. The fold limb dips at 45 degrees and a small volume element of the fold limb has been drawn as a parallelogram. The element has an area,  $A$ , which remains constant throughout the unfolding operation. Therefore, the volume of the fold remains constant during restoration.

In addition, the upper surface of the fold element in Figure 2-41 has a line in cross-section with the length  $L$ . When unfolded this line length remains constant, as opposed to the inclined shear restoration method where this line length changes. For parallel bedding, the true bed thickness (TBT) remains constant during unfolding, while the vertical bed thickness changes.

The flexural slip unfolding process takes place in two stages:

- a rotation of the upper fold surface and fold element to the horizontal (Stage 1 in Figure 2-41)
- a shearing operation to "undo" the flexural slip component of the folding (Stage 2 in Figure 2-41).

In order to carry out flexural slip unfolding, an unfolding direction and a pin surface location and orientation need to be defined. The concept of the pin plane is shown in Figure 2-42.

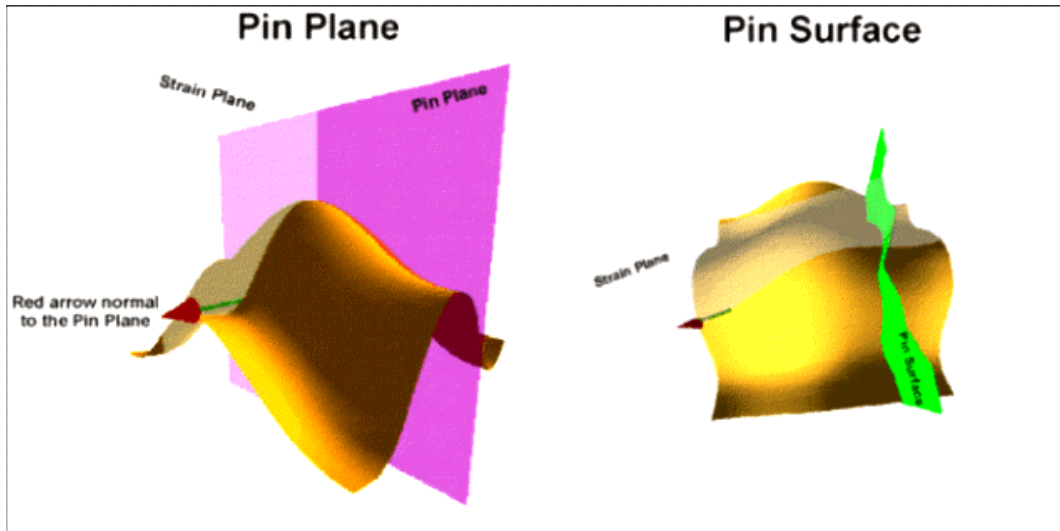


Figure 2-42 Orientation of the pin plane/surface and strain plane. Red arrow indicates the unfolding direction (from Midland Valley, 2000)

The sinuous line length ( $L$  in the diagram in Figure 2-43) is measured from the pin plane/surface intersection with the template surface, along the template surface in the direction of unfolding. The sinuous line lengths are measured for all vertices of the template surface. These sinuous distances are then propagated along the pin that may be vertical (as shown) or inclined. The line lengths are then translated along the target/datum in the unfolding direction on intersection with the datum or target surface.

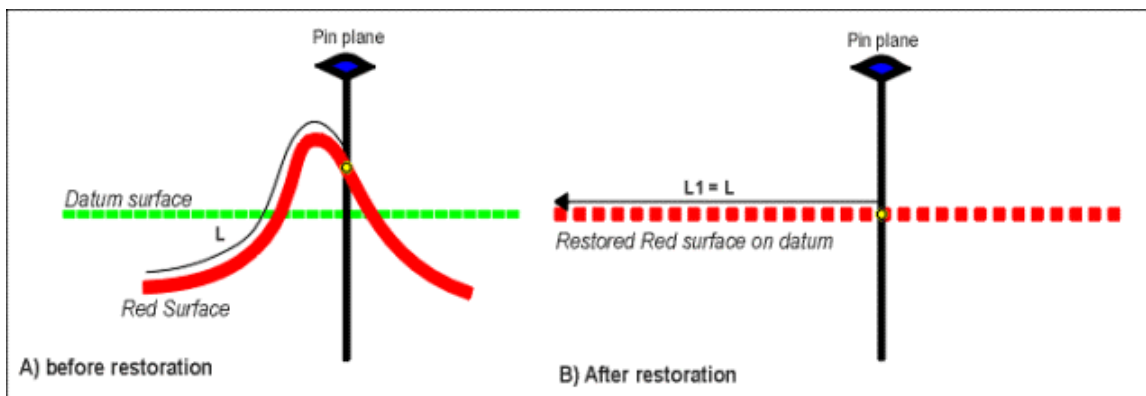
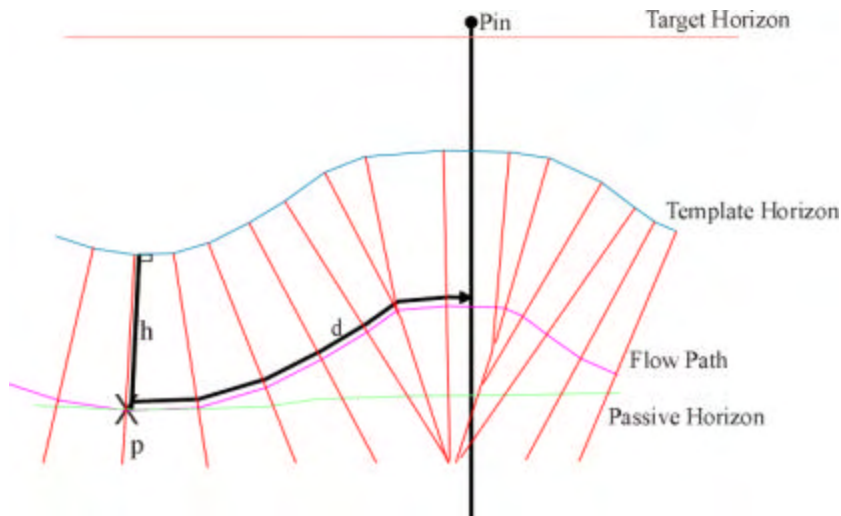


Figure 2-43 Maintaining sinuous line length with a vertical pin (from Midland Valley, 2000)

A slip system (shown in red) is generated from the dip domain bisectors projected from the template horizon (blue). Flow paths are calculated for all vertices of the passive objects in the unfolding direction. These flow paths ensure the orthogonal thickness and therefore fold volume, is maintained between the passive and the template horizons, (this is a similar system to the fault parallel flow algorithm). The sinuous distances to the pin plane of each vertex for all passive surfaces are calculated as illustrated in Figure 2-44. The illustration shows how the flow path (shown in purple) has been calculated for vertex P of the green passive horizon.



**Figure 2-44 Illustration of the bed linkage and the slip system for each vertex in the deformed formation (from Midland Valley, 2000)**

When the template horizon has been restored to the target surface or datum, each vertex of the passive horizons is translated along its individual flow path by the sinuous distance calculated in the deformed state. Bed linkage is achieved at the intersection of the template and passive objects with the pin plane and by maintaining orthogonal thickness,  $h$ , between the template and passive surfaces. The flexurally unfolded horizons are shown in Figure 2-45.

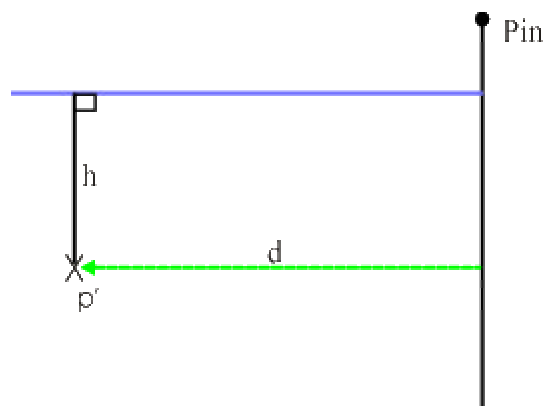


**Figure 2-45 Flexurally unfolded template and passive horizons (from Midland Valley, 2000)**

## 2.5.6 STRAIN ANALYSIS MEASURES

Strain can be quantified in terms of a bulk (non-directional) change in the rock volume, which is termed *dilation*, or by several other measures that incorporate anisotropy of changes with direction.

Geological materials that are strained pass through a large number of intermediate states before arriving at a final state. However, it is not possible to observe the intermediate stages of deformation for most, if not all, tectonic geological processes. In general, it is only possible to observe or quantify the initial undeformed state, the final present state, and perhaps one or two intermediate states. The result of the total deformation taking place from the initial state to the final state is termed the *finite state of strain*. In most situations, the finite strain for a volume of rock is not well modeled by a continuum or infinitesimal strain process. Because 3D palinspastic reconstruction produces a model of the geometry in the undeformed state, the final state, and perhaps a few intermediate states (for example, after folding but before faulting), finite strain measures are a useful way to quantify the deformation experienced by the rock. The next two sections describe the quantification of dilatational and directional finite strains.

### 2.5.6.1 Dilatation measures

Dilatation is the ratio of the change in length, area or volume of the strained object, relative to the unstrained value, this analysis can be applied to lines, surfaces and volumes. For example, the area dilatation for a surface would be calculated as follows:

$$\Delta_{area} = \frac{(a - a_0)}{a_0} \quad \text{Equation 2-7}$$

where  $D_{area}$  = the area dilatation,  
 $a$  = the area after strain, and  
 $a_0$  = the area before strain.

Increases in area produce positive area dilatation; decreases lead to a negative area dilatation.

If a surface doubles its area, the area dilatation would become  $(2a_0 - a_0)/a_0 = 1$ ;

If a surface quadruples its area, the area dilatation would become  $(4a_0 - a_0)/a_0 = 3$ ;

If a surface does not change its area, the area dilatation would become  $(a_0 - a_0)/a_0 = 0$ ;

If a surface halves its area, the area dilatation would become  $(a_0/2 - a_0)/a_0 = -1/2$ .

For a volume, the calculation is similar. Each region of interest is described as a tetrahedron (Figure 2-46). The strain is based on the change in position of each vertex in the tetrahedron relative to its initial position. By default, the X,Y,Z position of each vertex is expressed relative to the centroid of the tetrahedron. The change in position of the vertices of the strained tetrahedron, relative to the unstrained tetrahedron allows the

calculation of both a volumetric dilation and also the direction and magnitude of principal strains (Figure 2-46).

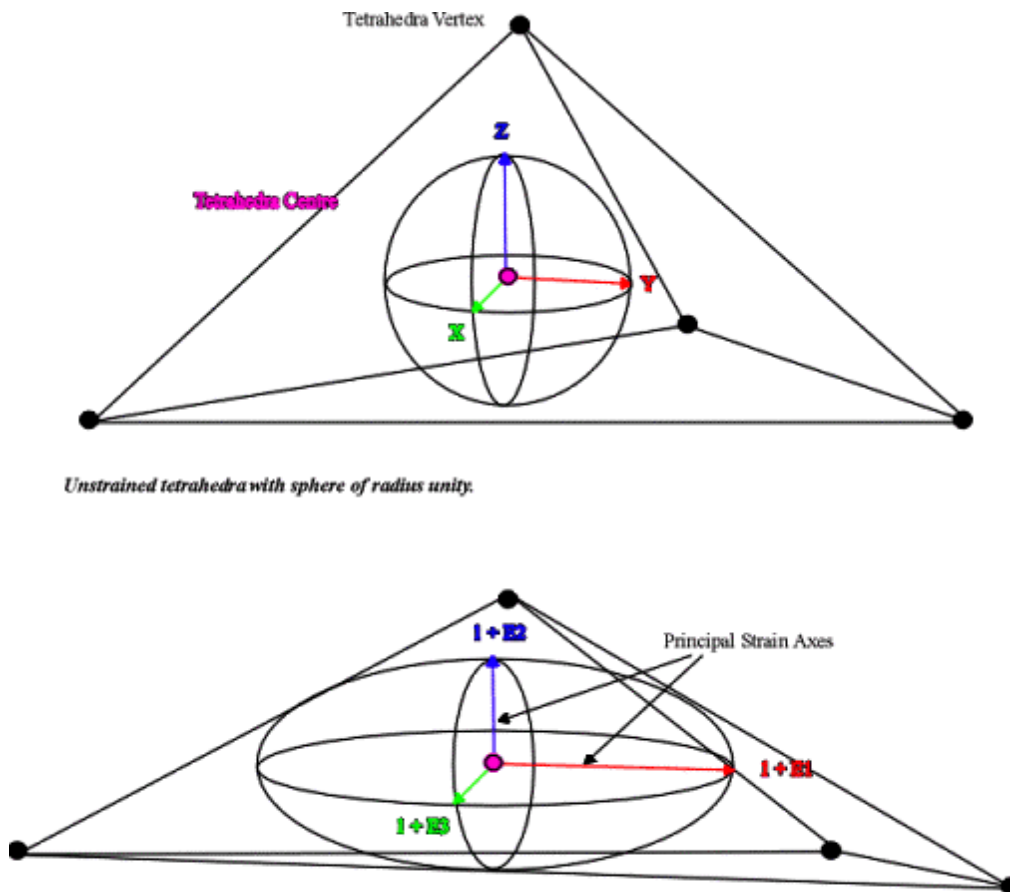
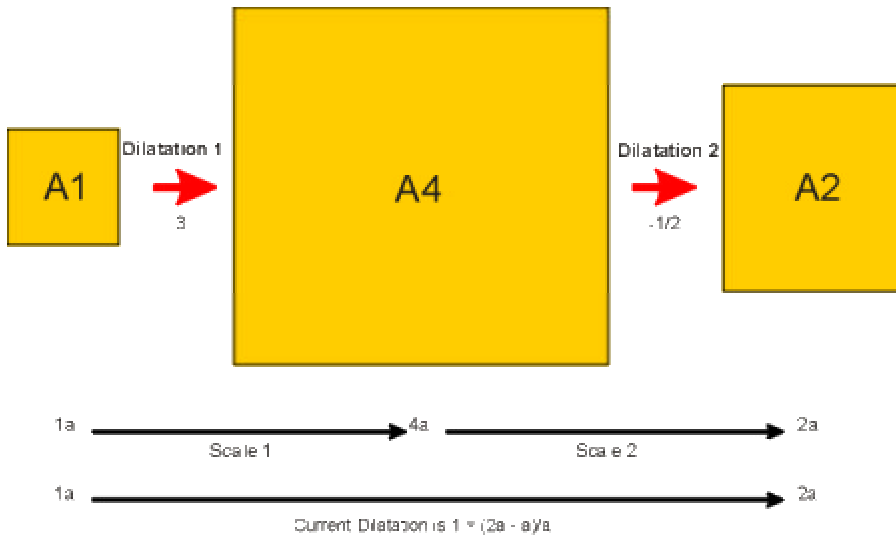


Figure 2-46 Strained tetrahedron with strain ellipsoid. The XYZ axes are eigenvectors of the strain field, and are the principal strain axes.

There are several ways to quantify the volumetric strain that occurs after multiple deformation events. These consist of:

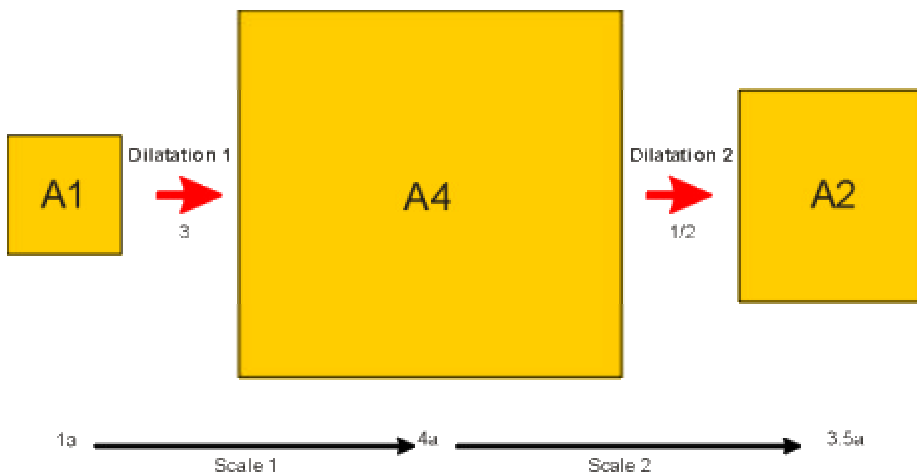
- current dilation,
- absolute, or cumulative dilation, and
- Root Mean Square (RMS) dilation.

Figure 2-47 and Figure 2-48 illustrate these strain measures.



**Figure 2-47 Example of the calculation of current dilatation (from Midland Valley, 2000)**

Figure 2-47 shows an object A1 with area  $a$  that undergoes an initial dilatation, becoming object A4 with area  $4a$ . After a second dilatation, the object becomes A2 with area  $2a$ . Current dilatation is then a measure of the strain incurred from the change in shape from A1 to A2. This is a change in area from  $a$  to  $2a$ , so the current dilatation is 1.0.



**Figure 2-48 Example of absolute and RMS dilatation calculations (from Midland Valley, 2000)**

The current dilatation does not take into account the strain history; it is only a function of the initial state and the current state. The other two measures (absolute and RMS dilatation) incorporate the effects of intermediate strain events.

Absolute strain measures the cumulative strain where the summed dilatation is taken as an absolute value:

$$\Delta_{abs} = \sum_{i=1}^n |\Delta_i| \quad \text{Equation 2-8}$$

where  $\mathbf{D}_{abs}$  = the absolute strain,  
 $\mathbf{D}_i$  = the strain after the  $i$ th strain event, and  
 $n$  is the number of strain events.

This means that even if the overall dilatation is negative, i.e. a contraction, the change will be a positive value. In the example above (Figure 2-48), the absolute dilatation would be  $|3| + |-0.5| = 3 + 0.5 = 3.5$

The RMS dilation is given by:

$$\Delta_{RMS} = \sqrt{\sum_{i=1}^n (\Delta_i^2)} \quad \text{Equation 2-9}$$

where  $\mathbf{D}_{RMS}$  = the RMS strain,  
 $\mathbf{D}_i$  = the strain after the  $i$ th strain event, and  
 $n$  is the number of strain events.

In the example above (Figure 2-48), the RMS dilation would be  $\sqrt{3^2 + (-0.5)^2} = 3.04$ .

Absolute strain will always produce a higher value than RMS.

### 2.5.6.2 Directional strain measures

Let  $e_i$  be the strain in the  $i$ -th direction, where  $e_i$  is the change in length divided by the original length, or:

$$e_i = \frac{l - l_0}{l_0} \quad \text{Equation 2-10}$$

or

$$l = (1 + e_i) * l_0 \quad \text{Equation 2-11}$$

where  $l_0$  = undeformed length,  
 $l$  = deformed length, and  
 $e_i$  = the strain in the  $i$ -th direction.

Another parameter, the *natural strain* ( $\mathbf{e}_i$ ), is often calculated from  $e$ :

$$e_i = \log(1 + e_i) \quad \text{Equation 2-12}$$

Through knowledge of the magnitudes and directions of strains in three different directions, it is possible to compute the *principal strains*. The principal strains are mathematically equivalent to the eigenvectors and eigenvalues of the strain matrix. These principal strains have the properties that they are:

1. mutually orthogonal; and
2. in directions in which there is no shear strain component.

The principal strains are denoted as  $e_1$ ,  $e_2$  and  $e_3$ , where  $e_1$  has the largest magnitude. The corresponding principal strain axes are denoted E1, E2 and E3.

Plane strain ratios are calculated from the ratios of the maximum and intermediate principal strains ( $1+e_1 / 1+e_2$ ), the intermediate principal strains ( $1+e_2 / 1+e_3$ ) and the minimum and maximum principal strains ( $1+e_3 / 1+e_1$ ). This information can be used to determine the nature of the strain; plane, constrictional or flattening using a Flinn diagram, (Flinn, 1962), as shown in Figure 2-49

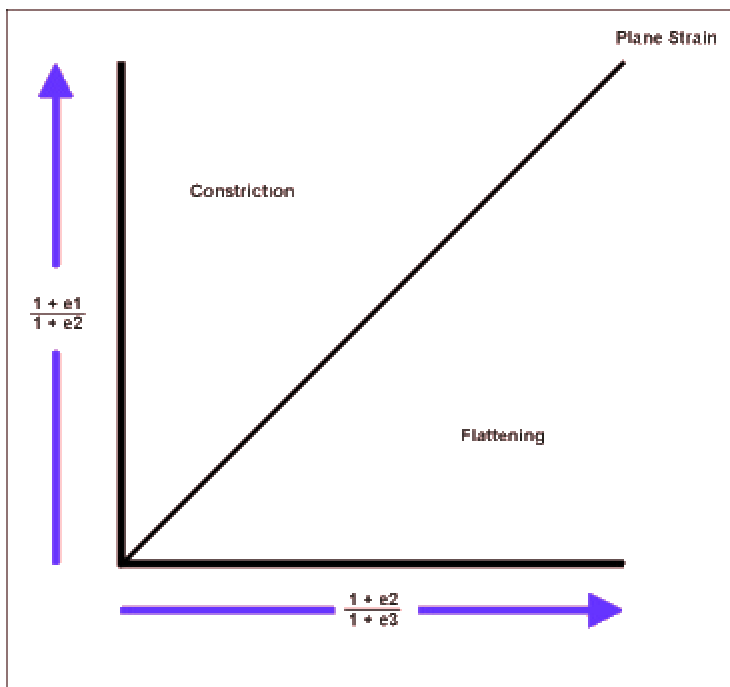


Figure 2-49 Flinn diagram showing the nature of the strain; plane, constrictional or flattening strain ellipsoid.

The volumetric dilation is a measure of the ratio of the change in volume of the strained object, relative to the unstrained volume, and can be written in a manner analogous to the areal strain (Equation 2-4):

$$\Delta_{vol} = \frac{(v - v_0)}{v_0} \quad \text{Equation 2-13}$$

where  $\Delta_{vol}$  = the volume dilation or strain,  
 $v$  = the volume after strain, and  
 $v_0$  = the volume before strain.

This can easily be re-written in a more common form:

$$\Delta_{vol} = \frac{(1 + e_1) * x_1 + (1 + e_2) * x_2 + (1 + e_3) * x_3 - x_1 x_2 x_3}{x_1 x_2 x_3}$$

*or*

$$\Delta_{vol} = (1 + e_1) * (1 + e_2) * (1 + e_3) - 1 \quad \text{Equation 2-14}$$

## 2.6 Experimental Techniques for Analysis of Subsurface Well Data

A variety of subsurface data was gathered for this project. The data included fracture image logs and spinner survey data from three wells chosen for their structural and stratigraphic diversity; two tracer experiments in differing reservoir formations and structural blocks; and single well transient pressure tests. Each subsurface data set contributed in different ways to building the overall model, and some data was used for more than one purpose. The sections that follow briefly describe the type of subsurface data acquired for this project.

### 2.6.1 FRACTURE IMAGE LOGS

Three new fracture image logs were acquired as part of this project. Dynamic flow logs (“Spinner” logs) were also run over the same intervals for this project. Locations of the wells are shown in Figure 2-50. Table 2-2 summarizes the structural, stratigraphic and depth coverage of the image logs. The logs were interpreted by Marathon to calculate the location and orientation of fractures, bedding plane, and borehole breakout information.

Well	Depth Range	Formations Logged	Structural Block	Log Type
Shoshone 65-37	616 ft to 1230 ft (187.8 m to 374.9 m) MD	Phosphoria, Tensleep	subthrust Block 6	FMI
Shoshone 66-07	720 ft to 973 ft (219.5 m to 296.6 m) MD	Tensleep	overthrust	FMS
Shoshone 66-14	745 ft to 1090 ft (227.1 m to 332.2 m) MD	Tensleep Marker portion of the	overthrust	FMS

		Phosphoria Formation and extends into the basal portion of the Tensleep Formation		
--	--	---	--	--

**Table 2-2. Coverage information for fracture image logs.**



**Figure 2-50. Location of wells in which fracture image log and spinner survey data was collected for the project. Shoshone 66-07 and Shoshone 66-14 are in the Overthrust block**

## 2.6.2 DYNAMIC FLOW LOGS

In order to further understand which features provide the flow paths for fluid flow, high-resolution (0.5 ft or 15.24 cm) injection profiles were obtained for Shoshone 65-37, Shoshone 66-07 and Shoshone 66-14, the wells in which FMI or FMS data had also been obtained. This overlap was intended to help interpret the regions with high or low flow in terms of their fracture intensity, fracture orientation and reservoir stratigraphy. Table 2-3 summarizes the coverage of these high resolution spinner and temperature logs.

Well	Depth Range	Formations Logged	Structural Block	Log Type
Shoshone 65-37	0 ft to 1220 ft (0 m to 371.9 m MD	Phosphoria, Tensleep	subthrust Block 6	Baker-Atlas
Shoshone 66-07	680.2 ft to 880.0 ft (207.3 m to 268.2 m) MD	Tensleep	overthrust	Baker-Atlas
Shoshone 66-14	600 ft to 1085 ft (182.9 m to 330.7 m) MD	Tensleep Marker portion of the Phosphoria Formation and extends into the basal portion of the Tensleep Formation	overthrust	Halliburton

**Table 2-3. Coverage information for spinner and temperature logs.**

## 2.6.3 SINGLE WELL PRESSURE BUILD-UP OR FALL OFF TESTS

A 44-hour Subthrust, Block 6, Phosphoria Formation falloff test was performed at Shoshone 65-20. This test was matched using commercial software and a uniform flux fractured well model in a radial composite reservoir. The analysis made it possible to calculate the permeability and permeability thickness of the zones, the fracture half-length, skin factor, mobility ratios, and the approximate distance to the high mobility zone using standard well test analyses (Horne, 2000).

Falloff data has been obtained at Shoshone 65-2, Shoshone 66-69, and Shoshone 66-2 in the Overthrust Tensleep. Interpretation of this fall-off data was carried out through Eclipse™ reservoir simulation and commercially available pressure transient interpretation software. Figure 2-51 shows the locations of these wells.



**Figure 2-51. Location of wells in which single-well buildup or fall-off test data was obtained for the project.**

#### 2.6.4 FALLOFF AND MULTI-WELL INTERFERENCE TESTING:

Multi-well interference testing was performed using Shoshone 65-20 as a central observation well. This testing was used to indicate the maximum permeability direction for the Phosphoria in Subthrust Block 6. Shoshone 65-53, Shoshone 65-37, and Shoshone 65-38 were pulsed. Figure 2-52 shows the location of these wells.

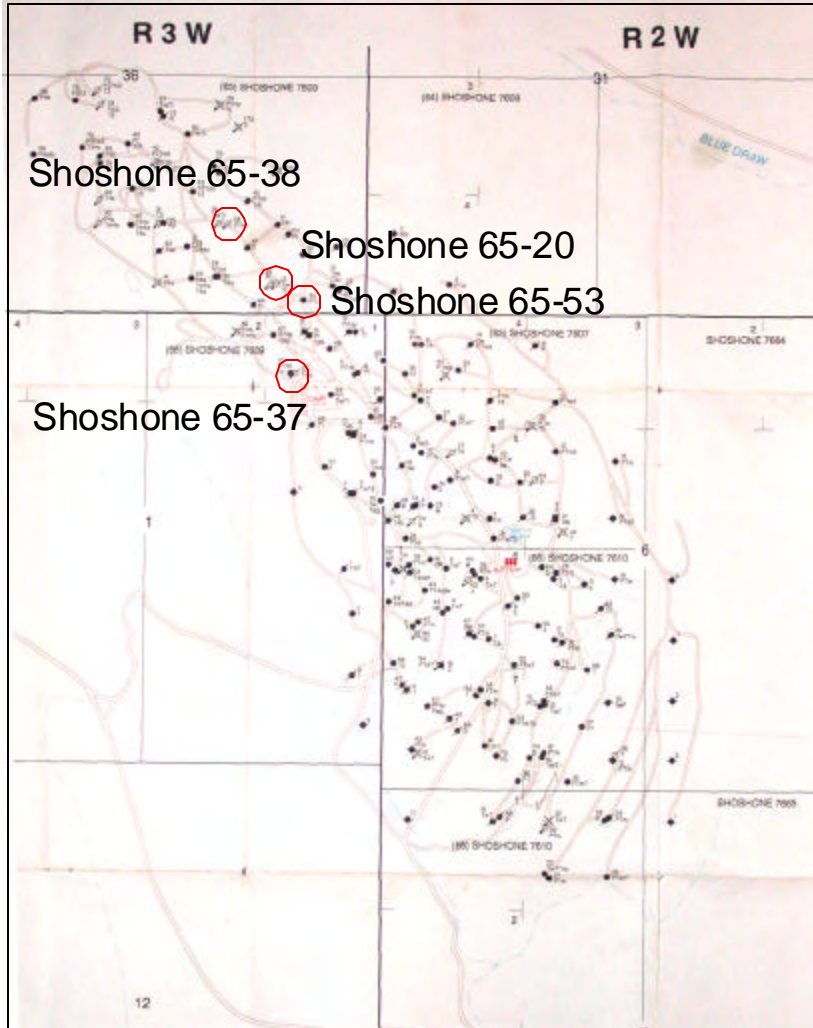


Figure 2-52. Location of wells used in multiwell interference testing.

## 2.6.5 INJECTED TRACER STUDIES

### 2.6.5.1 Nitrogen Injection Experiment

Two types of tracer tests were carried out for this project. The first test was a Nitrogen Injection experiment, in which nitrogen was injected into the Tensleep Formation in the overthrust block and monitored in wells with both Tensleep and Phosphoria completions.

Approximately 17.9 MMCF of nitrogen was injected into an upstructure Overthrust Tensleep well, Shoshone 65-02, during September, 2000. A total of 66 Circle Ridge wells were monitored for gas breakthrough. Bottom hole pressures (BHP) were monitored at the injector, Shoshone 65-02 and in seven zones in offset wells (Figure 2-53):

- Shoshone 65-03: Overthrust Tensleep

- Shoshone 65-03: Overthrust Phosphoria
- Shoshone 66-03: Overthrust Tensleep (Lost BHP data)
- Shoshone 66-08: Overthrust Tensleep
- Shoshone 66-49: Overthrust Tensleep
- Shoshone 66-68: Overthrust Tensleep
- Shoshone 66-69: Overthrust Tensleep

The nitrogen was injected at rates ranging from 1.6 to 2.1 MMCFPD over a 9.3-day period. Surface injection pressure at Shoshone 65-02 rose to 240 psi by the end of the test. Overthrust Tensleep gas cap pressure increased from approximately 3 psi to over 140 psi, as monitored in Shoshone 66-69, an offsetting observation well.



**Figure 2-53. Location of wells in which Bottom Hole Pressures (BHP) were monitored during the Nitrogen Injection experiment. Shoshone 65-02 was the injector.**

### 2.6.5.2 Bromide Tracer Experiment

The second tracer test was designed to test a subthrust Phosphoria block, and also to examine the connectivity between the Tensleep and Phosphoria Formations.

This Subthrust Block 6 tracer test was delayed due to permitting issues until November 2001. Permission to inject the tracer was requested from the United States EPA in mid-July 2001, but was not obtained until late October. The tracer test began November 15th

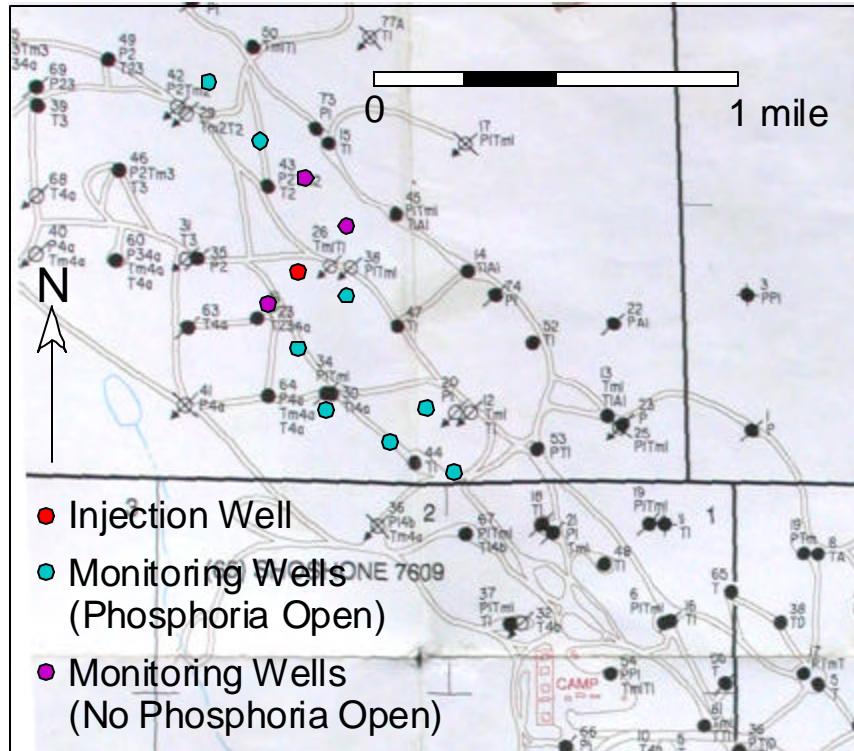


Figure 2-54. Location of injection well (Shoshone 65-20 – colored red) and monitoring wells (colored cyan and purple) used for bromide tracer test in the subthrust Phosphoria.

at the Phosphoria injector, Shoshone 65-20, and surrounding producers in Block 6. The test concluded in mid-December, 2001.

Background water samples from eleven producing wells, offsetting Shoshone 65-20, were collected during late October and early November. The furthest offsets were approximately 0.8 km in horizontal distance from the injector. Analysis, using a high-pressure liquid chromatograph, indicated background bromide concentrations of less than 1 ppm at all offsets. Eight of the wells, Shoshone 65-06, Shoshone 65-37, Shoshone 65-45, Shoshone 65-53, Shoshone 65-54, Shoshone 65-61, Shoshone 65-67, Shoshone 65-73, were completed in only the Phosphoria (Shoshone 66-73) or in both the Phosphoria and Tensleep. The additional wells (Shoshone 65-14, Shoshone 65-44 and Shoshone 65-52) were only open in the Subthrust Block 6 Tensleep Formation or Tensleep and

Amsden Formations. Figure 2-54 shows the location on these wells. Note that the wells not containing a completion in the Phosphoria are the wells closest in horizontal distance to the injector.

On November 15, 2001, 41 barrels of 24% NaBr aqueous solution were injected into the Subthrust Block 6 Phosphoria Formation at Shoshone 65-20. This aqueous solution contained 3,339 pounds (1,517.7 kg) of bromine and was gravity fed into the well at a rate of 2,300 barrels per day (365.7 m<sup>3</sup>/day). Following injection of the tracer slug, the well was returned to water injection at approximately 175 barrels (27.8 m<sup>3</sup>) water injected per day (BWIPD). Monitoring wells were sampled on an approximately daily basis.

## 2.6.6 ANALYSIS OF WELL TESTS USING DFN MODELS

Analysis of well tests involves both calculations based on the well test data itself, and also on simulations of these tests using DFN models. There are two broad types of well test simulations: those involving only pressure and flow, such as the single well pressure build-up or multiwell pressure interference tests; and those involving mass transport, such as the NaBr tracer experiment. The tracer tests may also offer the opportunity to simulate the pressure and flow without regard to mass transport. During the current project phase, simulations have involved only pressure and flow analyses, rather than mass transport, due to the 3-month delay in the permitting of the NaBr test.

The key parameter to simulate in transient pressure tests in fractured reservoirs is the pressure derivative. The analysis of the pressure derivative (Horne, 2000) was originally used to identify the radial-cylindrical, infinite-acting portion of the well test curve. The pressure derivative is calculated for each pair of time and pressure values in the well test as:

$$Derivative = t \frac{\partial p}{\partial t} \quad \text{Equation 2-15}$$

which produces a zero-slope line when the semi-log straight line condition of infinite-acting, radial-cylindrical flow is satisfied.

The pressure derivative is closely linked to transmissivity calculations. The permeability-thickness product ( $kh$ ) defines the flow capacity of a conducting feature. The pressure derivative is a method that was originally intended to identify the radial-cylindrical, infinite-acting portion of the well test curve. The pressure derivative is calculated for each pair of time and pressure values in the well test as  $t \frac{\partial p}{\partial t}$  which produces a zero-slope line when the semi-log straight line condition of infinite-acting, radial-cylindrical flow is satisfied.

The pressure derivative is closely linked to transmissivity calculations. The permeability-thickness product ( $kh$ ) defines the flow capacity of a conducting feature. The values of

the pressure derivative are semi-log slope of the well test, hence the derivative can be related to transmissivity by

$$\frac{\partial p}{\partial t} \equiv \text{derivative} = \frac{162.6(qB)\boldsymbol{\mu}}{kh} \quad \text{Equation 2-16}$$

(Horne 1995). Where  $kh$  is the permeability thickness,  $q$  is the flow volume,  $B$  is the formation volume factor and  $\boldsymbol{\mu}$  is the viscosity. By this simple transformation one can re-plot the derivative as a map of the transmissivity versus time during the well test. The permeability-thickness product  $kh$  can be represented in units of  $m^2\text{-m}$  (i.e.  $m^3$ ) (SI) or  $mD\text{-m}$  (oil field).

By this simple transformation, the derivative essentially expresses how transmissivity varies with time during the well test.

Although the single well simulation will help calibrate the fracture geometry and permeability necessary to match reservoir  $kh$ , simulating pressure response in the pumping wells is necessary to determine the relative permeability of one set to other sets. Multiwell pressure simulation was carried out by creating a multiwell-scale model using the calibrated parameters from the local, single well scale DFN model .

Simulating the pressure response in tracer tests with a DFN model for the nitrogen injection test presents some additional difficulties as there are potentially four phases acting: (1) Oil (2) Water (3) Natural Gas and (4) Nitrogen. However nitrogen dominates in the injector well and the fall off test can be used to calculate permeability thickness,  $kh$ . The initial simulation was carried out with a dual porosity Eclipse™ (Schlumberger) simulation to calculate permeability thickness. Next, a single-phase DFN model of the well was run, and the derivative of the pressure curve was used to determine the appropriate permeability and storage values for the individual fractures in the fracture system surrounding the wellbore.

## **2.7 Experimental Techniques for Comparison of Strain Values Calculated from 3D Palinspastic Reconstruction with Fracture Orientations and Intensity in Outcrop**

The construction of the field-wide DFN model for the Tensleep and Phosphoria Formations requires some way of specifying fracture properties away from well control. There are three possible alternatives for interpolating fracturing between wells:

- 1) Condition the fracture pattern to seismic attributes;
- 2) Interpolate from well data using statistical methods such as Geostatistics; or
- 3) Establish a model that relates fracture geometry to structural and/or lithological parameters.

There is no modern seismic data for the Circle Ridge Field, so the first option is not possible without the acquisition and processing of new, 3D seismic data. The second option is likely to lead to substantial errors, since statistical interpolation techniques assume that the rock behaves as a continuum between wells. Matrix properties often behave in this manner, but it is highly unlikely that variations in fracture properties vary in such a simple manner, especially when the fractures may have been produced by faulting and folding, which is inherently local and discontinuous in nature. Thus, the third alternative was adopted for this project.

In the Circle Ridge Field, fracture information is very sparse in the subsurface, coming from unoriented core and a few image logs. The methodology adopted in this project requires the comparison of the strain field in various structural positions relative to the fracture orientations, intensity and size. Subsurface data is not adequate as spatial coverage is very low and there is no direct information on fracture size. On the other hand, the top of the field is only a few hundred meters below the surface near the crest, so that the abundant outcrops above the field should reflect a similar deformation history, at least in the units below the detachment zone afforded by the Gypsum Springs Formation. Thus the fracture parameters necessary for ascertaining the structural controls on fracturing and developing input statistical distributions has been based upon studies of fracturing in outcrop.

As previously discussed, fracture data was obtained for this project along eleven different scanlines (Figure 2-55) in the Triassic Red Peak and Crow Mountain Members of the Triassic Chugwater Formation.



**Figure 2-55. Scanline used to measured fractures. Outcrop is of the Triassic Red Peak Member of the Chugwater Formation.**

The fracture data obtained in this manner represents the fracture pattern in several different structural positions and two different rock types. Although neither of these Members are reservoir units, field mapping and the structural reconstruction indicate that

they should have deformed in a manner analogous to the Tensleep and Phosphoria Formation reservoir units. Of particular interest are the orientation and intensity of fracturing along these scanlines.

The structural reconstruction of the Circle Ridge Field (Sections 3.3 and 3.4) suggested a sequence of folding and faulting events that likely produced the present-day structure. They found that the initially undeformed rock was first folded. Of the two algorithms tested, inclined shear folding produced better results than flexural slip folding. Following the folding, a series of faulting events occurred. The first large faulting is movement on the Gray Wash Fault that is the lowest structurally of all major faults. Upon encountering some obstacle or reaching the stress limit of strain release, the stress field then broke higher in the sequence, creating the Blue Draw Fault. Towards the south both these faults merge into the Red Gully Fault system, which at this time continued to move along an earlier established thrust plane. The imbrication process in the northern end of the field is repeated once again with the formation of the Yellow Flats Fault higher in the section. The final thrust displacement was focused on the Red Gully Fault that is structurally highest.

The Orange Canyon Fault obliquely cuts all these faults and was formed last of the large faults through the Circle Ridge anticline. The Orange Canyon and Green Valley Faults are dominantly strike-slip faults.

At each stage in the reconstruction, it is possible to calculate various types of volumetric strain and directional strain (Section 2.5.6).

Only directional strain parameters can be assessed as to their correspondence to fracture orientations, as volumetric strain measures have no associated directionality. The dominant joint (extension fracture) set should form orthogonal to the principal extension strain vector. Due to local stress redistribution, a second joint set orthogonal to the first and parallel to the principal pre-fracturing maximum extension direction might also occur.

Both the individual magnitudes of the directional strain components, as well as the volumetric strain measures, may relate to variations in fracture intensity (Jamison, 1997).

There are some uncertainties regarding the comparison of the calculated strains and the outcrop fracturing.

The structural reconstruction was carried out for the three principal reservoir formations, with particular emphasis on the Tensleep Formation. However, outcrop fracture data was obtained from the Crow Mountain and Red Peak Members, which are stratigraphically younger. Since there are no detachment horizons, such as the Gypsum Springs, intervening between the Crow Mountain and Red Peak units and the reservoir units, the principal directions of strain and relative strain magnitude variation of the Crow Mountain and Red Peak are likely to be very similar to that calculated for the Tensleep and Phosphoria Formations.

A greater source of uncertainty arises in the way that the outcrop data is spatially situated within the palinspastic modeling results. Ideally, the scanline site occurs in a structural position that should be compared to the strains in an equivalent structural position in the Tensleep Formation, for example. However, it is not possible to track equivalent structural positions in the reconstruction software. Thus it is assumed that two regions that occupy the same horizontal location occur in the same structural position. If the beds are flat lying, no error is made using this assumption. If the beds are steeply dipping, then some error will occur. In the restoration of structurally complex areas of the Field, strains may vary over a few tens of meters, or alternate between two common directions. The error introduced by assuming that horizontal equivalence equals structural equivalence might be on the order of a few tens of meters in some locations of the Field. Thus, the comparison of scanline fracture data with the strain in the reservoir formations should consider not only the strain at the equivalent horizontal position, but also in the general few tens of meters around the position.

With the exception of the rock in the area adjacent to the major faults, the strain produced by faulting is probably low. At some distance from the faults, the rock and any pre-existing fractures would be “translated” according to the fault geometry and slip vector, but the orientations of the fractures would be little changed unless there was significant block rotation. Fracture intensities, other than in areas adjacent to the fault, would also likely be unaffected. On the other hand, folding may produce significant rock strain, leading to the formation of fractures throughout the reservoir units.

Since the initial folding is the dominant strain event in the model, and it is the earliest significant event, it should have the highest probability of producing the fractures. If the fracture pattern does relate consistently to a major structural event, particularly the initial folding of the reservoir units, then the sensible geological explanation for the present-day fracture pattern lends confidence to the DFN model. It would be hard to have confidence in using the palinspastic model for predicting fracture patterns if only a minor, low-strain event seemed to correspond with the fracture patterns.

For these reasons, the correspondence between the fracture orientations and intensity with the various strain components calculated due to folding were closely evaluated.

## **2.8 Experimental Techniques For Validation of DFN Model Geometry and Connectivity Using Subsurface Fracture Geometry and Flow Data**

There are two levels or types of validation that can be used to assess the quality and usefulness of the palinspastic reconstruction. The first type of validation essentially evaluates the internal consistency of the restoration, and is based on whether various aspects of the model “balance”. This type of self-consistency checking guides the sequence and geometrical parameters governing the unfolding and unroofing of the model.

The second check on the model was to determine whether the connectivity of the fracture pattern at the reservoir scale was reasonable in terms of predicting flow patterns. This was done by comparing the connectivity and compartmentalization in the fracture network to patterns of tracer breakthrough. Thus, the validation was carried out through two series of comparisons:

1. Comparison of predicted fracture orientations and intensity of subsurface image log data; and
2. Comparison of predicted fracture pattern connectivity with subsurface flow results.

Comparison of the predicted and measured fracture geometry relies upon the model developed between strain components and fracturing. This strain/fracture model is applied to the reservoir at the locations where subsurface image log data has been collected (Figure 2-50).

The comparison of subsurface flow data with the connectivity properties of the fracture pattern inferred from the strain pattern is less quantitative. The data that provides the most independent check on the flow properties of the fracture network are the tracer tests. The reason for this is that:

1. Tracer tests involve a number of wells covering a larger area than any single well test, and so reflect the larger scale heterogeneity important for reservoir engineering optimization design involving secondary or tertiary recovery schemes;
2. Tracer tests not only identify areas with very high or low pressure communication, but also identify zones of higher or lower mass transport, which is of importance when designing surfactant injection processes or heat injection processes; and
3. Simulation of single well tests requires specification of fracture permeability and storativity, which can only be derived through calibration against the well tests, and so are not independent checks on the DFN model.

Thus, additional validation is provided by comparing the pattern and timing of tracer breakthrough and pressure interference with the connectivity of the fracture network (Figure 2-53 and Figure 2-54).

## **2.9 Integration of the Matrix and Fault Block Architecture Into a Single Numerical Reservoir Model**

An important aspect of this project is the creation of an integrated matrix/fault block/fracture numerical model. This model will allow the visualization of the fractures in 3-D and their relation with other parameters, and will provide the numerical parameter values to reservoir simulations or other calculations to design and evaluate options to enhance production.

The Circle Ridge Field is encompassed within a complex structural setting. The basic structure that defines the field is an anticline. The complexity enters due to the faulting of the anticline structure. This complexity is not just due to the number of the faults observed and modeled, but also the type of faulting in the Field. Many faults intersect other faults, cross other faults, or die out. The Circle Ridge Field has not only nearly vertical faulting which is fairly simple to model, but also shallowly dipping faults and in particular, shallowly dipping reverse faults. This last type of fault is difficult to incorporate in many 3D modeling software systems.

Of the modeling software packages that can handle the complex types of faulting that occur at Circle Ridge, further classification of the software can be made in their ability to upscale the geo-cellular model to reservoir simulation models. This process of upscaling has been addressed in some of the software so that directly readable grid files are written that can be read by the reservoir simulation software. This becomes important in order to allow the operator of the field a method of evaluating the best economic methods of extracting the most reserves from the field. The ability of geo-cellular models to easily output simulation modeling grids is an important point to consider in picking the geologic modeling software.

Initial experiments with importing the data into Roxar's RMS™ software showed that the current release of RMS cannot handle reverse faults without breaking the model into several pieces, which is cumbersome for use in later simulation or other types of calculation. Currently, modeling is being carried out using Technoguide's Petrel™ and Gocad™ to determine the best piece of software to be used for this project.

## **2.10 Assessment of Compartmentalization/Tributary Drainage in Fracture Networks**

Compartmentalization refers to the delineation of the spatial extent of portions of the fracture system that form well-connected networks (Figure 2-56). Within these network clusters, fluids can move more easily throughout the fracture system. These networks are isolated or partially isolated from other well-connected networks by regions of much more poorly connected fractures, so that fluid movement between fracture compartments either occurs through the matrix, or is retarded by much more poorly connected fracture systems. Tributary analysis is similar to compartmentalization analysis. It essentially focuses on the extent of fracture connectivity around existing or hypothetical wells.

Figure 2-56 shows the concepts of both fracture network compartmentalization and tributary drainage. The DFN model on the left of the figure shows all of the fractures generated. Circles colored white, red and purple indicate three wells.

While the fractures in the left portion of the model look entirely connected, they are not. The DFN model on the right side of the figure shows the fracture compartments. There

are two large compartments, shown in green, and several much smaller compartments, shown in other colors and mainly obscured by the two large compartments.

The amount of tributary drainage is a function of the location and orientation of the well relative to the fracture compartments that develop. The white well appears to access the large northern compartment, while the red and purple wells appear to access the large southern compartment. In fact, neither the white well nor the purple well intersect any of the fractures. Only the red well actually intersects fractures in the large southern compartment.

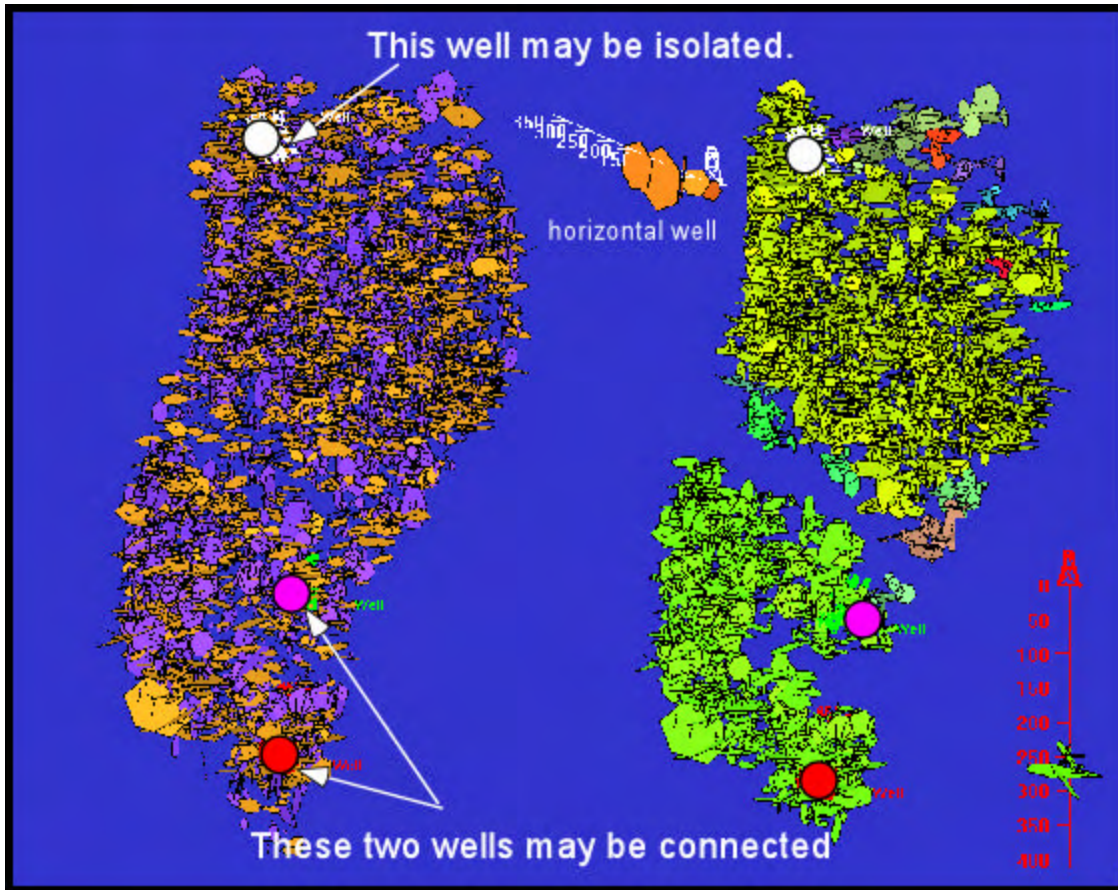


Figure 2-56. DFN model for subthrust block 6, showing fracture compartments formed due to variation in intensity related to folding. The diagram on the left shows all fractures and three vertical well locations. The diagram on the right shows the fracture compartments.

With stimulation, the white and purple vertical wells would probably connect better to the fracture compartments. Or, as shown with the white well, a horizontal completion, rather than a vertical, would intersect a number of fractures and be well-connected to the northern compartment. The tributary drainage volume is the volume of reservoir (matrix) that is potentially accessed by the well through the connected fracture system. Particularly where the fracture permeability is much greater than the matrix permeability, the amount of matrix that can be produced, or subjected to water floods or steam floods is related to the volume of matrix accessed by the compartment that the well connects to.

Thus, the red well potentially could access the matrix tributary to the large southern fracture compartment.

The experimental method for determining compartmentalization and tributary drainage is thus a calculation based upon the fracture network connectivity and its spatial extent. One way to calculate compartmentalization and tributary drainage for a field is to first build a field-wide DFN model, calibrate it to all available data, history match it, and then carry out a connectivity analysis on the DFN model. This alternative requires a full-field history matching simulation, which is not part of the Circle Ridge project's scope, and would also be undesirable, as the only portions of the reservoir that *could* be history matched are the overthrust block and one or two subthrust imbricate blocks. Since there is little or no production in the remaining blocks, these significant potential reservoir additions could not be studied.

Another way to analyze the compartmentalization and tributary drainage is to examine the connectivity geometry as inferred from the palinspastic strain maps, and qualitatively calibrate these strain patterns to the connectivity seen in the nitrogen injection test and the bromide tracer test.

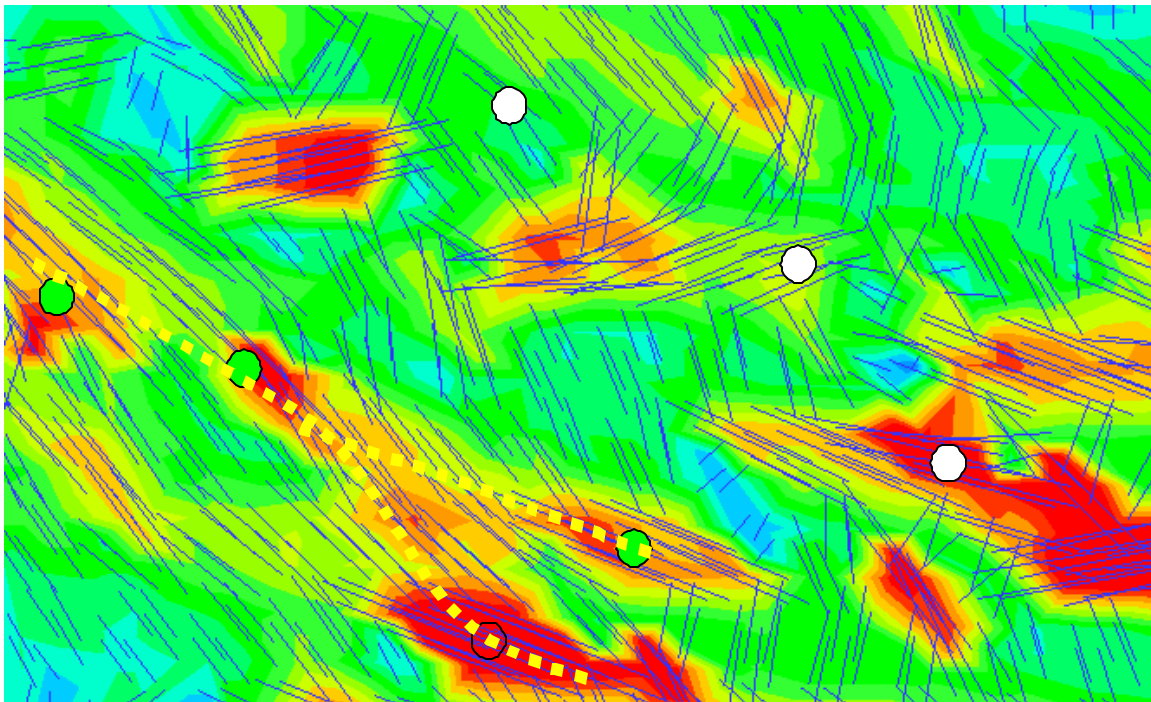


**Figure 2-57. Hypothetical example of how strain maps and subsurface tracer data can be related to understand compartmentalization and tributary drainage. Green circle represent wells that appear to have strong pressure or flow connection in a tracer test, while white-shaded circle represent wells that appear disconnected. The contour colors denote the magnitude of strain, while the blue arrows indicate the trend of the dominant extensional fracture set predicted from the strain tensor.**

Figure 2-57 shows a hypothetical example of how subsurface tracer breakthrough data can be combined with strain data to delineate the fracture connectivity structure and qualitatively assess the size and shape of fracture network compartments and tributary drainage patterns.

In this hypothetical example, the superimposition of the strain pattern, the dominant extensional fracture strike and the breakthrough pattern in wells can be used to calibrate the strain map and allow it to be interpreted as a connectivity map. High strain regions (shaded red and yellow in Figure 2-57) should represent regions where fracture development is also high. The orientation of the strain field can be used to infer the direction of the dominant extension fracture strike (shown by the blue lines in Figure 2-57). Regions of high strain connected to each other or by fracture corridors should exhibit strong pressure or tracer breakthrough responses. The yellow dotted lines in the figure indicate possible fracture corridors, which are formed by spatially contiguous regions in where the dominant fracture strike is parallel or subparallel. If there are fracture corridors developed in relation to the strain, then wells, such as those shown as green circles in Figure 2-57 should show good communication. Also, wells not connected by fracture corridors, such as those shown as white circles, should show much poorer response. Thus, if there is a geological understanding of why the zones of high strain have occurred, and it can be shown that the strain corridors and orientations and variations in fracture intensity do correspond to fracture orientations as seen in the subsurface from image logs or core, and the pattern of tracer breakthroughs is reasonably well-explained by the strain corridor pattern, then the spatial structure of the strain corridors can be used to quantify the connectivity of the reservoir.

## **2.11 Calculation of Effective Reservoir Properties**

A major goal of this project is to calculate fracture porosity, fracture permeability and the parameters that relate the exchange of fluids between the matrix and the fracture system for the entire Field from the fracture model constructed and validated from the outcrop, well log and well test simulation work. The experimental procedure for carrying out this calculation goes through three stages: derivation of the parameter values needed to create a 3D DFN model of the reservoir; generation of the DFN model; and calculation of parameter values from the DFN model.

### **2.11.1 CALCULATION OF PARAMETERS FOR THE DFN MODEL**

The methodology for calculating the input to the DFN model has largely been covered in previous project semi-annual reports. It is useful to summarize the parameters that are needed, and how they were obtained, as a basis for better understanding of the actual procedure used to generate the DFN models. A DFN model is first based on identifying individual fracture sets, and then calculating a series of parameter values for each set. Parameters typically are not single numerical values, but are represented as statistical distributions and are related to underlying geological factors.

### 2.11.1.1 Identification of fracture sets

A fracture set may be interpreted differently depending upon the use. In typical geological usage, a fracture set is a group of fractures with more or less the same orientation. There may also be some additional constraints such as the fractures also formed from the same geological processes and at the same time. Petrophysicists tend to separate fractures based on orientation similarity and also by aperture class: open, partially open, solution enhanced, or filled, because this additional characteristic has implications for fluid flow, which is of primary concern.

For DFN modeling, a slightly different definition is used: a fracture set is a group of fractures that can be characterized and generated stochastically from the same statistical distributions and geological constraints or conditioning functions. While orientation similarity, aperture or filling, and mode of formation all may play a role in defining these sets, they may also be ignored. For example, fractures belonging to the same orientational set that might be classified on an image log as open, partially open or closed, may be combined into a single set with an aperture distribution that reflects all of these class states. Likewise, if there were two fracture populations with similar statistical and geological constraints, except that one portion of the population formed early, and the other during a later event, then there would be no practical reason to treat them as two individual sets from the standpoint of generating the DFN model.

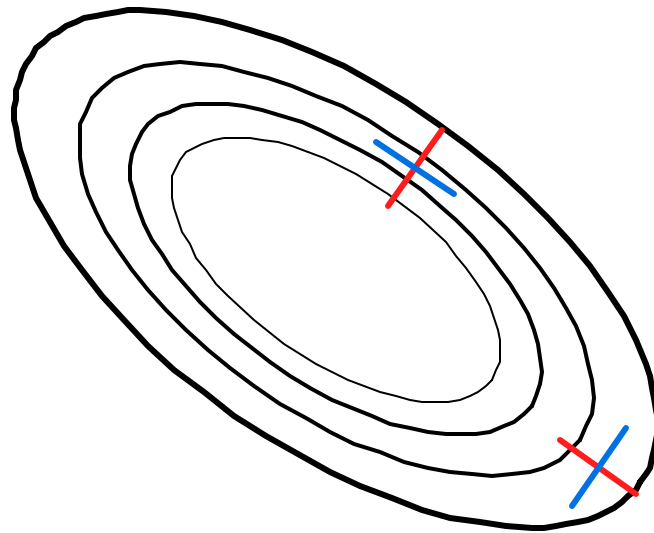


**Figure 2-58. Example of fractures of identical orientations belonging to different sets.**

Moreover, the concept of orientation similarity needs care as well, particularly where folding has led to fracture formation, as it has in Circle Ridge. Two fractures may have the same absolute orientation, for example, vertical and striking northeast. Just because these two fractures have an identical orientation does not mean that they are necessarily

part of the same set. If the fold is somewhat more complex, for example, having a double plunge like Circle Ridge, then a northeast striking fracture in one portion of the fold may be dip-parallel, while a northeasty striking fracture in another portion may be strike parallel.

Figure 2-58 shows such an example. The red fracture set is always dip parallel (the black lines in the figure denote bedding in this plan-view figure), while the blue fractures are always strike parallel. Typically, the dip parallel fractures have very similar geometrical and fluid flow characteristics, while the strike parallel fractures have internally similar characteristics as well, but characteristics that differ from the dip parallel fractures. Blindly combining all northeast fractures into a single set, and all northwest fractures into a single set, would obscure these differences and decrease the DFN model's usefulness.

The process for defining sets was based on an iterative analysis of outcrop fracture data, downhole image log data, comparison of outcrop and image log data with extensional strain data calculated from palinspastic reconstruction of the field, inferences drawn from well test modeling, and consideration of nearby outcrop analogs.

The process was to start with the outcrop data at eleven outcrop sites, and define the local orientational groupings at each site. Each set was evaluated in terms of its relation to bedding strike and dip. It was found that there were typically two sets present, both nearly orthogonal to bedding and to each other. Very often the two sets subparallel bedding strike and dip.

While the process could have been carried out in different order, the next information for delineating sets came from the strain maps calculated from the palinspastic reconstruction of the reservoir formations. The strain components for various stages in the reconstruction (different folding and faulting events) were compared with the outcrop fracture orientations and intensity, and it appeared that the direction of maximum extensional strain produced during the initial folding of the field was a good predictor of the fracture orientations in outcrop.

Image log data from three wells, two in the overthrust Tensleep, one in the subthrust Phosphoria, showed that the fracture sets in the image log had the same relation to the extensional strain as the outcrop fracture pattern. Further comparison of outcrop data in outcrops adjacent to the wellheads for the two overthrust image log wells showed similarity between the outcrop pattern and the subsurface pattern in the reservoir.

Transient well test matching further indicated that a model consisting of two fracture sets, orthogonal to bedding and oriented relative to the strain field, could reproduce the transient well test behavior.

Inspection of Tensleep and Phosphoria outcrops in the Wind River Canyon and in the Bighorn Basin also indicated that there were commonly two sets developed that were orthogonal to bedding and to each other.

Thus, the DFN model defined two fracture sets that were orthogonal to bedding and to each other, and were oriented relative to the direction of maximum extensional strain calculated from the palinspastic reconstruction of the field.

#### 2.11.1.2 *Fracture Orientation Variability for Each Set*

The orientation variability for each set was based upon data collected from outcrop and from the three image logs. The image log data was further analyzed to determine if variability or orientation changed according to lithology or depth.

Because the fracture sets did not maintain a single global orientation, but varied according to the strain field changes, only the variation of fracture orientation about the mean was used. The local mean orientation was based on the orientation of the calculated extensional strain.

#### 2.11.1.3 *Fracture Intensity*

Fracture intensity is a term that is often used to describe a number of different measures of how many fractures there are in a particular portion of the reservoir (Dershowitz and Herda, 1992). Most often it refers to the number of fractures per meter of core or image log.

However, fractures are essentially two-dimensional objects in three-dimensional space, and so a three-dimensional measure is needed for constructing a DFN model. A mathematically convenient measure of three-dimensional fracture intensity for DFN models is the total fracture surface area per volume of reservoir, often denoted as  $P_{32}$  (Dershowitz and Herda, 1992).

There are several possible approaches to calculating  $P_{32}$ . One approach is to estimate the value from the number of fractures per meter, incorporating knowledge of the fracture orientations and the orientation of the wellbore. This approach is a type of non-linear optimization, in which a DFN model is constructed having the correct orientation model and a guess for  $P_{32}$ . A well is inserted into the DFN model and used to sample the number of fractures intersected per meter in this synthetic well. This calculation is then compared to the actual number of fractures per meter. The guess for  $P_{32}$  is then adjusted up or down accordingly until a close match is achieved.

This guess can also be adjusted for the difference between conductive and non-conductive fractures. With flow meter data or similar logs that distinguish conductive from non-conductive fractures, a ratio of these can be calculated. This same ratio is then applied to the calculated  $P_{32}$  value to finally arrive at a conductive  $P_{32}$  for the model.

Another strategy for calculating conductive  $P_{32}$  is to derive it from matching transient well tests using DFN models. The intensity for each set is one parameter that can be adjusted to obtain a match. The advantage of this approach is that the intensity calculated is the *conductive*  $P_{32}$  itself; it is not necessary to rely upon a ratio inferred from flow meter results.

At Circle Ridge,  $P_{32}$  was estimated primarily from transient well test matching. A correlation was established between this value and the value of extensional strain. The value of the local  $P_{32}$  intensity was thus based upon the local extensional folding strain magnitude and the correlation function.

#### 2.11.1.4 Fracture Size

Fracture may be estimated from fracture trace length statistics, by matching the “pad intersection” percentages, from image logs, or from well test matching DFN simulations where size is treated as a “free” parameter in the matching (La Pointe and others, 1993).

The matching of trace lengths to estimate fracture sizes relies upon DFN simulation. In this approach, fractures are realized as circular discs with a radius distribution drawn from some assumed statistical distribution, such as lognormal with mean equal to 50 m and standard deviation equal to 27 m. An outcrop, represented by a plane, is inserted into the model and the resulting trace length distribution on the plane is converted to a trace length frequency distribution. This distribution is then compared to the measured trace length frequency distribution. The parameters of the DFN mode are adjusted in order to achieve a statistically significant match either through manual adjustment or through nonlinear optimization.

The procedure to estimate size from image log data follows a similar approach. FMI and other fracture imaging tools use from 4 to 8 pads to image the fractures. Many, if not most, of the fractures are imaged on all pads. Some fractures appear on fewer than all of the pads. One reason for a fracture to appear on fewer than all of the pads is related to fracture size. If a fracture were a kilometer in radius and intersected a wellbore, the probability that it would cut entirely through the wellbore is very high. If the fracture is very small, on the order of centimeters, then the probability that it would cut entirely through the wellbore and appear on all pads is much, much lower. Using this principle, a DFN model for each set is made with the already calculated fracture orientation model and intensity, but with a guess as to the size distribution of the fracture set. This model is sampled with a synthetic wellbore, and how many pads each intersecting fracture would have appeared on is recorded automatically. The percentages of fractures appearing on all of the pads, some of the pads or only a few of the pads are then compared to the actual pad intersection percentages. The fracture size parameters are then adjusted by hand or through a nonlinear optimization procedure to achieve a statistically significant match. This is done for each set and each well separately.

As in the case of fracture intensity, estimation of fracture sizes from image logs or traces in outcrop produces an estimate of the size distribution of both non-conductive and conductive fractures together. Estimation from well test simulation, on the other hand, produces an estimate that probably better characterizes the size distribution of the conductive fractures that play an important role in the reservoir-scale flow processes.

Essentially, fracture size is treated as a free parameter to be adjusted when matching transient well tests. The only constraints on the results of this approach are that the resulting conductive fracture sizes should be at least as large as the non-conductive; and the statistical distribution calculated should not produce fractures that stretch geological credibility or available outcrop analogs. The important portion of the transient well test curve to match is the longer time portion, as this best captures how larger volumes of the reservoir away from the immediate wellbore are responding.

At Circle Ridge, image log data did not produce enough fractures to compute robust pad intersection statistics. The outcrop data was not used because (1) it was in the Crow Mountain and Red Peak Members of the Chugwater Formation, not the Tensleep or Phosphoria Formations, and could thus be different; and (2) the trace length data in the outcrops was heavily censored, making the trace length matching calculation highly non-unique. Thus, the size distribution was derived from well test matching and checked against outcrops of the Tensleep and Phosphoria Formations in the Wind River Basin.

#### 2.11.1.5 *Fluid Flow Properties for Individual Fractures*

A DFN model is composed of individual fractures, and each of these individual fractures must have a value of transmissivity and storage (or alternatively permeability and compressibility) assigned to it. These parameters cannot be measured directly in situ. They are derived by treating them as free parameters in well test matching or other types of subsurface flow and transport modeling, such as tracer test simulations. For Circle Ridge, these parameters were estimated through matching aspects of the Nitrogen Injection tracer test results.

#### 2.11.2 GENERATION OF THE DFN MODELS

The method used to generate the DFN models for the Circle Ridge Field relied upon the Golder's commercial FRED fractured reservoir characterization and simulation software. The steps in the process are as follows:

1. Specify the input parameters for each fracture set described in 2.11.1 (Figure 2-59).
2. Generate or "realize" each set (Figure 2-60). This is done for each structural block and reservoir formation separately.
3. Clip the fractures against formation boundaries (Figure 2-61)
4. Save each set (Figure 2-62)
5. Combine data sets for different structural blocks and formations into a single model (Figure 2-63).

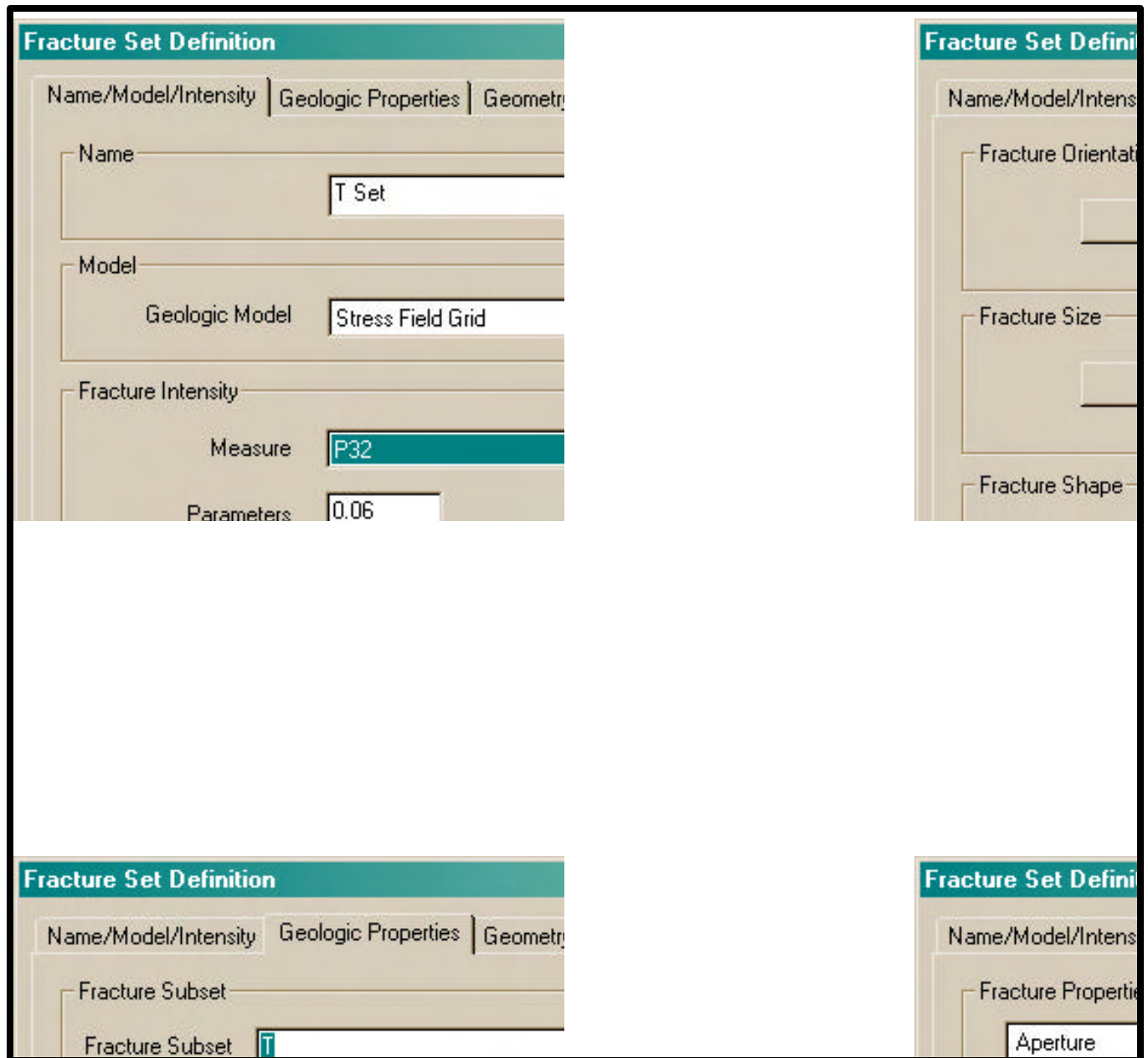
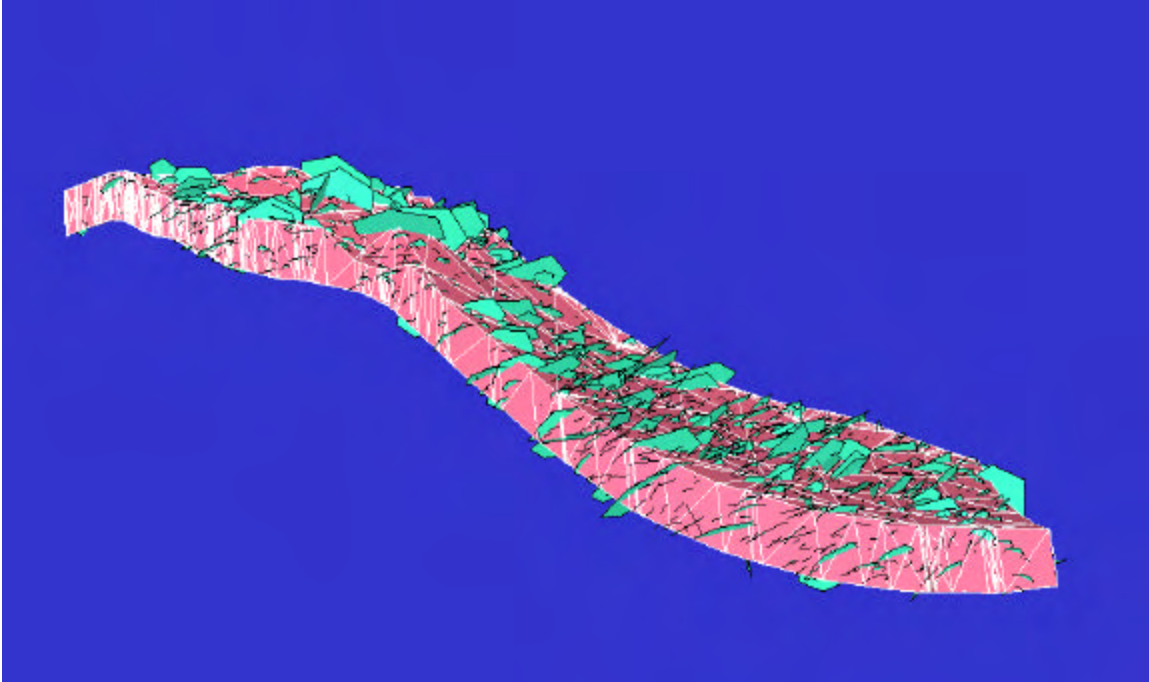
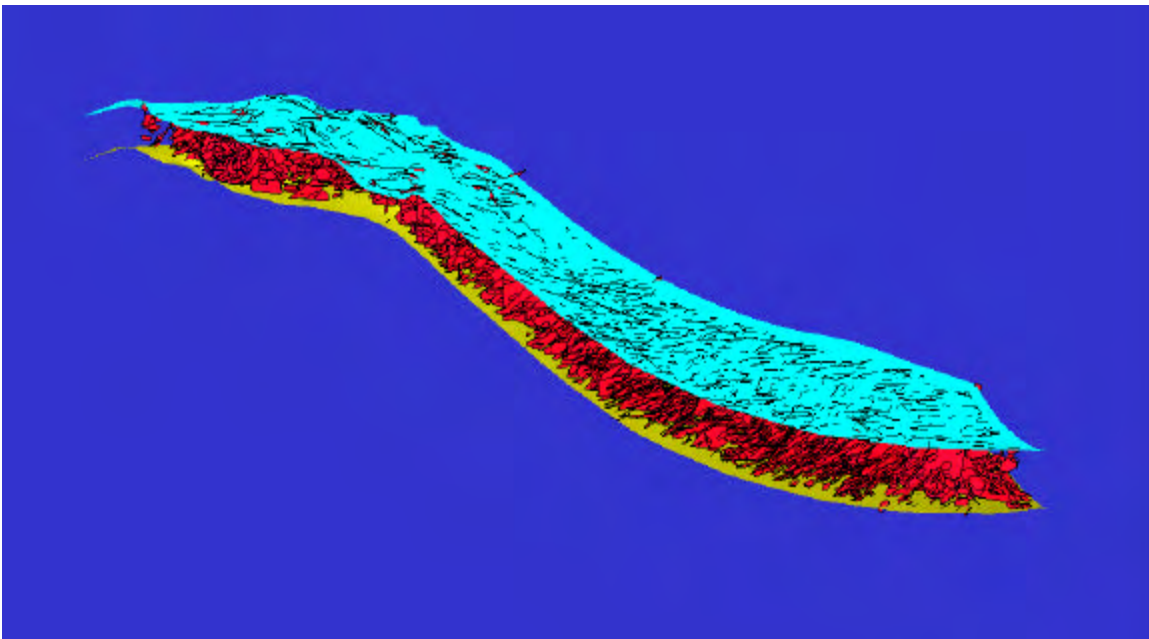


Figure 2-59. Example of data being entered into FRED for generation of a fracture set.



**Figure 2-60. Generation of one fracture set in a DFN model. The block shown is Block 6, Tensleep Formation, viewed from east to west. The grid shown is the tetrahedral grid containing extensional strain values and orientations produced in the palinspastic reconstruction of the field.**



**Figure 2-61. Example of fracture set clipped against upper and lower boundaries of Tensleep Formation, Block 6.**

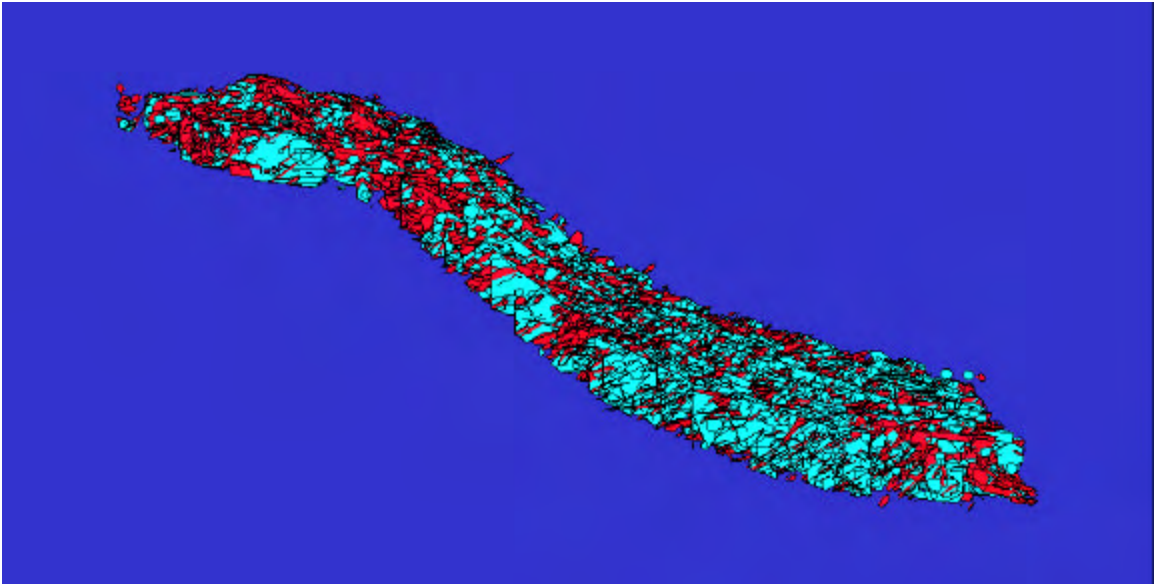


Figure 2-62. Final DFN model for Tensleep Formation, Block 6, including both major fracture sets clipped against the upper and lower boundaries of the Tensleep Formation.

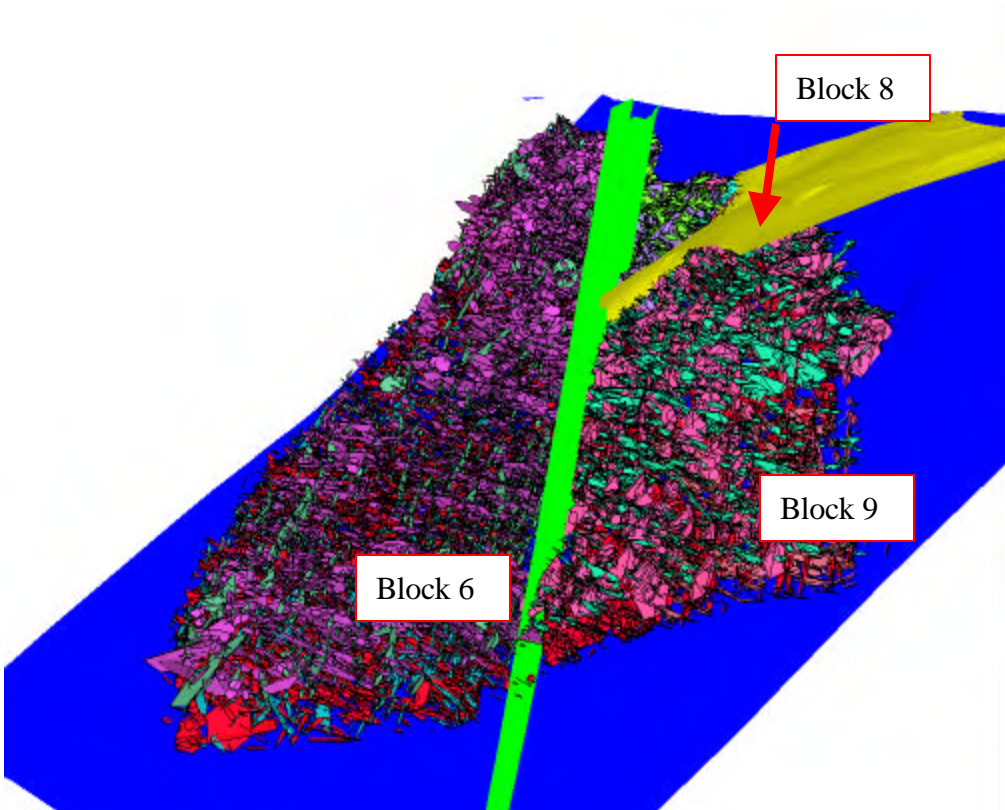


Figure 2-63. DFN model of structural blocks 6, 8 and 9 for both Tensleep and Phosphoria Formations. Also shown are the Green Valley, Yellow Flats and Blue Wash Faults.

### 2.11.3 CALCULATION OF EFFECTIVE RESERVOIR PROPERTIES

Once the DFN model has been generated for the entire reservoir, the next step is to calculate effective fracture properties from the DFN model. The properties of interest are fracture porosity, fracture intensity, directional fracture permeability, and sigma factor, a parameter that is used in many reservoir simulators to approximate how fluids move between the matrix and the fracture systems under a pressure gradient. By their very nature, these properties encompass a volume of reservoir, and therefore must be calculated over reservoir volumes.

If a reservoir simulation grid has been defined for the reservoir, then this is the most desirable assemblage of subvolumes (the simulator grid cells) over which to calculate the effective properties. In practice any grid can be used. Because a field-wide reservoir simulation grid has not been prepared for the Circle Ridge Field, grids were generated individually for each formation and structural block. The number of grid cells in each block and formation was specified so that the mean horizontal dimensions of each grid cell were on the order of 50 m, and the mean thickness of each grid cell was on the order of 25 m. These values were chosen as they are on the order of size of typical reservoir simulation grid cells, and they are large enough that each cell contains a number of fractures. Where the reservoir layer thins appreciably over the structural block, the vertical thickness of the cell may be less than the target 25 m since the number of grid layers is always preserved. Figure 2-64 shows an example of such a grid. The grid in this figure was generated for the Tensleep Formation in Block 6.

The calculation of the effective fracture properties in an individual grid cell (Dershowitz and others, 2000) is based on the actual fractures found in each cell. An example of calculation results for an entire grid is shown in Figure 2-65. The cells are color coded according to the value of vertical permeability calculated for each grid cell. The FRED software carries out these calculations for all of the grids for every structural block and reservoir formation, and outputs the values as ASCII files containing the centroid location of each grid cell, its dimensions and orientation, and the effective properties. The effective properties consist of:

- fracture count;
- $P_{32}$  fracture intensity;
- Fracture porosity;
- the full permeability tensor such that the  $P_{xx}$ ,  $P_{yy}$  and  $P_{zz}$  components are aligned with
- the global (X, Y and Z) coordinate system;
- the full permeability tensor such that the  $P_{xx}$ ,  $P_{yy}$  and  $P_{zz}$  components are aligned with
- the local (I, J, K) coordinate system; and
- sigma factor

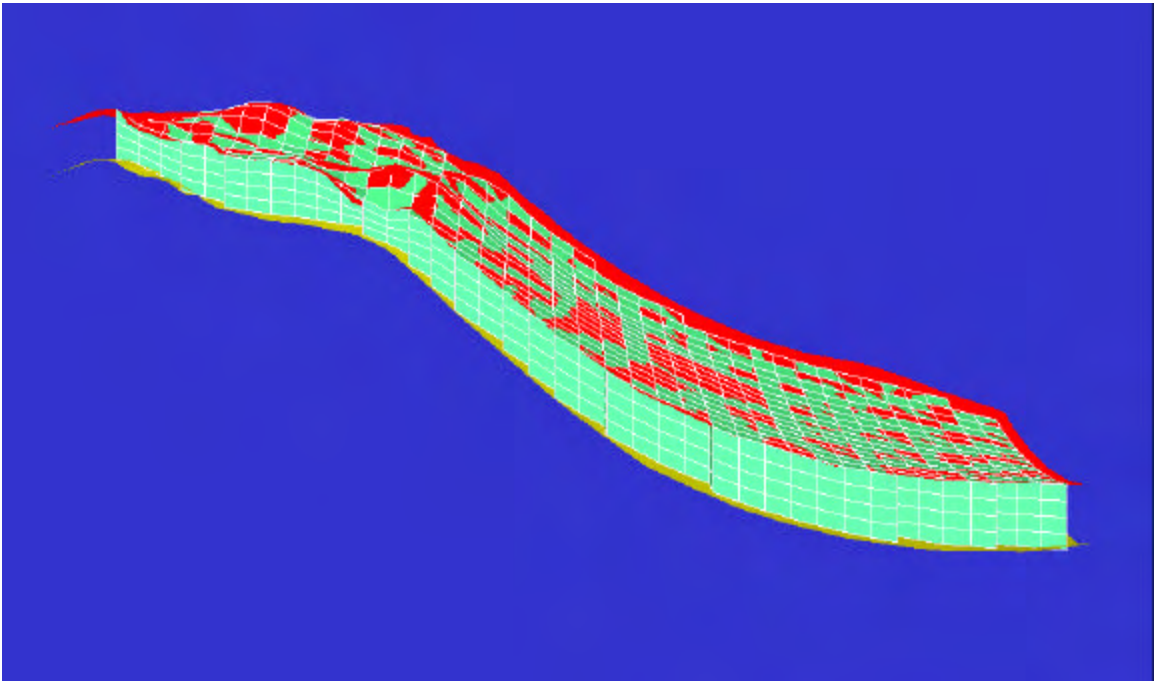


**Figure 2-64.** Example of a grid (cyan) generated between the upper (red) and lower (green) Tensleep boundaries for Block 6.

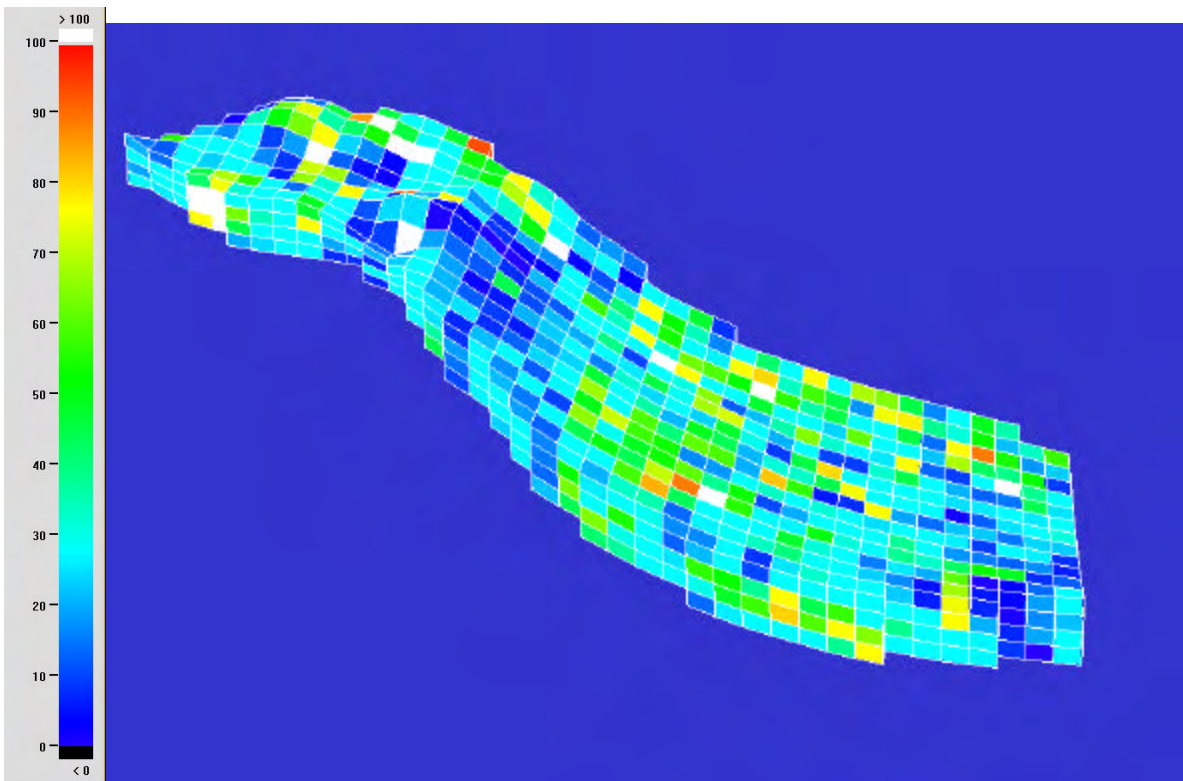


**Figure 2-65.** Values of vertical permeability calculated for grid shown in Figure 2-64. Values are in mD.

## 2.12 Integration of the Matrix and Fault Block Architecture Into a Single Numerical Reservoir Model

An important aspect of this project is the creation of an integrated matrix/fault block/fracture numerical model. This model will allow the visualization of the fractures in 3-D and their relation with other parameters, and will provide the numerical parameter values to reservoir simulations or other calculations to design and evaluate options to enhance production.

The Circle Ridge Field is encompassed within a complex structural setting. The basic structure that defines the field is an anticline. The complexity enters due to the faulting of the anticline structure. This complexity is not just due to the number of the faults observed and modeled, but also the type of faulting in the Field. Many faults intersect other faults, cross other faults, or die out. The Circle Ridge Field has not only nearly vertical faulting which is fairly simple to model, but also shallowly dipping faults and in particular, shallowly dipping reverse faults. This last type of fault is difficult to incorporate in many 3D modeling software systems.

Of the modeling software packages that can handle the complex types of faulting that occur at Circle Ridge, further classification of the software can be made in their ability to upscale the geo-cellular model to reservoir simulation models. This process of upscaling has been addressed in some of the software so that directly readable grid files are written that can be read by the reservoir simulation software. This becomes important in order to allow the operator of the field a method of evaluating the best economic methods of extracting the most reserves from the field. The ability of geo-cellular models to easily output simulation modeling grids is an important point to consider in picking the geologic modeling software. With these considerations, the software system that proved most useful was GoCad™ (<http://www.ensg.u-nancy.fr/GOCAD/>).

The data used to create the model derives from the four main project tasks. The matrix data is derived from interpretations made from well logs. Task 1 of this project supplemented the existing interpretations made from modern well logging suites with data derived by calibrating logs from 113 older wells. This provided for a data set on matrix properties for the Tensleep and Phosphoria Formations for the Overthrust Block and most of the imbricate blocks lying in the footwall of the Red Gully Fault. The well data was interpolated between well control using the geostatistical algorithms available in GoCad™.

The second component of the integrated reservoir model are the major faults: the Red Gully Fault, Green Valley, Yellow Flats, Blue Draw, Grey Wash, Orange Canyon and Purple Sage faults. Prior to this project, the geometry of the faults at depth was poorly constrained. Through the 3D palinspastic reconstruction based on the additional well control also provided by the well log recalibration, and the three new cross sections, it was possible to greatly improve the constraints on fault surface geometry of these seven major faults. The faults themselves were exported from the palinspastic reconstruction software, and converted into triangular meshes that could then be reformatted into native

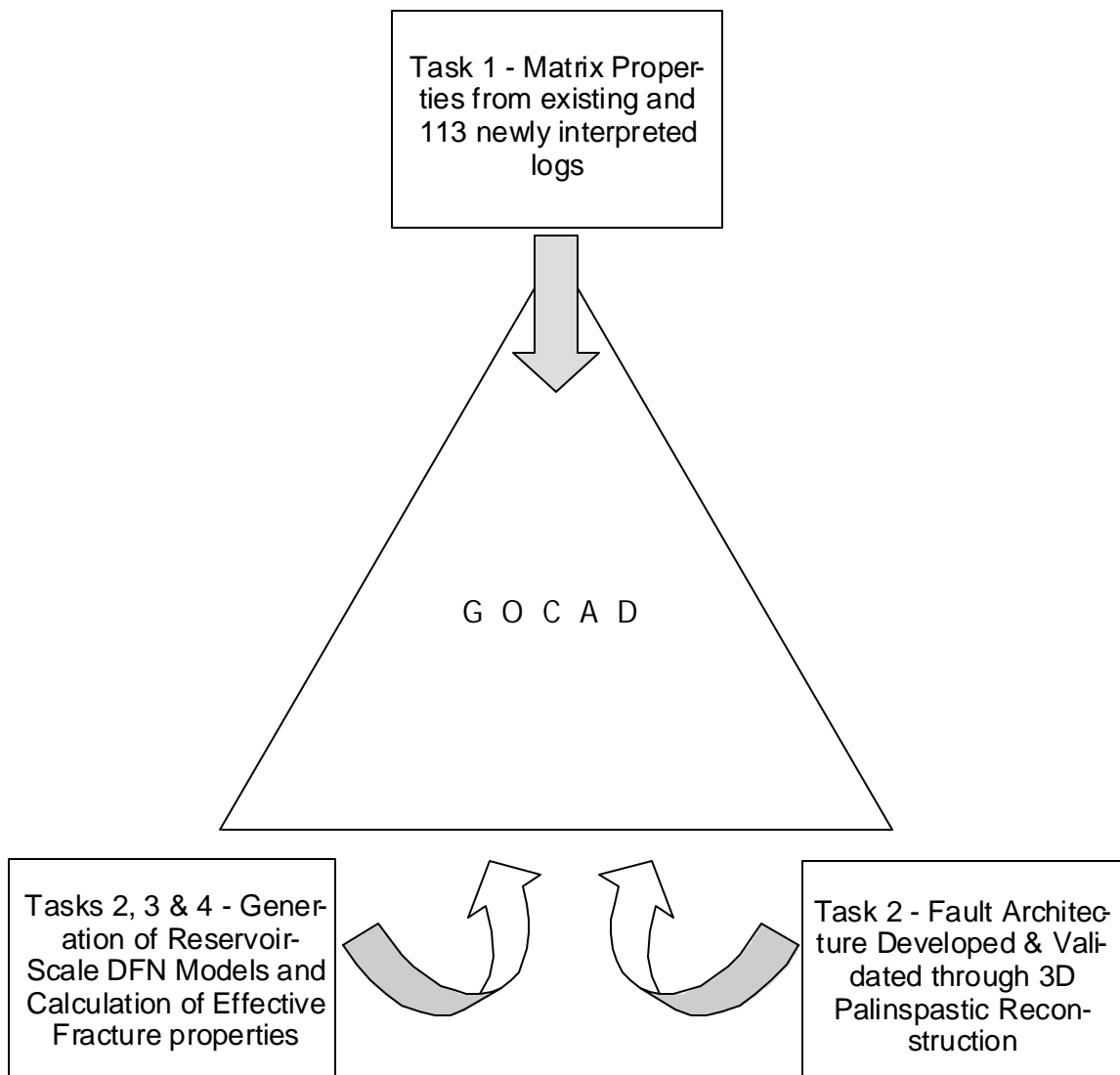


**Figure 2-66. Data flow from project tasks into the integrated reservoir model.**

GoCad™ surface files.

The reservoir-scale fractures themselves are not explicitly represented as individual objects in the final integrated reservoir model. Rather, the effective fracture parameter values derived from them are incorporated into the model.

Field work on outcrops, fracture image logs from three wells, well tests and tracer tests were all used to generate a validated discrete fracture network model for the Tensleep and Phosphoria Formations for all structural blocks making up the Circle Ridge Field. As described in Section 2.11, the formations were gridded and the effective fracture properties calculated for each grid cell. The values for each parameter were then imported into the integrated reservoir model.

## 3 RESULTS

### 3.1 Overview

This section describes the results of this project for the three major elements of the integrated reservoir model (matrix, fault block architecture and reservoir-scale fractures), and the calculation and preliminary use of the model for reservoir engineering applications leading to improved recovery. This later section includes the calculation of effective fracture network permeability, fracture porosity, sigma factor and other reservoir parameters typically required for numerical reservoir simulation. In addition, the connectivity of the fracture network was quantified and areas of higher and lower connectivity were identified and related to the structural development of the Circle Ridge Field.

The goal of subsections on the components of the 3D reservoir model is to show in a logical sequence how the model was built, what assumptions were made, and what the final result looks like. Many of the components of this model and the data on which it is based are described or available for download from the project website (<http://www.fracturedreservoirs.com>). When this is the case, the steps needed to access this data on the website are described.

The last subsections focus on the use of the integrated model. The structure of each of these subsections is to describe the specific outcomes of several of the key steps outlined in a more general sense in Section 2, the assumptions required as the model was being analyzed, and the final results.

Most of the products described in these subsections underwent one or more forms of validation. For example, the fault block architecture was validated by a successful palinspastic reconstruction that restored the reservoir formations to an original unfolded and unfaulted state while maintaining or fulfilling various kinematic constraints. The preliminary discrete fracture network model that was largely derived from outcrop data was validated against the strain field and subsurface image log, well test data and tracer experiments. Where appropriate, these validations are described in detail.

Some of the results presented are final calculations, such as the sigma factor data or the directional permeability. These data are only presented in this Section (and provided numerically for download from the project web site). While it would be possible to further validate these reservoir engineering parameters, and to refine them, this would require an extensive history-matching exercise which was not part of the project scope, and so is not included in this report.

This penultimate subsection describes an early use by Marathon Oil of the 3D integrated model with respect to well planning in the overthrust block.

The final subsection describes the results of the four technology transfer efforts include as part of this project. These consisted of the project website; conference presentations and reports; tribal workshops; and project progress reports. Additions to the project website and publications resulting from project activities are anticipated to continue even after the completion of the project.

Overall, this section focuses on the major project results. It does not contain recommendations for future work to extend the project benefits, nor a final summary of the project accomplishments. These are discussed in Section 4.

### 3.2 Matrix Property Calculations

The knowledge concerning matrix porosity and fluid saturation was greatly expended through the innovative re-calibration of the older vintage wireline log data. Thirty-nine wells (one more than originally planned) that had modern logging suites were analyzed in both the overthrust and subthrust portions of the reservoir. Information from an addition 113 wells was produced through the re-calibration (Figure 3-1). Results for these wells were posted to the project web site, provided as electronic files, and passed on to Marathon personnel for use in building the complete 3D reservoir matrix model.

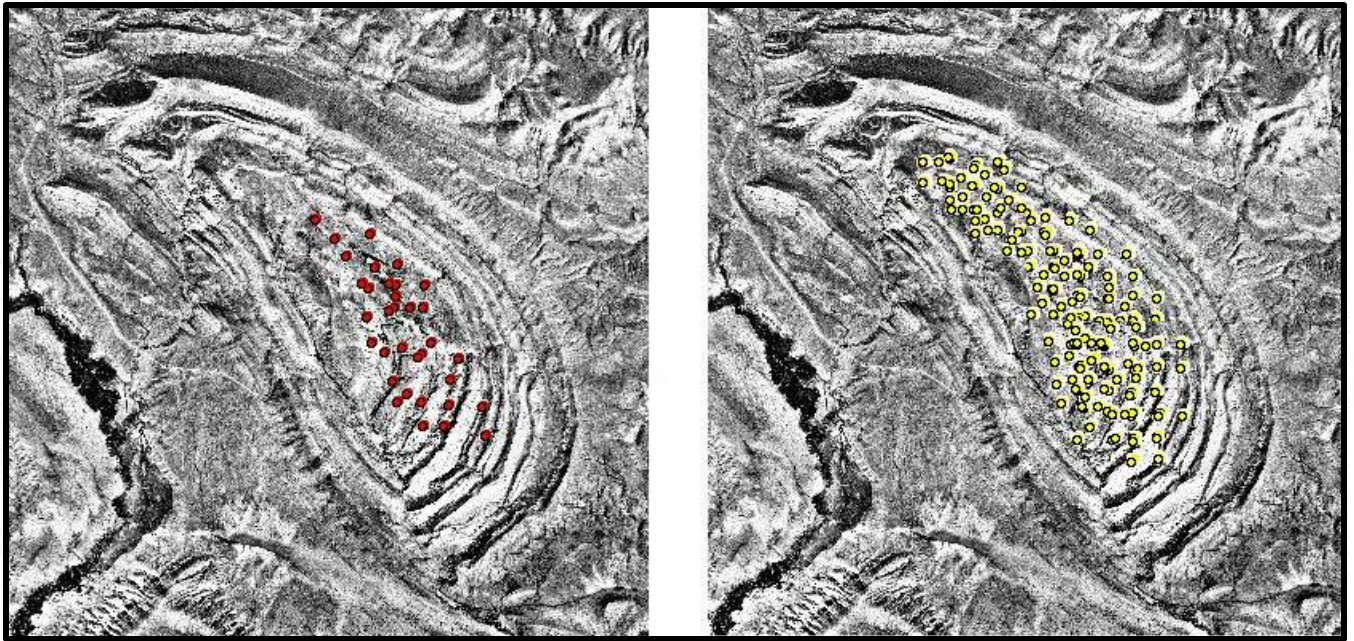


**Figure 3-1. Expansion of matrix property data through re-calibration of older logs. Photograph on left shows wells (red circles) where modern logs had previously made it possible to calculate matrix porosity and oil saturation. Photograph on right shows wells (yellow circles) in which re-calibrated logs were used to estimate matrix properties.**

Retrieval of the data has been facilitated through the project website (<http://www.fracturedreservoirs.com>). Figure 3-2 shows how this may be done:

Circle Ridge Project Data Warehouse

Project Data Warehouse

Please use the map or the drop-down menu below to navigate to the currently available data.  
Note: This interactive webpage uses features that require Internet Explorer 5.5 or higher, or Netscape 6.0 or higher.

Well List

- Layers
- Color
- Scale
- Width
- Height
- Low Res. Well
- Scale
- Color
- Scale
- Width
- Height
- Core Data
- Log Data
- Well Tools
- Stracer
- Team

Low Resolution Well

Select a Well

- SWS0306 61\_02
- SWS0306 61\_04
- SWS0306 61\_06
- SWS0306 61\_08
- SWS0306 61\_10
- SWS0306 61\_12
- SWS0306 61\_14
- SWS0306 61\_16
- SWS0306 61\_18
- SWS0306 61\_20
- SWS0306 61\_22
- SWS0306 61\_24
- SWS0306 61\_26
- SWS0306 61\_28
- SWS0306 61\_30
- SWS0306 61\_32
- SWS0306 61\_34
- SWS0306 61\_36
- SWS0306 61\_38
- SWS0306 61\_40
- SWS0306 61\_42
- SWS0306 61\_44
- SWS0306 61\_46
- SWS0306 61\_48
- SWS0306 61\_50
- SWS0306 61\_52
- SWS0306 61\_54
- SWS0306 61\_56
- SWS0306 61\_58
- SWS0306 61\_60
- SWS0306 61\_62
- SWS0306 61\_64
- SWS0306 61\_66
- SWS0306 61\_68
- SWS0306 61\_70
- SWS0306 61\_72
- SWS0306 61\_74
- SWS0306 61\_76
- SWS0306 61\_78
- SWS0306 61\_80
- SWS0306 61\_82
- SWS0306 61\_84
- SWS0306 61\_86
- SWS0306 61\_88
- SWS0306 61\_90
- SWS0306 61\_92
- SWS0306 61\_94
- SWS0306 61\_96
- SWS0306 61\_98
- SWS0306 62\_00
- SWS0306 62\_02
- SWS0306 62\_04
- SWS0306 62\_06
- SWS0306 62\_08
- SWS0306 62\_10
- SWS0306 62\_12
- SWS0306 62\_14
- SWS0306 62\_16
- SWS0306 62\_18
- SWS0306 62\_20
- SWS0306 62\_22
- SWS0306 62\_24
- SWS0306 62\_26
- SWS0306 62\_28
- SWS0306 62\_30
- SWS0306 62\_32
- SWS0306 62\_34
- SWS0306 62\_36
- SWS0306 62\_38
- SWS0306 62\_40
- SWS0306 62\_42
- SWS0306 62\_44
- SWS0306 62\_46
- SWS0306 62\_48
- SWS0306 62\_50
- SWS0306 62\_52
- SWS0306 62\_54
- SWS0306 62\_56
- SWS0306 62\_58
- SWS0306 62\_60
- SWS0306 62\_62
- SWS0306 62\_64
- SWS0306 62\_66
- SWS0306 62\_68
- SWS0306 62\_70
- SWS0306 62\_72
- SWS0306 62\_74
- SWS0306 62\_76
- SWS0306 62\_78
- SWS0306 62\_80
- SWS0306 62\_82
- SWS0306 62\_84
- SWS0306 62\_86
- SWS0306 62\_88
- SWS0306 62\_90
- SWS0306 62\_92
- SWS0306 62\_94
- SWS0306 62\_96
- SWS0306 62\_98
- SWS0306 63\_00

Download

Use the link below to start downloading the Log Data for SWS0306 62\_98

1. The user selects a well either with the cursor or from the list.

2. Next, the user may download the interpreted wireline data file

3. The file is in zipped format, and when unzipped, displays the log data as ascii text

```

-Variable Information Block
=====
WELL : SWS0306 61_04
WELL : SWS0306 61_04
=====
-Well Information Block
=====
WELL : SWS0306 61_04
WELL : SWS0306 61_04
=====
-Log Data Block
=====
WELL : SWS0306 61_04
WELL : SWS0306 61_04
=====
-Parameter Information Block
=====
WELL : SWS0306 61_04
WELL : SWS0306 61_04
=====

```

DEPTH	RHOB	GR	PHIC	PHIT	PHIC	PHIT
2.0688	735.0000	109.0467	10.3262	57.9320	0.0017	5.3296
2.0531	735.0000	173.4243	10.3264	90.5514	0.0116	5.6077
2.5571	734.0000	233.9731	10.3447	340.4890	0.0194	5.0062
2.4982	734.0000	313.1646	10.3472	205.2794	0.0282	5.6054

Figure 3-2. Use of project website to download interpreted well log data, including matrix porosity and saturations.

First, the user goes to the Data page, which contains the photograph of the Circle Ridge Field. Next, the user selects “Low Res Wells” and the web page then displays the yellow circles that are situated at the surface locations of the wells. An individual well may be selected graphically on the display using the cursor, or from the list. Double clicking on a well allows the user to open or download the well file.

### 3.3 Fault Block Reconstructions

The fault-block reconstructions were used for two different purposes in building the reservoir model. The first use was to develop a much-improved model of the geometry of the major faults in the field, particularly at depth where previous work had left many uncertainties. The second use was to provide a quantitative understanding of the deformation/strain history of the field, in order to determine if the present day fracture pattern could be related to one or more deformation events, and then to use that relation to condition the reservoir-scale fracture orientations and intensity variations in the final 3D reservoir model. Figure 3-3 shows the goal of the fault block reconstruction. The reconstruction began with making a preliminary model of the fault surfaces and key reservoir horizons in the field.

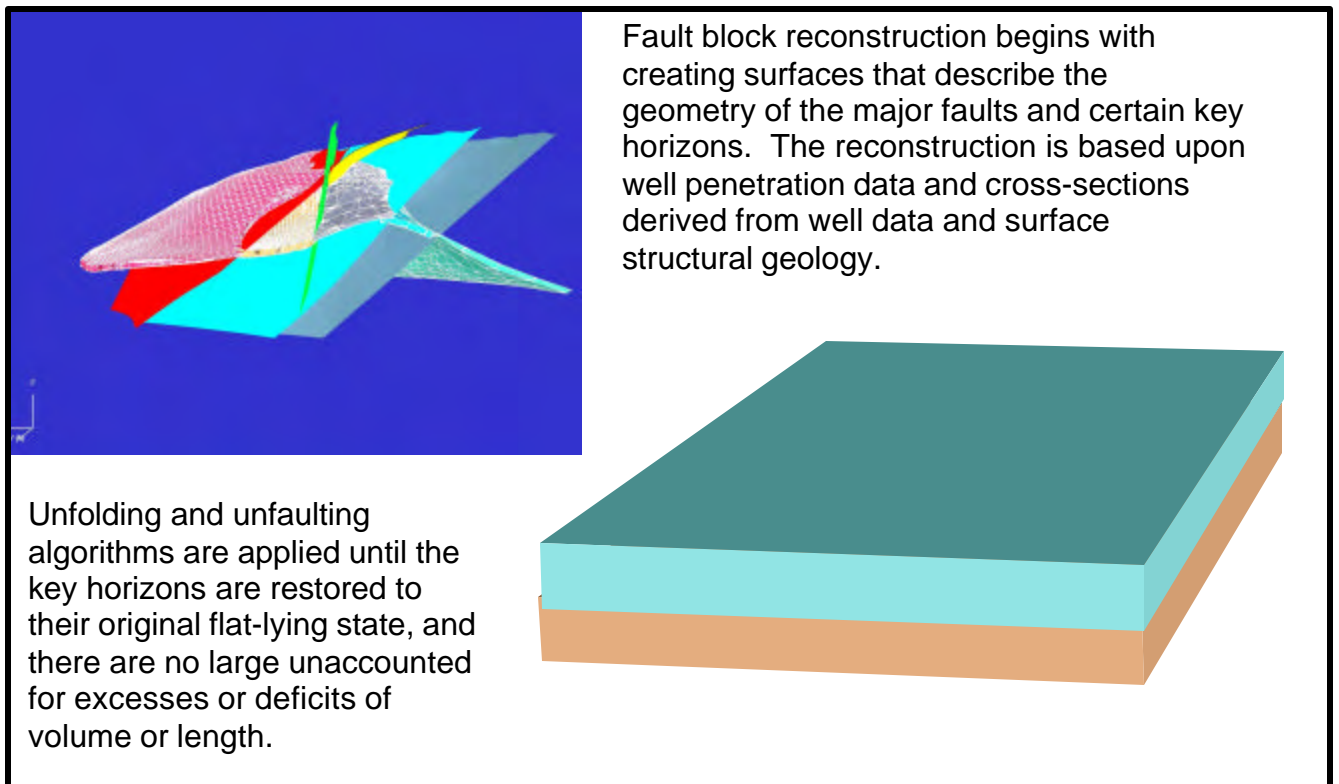


Figure 3-3. Determining fault block geometry through a 3D balanced reconstruction.



**Figure 3-4. The field mapping team for the cross-section and fracture data collection. From left to right: Paul La Pointe (Golder); Jan Hermanson (Golder); Sherry Blackburn (enrolled member of the Northern Arapaho Tribe & Marathon Oil intern).**



**Figure 3-5. The cross sections were mapped using GPS locations of contacts. The sections were anchored to benchmarks (like the one shown in the photo) and routed through or very near to wells in key areas of the fields.**

The fault surfaces and horizon surfaces were created through reconstructions from well penetrations and surface structural mapping (Figure 3-4 and Figure 3-5) in locations chosen to gain additional structural control in key areas.

### 3.3.1.1 Faults

Faulting observed on the surface are of two types: reverse faults and strike-slip faults (both synthetic and antithetic). Minor normal faults have also been observed, mainly at high angles to the main anticline (Figure 3-6). A few large faults dominate the geology of the Circle Ridge field. Below follows a brief description of each larger fault.



**Figure 3-6 Example of minor normal and strike slip faults in the northeastern corner of the field. Gypsum Springs is offset in several sections by less than 20 ft.**

#### 3.3.1.1.1 Red Gully Fault

The Red Gully Fault forms the main thrust through Circle Ridge. Anderson and O'Connell (1993) report that the reverse Red Gully Fault has a surface displacement of at least 1000 feet (305 m) along the western side of the central Dinwoody/Phosphoria hill in the core of the anticline. It juxtaposes Permian Phosphoria over Triassic Red Peak shales and sands that are overturned and dipping 50 degrees towards the east. The Fault is also observed in the north end of the anticline, offsetting Popo Agie and Nugget (Figure 3-7). It is not observed above Gypsum Springs. Quaternary alluvium conceals much of the central portions of this fault but its location is known from several well bores. Several splay structures relate to the Red Gully Fault; i.e. the Yellow Flats, Blue Draw and Gray Wash faults.

#### 3.3.1.1.2 Green Valley Fault

The reverse Green Valley Fault is possibly a direct splay to the Red Gully Thrust. The fault is observed east of the northern part of the Red Gully fault, and offsets Popo Agie and Gypsum Springs (Figure 3-7). Beautiful examples of imbricated Popo Agie show the intense deformation along this fault. The displacement is in the same order as the Red Gully Fault. The fault dies out in the Sundance Formation, with several small folds to accommodate the movement.



**Figure 3-7 Photograph showing the Green Valley Fault offset in the Gypsum Springs and the Popo Agie where finger is pointing. The Red Gully Fault runs through the larger gap in the Popo Agie member below the hand.**

#### 3.3.1.1.3 Orange Canyon Fault

The orange Canyon fault is a right lateral strike-slip fault with an additional normal fault component. The fault runs through a NE-SW trending drainage canyon in the northern part of the field that exposes orange sands and silts of the Popo Agie member. It is observed in all formations down to Gypsum Springs. This fault is possibly connected to the Blue Draw fault.

#### 3.3.1.1.4 Blue Draw Fault

This is a reverse fault in the extreme northern end of the anticlinal structure and in the Blue Draw, which is the strike valley formed on Mowry shales north of Circle Ridge. As mapped it cuts through the Mowry – Muddy – Thermopolis section, the Rusty Beds and Morrison, then dies out toward the southeast within Sundance failing to offset basal Sundance limestones or the Gypsum Springs.



**Figure 3-8 View down the Orange Canyon with Red Peak shales and sands to the left and Gypsum Springs to the right.**

#### 3.3.1.1.5 Other Subthrust Faults

The Subthrust Block (footwall block of the Red Gully Fault) consists of several sub-blocks divided by the Blue Draw Fault, Gray Wash Fault, Purple Sage Fault, and Yellow Flats Fault that compartmentalize the reservoirs. The Blue Draw Fault (as explained above), like the Red Gully Fault, has surface exposure while the others are recognized only from well top data.

However, these subthrust faults play an important role in the sequence of restoration of the Circle Ridge structure as will be explained below

#### 3.3.1.2 *Fault blocks*

The Anderson Model contains sixteen fault blocks according to the original interpretation. However, seven of these blocks are very small or do not involve the producing formations at depth, i.e. Phosphoria, Tensleep and Amsden formations. The following fault blocks have been included in the palinspastic reconstructions; Block 1, 6, 8, 9, 11, 12, 14, 15 and block 16 as illustrated in Figure 3-9.

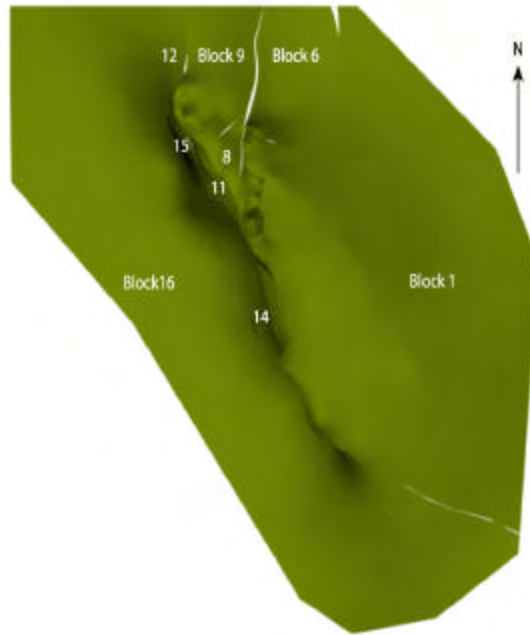


**Figure 3-9 Top view of the location of major fault blocks in the Phosphoria formation.**

The surfaces of most formations of the Anderson Model are complex and exhibit dramatic undulating geometries to honor all well information. The interpreted extensions of surfaces between wells are questionable many times when wells at close distance have tops with large differences in elevation. As the undulations occur mostly in the northern end of the reservoir where faulting is most intense, it is more likely that the elevation differences are due to minor fault movements between wells. However, these small faults are too minor to be included into the reservoir scale model.

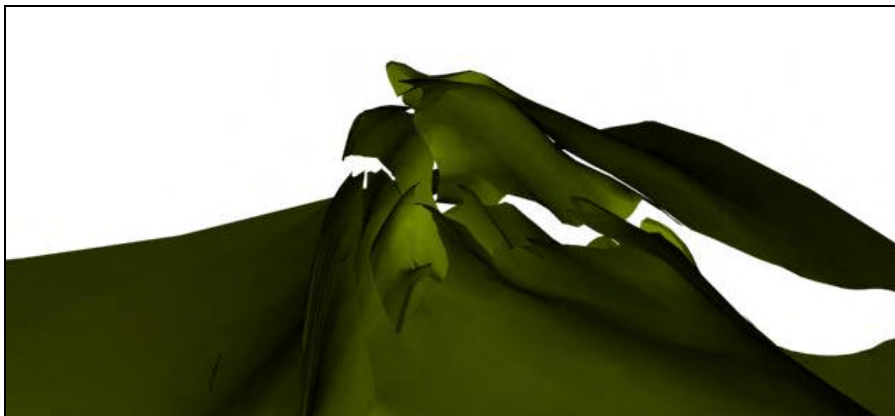


**Figure 3-10 Illustration of the undulating extension of the top of the Phosphoria formation. The undulation of the surface is controlled by well top information from the Anderson and O'Connell database.**

### 3.3.1.3 Observations in the field: Update of fault extensions

The field work during the summer of 2000 updated the extension of some of the faults in the Anderson Model. The Anderson and O'Connell (1993) extension of The Red Gully Fault up into the northern part of the field is questionable from observations in the field. Tracing the extension of both the Green Valley Fault and the Red Gully Fault suggests that the main plane of movement could be accommodated along the Green Valley Fault and not along the northern part of the Red Gully Fault. Observations of the well top information does not reject this interpretation, but shows that the Green Valley Fault needs to have a steeper inclination than the Red Gully Fault.

Based on the 3D extensions it seems plausible that the Red Gully continues as Anderson and O'Connell have proposed but that the Green Valley Fault is interpreted as an imbricate to the Red Gully Fault. This interpretation fits very well with Anderson and O'Connell's interpretation that the Circle Ridge structure is a fault propagation fold. The steeper angle of the Green Valley Fault is also supported by the mechanisms of fault propagating folds as proposed by Mitra (1990) where shortening of lower units during the propagation produces high angle fold hinge planes and faults above the basement fault.

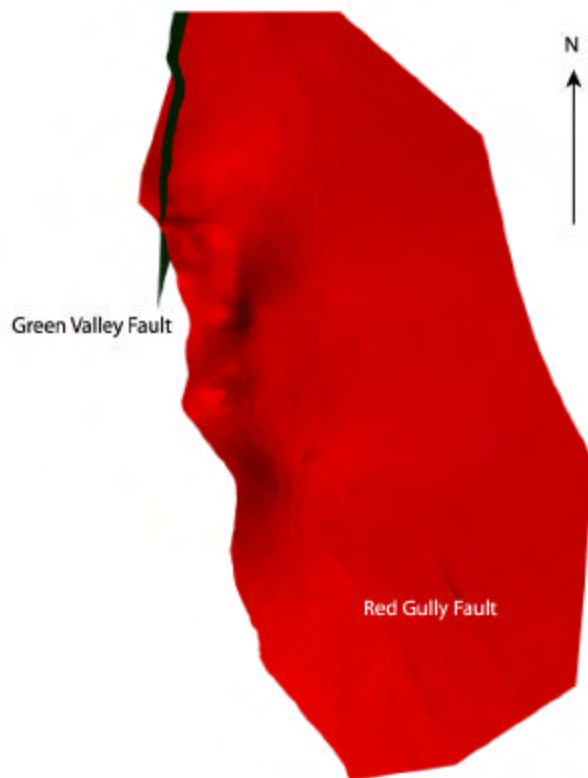


**Figure 3-11 3D Illustration of the extension of the Red Gully Fault and the Green Valley Fault based on the well tops and the surface geology. The intersection between the two shows that the Green Valley Fault needs to be steeper than the Red Gully Fault in order to honor the well top data.**

The original 3D interpretation of the Orange Canyon Fault extends in a bow like shape below the Circle Ridge structure (Figure 3-12). This interpretation has no basis in the well top data and does not show up in outcrops. The Orange Canyon Fault can only be observed in one location, running parallel to the Orange Canyon and in a few well tops. The orientation of the fault from field observations does not indicate any curvature at depth, nor does well intersections. This interpretation is therefore re-evaluated in such a way that the fault extension stops just below the last known intersection point in the wells and is indicated as a red line on the fault surface in Figure 3-12.

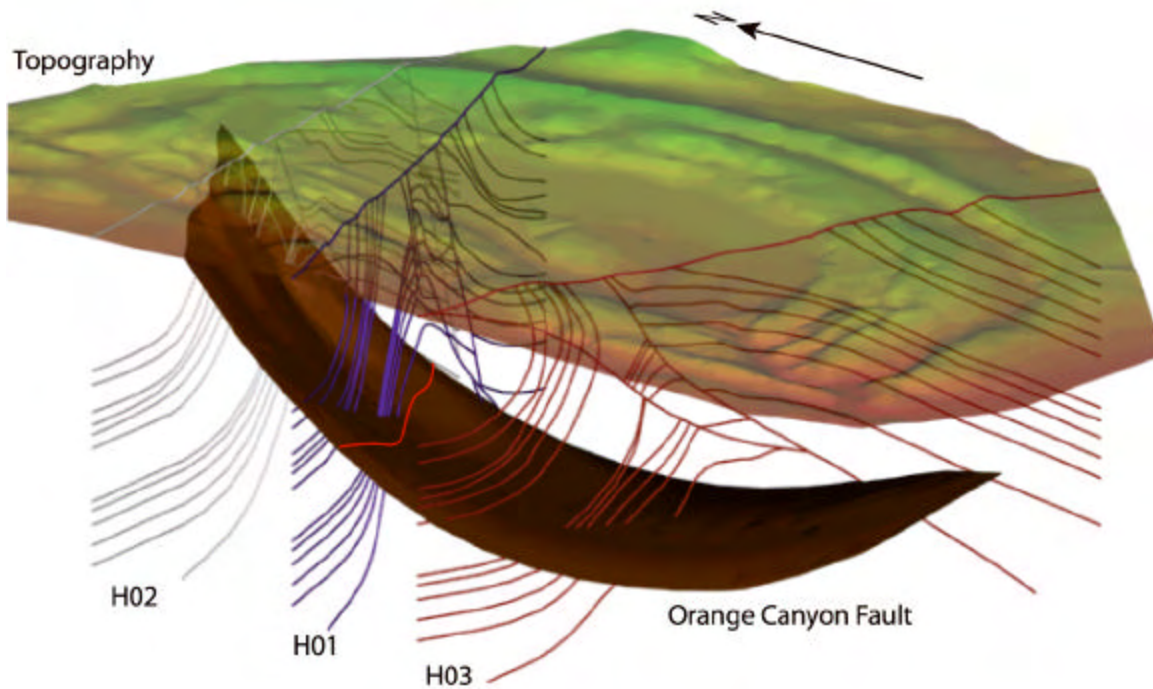


**Figure 3-12 Illustration of the original extension of the Orange Canyon Fault in a bow shape below the Circle Ridge structure. This extension has no basis in well top information and has been excluded in the restoration process. The red line on the fault surface indicates where the new interpretation ends. Cross-sections are shown for a better 3D understanding of the extension of the fault.**

The Anderson and O'Connell (1993) study produced a number of cross-sections out of which two were balanced (P-P' and T-T') and published (Figure 3-13). The background material for their study also contained another cross-section (Z-Z') in the complex northern part of the block that was initially used in the interpretation the Circle Ridge structure. However, it was soon discovered that the interpretation of the northern part of the field needed to be revisited and re-evaluated and this cross-section was not used further.

The field campaign from the summer of 2000 produced three new cross-sections (Figure 3-13), two from the northern part of the field (H01-H01' and H02-H02') and one E-W trending section through the southern most productive part of the field (H03-H03'). These sections were complemented with subsurface information from nearby wells and coupled to the 3D interpretation of the formation surfaces.

The new cross-sections have been incorporated and balanced together with the 3D palinspastic reconstruction of the whole model. However, if scrutinized in detail each of the H01 to H03 cross-sections contain fault movements of layers above the Phosphoria Formation that do not entirely balance. This is partly due to lack of surface (formation extension) control and as a result, have not been used in the balancing of the model. Only Phosphoria, Tensleep and Amsden Formations have been used in the reconstruction work as will be explained below.

All cross-sections that were used are presented in Figure 3-14 through Figure 3-18.

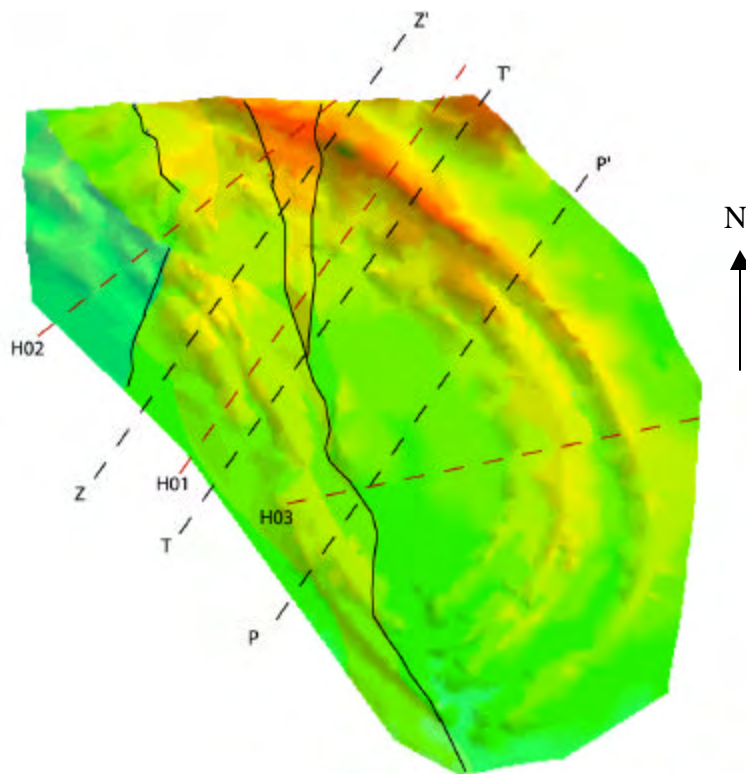


Figure 3-13 The location of the Anderson and O'Connell cross-sections (P-P', T-T' and Z-Z') and the new cross-sections assembled during the 2000 summer field campaign (H01 to H03). The black lines represent the main fault traces of the Red Gully, Green Valley, Orange Canyon and Blue Draw faults.

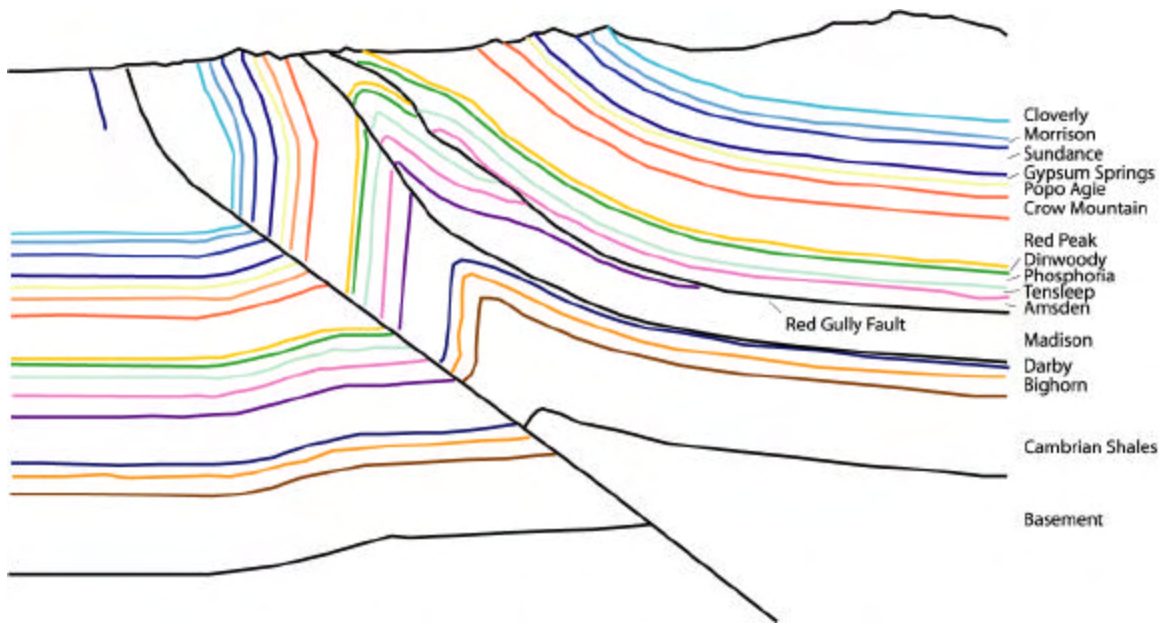


Figure 3-14 Cross-section P to P' after Anderson and O'Connell (1993)

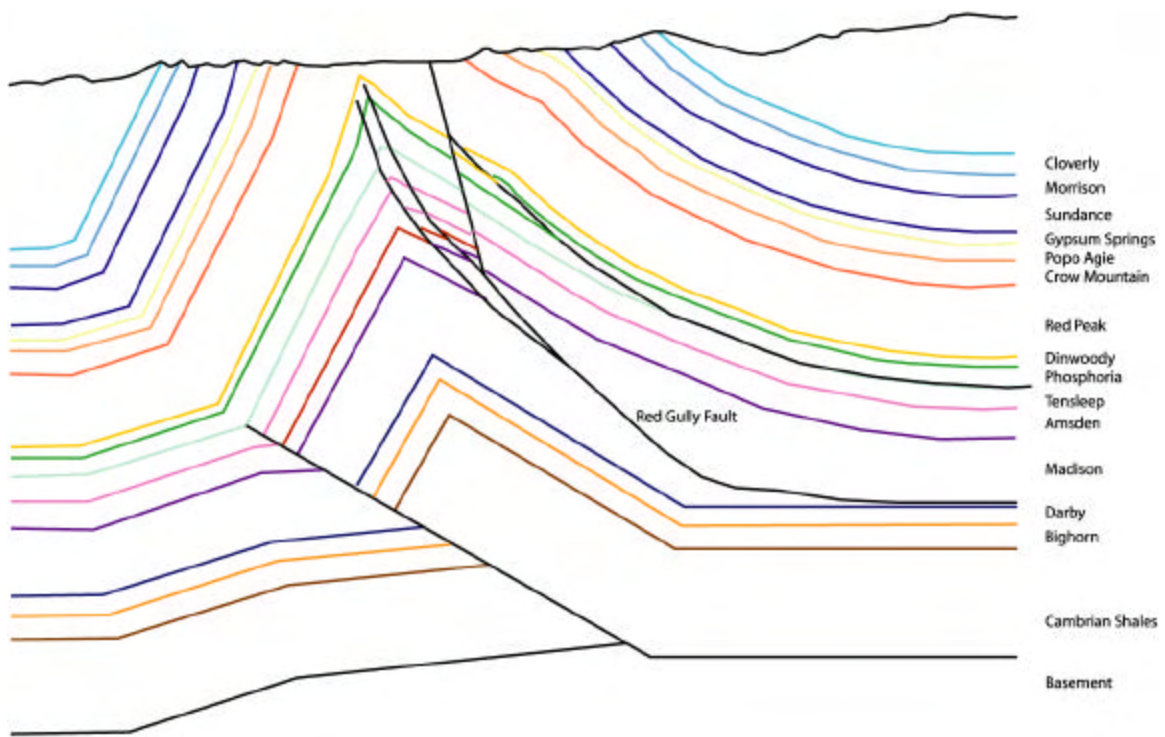


Figure 3-15 Cross-section T to T' after Anderson and O'Connell (1993)

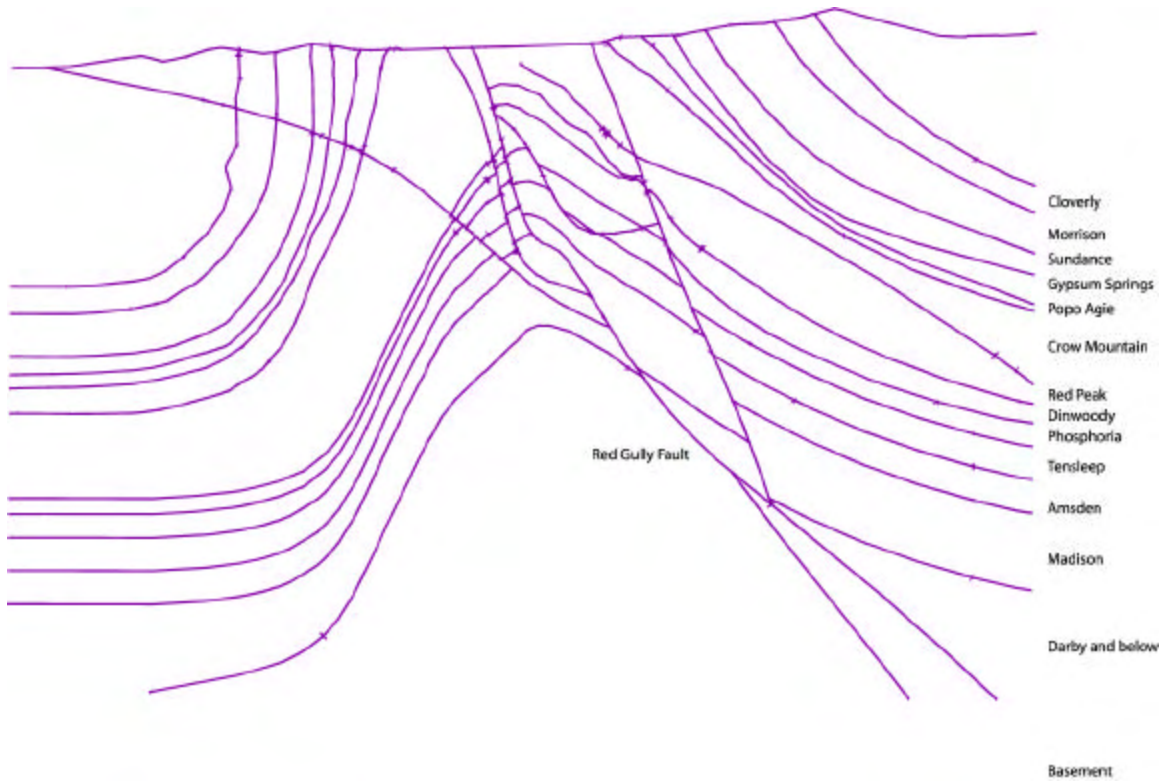


Figure 3-16 The H01-H01' cross-section

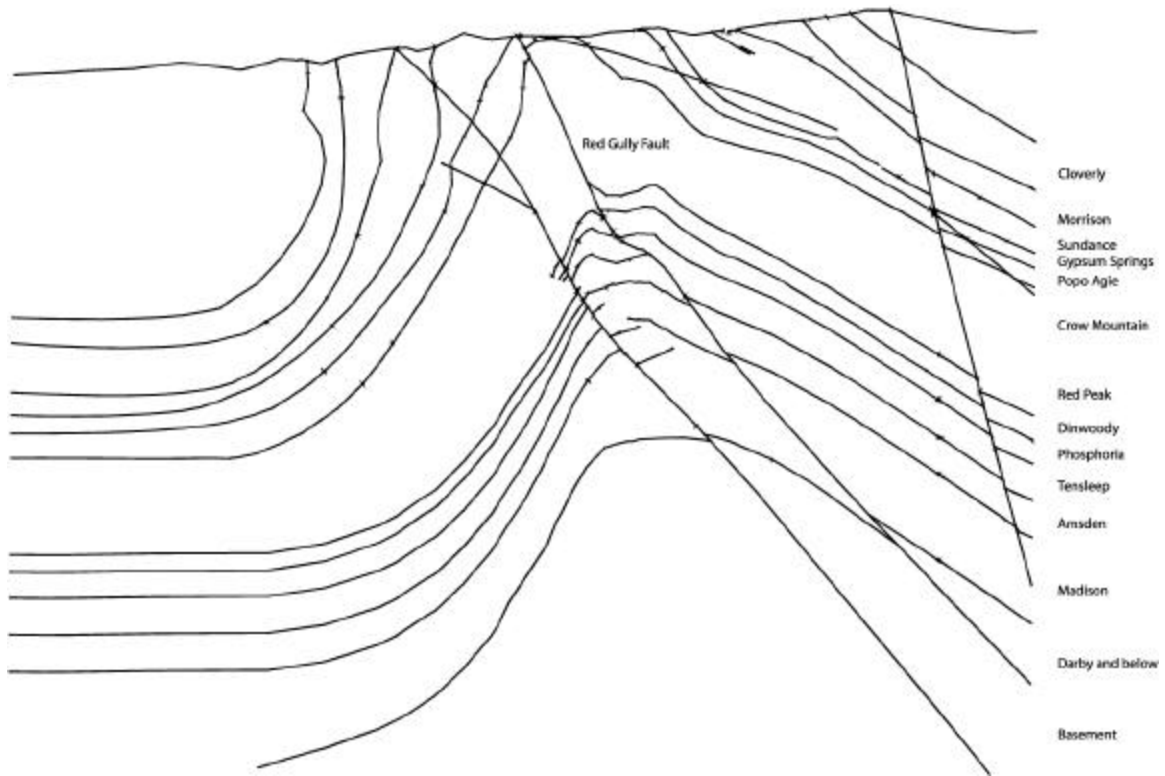
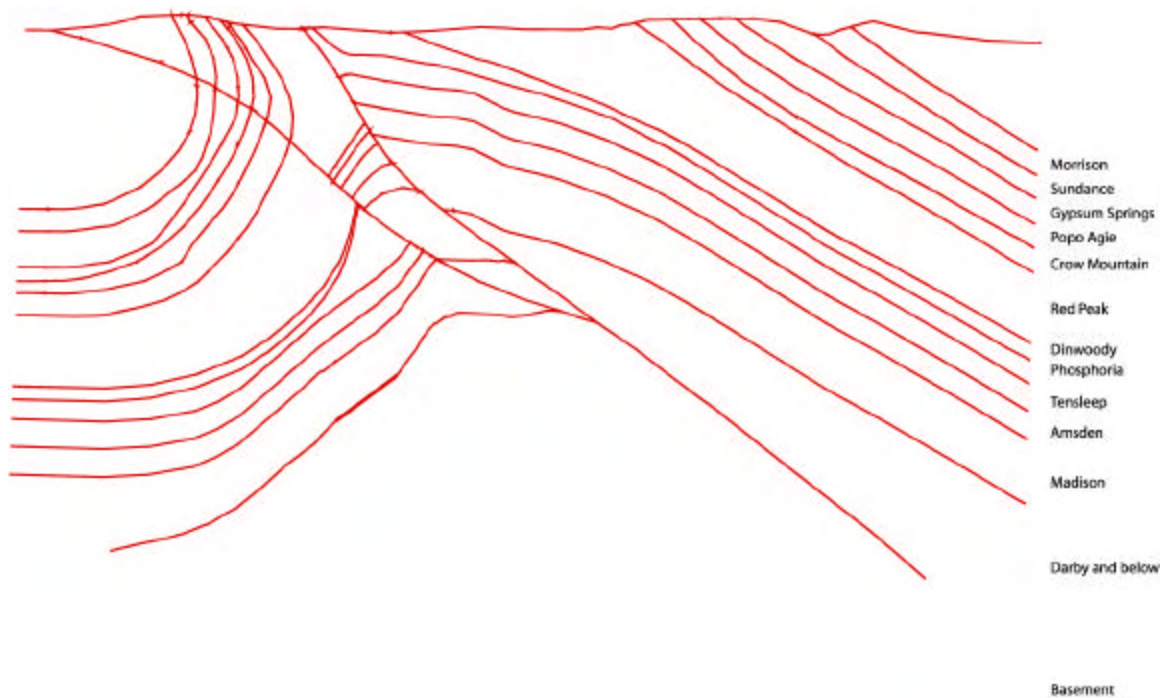


Figure 3-17 The H02-H02' cross-section



**Figure 3-18 The H03-H03' cross-section**

These cross-sections were then used to create the fault and lithologic surfaces for the 3D palinspastic reconstruction.

Figure 3-19 shows the top of the reservoir units and the major faults (with the exception of the Orange Canyon Fault, which is hidden in this perspective view).

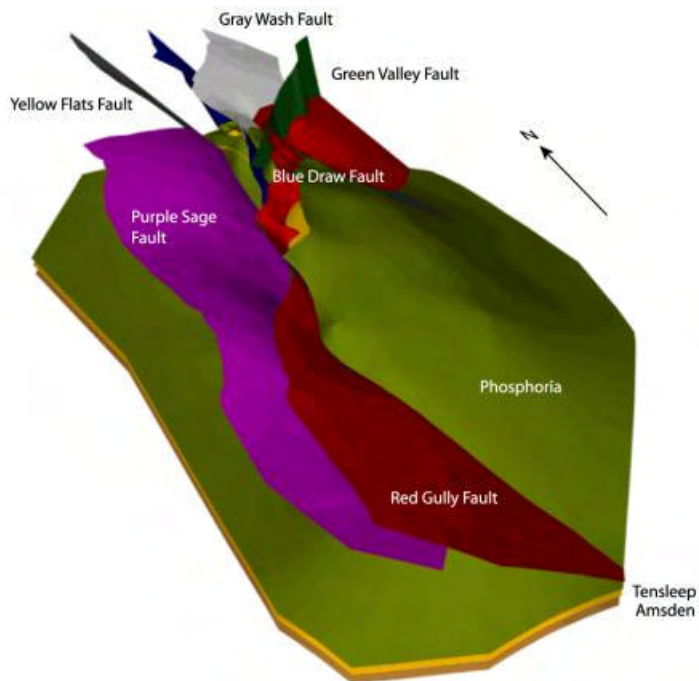


**Figure 3-19. Fault reconstructions for the Circle Ridge Field.**

### **3.4 Validation of Cross Sections Using Retrodeformation Software**

#### **3.4.1 OVERVIEW**

The validation of the cross sections was accomplished through balancing then according to the experimental methods outlined in Section 2 of this report. It is important to note that, while many Formations are depicted in the cross-sections, the balancing focused only on the three most important reservoir units: the Amsden, Tensleep and Phosphoria Formations. Other units have not been subjected to balancing requirements; their deformation is calculated by allowing them to deform passively according to the deformation of the three key reservoir units.

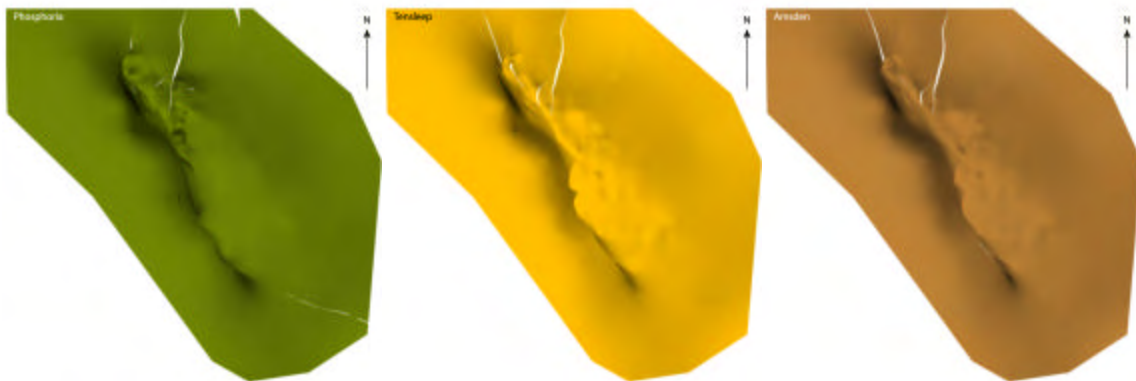


**Figure 3-20 The Phosphoria, Tensleep and Amsden formation top surfaces**

The palinspastic reconstructions of the Circle Ridge structure have been constrained only by the Phosphoria, Tensleep and Amsden Formations due to three reasons;

1. The complexity of the reconstruction is minimized with limited amounts of formations involved
2. The computer resources limits the number of geometric elements that can be involved in the restoration process
3. These three formations contribute 95% of the production.

The three chosen formations have been reconstructed down to its pre-deformations state with the following assumptions;

- The formations were deposited horizontally throughout the field
- The sedimentary deposition was completed by the time of the folding and faulting deformation events

These two assumptions are supported by the background geological history as presented in Section 1.2.

### 3.4.2 IMPLICATIONS OF RESTORING THE GEOLOGICAL MODEL

The calculation of retro-deformation during the reconstruction requires that each polygon of the geometric representation of the surface or volume are tracked. The number of polygons directly effects the processing time of the strain calculations and is thus a major constraint in the restoration process. In the original Anderson Model, as represented by Smith (2000), the Phosphoria surface contains about 12000 polygonal elements. The polygonal surfaces are irregular, with most of the polygons along the borders of the surfaces (Figure 3-21), making unnecessarily complex surfaces, which will slow down strain calculations.



**Figure 3-21 Close-up of the polygons of fault blocks 6 and 9 on the Phosphoria surface as defined by Smith (2000).**

Further, the interpreted extension between wells of the chosen formations results in surfaces with very complicated undulations. The reasons for the undulations may be due to:

- Limited surface control due to few well tops
- Minor scale faulting between wells
- Variable thickness of the units
- Poor knowledge of exact depth of tops in old wells

To achieve a good understanding of the large-scale strain pattern and how this affects the formation of the fracture network in the reservoir, it is important to minimize the effect of anomalous strains generated by unknown small-scale undulations of the formation surfaces. Each formation surface has therefore been smoothed to minimize the

undulations, but also to minimize the potential deviation from the actual well top data. The smoothing process is also performed in conjunction with making a more regular grid of each formation surface by using the method of resampling of the grid. The Resample algorithm used in 3D Move, when decreasing data density, uses a grid (oriented parallel to the regional plane of the surface). The resampling methodology seeks to:

- **Maintain volume:** Resampling attempts to maintain the volume between the resampled surface and a datum. In attempting to maintain the volume the overall shape of the surface is maintained, though local shape changes will occur.
- **Minimize lateral spreading:** In the down sampling mode, the boundary of a resampled surface may spread laterally, as can be seen if a resampled surface's edges are compared to the original surface edges.

The end result of the resampling exercise is a regular grip with fewer polygons that is smoother and exhibits less undulation than the original surfaces.

### 3.4.3 CREATION OF POLYGONAL VOLUMES

To be able to calculate all three principal components of strain during retro-deformation, it is necessary to create volumes between the formation top surfaces. The volumes are created by populating the space between the surfaces with polygonal elements. All three principal axes of strain is recorded in each polygonal element during the restoration process.

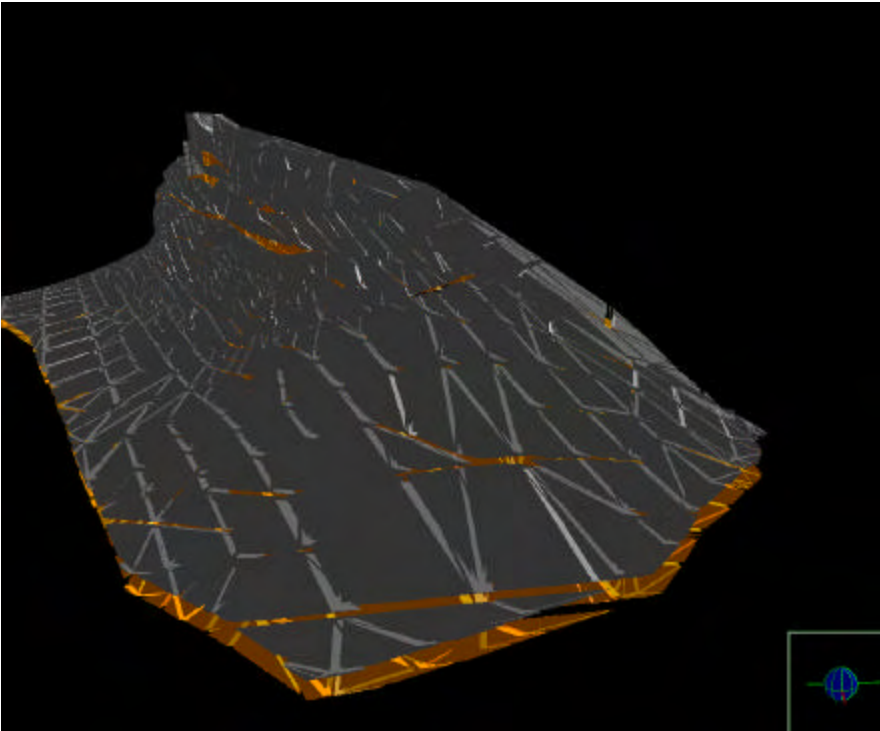


**Figure 3-22 Phosphoria and Tensleep volume elements**

#### 3.4.4 RESTORING FAULTS AND THRUSTS

The faulting and thrusting sequence of Circle Ridge has been suggested by Anderson and O'Connell (1993) to start with the movement of the Gray Wash fault that is the lowest structurally. This initial faulting occurred subsequent to most of the folding found at the Circle Ridge anticline. Upon encountering some obstacle or reaching the stress limit of strain release, the stress field then broke higher in the sequence, creating the Blue Draw Fault. Towards the south both these faults merge into the Red Gully Fault system, which at this time continued to move along an earlier established thrust plane. The imbrication process in the northern end of the field is repeated once again with the formation of the Yellow Flats fault higher in the section. The final thrust displacement was focused on the Red Gully Fault that is structurally highest.

The Orange Canyon Fault obliquely cuts all these faults and was formed last of the great faults through the Circle Ridge anticline.

The palinspastic fault reconstruction was performed in the reverse order, restoring the fault movements fault by fault back to the unfaulted anticline.

The chosen process for fault movements was Fault Parallel Flow.

The Fault Parallel Flow process was performed on the Tensleep Formation, with all other formations following passively. This approach helps showing whether interpretations of the surface extensions are valid, or if other processes have to be involved in order to restore each hanging wall unit back to its matching level on the footwall.

The Tensleep Formation was chosen as the main restoration surface because of its relative competence compared to the more shaly and limestone rich formations of Phosphoria and Amsden and because its location in the middle of the restored pack of surfaces.

The unfaulted Tensleep Formation is illustrated in Figure 3-23. The recorded strain during the restoration is saved incrementally in each grid cell, both in the surfaces and in the volumes.

#### 3.4.5 RESTORING THE INITIAL FOLD STRUCTURE

The initial folding of the Circle Ridge anticline is restored back to its flat depositional state using two different methods: Vertical Shear Unfolding and Flexural Slip Unfolding.

The accumulated strain is recorded for each type of restoration and plotted on to of each formation surface after deformation, as illustrated in Figure 3-24.

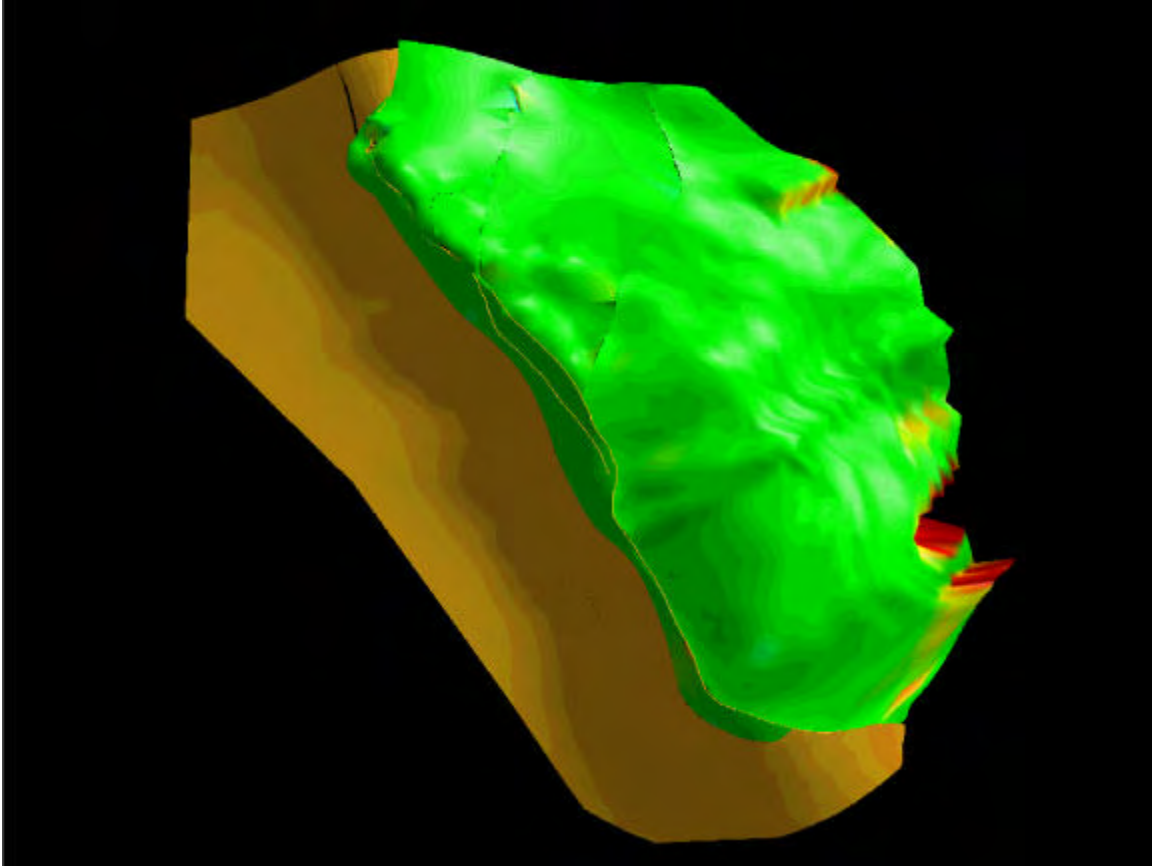


**Figure 3-23 Illustration of the unfaulted Tensleep formation showing fault blocks 1, 6, 8, 9, 11 and 14 in green color as part of the overthrust and the top of the anticline.**

The result of the Flexural slip unfolding shows that parts of the anticline still exhibit small-scale undulations that cannot be attributed to the main anticline folding. The perturbations on the surface reflects the fact that other smaller events has occurred, like smaller folds or minor faults which has not been part of the model. The important pattern to be distinguished is the highly deformed green-red band in the overturned limb of the anticline (left in Figure 3-24). Further, it is anticipated that the previously interpreted major fault block 1 (overthrust) are problematic to restore without generating large strains in bands across the block. This might suggest that there are other faults in this unit which have not been part of the model.

The Vertical Shear Unfolding results are illustrated in Figure 3-25, Figure 3-26 and Figure 3-27 for the Tensleep, Phosphoria and Amsden Formations, respectively. The accumulated strain pattern shown in these illustrations are similar to that of using Flexural Slip Unfolding.

It is also possible to see the mismatches between fault blocks on the two formations that have been restored passively together with the Tensleep formation. These mismatches indicate that the interpretations of the fault blocks are not perfect. The reasons for the mismatches can be due to:

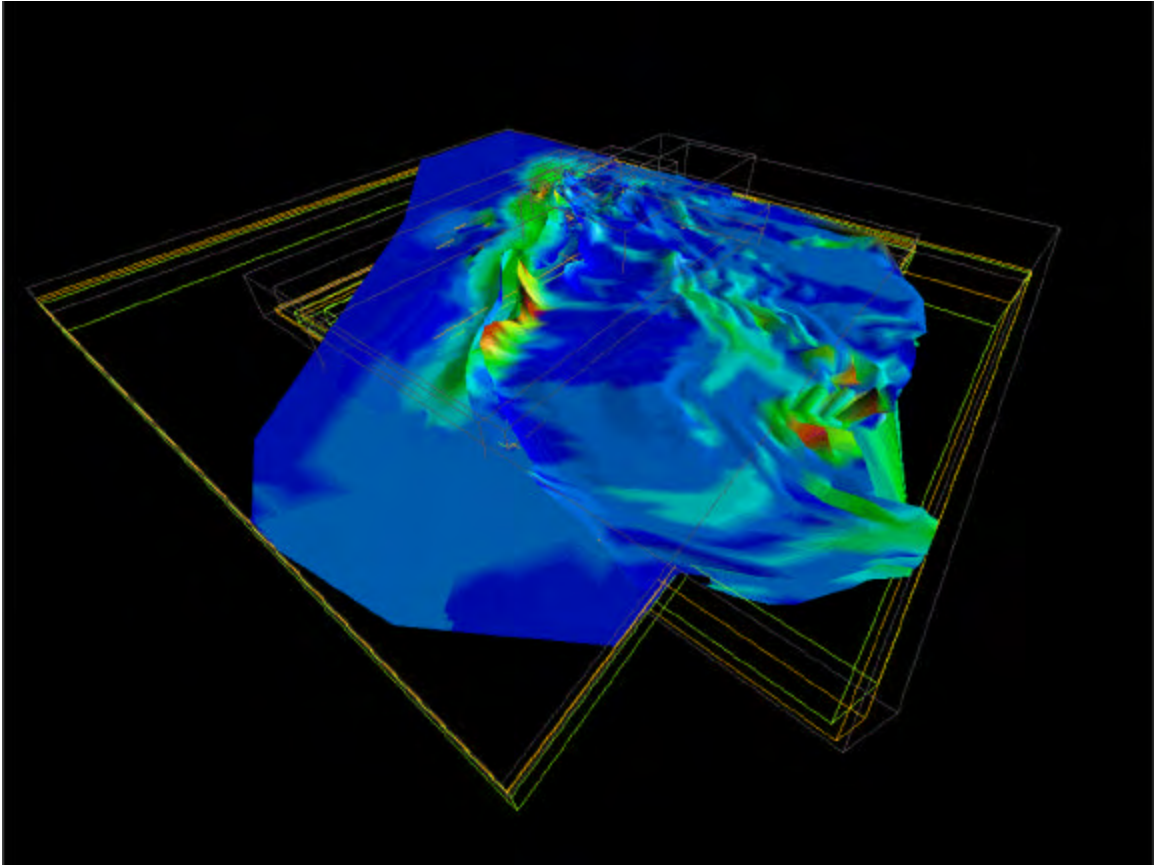


**Figure 3-24 Completely restored Tensleep formation using Flexural Slip Unfolding. The color map reflect the amount of accumulated strain throughout the restoration process where blue colors are lowest recorded strains and the red are the highest.**

1. volume changes in the formations during deformation have not been considered
2. the shape of the faults are different
3. the shape of the fault blocks are different
4. the extension of the surfaces between the well tops are different
5. the restorations processes requires more steps to restore minor structures like small faults or small scale folding
6. the thickness of the layers are not constant
7. the original depositional environment may not be planar

However, the mismatches are comparatively small and are interpreted to be of a minor effect to the understanding of the overall strain pattern of the Circle Ridge anticline. Most of the Strains are accumulated in the overturned limb that is exactly what to expect in a structure like this. The most interesting feature of the reconstructions is the accumulation of strain in the central part of fault block 1 which contains the most productive wells in Circle Ridge today. This is a likely place for a relatively higher intensity of fracturing, which seems to be reflected in the production history of the field.

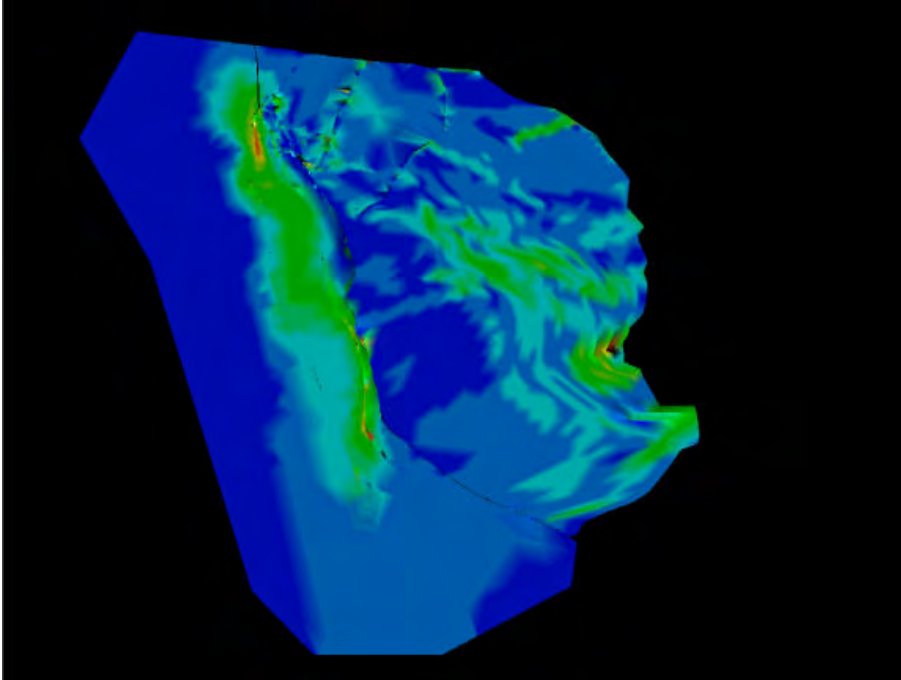


**Figure 3-25 Vertical Shear Unfolding of the unfaulted Tensleep formation (top view). The color map shows the accumulated strain, with blue colors showing the lowest recorded strains and the red colors the highest.**

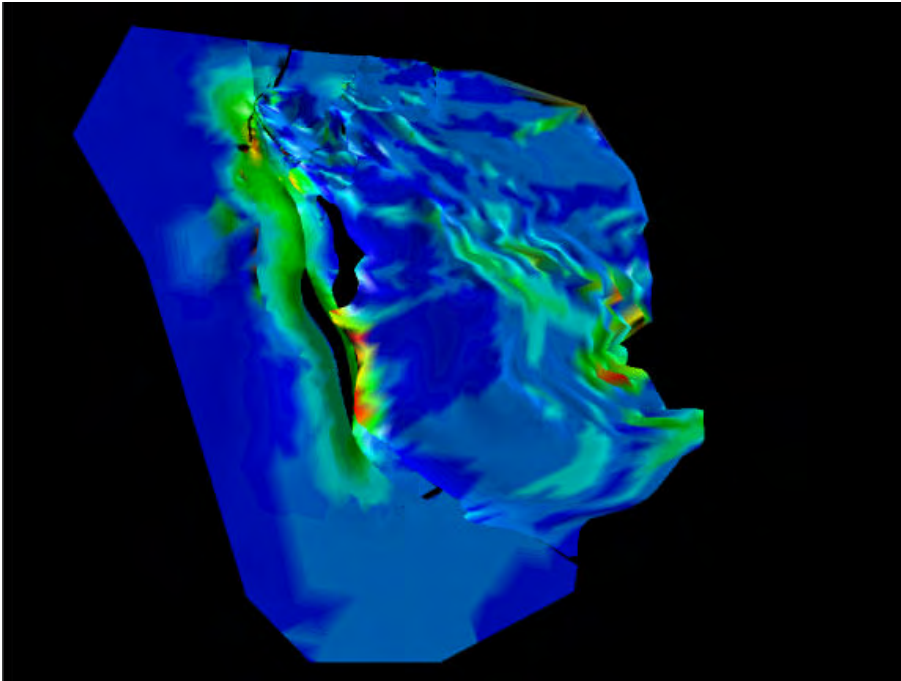


**Figure 3-26 Vertical Shear Unfolding of the unfaulted Phosphoria formation (top view). The color map shows the accumulated strain, with blue colors showing the lowest recorded strains and the red colors the highest.**

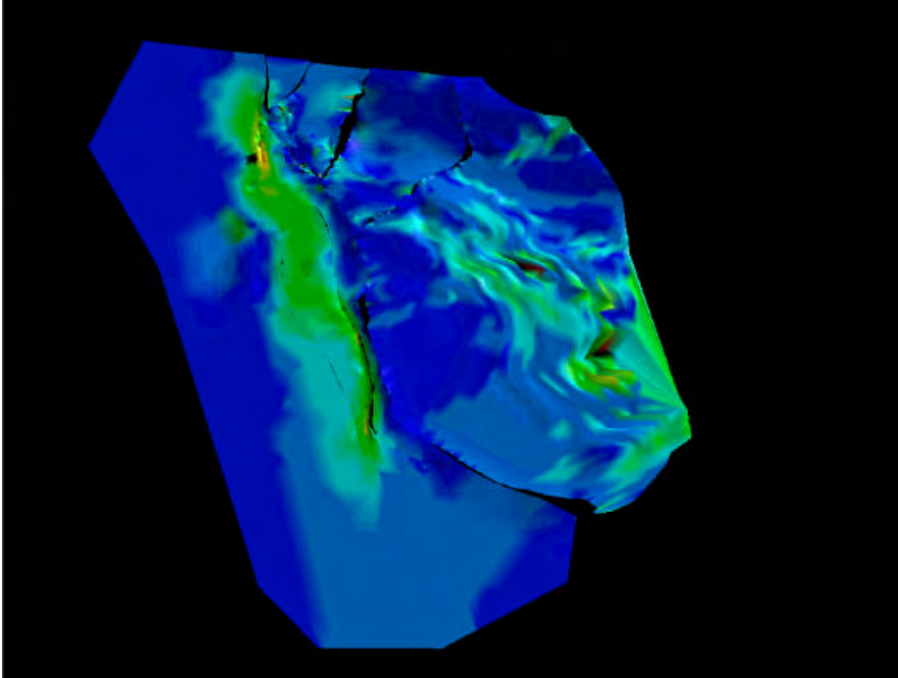


Figure 3-27 Vertical Shear Unfolding of the unfaulted Amsden formation (top view). The color map shows the accumulated strain, with blue colors showing the lowest recorded strains and the red colors the highest.

## 3.5 Geological Controls on Fracture Development in the Reservoir

### 3.5.1 FIELD DATA COLLECTION & ANALYSIS

Eleven sites were analyzed in the Crow Mountain and Red Peak Members to obtain fracture data in areas where the structural deformation should have produced fracture patterns with different orientations and intensity. The goal was to compare these variations in orientation and intensity to the strain field calculated from the 3D palinspastic reconstruction, to determine what deformation events controlled fracture development. The model developed from the scanline data was then tested and refined using subsurface data (Section 3.5.2).

#### 3.5.1.1 Sets & orientations

The orientation and number of fracture sets has been determined for all of the scanline sites, and results summarized in Figure 3-28 through Figure 3-37.

Many of the stereoplots show fracture sets, that when rotated relative to bedding, plot as pole concentrations at the top and bottom of the plot (indicating a fracture set orthogonal to bedding and striking parallel to bedding dip), or on the left and right sides (indicating a fracture set orthogonal to bedding and striking parallel to bedding). These fracture sets are evident in the plots for Scanlines 4,5,6,7,8,9 and possibly 11. The fracturing extant at Scanlines 1,2 and 3 differ. Scanlines 1 and 2 are similar in that they show evidence for a

set orthogonal to bedding, but the strikes are at substantial angles from the strike and dip of the bedding. The fracturing at Scanline 3 differs the most: the one set present is neither orthogonal nor parallel to bedding, nor does its strike appear to be related in any way to bedding strike or dip.

Scanlines 1 and 2 are also in a more highly faulted and folded area of the Field. These two scanlines are located in the area where the Red Gully Fault cuts the section, and also where the anticline is more tightly folded. Scanline 3 is located in the nose of the tightly folded northwesterly part of the anticline, and so also may have a more complex strain history. The other scanline sites, particularly sites 5 through 9, are located along the eastern and northern flanks of the anticline where there is little large-scale faulting and folding is much more gentle and regular. Scanline sites 10 and 11 are near the southeastern end of the Red Gully Fault, in the subthrust portion to the southwest, and although not as tightly folded as the rock in the vicinity of scanlines 1-3, still may be in an area of increased strain.

The results of these stereoplots suggest that at least some of the fracturing is probably due to the strain produced by the folding that created the anticline. In regions where the folding is tighter and major faulting occurs, there may be additional fracture sets.

### *3.5.1.2 Fracture intensity*

Fracture intensity is another important component in building the discrete fracture reservoir model. Fracture intensity was studied at each of the scanline sites.

One of the goals of these analyses was to establish whether there is a single intensity value that characterizes fracturing at each site, whether for all scales or only for scales above a certain minimum size. This latter case is what is often termed a Representative Elementary Volume, or REV. At the scale of the REV or at larger scales, parameter values do not change with the scale. At scales below the REV scale, parameter values show scale dependence.

The scaling properties of intensity are studied through the Mass fractal dimension. Mass dimension for scanline fracture data can vary between 0.0 and 1.0. A value of 1.0 indicates scale independence for intensity, so if a mass dimension plot has a slope approaching 1.0 for all or a threshold scale, then it is behaving as an REV. Values appreciably less than 1.0 indicate scale dependence for fracture intensity.

The mass dimension plots (Figure 3-38 and Figure 3-39) that, with the exception of Scanline 5, the slope of the mass dimension plot approaches 1.0 for scales 3 m and greater for all scanline sites. This indicates that, while fracture intensity shows some scale dependence for scales smaller than a few meters, intensity in the direction parallel to bedding behaves in a scale-independent fashion for scales greater than a few meters. Fracturing measured at Scanline 5 shows significant scale dependence up to the largest scale that could be measured – 10 m.

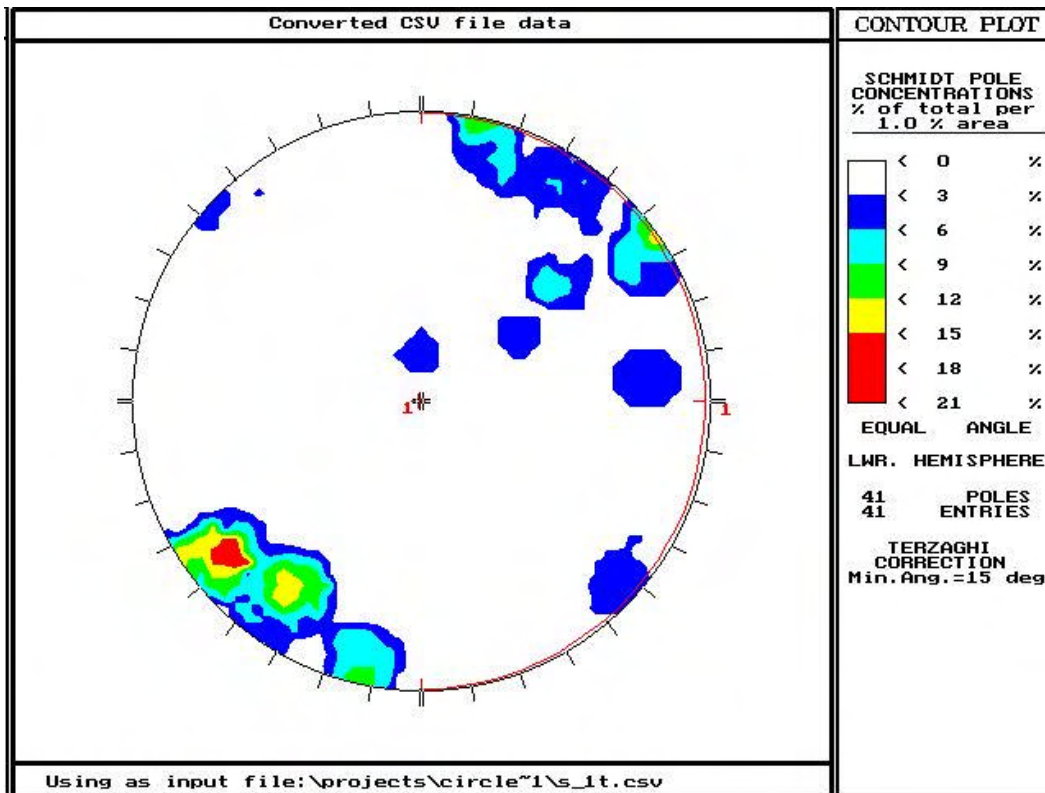


Figure 3-28. Stereoplot for Scanline 1, rotated relative to bedding plane.

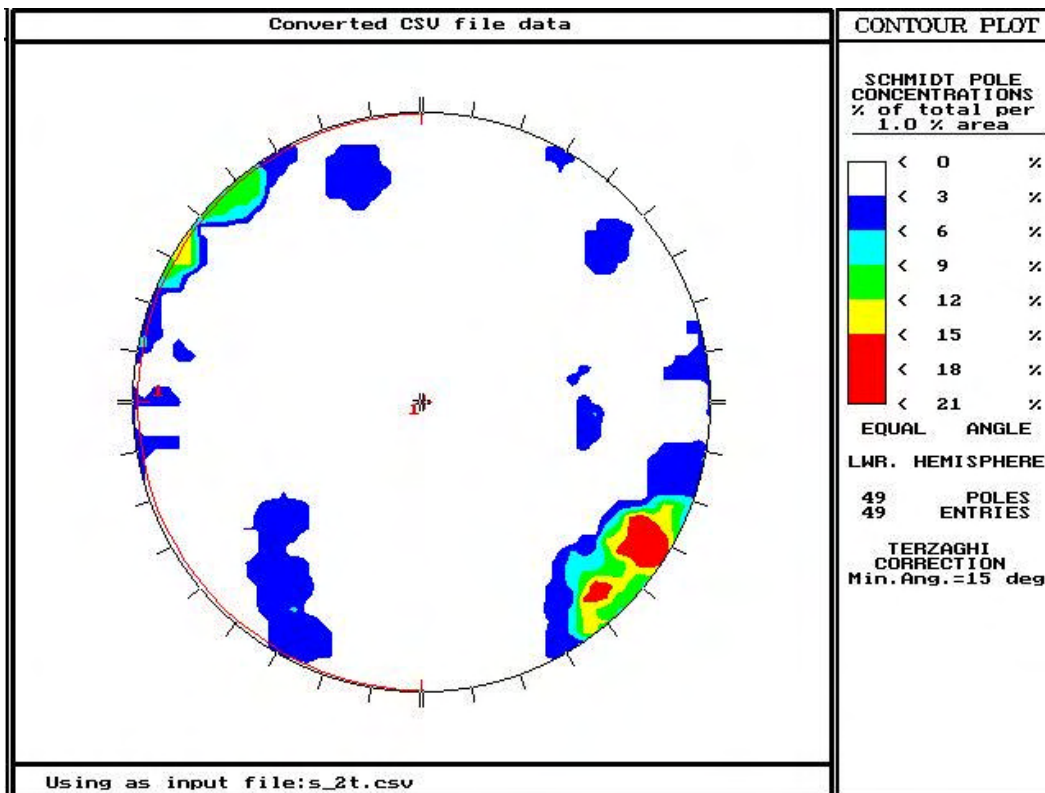


Figure 3-29. Stereoplot for Scanline 2, rotated relative to bedding plane.

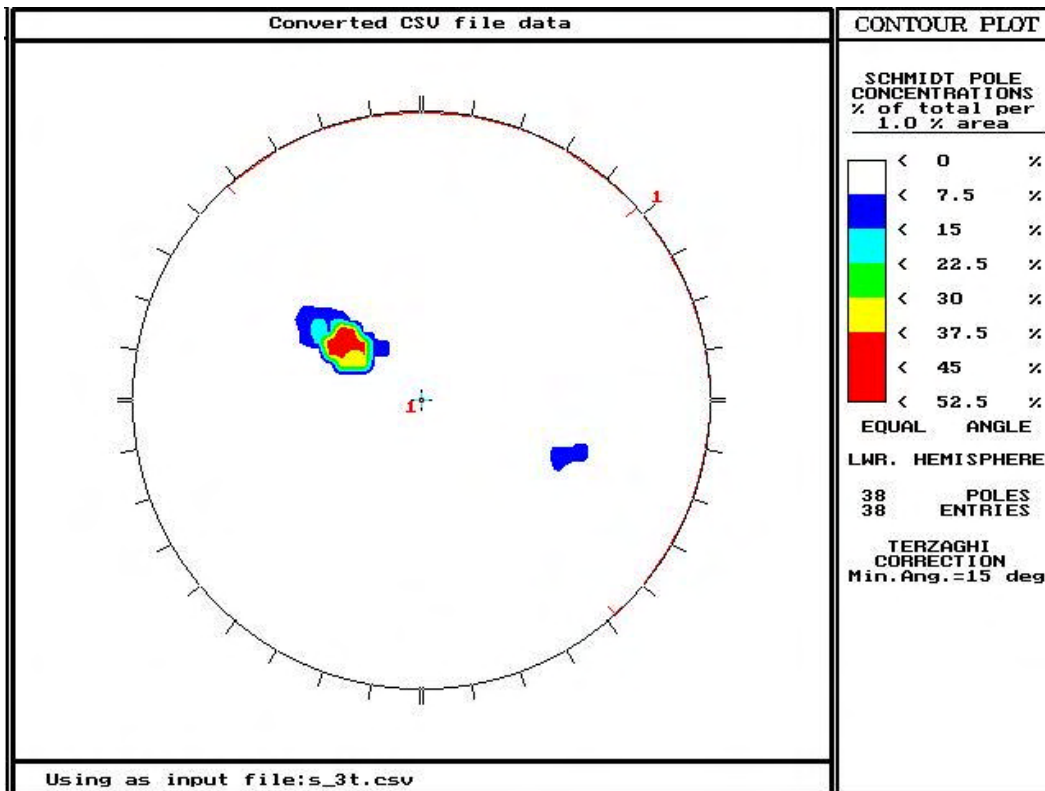


Figure 3-30. Stereoplot for Scanline 3, rotated relative to bedding plane.

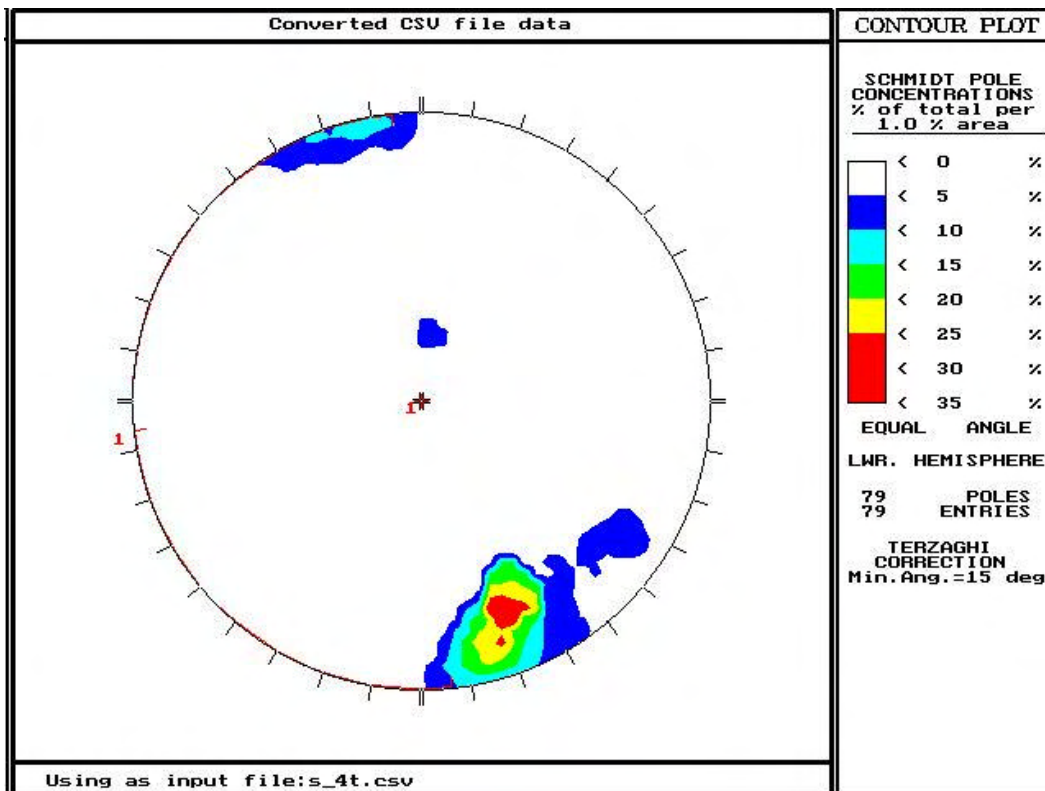


Figure 3-31. Stereoplot for Scanline 4, rotated relative to bedding plane.

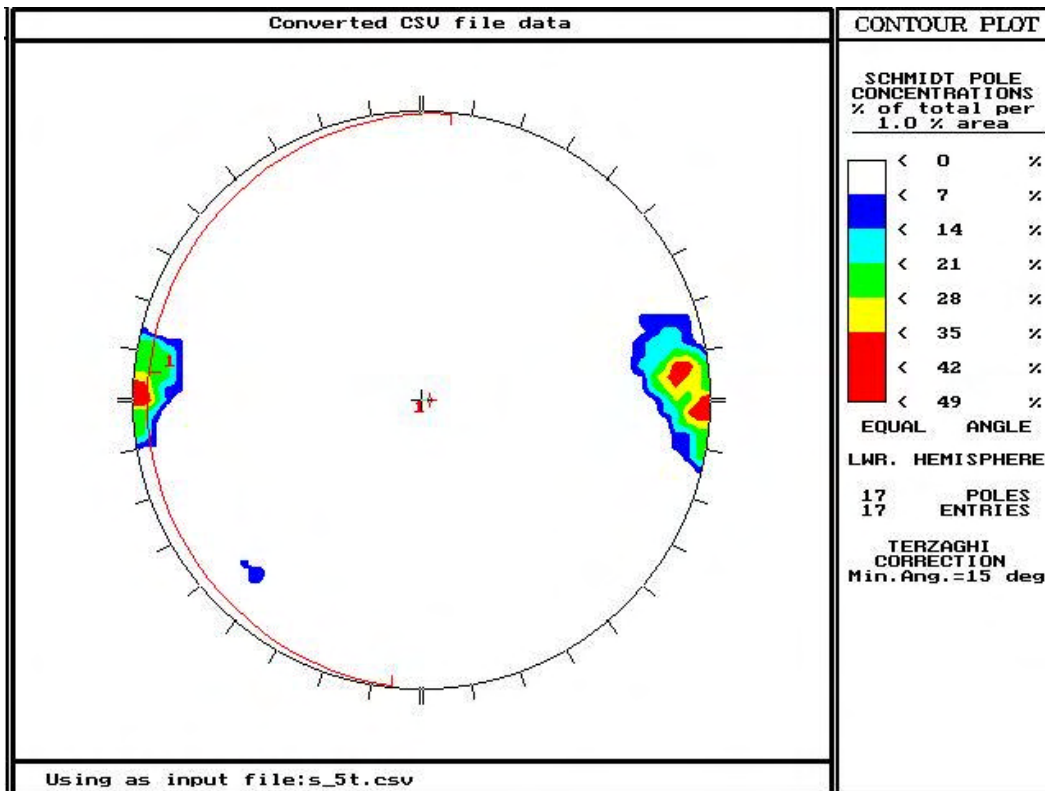


Figure 3-32. Stereoplot for Scanline 5, rotated relative to bedding plane.

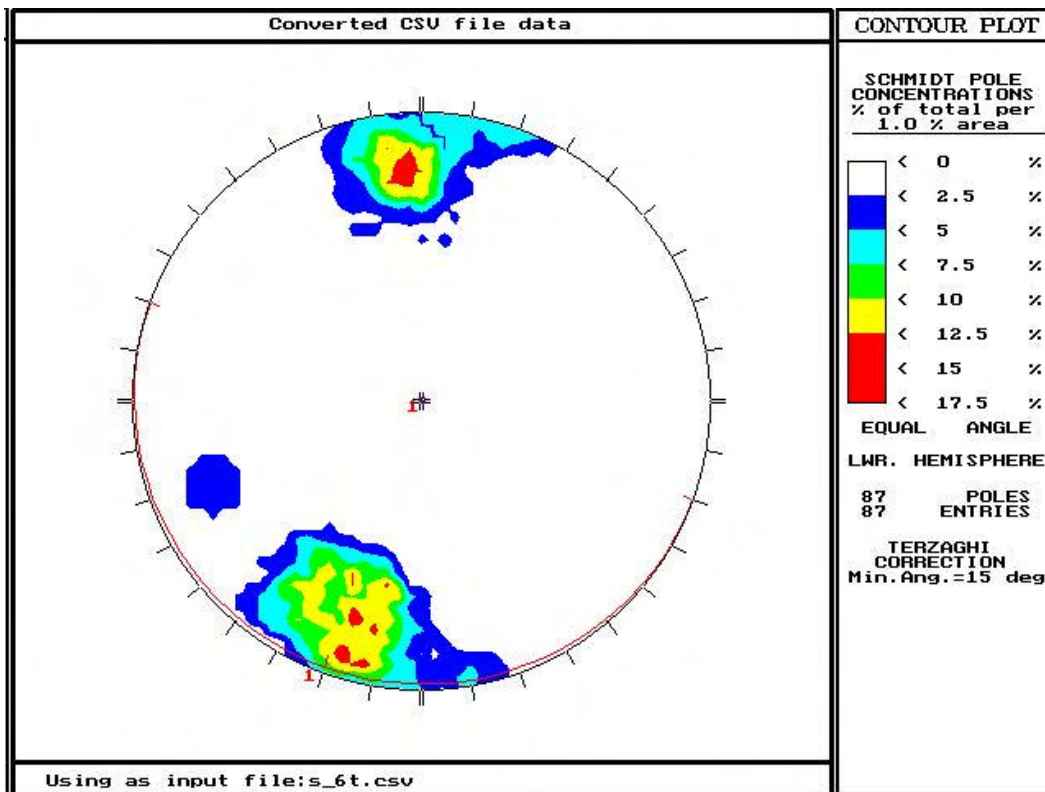


Figure 3-33. Stereoplot for Scanline 6, rotated relative to bedding plane.

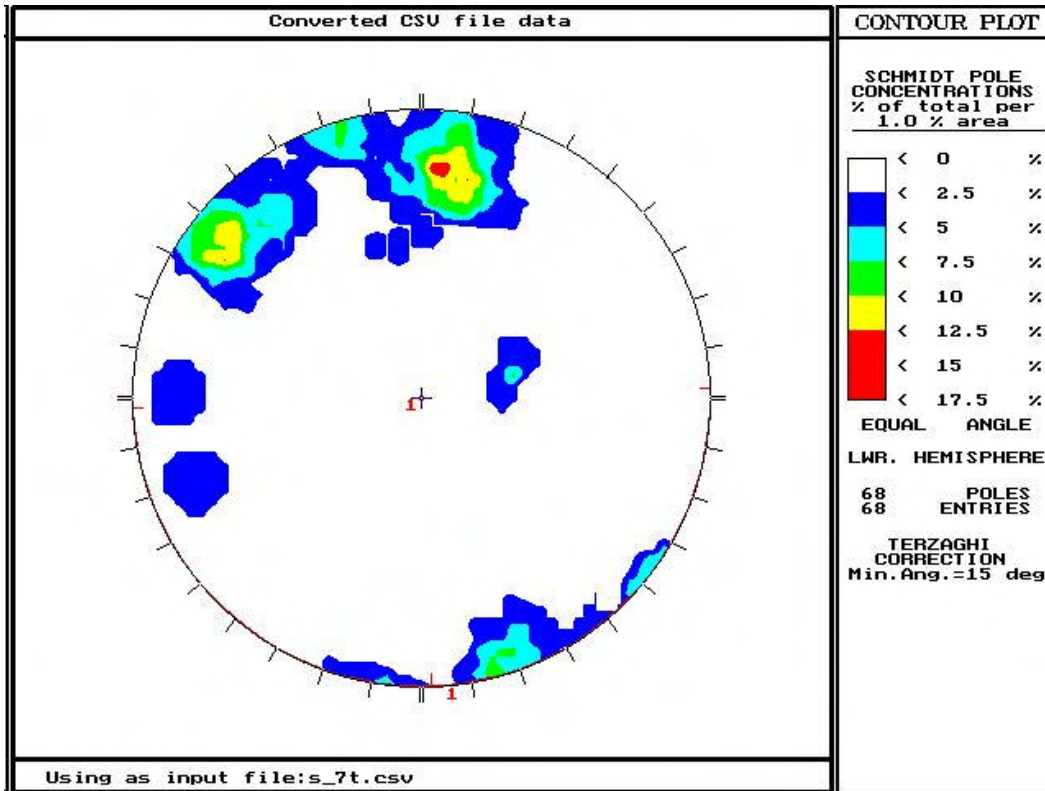


Figure 3-34. Stereoplot for Scanline 7, rotated relative to bedding plane.

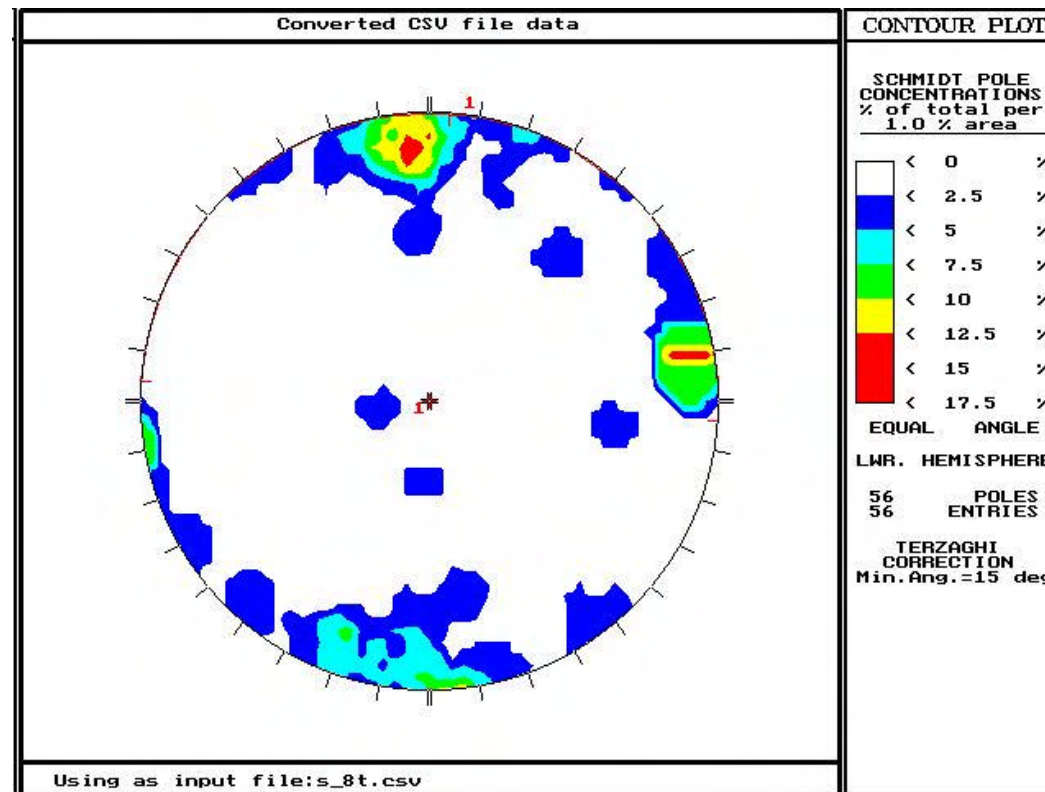


Figure 3-35. Stereoplot for Scanline 5, rotated relative to bedding plane.

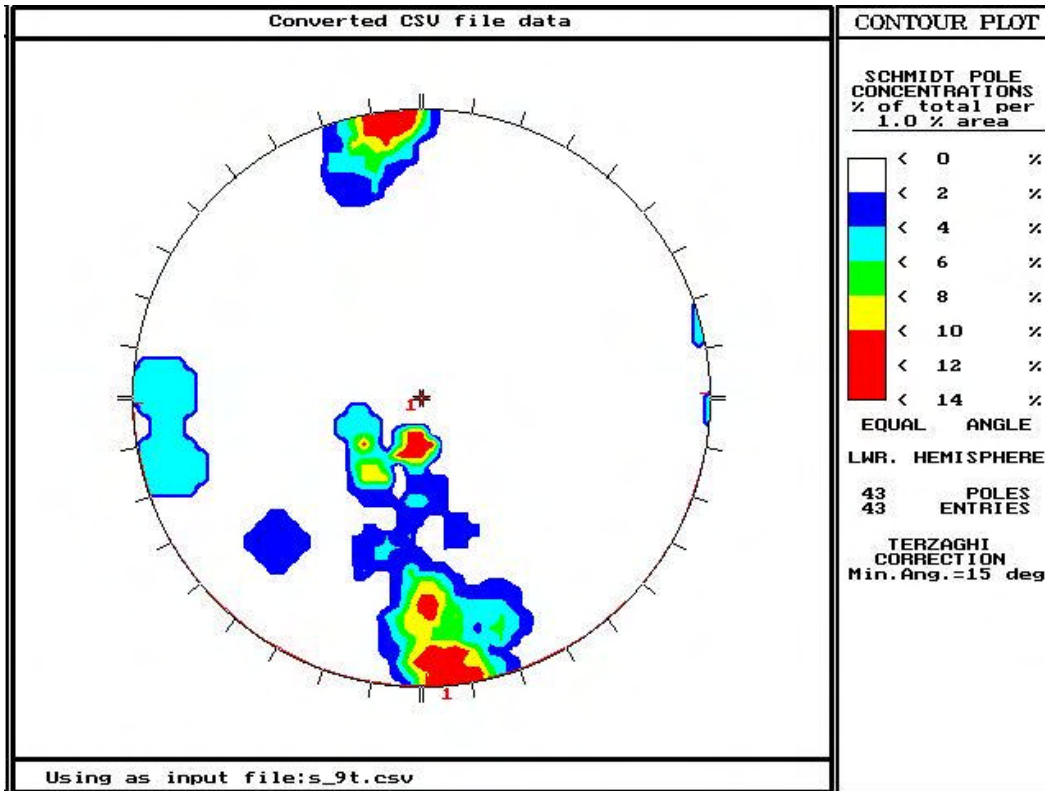


Figure 3-36. Stereoplot for Scanline 9, rotated relative to bedding plane.

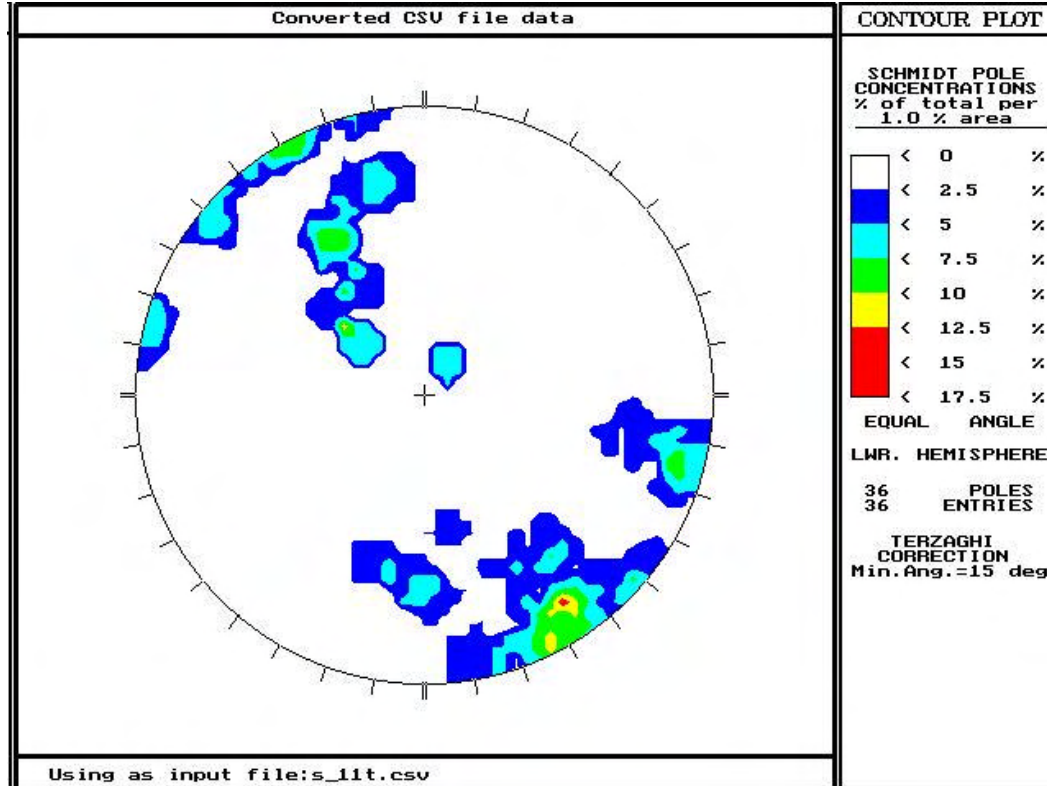


Figure 3-37. Stereoplot for Scanline 11, rotated relative to bedding plane.

These results pertain only to intensity scaling parallel to bedding, and not to possible changes perpendicular to bedding, as the scanlines were set up to remain in mechanical layers defined by one or more beds. The implication of these results is that fracture intensity within a mechanical layer appears to be scale independent at scales of tens of meters. Intensity among different scanline sites, however, shows that there may be some variations at these larger scales (hundreds of meters). These results imply that intensity within a reservoir simulation grid cell, typically on the order of 50 m to 100 m in horizontal extent, should be homogeneous; but that variations among cells may occur. In other words, the measured horizontal variation in fracture intensity is at about the same scale of discretization as a typical reservoir simulation grid.

For example, the mass dimensions for scanline sites 1 and 2 show values close to 0.66, which is distinctly different than for the other sites. With the exception of Scanline 5, the mass dimensions of the remaining scanlines are generally quite high. The reason for the low value (0.51) for Scanline 5 stands out. The reason for this may be due to the very low intensity of fracturing at this location.

Scanlines 4 through 7 are in the Crow Mountain Member, while the others are in the Red Peak Member. Table 3-1 indicates by colored shading which member the scanline was in. This Table does not show any obvious correspondence between the mass dimension and the Member.

The fracture intensity at scales above the REV threshold (essentially the value of the ordinate at the largest scales displayed in the plots) shows that Scanline 6 has the highest intensity, followed by 4 and 3. Slightly below these three scanlines are a group of five scanlines – 11, 2, 7, 8 and 10 – that all have a nearly identical intensity. The scanlines with the lowest intensity, in decreasing order, are 1, 9 and 5. Once again, absolute intensity does not appear to correspond to whether it is in the Crow Mountain or Red Peak Member.

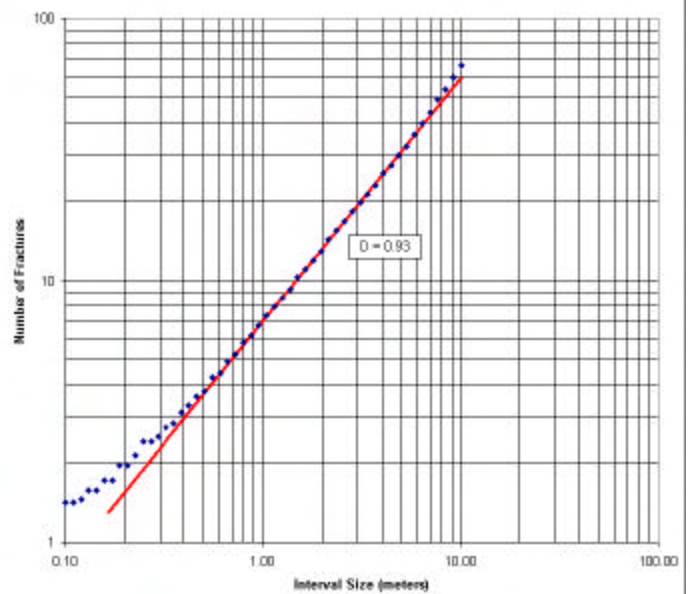
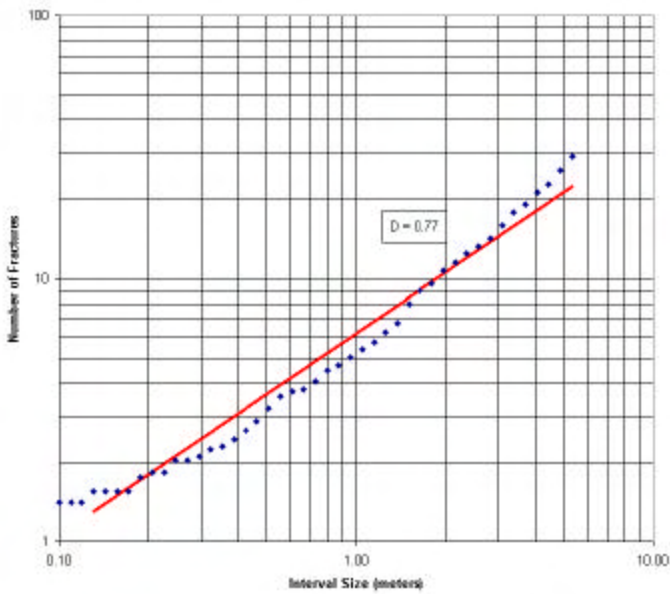
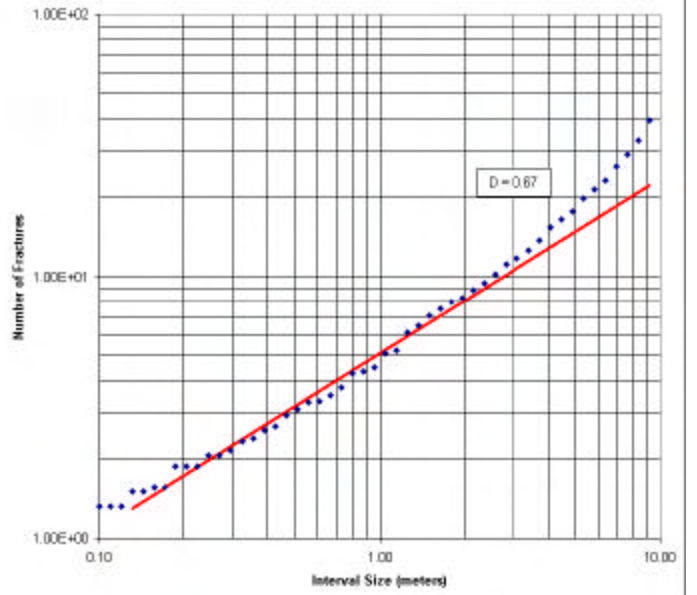
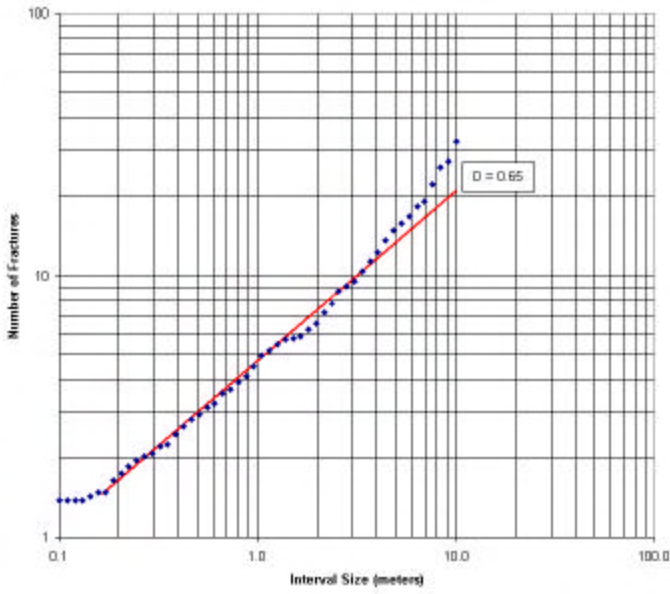
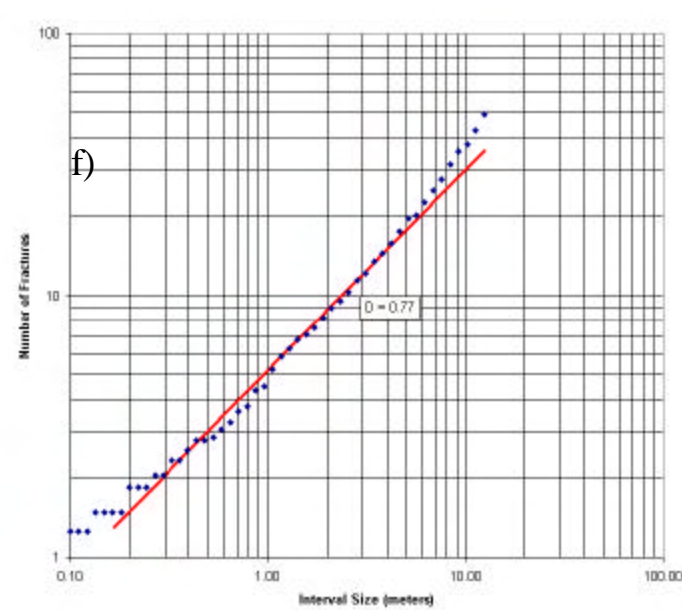
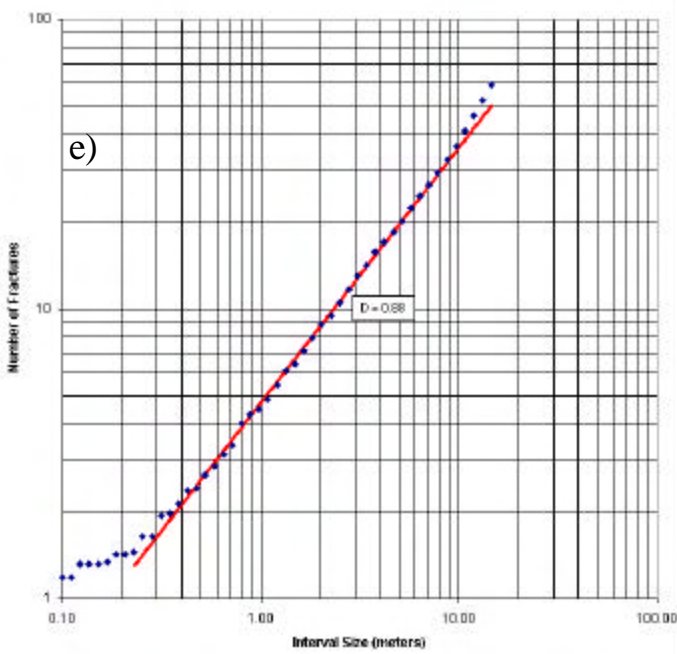
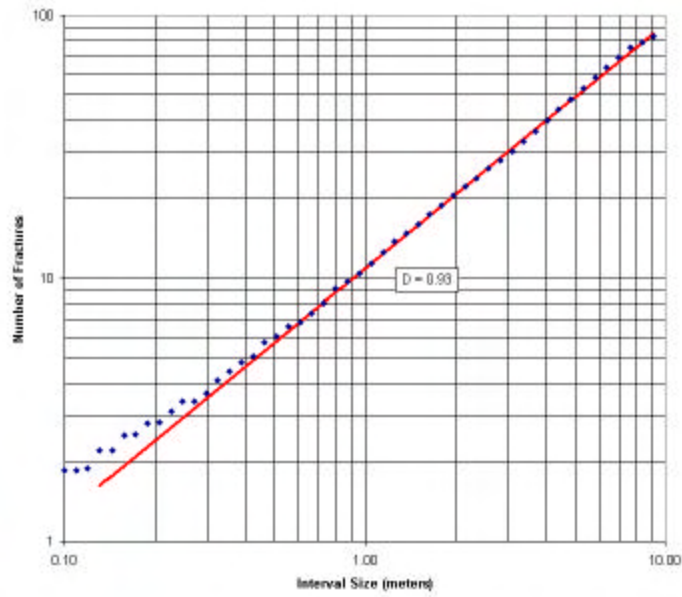
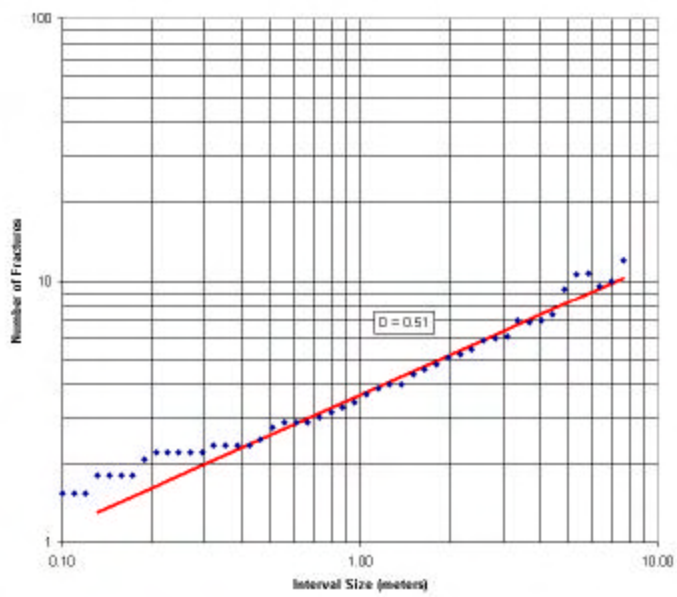
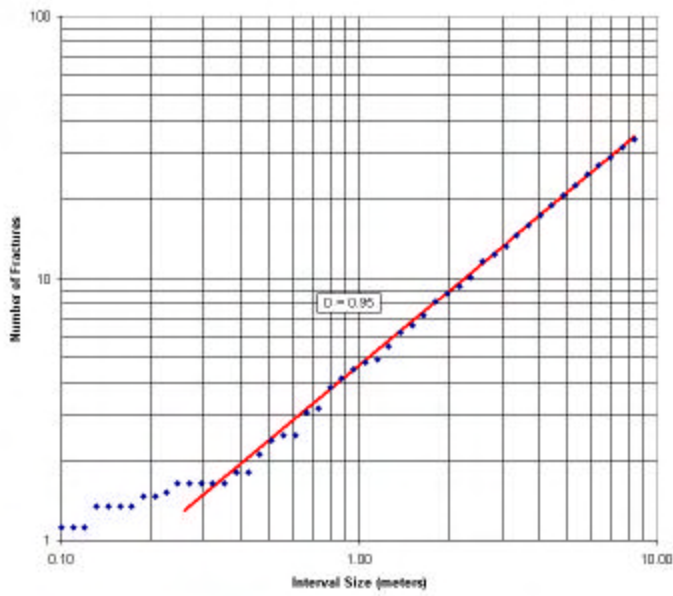
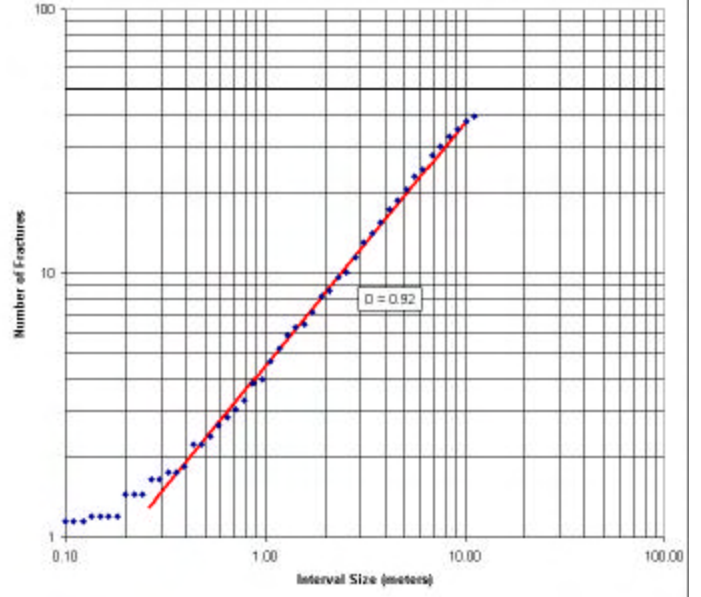
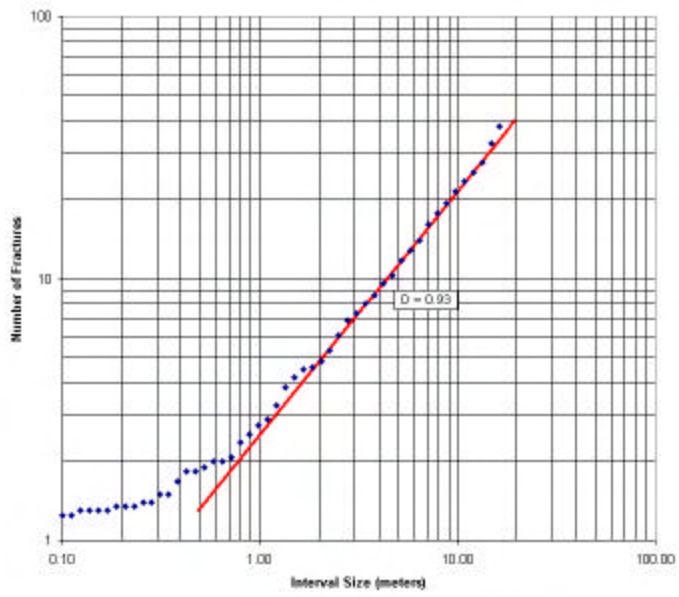


Figure 3-38. Mass dimension calculations for the 11 scanline sites. Plots a through k are, in order, for scanlines 1 through 11.



g)

h)



i)

j)

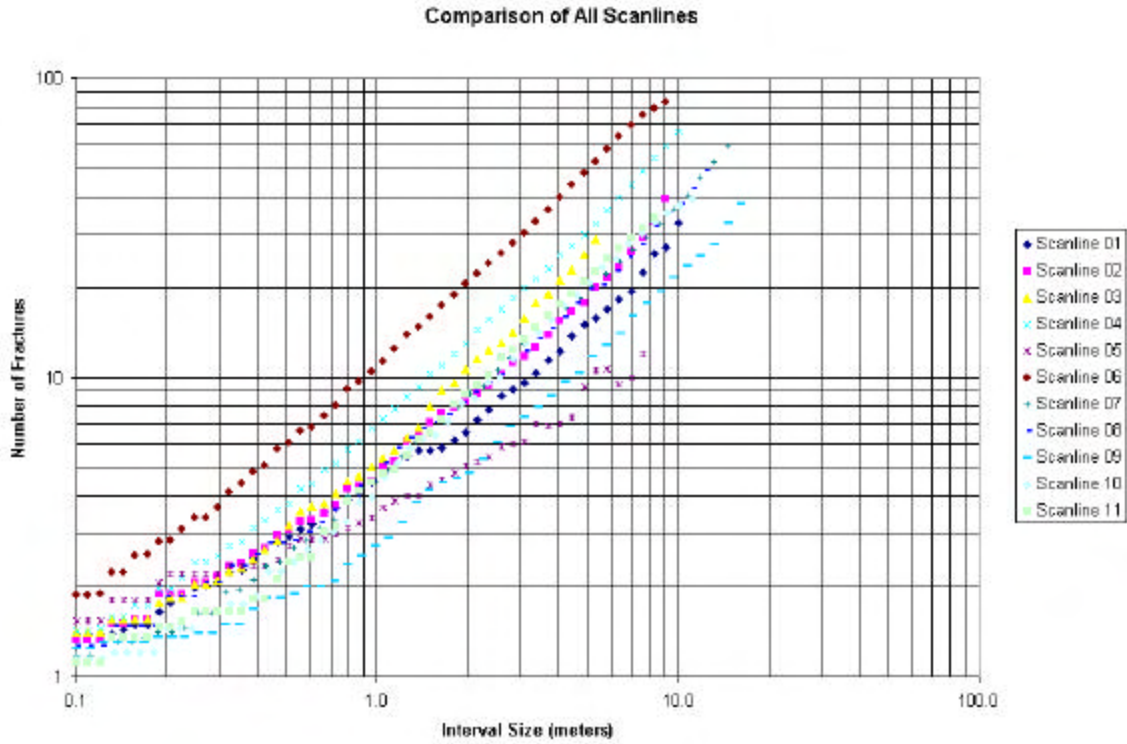


Figure 3-39. Composite plot of mass dimension calculations for all 11 scanlines.

Scanline	Mass Dimension
1	0.65
2	0.67
3	0.77
4	0.93
5	0.51
6	0.93
7	0.88
8	0.77
9	0.93
10	0.92
11	0.95

Table 3-1. Summary of mass dimensions for all 11 scanlines. Orange shading indicates Red Peak Member, while light blue shading indicates Crow Mountain Member.

### 3.5.2 COMPARISON OF OUTCROP & SUBSURFACE FRACTURE ORIENTATIONS AND INTENSITY WITH STRUCTURAL HISTORY

#### 3.5.2.1 Outcrop Data

The next step was to determine whether and how the fracture pattern in the reservoir related to the deformation history. This was done by examining the strain calculated from the palinspastic reconstruction with the orientations and intensity variations of fractures in outcrop and in the subsurface. The locations of the scanline locations are shown in Figure 3-40. The outcrops in the Overthrust block (Scanlines 5-9) are examined first.

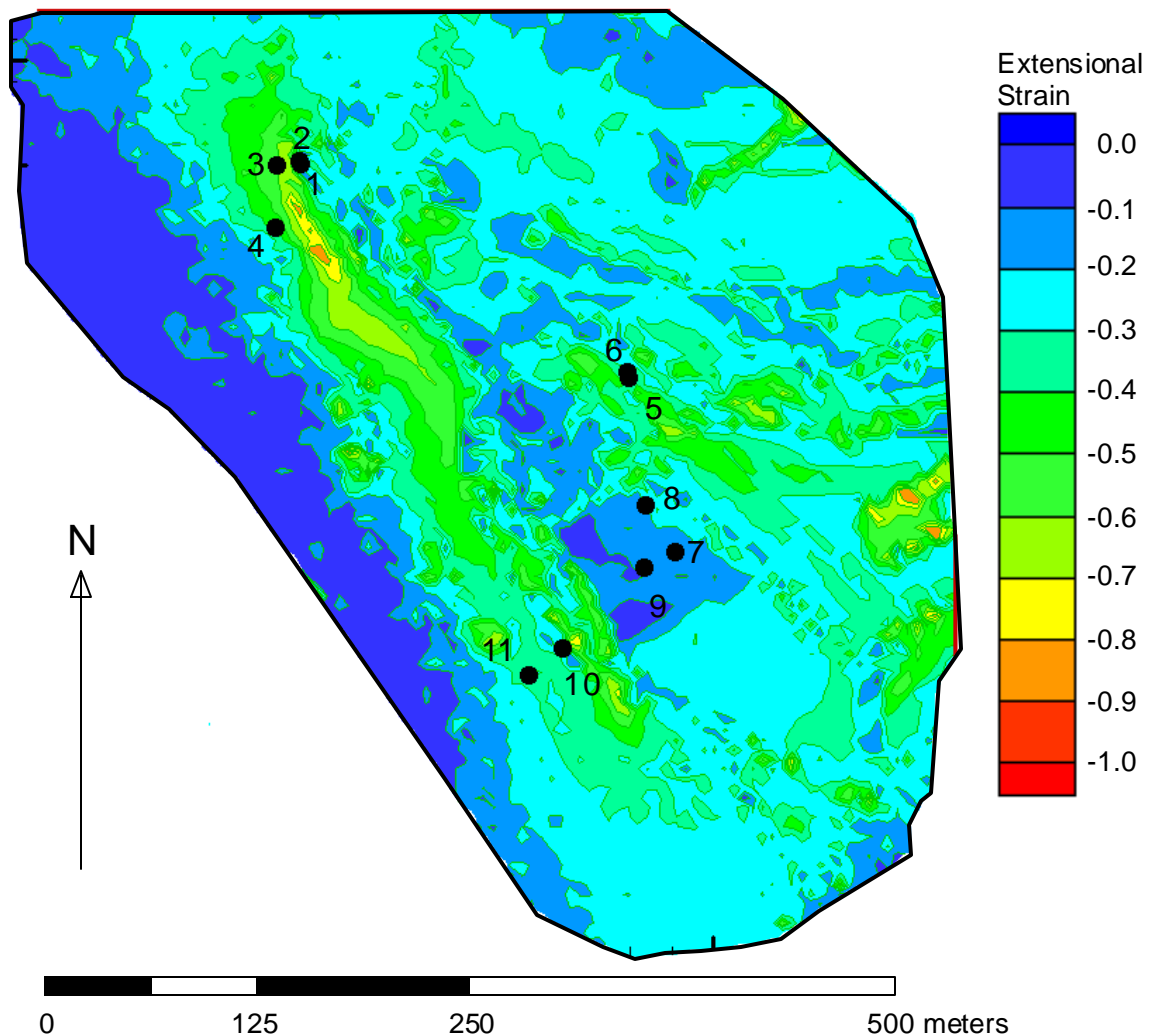


Figure 3-40. Map of principal extensional strain magnitude produced by folding. The contour map shows the approximate horizontal limits of the fault blocks used in the reconstruction. The location of the eleven scanline sites are shown on the map. The strains shown have been mapped on the present-day structural configuration of the Circle Ridge Field, and represent deformation in the Tensleep Formation.

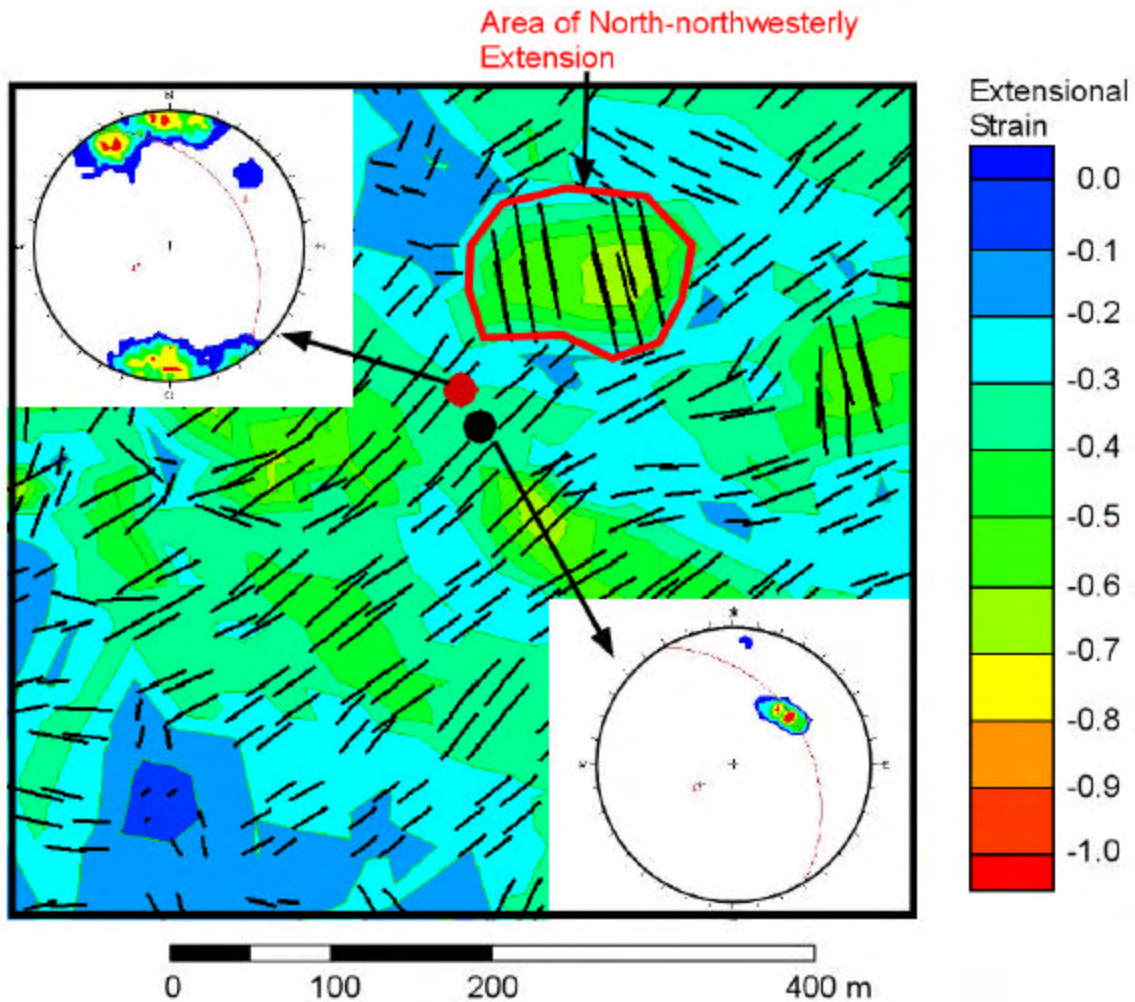
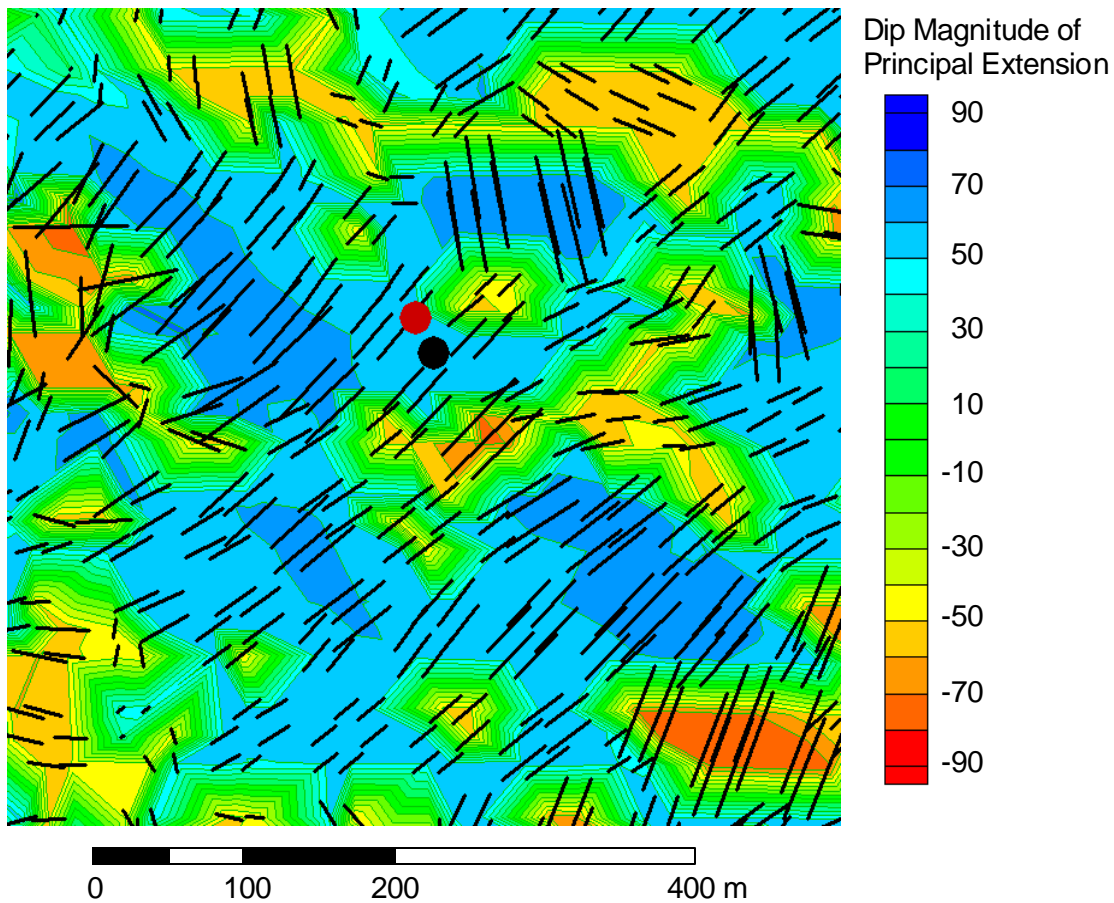


Figure 3-41. Fracture orientations measured at scanlines 6 (red circle) and 5 (black circle). Black lines indicate trend of principal extension. Lines lengths are proportional to the magnitude of extension.

The prevalent northeasterly direction of strain (Figure 3-41) is consistent with the fracture orientations shown at Scanline 5, and is also possibly evident in a minor set at Scanline 6. The north to north-northwesterly strain in the area immediately to the northeast of Scanline 6 is consistent with the dominant orientations shown in the joint stereoplot for Scanline 6. Both stereoplots suggest that the principal direction of extensional strain in the vicinity of the scanlines is perpendicular to the strike of the joint sets found in outcrop along the scanlines.

The direction of greatest extension in the vicinity of Scanline 5 plunges  $50^{\circ}$  to  $60^{\circ}$  to the northeast (Figure 3-42), which makes it almost exactly perpendicular to the dominant joint set shown in the stereoplot. The northeasterly extension near Scanline 6 plunges  $20^{\circ}$  to  $50^{\circ}$  to the northeast, which is nearly orthogonal to the secondary set. To the northeast of Scanline 6, the north-northwesterly extension in this region dips over a large range



**Figure 3-42. Plunge of principal direction of extension (contours) and trend of maximum extension direction. Plunge at Scanline 6 (red circle) is about 50° to the northeast. Plunge at Scanline 5 (black circle) is similar. Black lines indicate trend of principal extension. Lines lengths are proportional to the magnitude of extension.**

from 20° to about 70° in a south-southeasterly direction. The shallower dips are consistent with the dominant joint set dip, but the steeper dips are not.

Figure 3-43 shows the trend of the principal extensional strain for the region around Scanlines 7,8 and 9. At Scanline 7, the principal direction of extension is to the northeast or north-northeast. This is nearly perpendicular to the strike of the dominant joint set, which strikes northwesterly and dips steeply to the southwest. Some nearly north-south extension occurs just to the east of Scanline 7, which is nearly perpendicular to the strike of the other prominent joint set. Scanline 8 has a dominant west-northwesterly striking subvertical joint set, and a secondary set orthogonal to it that strikes north-northeasterly. The dominant direction of extension is nearly perpendicular to the west-northwesterly striking primary set. Scanline 9 exhibits a very similar joint orientation pattern, however, the azimuth of the direction of principal extension is northeast-southwest, some ten to fifteen degrees from being perpendicular, although the extension direction just to the west of the scanline is nearly exactly perpendicular.

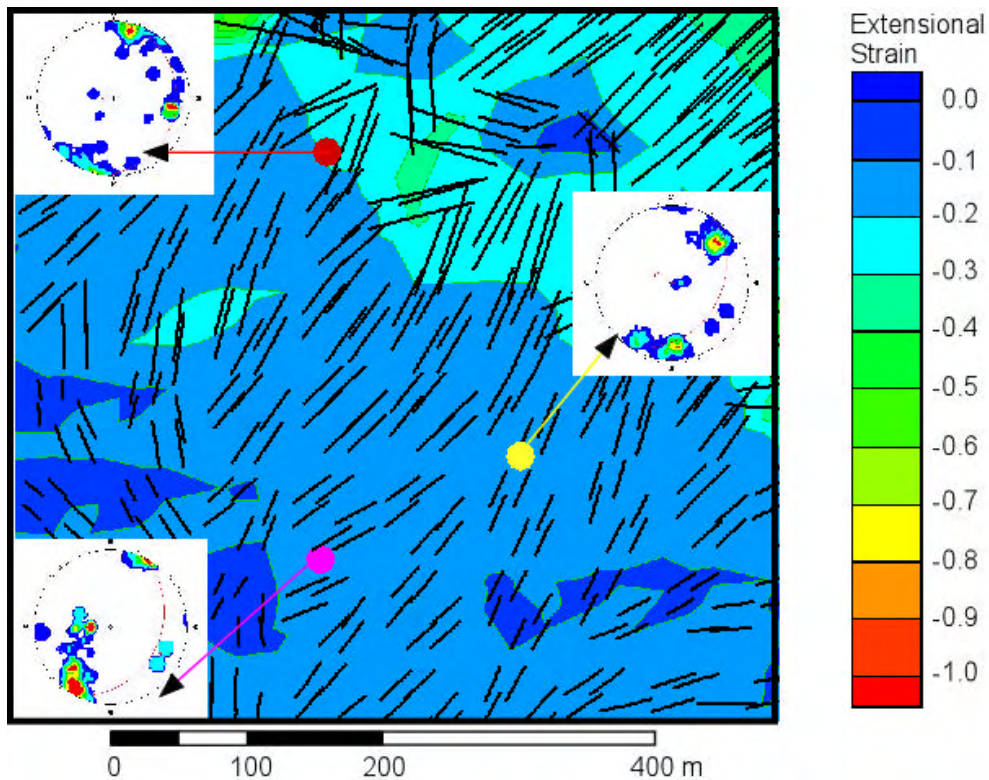


Figure 3-43. Comparison of extensional strain and fracture orientations measured at scanlines 7 (yellow circle), 8 (red circle) and 9 (violet circle). Black lines indicate trend of principal extension. Lines lengths are proportional to the magnitude of extension.

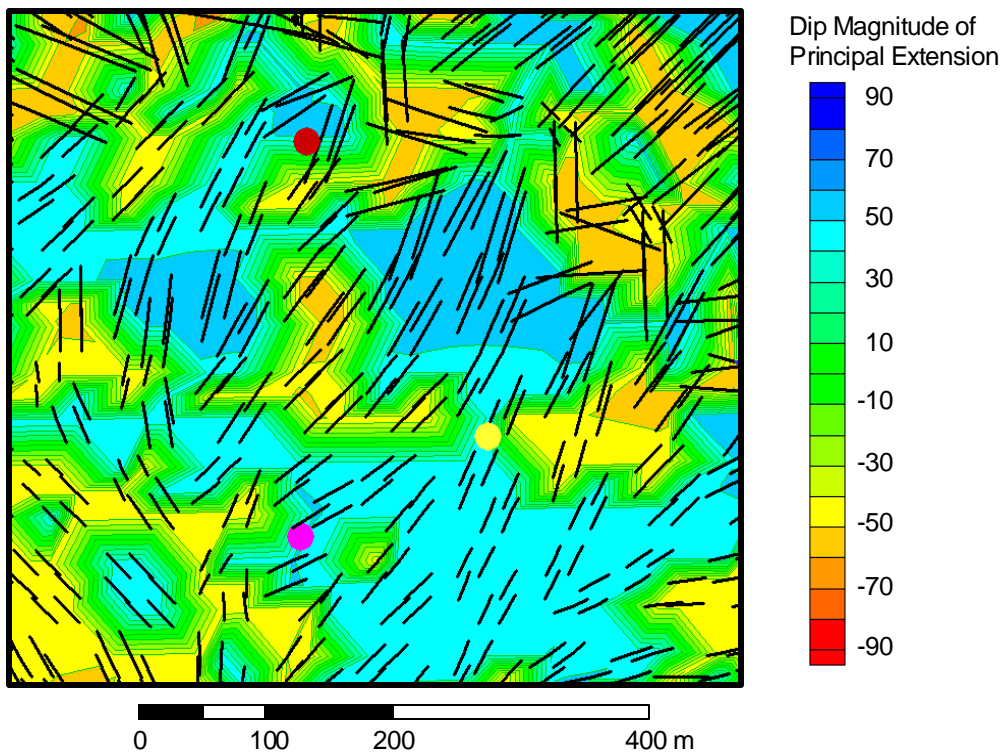


Figure 3-44. Plunge of principal direction of extension (contours) and trend of maximum extension direction. Green shading indicates very shallow plunges. The three scanlines generally are in the vicinity of very shallow plunges, varying from  $-30^{\circ}$  to  $+30^{\circ}$ . This is consistent with the steep dips shown by all of the major joint sets in Scanlines 7, 8 and 9. Black lines indicate trend of principal extension. Lines lengths are proportional to the magnitude of extension.

Figure 3-44 shows the plunge of the principal extension vector. The three scanlines generally are in the vicinity of very shallow plunges, varying from  $-30^{\circ}$  to  $+30^{\circ}$ . This is consistent with the steep dips shown by all of the major joint sets in Scanlines 7, 8 and 9.

The final scanline in Block 1 is Scanline 10. The trend of the principal extension (Figure 3-45) is nearly perpendicular to the strike of the dominant joint set. There is some evidence in the stereoplot of another joint set nearly orthogonal to the first. The plunge of the principal extension vector (Figure 3-46) show that the plunges of the principal direction of extension are on the order of  $10^{\circ}$  in the vicinity of Scanline 10 (red circle) to the southeast.

Overall, the joint pattern for the six scanline sites in Block 1 indicate a very consistent relation to the trend and plunge of the principal extension vector. The dominant set is generally very close to being orthogonal to the extension vector, and occasionally there is a secondary joint set that is approximately orthogonal to the primary set and striking parallel to the trend of the extension vector.

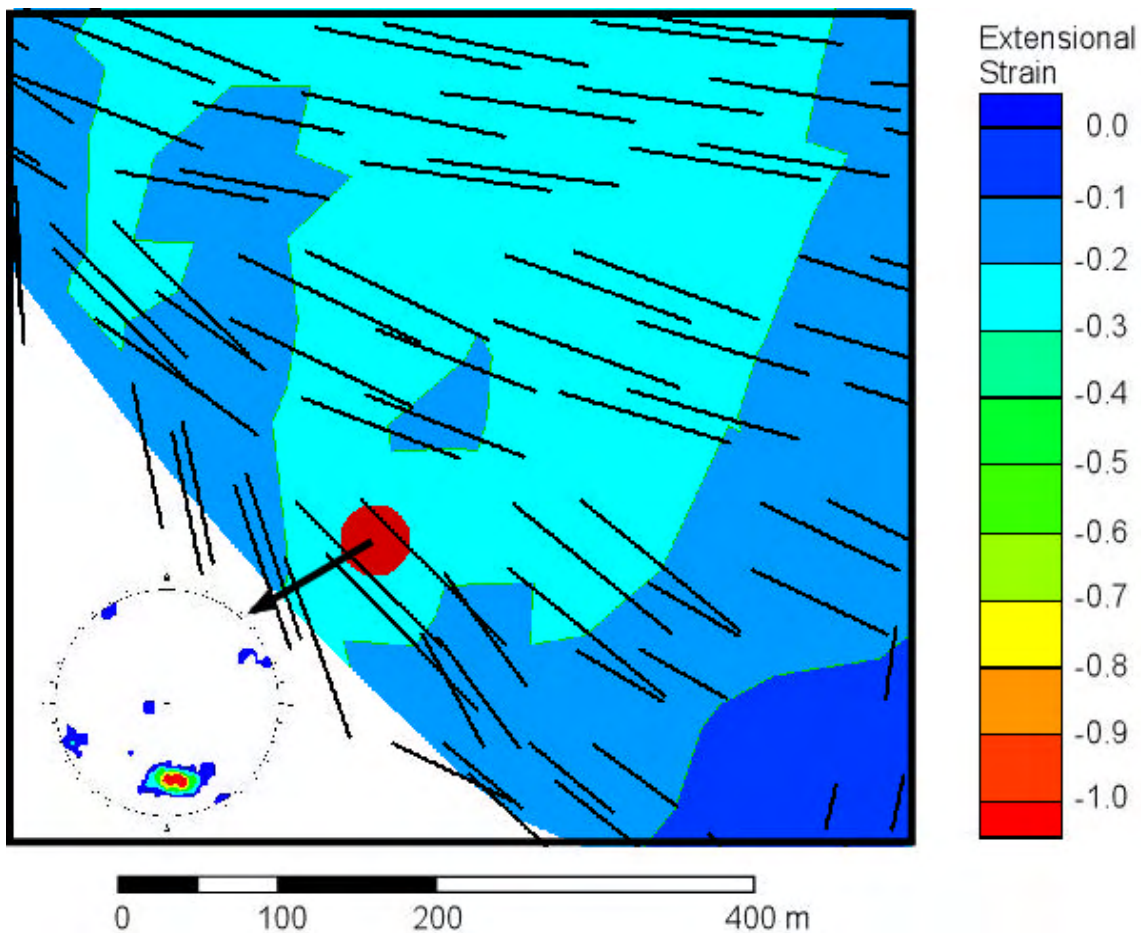
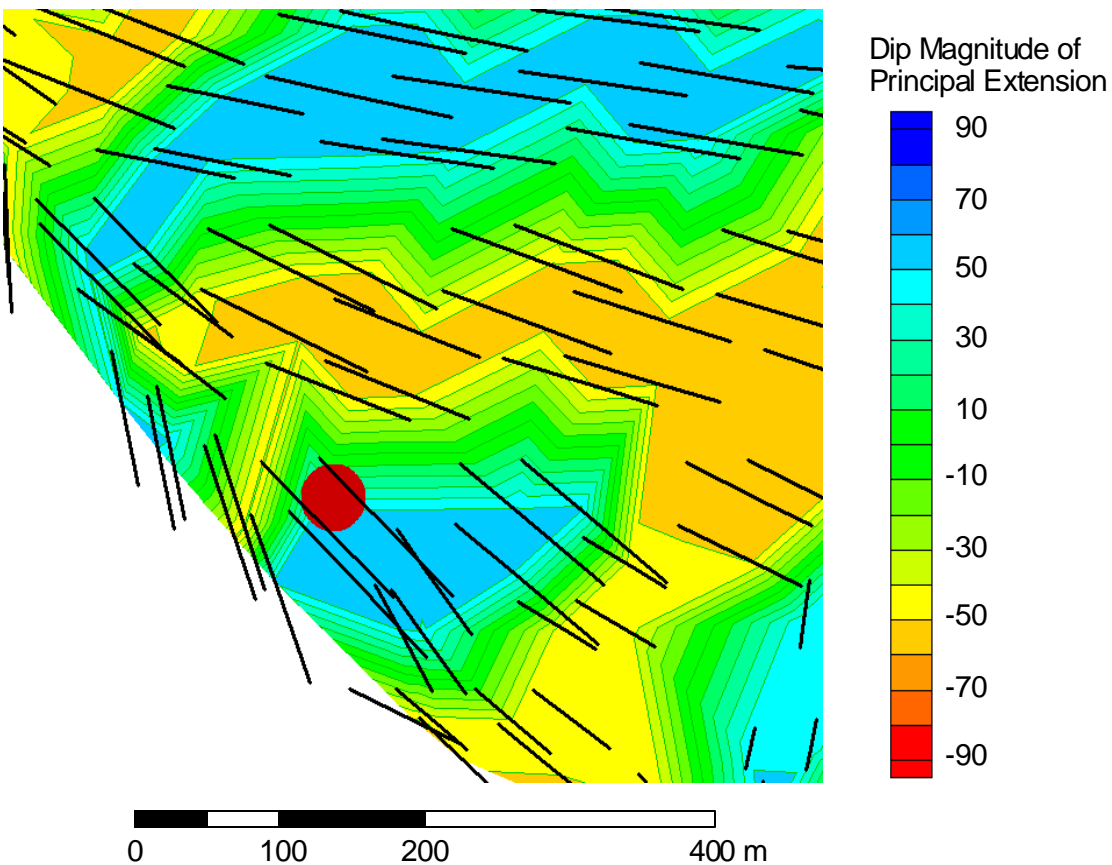


Figure 3-45. Orientation of joints and principal extensional strain for Scanline 10 (Red Peak). The direction of strain is perpendicular to the dominant northeasterly-striking joint set. Black lines indicate trend of principal extension. Lines lengths are proportional to the magnitude of extension.

At least in Block 1, it seems as if the joint sets measured along scanlines are consistently orthogonal to the direction of principal extension during the folding event.

The remaining scanlines are in other blocks, including subthrust blocks to the southwest of the Red Gully Fault.

Scanline 11 lies a few hundred meters to the southwest of Scanline 10, but is on the opposite of the Red Gully Fault in the footwall block (Figure 3-40). Unlike the Scanline data from Block 1, the trend of the direction of principal extension (Figure 3-47) is not perpendicular to the strike of the dominant joint set. Rather, the strike is sub-parallel to slightly oblique to the trend of the principal extension vector. It is not clear why this might be the case, although the rock becomes increasingly tightly folded in the southeastern end of the field, in some cases leading to overturned beds and abundant minor faulting. It is possible that the joint pattern measured in outcrop reflects these local structures, which due to their small scale, were not incorporated into the field-wide reconstruction. In general, the joint pattern in outcrop strikes sub-perpendicular to the trend of the Red Gully Fault near the scanline location, which is the extension fracture



**Figure 3-46. Plunge of principal direction of extension (contours) and trend of maximum extension direction. The contours show the amount of plunge of the principal direction of extension. Green shading indicates very shallow plunges. Black lines indicate trend of principal extension. Lines lengths are proportional to the magnitude of extension.**

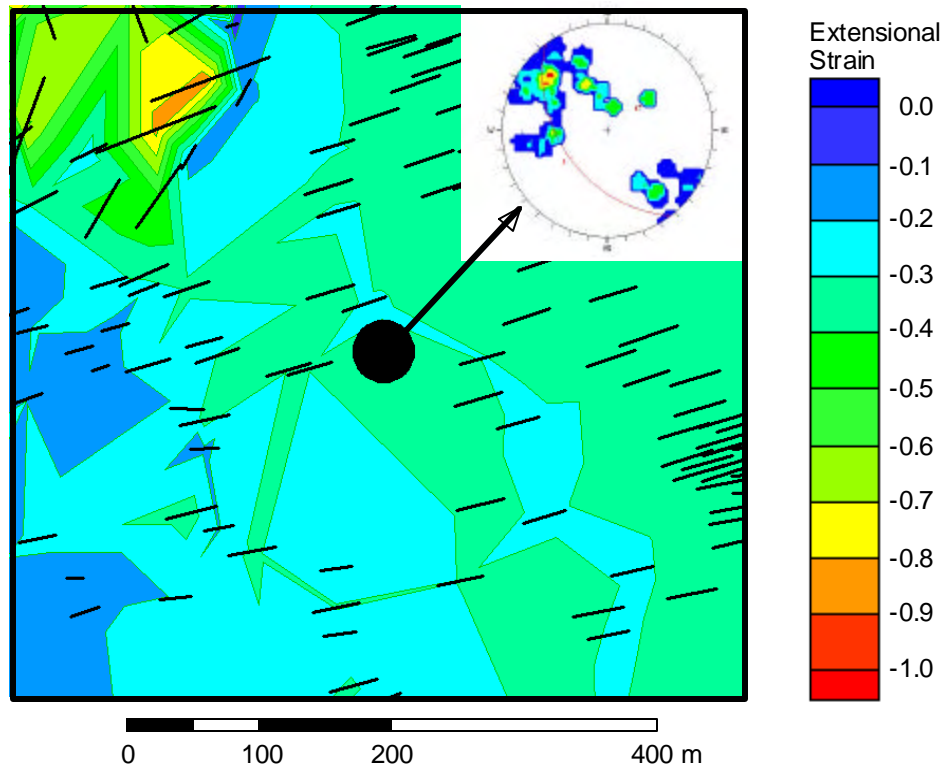


Figure 3-47. Orientation of joints and principal extensional strain for Scanline 11 (Red Peak). The direction of strain is perpendicular to the dominant northeasterly-striking joint set. Black lines indicate trend of principal extension. Lines lengths are proportional to the magnitude of extension.

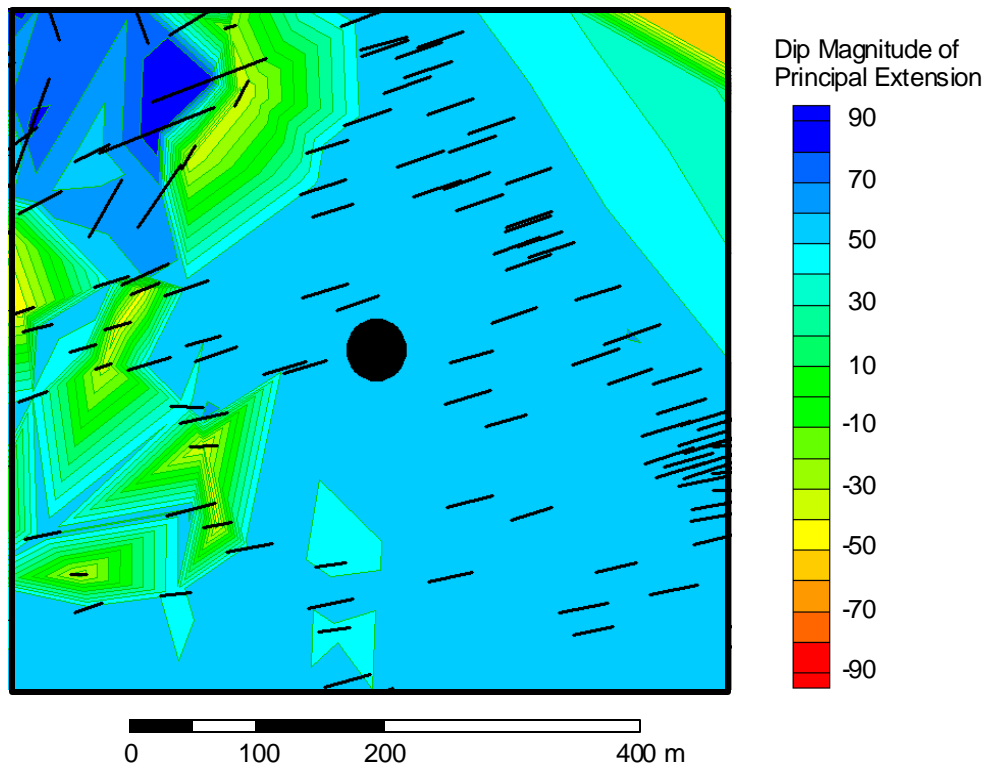


Figure 3-48. Plunge of principal direction of extension (contours) and trend of maximum extension direction around Scanline 11. The contours show the amount of plunge of the principal direction of extension. Light blue shading indicates shallow plunges. Black lines indicate trend of principal extension. Lines lengths are proportional to the magnitude of extension.

orientation that would be expected due to compression from the northeast. Why the strains from the palinspastic reconstruction do not trend in a direction subparallel to the Red Gully Fault is not clear.

The trend of extension in the northern end of Block 16 (the major footwall block) is dominantly to the east-northeast in the vicinity of Scanlines 1 through 3, and northeasterly for Scanline 4 (Figure 3-49). Scanlines 1 and 2 are close together, and so are represented as a single circle on this plot (Scanline 2 is slightly to the north of Scanline 1). The dominant joint set at Scanline 1 strikes approximately parallel to the trend of principal extension, while the dominant joint set at Scanline 2 strikes approximately perpendicular to the trend of maximum extension. The plunge of the maximum extension vector in the vicinity of Scanlines 1 and 2 (Figure 3-50) is shallow, somewhere on the order of  $10^\circ$ . The dominant joint set at Scanline 2 is thus essentially orthogonal to the maximum extension vector, while the dominant joint set at Scanline 1 is sub-parallel to it. These are the same relations as seen in Block 1. Scanline 3 at first appears to have little relation to the direction of principal extension. The contour concentration at the center of the stereoplot indicates that the dominant joint set is subhorizontal with a slight southwesterly dip, although there is a small concentration of poles (blue contours) at the edge of the stereoplot that indicates a vertical joint set striking northeast to east-northeast.

However, the plunge of the extension vector in the vicinity of Scanline 3 (Figure 3-50) indicates very steep plunges, on the order of  $60^\circ$  to  $70^\circ$ . Thus, the shallowly dipping joint set in outcrop is with ten degrees or so of being orthogonal to the principal extension vector.

The dominant joint set at Scanline 4 strikes east-northeast and dips steeply. The principal extension vector trends more northeasterly, and dips steeply. The trend of the extension vector becomes more easterly to the east of the scanline location, becoming more nearly parallel.

In general, the relation between the dominant joint sets in outcrop and the principal extension vectors are more complex than they were in Block 1, but still show a consistent relation to the vector. The joint sets seen in Scanlines 1 through 4 and 11 typically strike either parallel to or perpendicular to the trend of the principal extension vector. If the joint set strikes perpendicular, it is generally orthogonal or close to orthogonal to this vector. If the joint set strikes subparallel, then it is often a subvertical set and has no relation with the plunge of the principal extension vector.

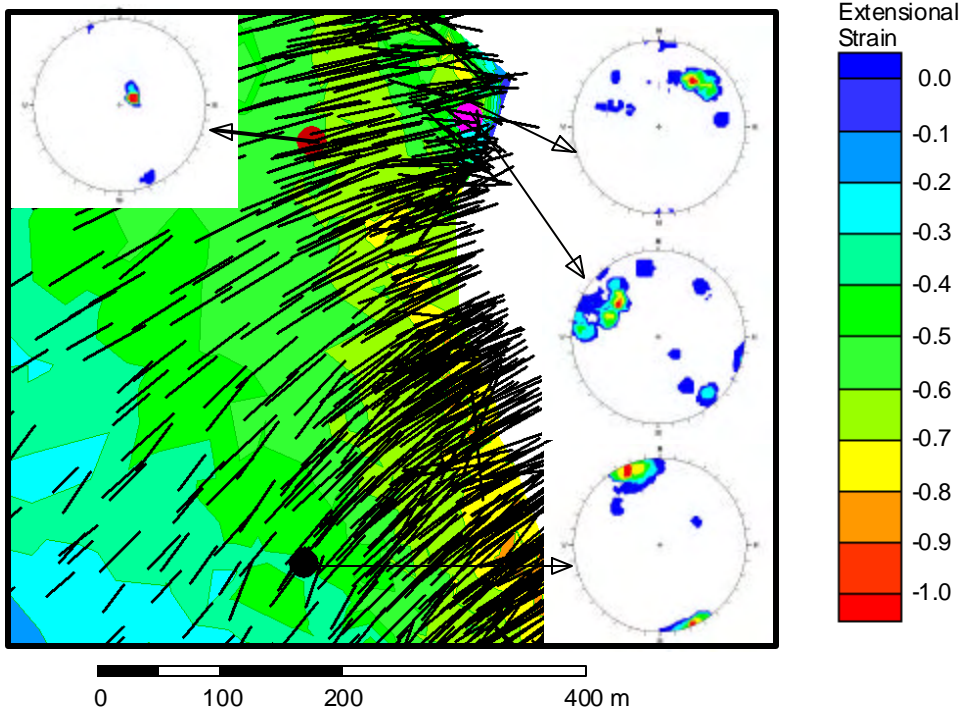


Figure 3-49. Orientation of joints and principal extensional strain for Scanlines 1 and 2 (pink circle), Scanline 3 (red circle) and Scanline 4 (black circle). Black lines indicate trend of principal extension. Lines lengths are proportional to the magnitude of extension.

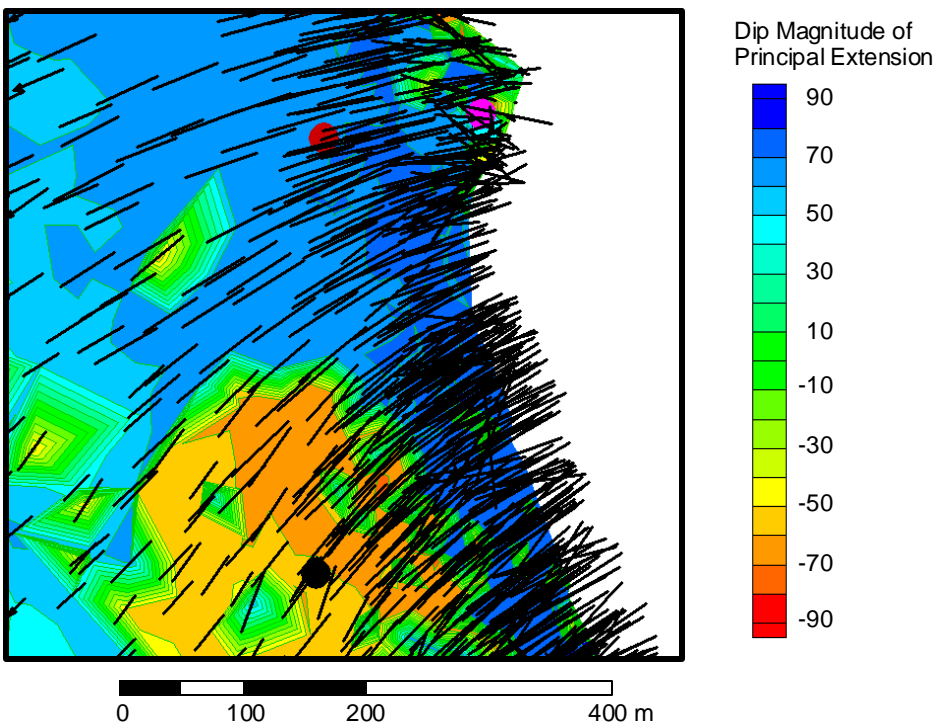
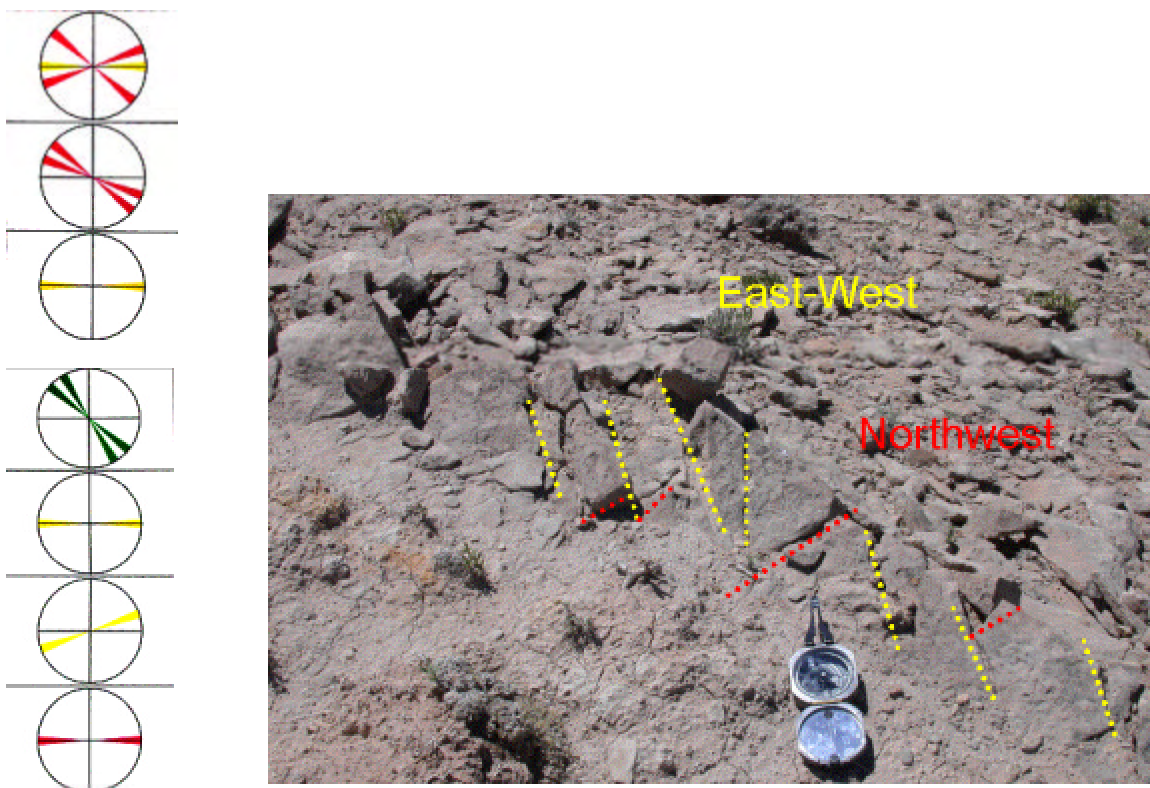


Figure 3-50. Plunge of principal direction of extension (contours) and trend of maximum extension direction around Scanlines 1, 2 (pink circle) 3 (red circle) and 4 (black circle). The contours show the amount of plunge of the principal direction of extension. Dark blue and orange/red shading indicates steep plunges. Black lines indicate trend of principal extension. Lines lengths are proportional to the magnitude of extension.

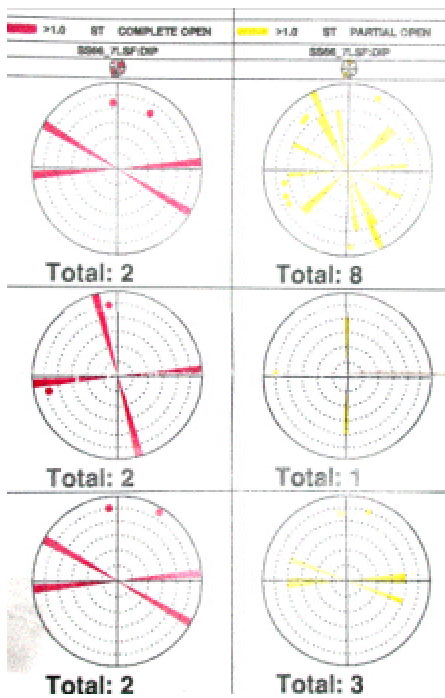
### 3.5.2.2 Comparison of Outcrop and Subsurface Fracture Orientations

The geological field reconnaissance and the palinspastic reconstruction suggest that the Red Peak and Crow Mountain Members should have experienced a strain history similar to the Phosphoria and Tensleep Formations, since there is no structural or stratigraphic de-coupling between the reservoir units and the outcrop units. It is possible to test this hypothesis in two areas of the field by comparing the outcrop fracture orientations in the Red Peak or Crow Mountain with the fracture orientations measured in the FMS and FMI data in Shoshone 66-14 and Shoshone 66-07 (no outcrops were adjacent to Shoshone 65-37, so this well could not be used to evaluate the hypothesis. Figure 3-51 and Figure 3-52 compare outcrop fracture orientations with the subsurface data.



**Figure 3-51. Comparison of fracture orientations in outcrop and in the subsurface for Shoshone 66-14.**

Figure 3-51 shows the strikes of the open fractures (red), partially open fractures (yellow) and solution-enhanced fractures (green) for Shoshone 66-14. These rosettes indicate that the dominant strikes of fractures in the subsurface are east-west and northwest-southeast. The photograph shows an outcrop of Crow Mountain only a few meters from the wellhead. The compass in the photo points towards East. The yellow dotted lines in the photo show a common east-west set, while the red dotted lines show a common northwest-southeast set. There appears to be a good correspondence for this well between the dominant open fracture set orientation in the Crow Mountain and the subsurface fracture orientation in the adjacent Shoshone 66-14



Shoshone 66-07

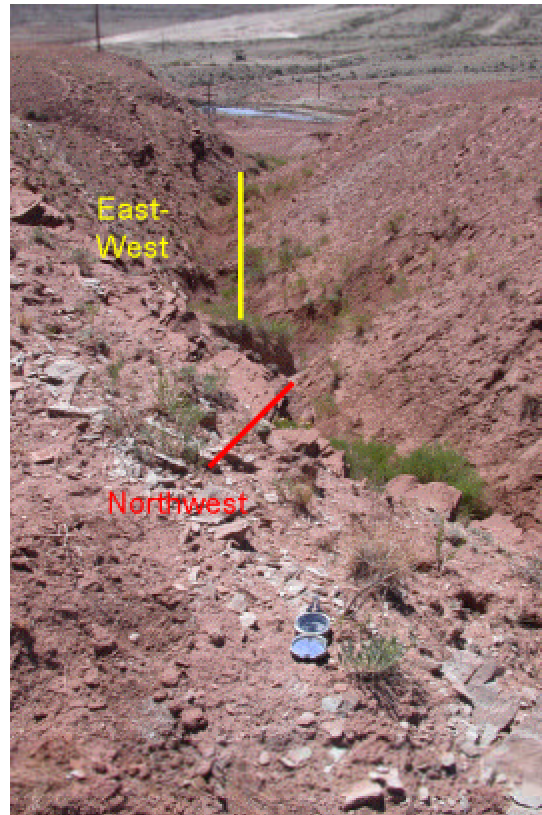


Figure 3-52. Comparison of fracture orientations in outcrop and in the subsurface for Shoshone 66-07.

Figure 3-52 compares the orientations in Shoshone 66-07 with open fracture orientations in an outcrop adjacent to the wellhead. As in Shoshone 66-14, the dominant open (red) and partially open (yellow) fractures in the subsurface strike east-west and northwest-southeast. The upper right photograph in this figure indicates these two strike directions. The yellow solid line goes down the axis of a small valley. The red line shows the orientation of a prominent set developed along the outcrop edge that strikes northwesterly. The lower photo in the figure is a close-up of the outcrop edge. The dotted yellow lines show an east-west set. Thus, there seems to be good agreement between the outcrop fracture orientations and subsurface fracture orientations at the two locations where this could be tested.

### *3.5.2.3 Comparison of Subsurface Image Log Fracture Orientations and Palinspastic Strain*

The next sets of tests involved the comparison of the subsurface image log fracture orientations with the orientations of the maximum extension during folding of the reservoir units. Figure 3-53 through Figure 3-55 show the results for Shoshone 65-37, Shoshone 66-14 and Shoshone 66-07, respectively. In each of these three figures, the contours correspond to the magnitude of maximum extensional strain (blue = low strain; red = high strain). The solid lines indicate the orientation of the extension, and the length of the line is also proportional to the strain magnitude. The approximate location of the well within the reservoir unit is shown too.

Figure 3-53 shows an excellent agreement between the orientations in the subsurface and the directions of extension. The red lines in the vicinity of the well strike to the northeast, implying that joints (extension fractures) should open up perpendicular to this direction. The stereoplot embedded in the figure in the upper right-hand corner shows the orientation of poles to joints

The results for Shoshone 66-14 are shown in Figure 3-54. Most of the extensional strain in the vicinity of this well has a north-northwesterly azimuth. This would imply that the dominant extension fracture set would be oriented east-northeast. Inspection of the stereoplot set into the figure shows that the primary concentration of fracture poles indicates a predominant joint orientation of east-northeast.

The results for the third well, Shoshone 66-07, are shown in Figure 3-55. There are two dominant strain azimuths: north-south and northeast-southwest. These azimuths would imply that there should be two dominant joint set orientations: east-west and northwest-southeast. The rosette diagrams indicate that both east-west and northwest-southeast open and partially open joints are common in the subsurface.

Overall, there is very good agreement between the orientation of the fractures in the subsurface and the azimuth of the maximum extensional strain.

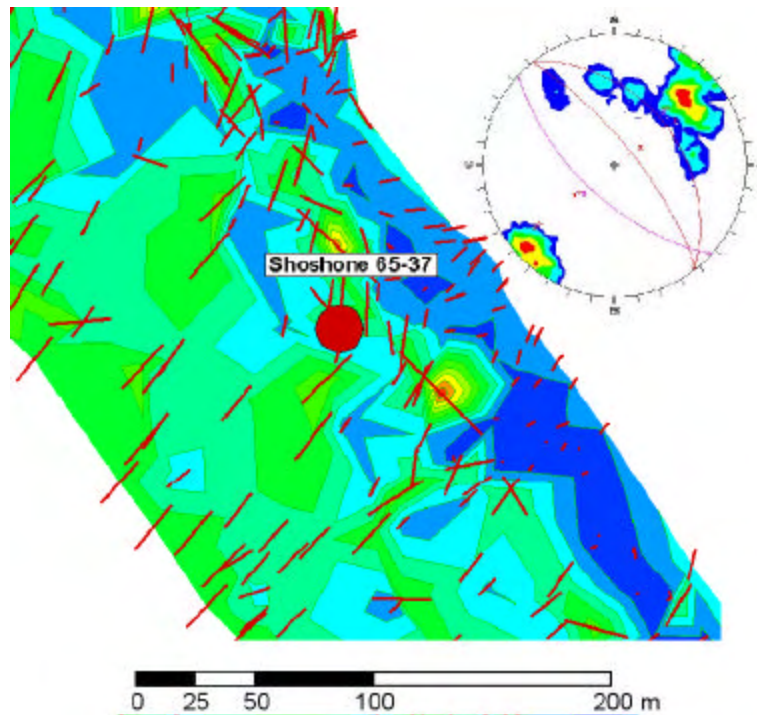


Figure 3-53. Comparison of fracture orientations in Shoshone 65-37 with direction of maximum extension.

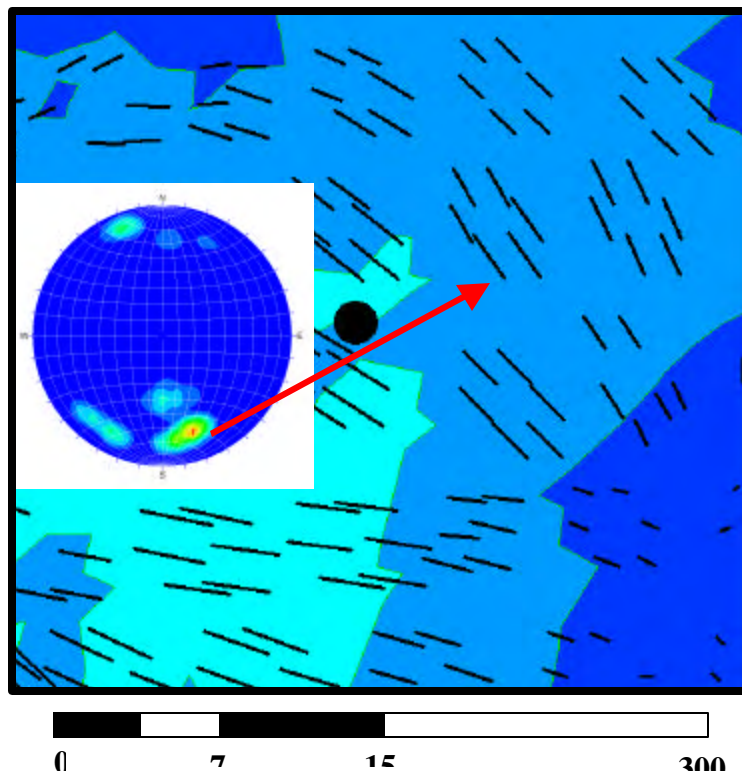


Figure 3-54. Comparison of fracture orientations in Shoshone 66-14 with direction of maximum extension.

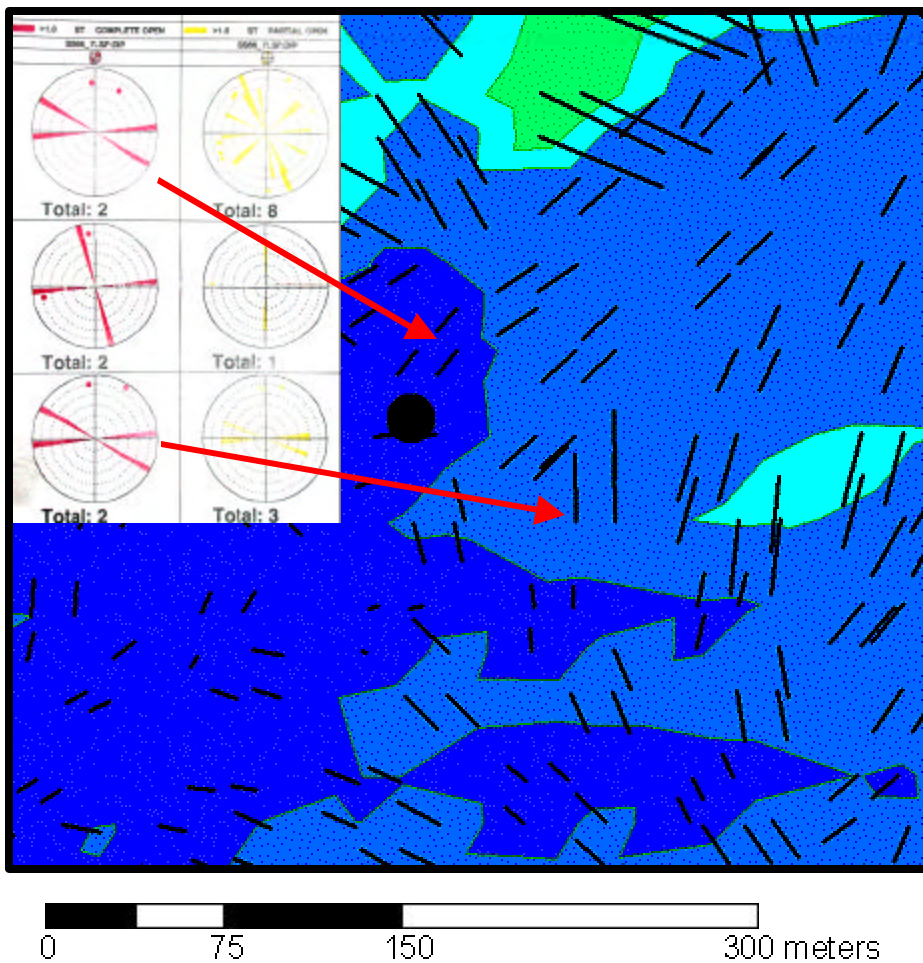


Figure 3-55. Comparison of fracture orientations in Shoshone 66-07 with direction of maximum extension.

#### 3.5.2.4 Fracture intensity variations & extensional strain magnitude

Figure 3-53 through Figure 3-55 show the magnitudes of extensional strain in the vicinity of the three wells. These figures show that the strain around Shoshone 66-14 and Shoshone 66-07 is both similar and low. The blue/light blue contour colors indicate magnitudes in the range  $-0.1$  to  $-0.2$ . The strain magnitude for Shoshone 65-37 is clearly much higher; the contour colors around this well represent a range from  $-0.3$  to  $-0.5$ . Thus, the palinspastic model predicts higher extensional strain for Shoshone 65-37, and similar but lower strains for the other two wells.

The fractures in the image logs have been categorized into open, partially open and filled fractures. The fracture intensity for each of these three wells has been computed and is presented in Table 3-2. Figure 3-56 shows the relation graphically.

Well	Fracture Intensity (fracs/m)	Strain Magnitudes
Shoshone 65-37	0.079	-0.3 to -0.5
Shoshone 66-07	0.034	-0.1 to -0.2
Shoshone 66-14	0.031	-0.1 to -0.2

Table 3-2. Fracture intensity vs. extensional strain.

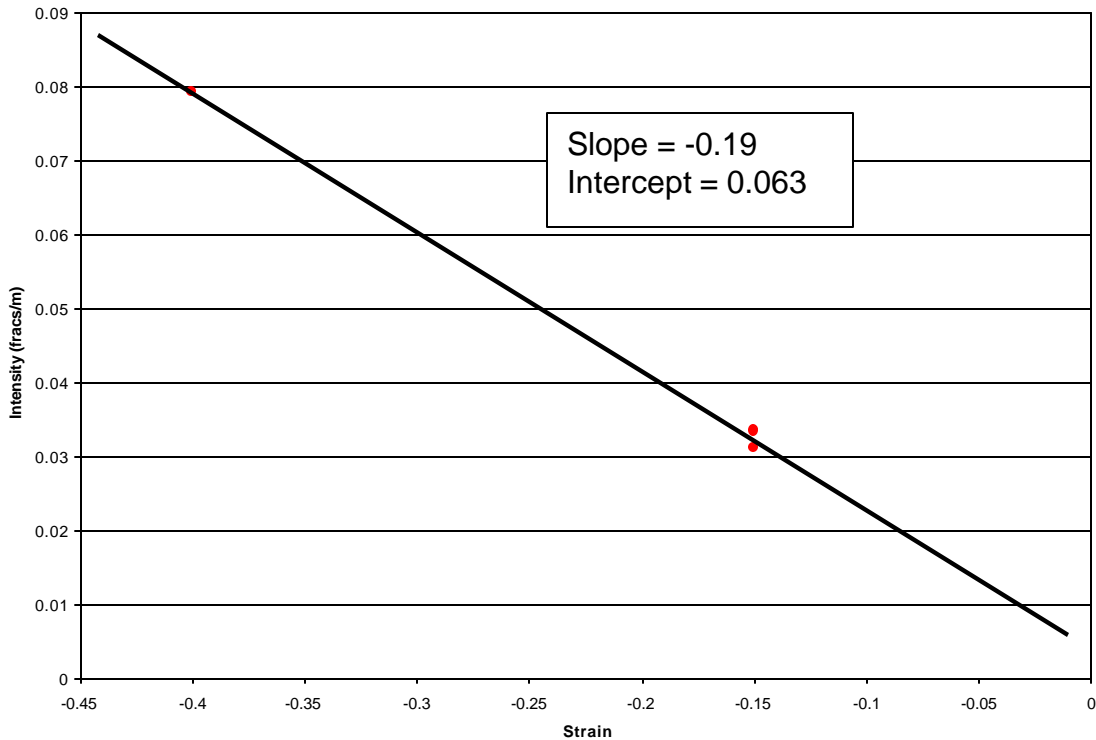
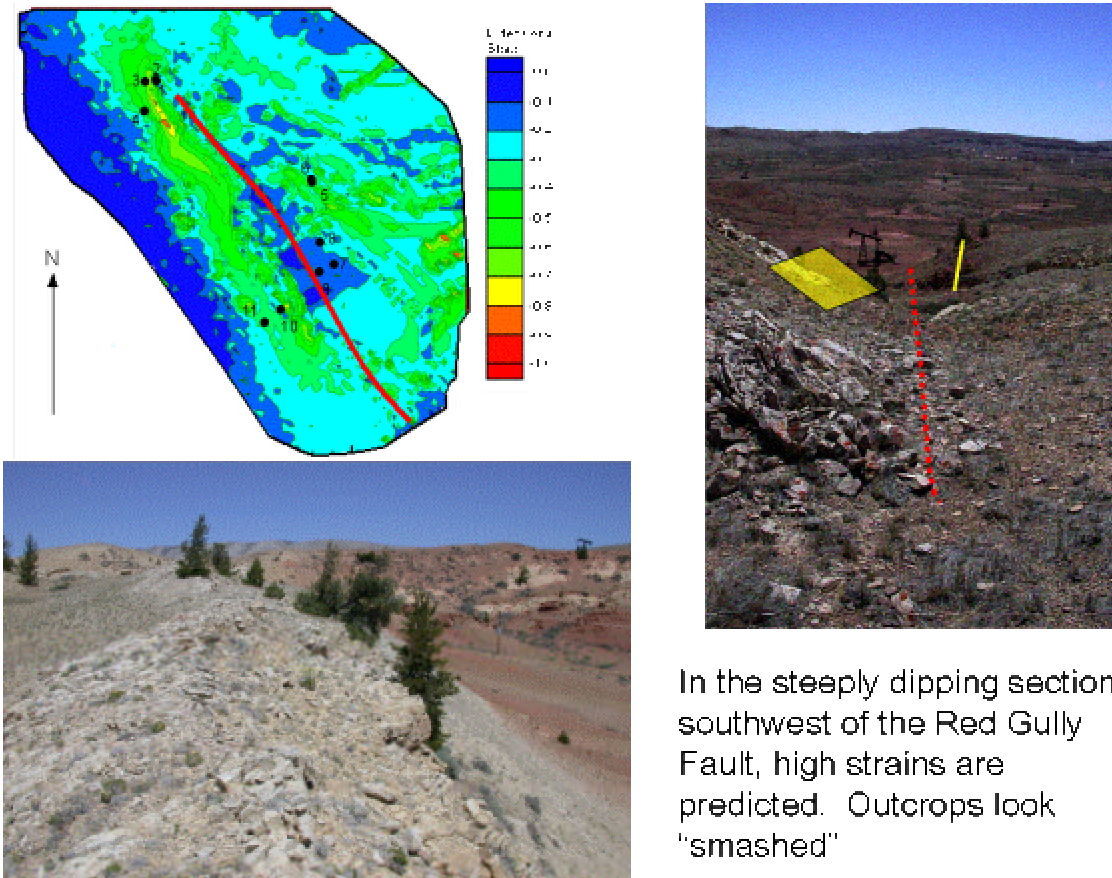


Figure 3-56. Graph of fracture intensity vs. extensional strain magnitude.

Both the table and the graph show a consistent relation between strain magnitude and fracture intensity. The significance of the straight-line fit to the data is probably not appropriate at small values of strain, since a strain value of 0.0 indicates that there would still be *some* fracturing, a physical impossibility. This discrepancy might be due to the fact that a few fractures encountered in the subsurface were formed by some structural event other than the folding; that the relation between strain and fracture intensity is not linear for small strain values; or might even be within the uncertainty surrounding the regression of three points.

What is significant is that the magnitude of extensional strain seems to be at least a very good qualitative predictor of the relative fracture intensity variations, and appears as if for the values greater than -0.1 to be linear.

The fracturing in outcrops also supports the usefulness of the strain magnitude for predicting relative fracture intensity.



**Figure 3-57. Comparison of strain magnitude and fracture intensity in outcrop near the northwest nose of the anticline.**

Figure 3-57 shows an area of the field where extensional strain is predicted to be very high. The red line in the upper left hand figure is the surface trace of the Red Gully Fault. The yellow and red colors in this map near scanline 4 indicate very high strains. Looking southeastward from the approximate northwest end of the Red gully Fault, the bedding orientation (shown as yellow planes in the photo on the right side) changes from shallowly dipping to nearly vertical. The area of the near-vertical beds is close to the scanline 4 location. The rock in this area is nearly rubblized (lower left-hand photograph), consistent with the predicted high strains.

### 3.5.3 EVOLUTION OF FRACTURE FAIRWAYS DUE TO DEVELOPMENT OF STRUCTURAL HINGES

Many of the regions of higher strain formed during the folding of the reservoir formations appear as horizontal or down-dip linear bands (Figure 3-58 and Figure 3-59). The first figure shows three of the uppermost imbricate blocks (Blocks 6, 8 and 9). The contours shown are those of maximum extensional strain produced by folding. In the palinspastic reconstruction, the formations were not folded uniformly, but rather along these flexural hinge zones. The 3D perspective view (Figure 3-59) shows this more clearly. The orange dashed lines in this figure delineate the horizontal hinge zones along which the formations were upwarped (lower line) and then flattened (upper line) during the palinspastic reconstruction process. These hinge zones developed prior to any faulting in the reconstruction.

Since these are such large-scale features, they should also be manifest in surface outcrops, at least in formations lying below the Gypsum Springs Formation. Outcrops in the field in fact do show the development of both horizontal and dip-parallel hinge zones.

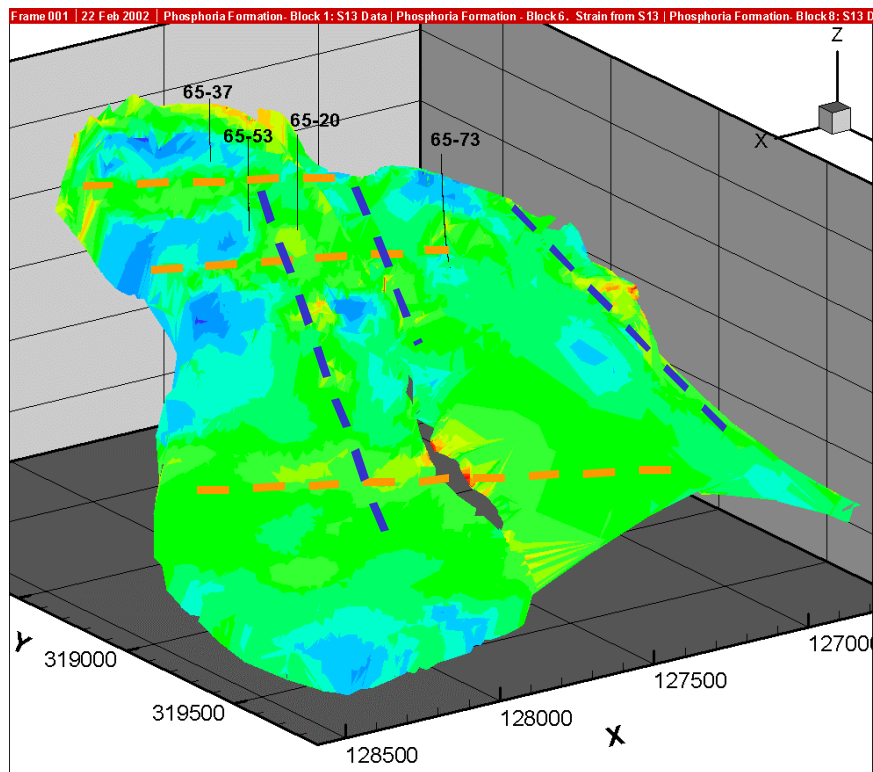
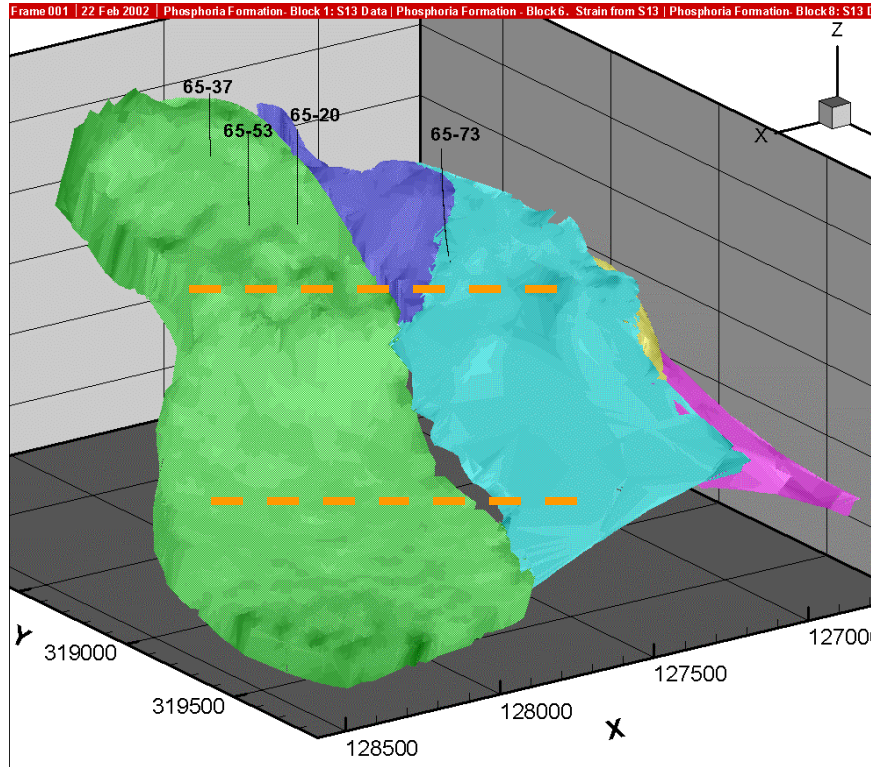


Figure 3-58. 3D view of imbricate blocks 6, 8 and 9 from the north looking south. The orange and blue dashed lines correspond to high strain corridors that separate the rock into panels that have more or less constant dip



**Figure 3-59. 3D view of imbricate blocks and illustration of two horizontal “hinges” or flexure zones (orange dashed lines) formed during the initial folding of the field.**

Figure 3-60 shows an example from the northwest end of the Field. This photograph shows a horizontal flexure zone. If rock were an elastic plate, then the beds would deform continuously without any discontinuities, as shown by the cyan-colored line in the photo. However, the rock actually deformed by breaking into blocks or panels. Within each block, the orientation of bedding is more or less constant, as shown by the red lines in the photo. The hinge zone separating these blocks is more highly fractured and eroded, and hence outcrops are rare or nonexistent.

Figure 3-61 shows a dip-parallel flexural hinge. This hinge occurs in the eastern portion of the field. Bedding orientation in the blocks on either side of the flexure zone strike more than  $18^\circ$  differently, and also have different amounts of dip on either side. In between these two blocks is a gully that delineates the flexure zone. In this zone, the rock is much more highly fractured, and as a result, eroded. Vegetation is also much more common in these gullies, probably due to a combination of the physical funneling of surface water through the gully, and the higher permeability of the rock.

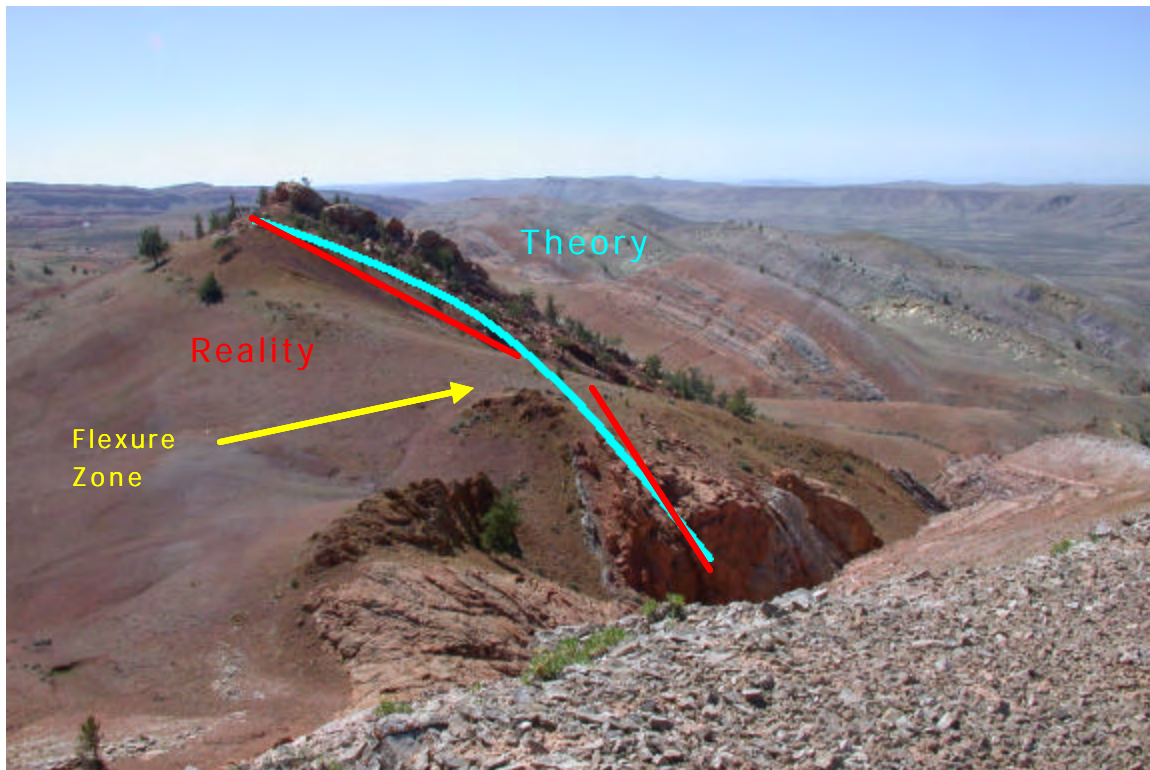


**Figure 3-60. Example of a horizontal flexure zone. Most rock does not deform in a continuous curve (cyan-colored line), but rather as panels with more or less constant curvature that deform in zones of higher intensity fracturing or faulting between panels (red lines). The more highly fractured nature of these hinge zones typically leads to greater erosion on the surface.**

As shown in these figures, the development of the hinge zones tends to fracture the rock far more than the surrounding rock. As a result, these zones erode easily in the surface, forming gulleys for the down-dip hinges, while the horizontal zones generally correspond to a loss of outcrop. They are often more permeable than the surrounding rock, as demonstrated by the increased density of vegetation.

One question remains concerning how significant these strain corridors formed through flexural hinge development are for controlling reservoir-scale flow patterns. Among other benefits of the tracer tests that were run for this project, they also make it possible to see if breakthrough patterns can be explained by the geometry of these hinge zones.

First, the bromide tracer test will be discussed. This test was carried out in the imbricate blocks 6, 8 and 9. It was designed not only to examine the connectivity in these imbricate blocks, but also to evaluate the connectivity between the Phosphoria and Tensleep Formations. The second test discussed is the Nitrogen Injection pilot carried out in the Overthrust (Block 1).

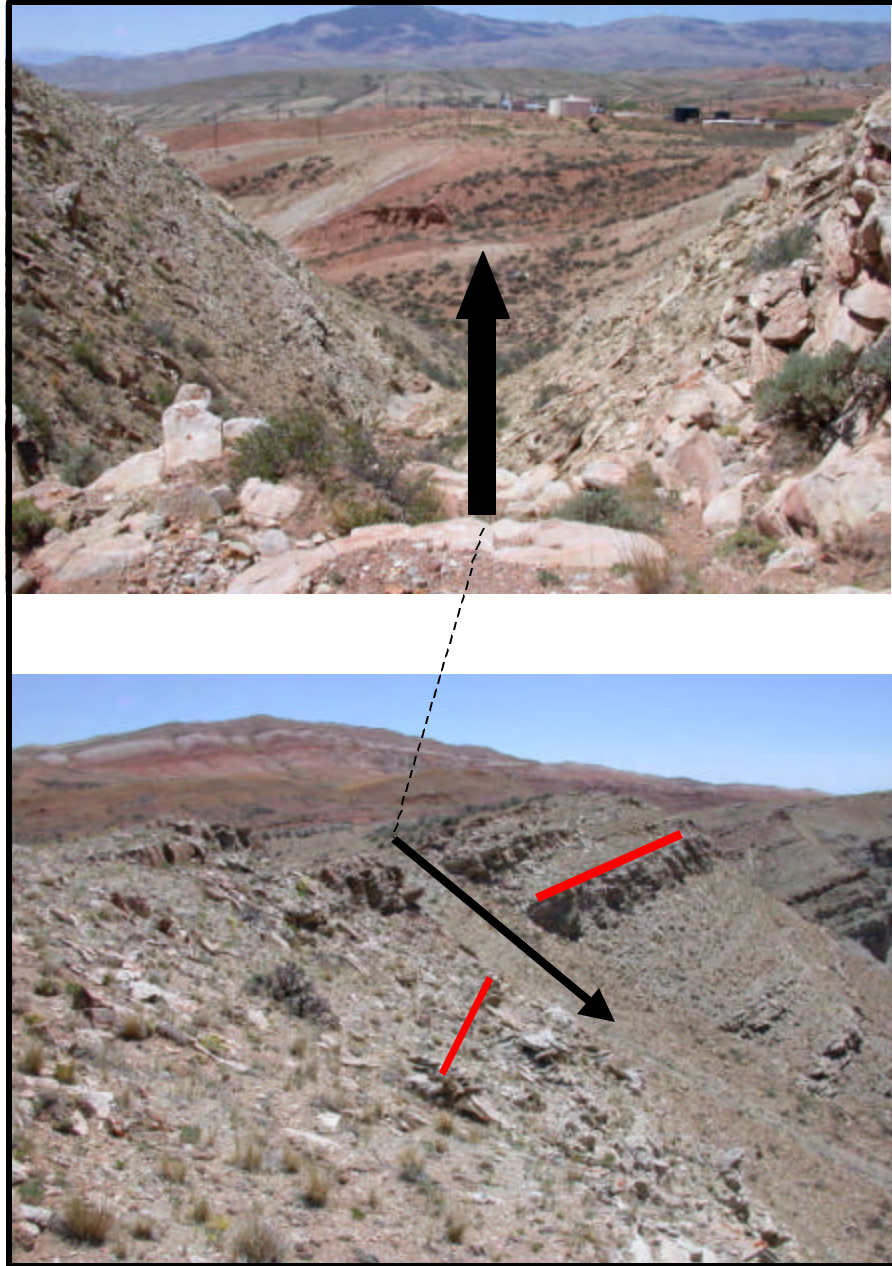


**Figure 3-61. Example of a dip-parallel flexural hinge zone. The lower photo shows approximate bedding orientation for two blocks of Crow Mountain in the eastern portion of the Field. The difference in strike is over  $18^\circ$ , although the perspective of the photo makes this less obvious. The black arrow indicates the location of the flexural hinge, and as seen in both the top photo and the lower photo, this zone is much more highly fractured and eroded than the adjacent rock blocks. The top photo is taken at the top of the flexural hinge gully looking downward in the direction of the arrow in the lower photo.**

### 3.5.3.1 Analysis of bromide tracer experiment

The bromide tracer experiment had several purposes: to test the connectivity between the Tensleep and Phosphoria Formations; to delineate the geometry of major flow conduits; to provide a basis for ascertaining whether the large scale fracture connectivity structure deduced from the palinspastic reconstructions and implied fracture patterns are consistent with the flow conduits or in fact could have been used to predict them; and to develop additional fluid flow properties for the DFN model.

The bromide tracer experiment involved a number of wells completed in the Tensleep and/or Phosphoria in imbricate blocks 6, 8 and 9 (Figure 3-62). Table 3-3 presents the data obtained at the injector and the monitoring wells over the course of the experiment. This raw data was converted to time vs. concentration plots (Figure 3-63). This graph shows the rapid breakthrough seen in Shoshone 65-53, the later breakthroughs in Shoshone 65-37 and Shoshone 65-73, and the lack of tracer breakthrough in the remaining monitored wells. Table 3-4 summarizes the time between injection and the highest measured bromide concentration in each monitoring well.

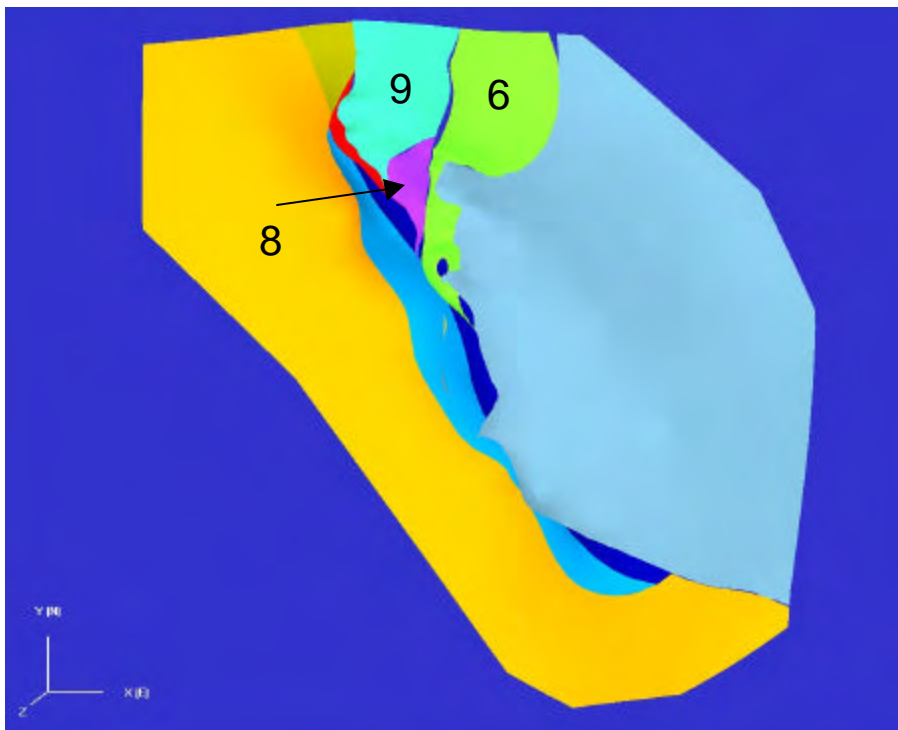


**Figure 3-62. Structural blocks involved in the Bromide Tracer experiment in the Phosphoria Formation. Blocks 6, 8 and 9 are the uppermost imbricate fault blocks.**

Bromide Results for Offsets on:											SHOSHONE 65-20 P				
	10/26	10/29	11/02	11/05	11/08	11/15	11/16	11/17	11/19	11/21	11/23	11/25	11/27	11/30	
INJECTOR DATA															
# BROMIDE INJECTED						3339									
CONC. SODIUM BROMIDE %						24									
INJECTION RATE BPD						400									
DAYS SINCE INJECT.						0.229	0.840	2	4	6	8	10	12	15	
DISPLACEMENT BBLs.						40	166	572	1352	2202	3348	4494	5640	7253	
OFFSET DATA															
Shoshone 65-8															
BROMIDE, PPM	0.18	0.08	0.08	0.11	0.06	0.07	0.08	0.07	0.41	0.09	0.08	0.10	0.14	0.09	
BR-BGRD, PPM						0.00	0.00	0.00	0.31	0.00	0.00	0.00	0.03	0.00	
BWPD						303	303	303	303	303	303	303	303	303	
# BR PROD.						0.00	0.00	0.00	0.03	0.00	0.00	0.00	0.00	0.00	
CUM # BR PROD.						0.00	0.00	0.00	0.03	0.07	0.07	0.07	0.07	0.07	
% RECOVERY						0.00	0.00	0.00	0.00	0.00	0.00	0.00	0.00	0.00	
NOTES															
Shoshone 65 14TA															
BROMIDE, PPM	0.07	0.06	0.01	0.10	0.08	0.05	0.09	0.09	0.09	0.11	0.13	0.14	0.45	0.12	
BR-BGRD, PPM						0.00	0.03	0.02	0.02	0.04	0.06	0.08	0.39	0.06	
BWPD						98	98	98	98	98	98	98	98	98	
# BR PROD.						0.00	0.00	0.00	0.00	0.00	0.00	0.00	0.01	0.00	
CUM # BR PROD.						0.00	0.00	0.00	0.00	0.01	0.01	0.01	0.03	0.05	
% RECOVERY						0.00	0.00	0.00	0.00	0.00	0.00	0.00	0.00	0.00	
NOTES															
Shoshone 65 37PT															
BROMIDE, PPM	0.15	0.22	0.14	0.21	0.13	Down	Down	0.50	105.69	532.54	448.01	288.85	157.10	115.14	
BR-BGRD, PPM						0.00	0.00	0.32	105.52	532.37	447.84	288.67	156.93	114.97	
BWPD						14	14	14	14	14	14	14	14	14	
# BR PROD.						0.00	0.00	0.00	0.50	2.52	2.12	1.36	0.74	0.54	
CUM # BR PROD.						0.00	0.00	0.00	0.50	3.51	8.15	11.63	13.73	15.66	
% RECOVERY						0.00	0.00	0.00	0.02	0.11	0.24	0.35	0.41	0.47	
NOTES															
Shoshone 65 44T															
BROMIDE, PPM	0.06	0.09	0.10	0.00	0.00	0.09	0.91	0.94	1.07	1.33	1.27	1.30	0.89	0.76	
BR-BGRD, PPM						0.04	0.86	0.89	1.02	1.28	1.22	1.25	0.84	0.71	
BWPD						227	227	227	227	227	227	227	227	227	
# BR PROD.						0.00	0.07	0.07	0.08	0.10	0.10	0.10	0.07	0.06	
CUM # BR PROD.						0.00	0.02	0.10	0.26	0.44	0.64	0.83	1.00	1.18	
% RECOVERY						0.00	0.00	0.00	0.01	0.01	0.02	0.02	0.03	0.04	
NOTES															
Shoshone 65-45PTA															
BROMIDE, PPM	0.12	0.03	0.12	0.10	0.11	0.41	0.12	0.12	0.13	0.14	0.21	0.19	0.41	0.28	
BR-BGRD, PPM						0.31	0.02	0.03	0.03	0.05	0.11	0.09	0.32	0.19	
BWPD						144	144	144	144	144	144	144	144	144	
# BR PROD.						0.02	0.00	0.00	0.00	0.00	0.01	0.00	0.02	0.01	
CUM # BR PROD.						0.00	0.01	0.01	0.01	0.02	0.02	0.03	0.06	0.09	
% RECOVERY						0.00	0.00	0.00	0.00	0.00	0.00	0.00	0.00	0.00	
NOTES															
Shoshone 65-52I															
BROMIDE, PPM	0.00	0.00	0.00	0.00	0.00	0.18	0.16	0.09	0.09	0.10	0.10	0.11	0.16	0.17	
BR-BGRD, PPM						0.18	0.16	0.09	0.09	0.10	0.10	0.11	0.16	0.17	
BWPD						638	638	638	638	638	638	638	638	638	
# BR PROD.						0.04	0.04	0.02	0.02	0.02	0.02	0.02	0.04	0.04	
CUM # BR PROD.						0.01	0.03	0.06	0.10	0.14	0.19	0.24	0.30	0.41	
% RECOVERY						0.00	0.00	0.00	0.00	0.00	0.01	0.01	0.01	0.01	
NOTES															
Shoshone 65-53PT															
BROMIDE, PPM	0.00	0.00	0.00	0.00	0.00	703.73	543.19	231.40	203.32	121.07	85.18	59.20	42.43	38.00	
BR-BGRD, PPM						703.73	543.19	231.40	203.32	121.07	85.18	59.20	42.43	35.00	
BWPD						1564	1564	1564	1564	1564	1564	1564	1564	1564	
# BR PROD.						385.22	297.34	126.67	111.30	66.27	46.63	32.40	23.23	19.16	
CUM # BR PROD.						88.22	296.74	542.67	780.63	958.20	1071.10	1150.13	1205.76	1269.34	
% RECOVERY						2.64	8.89	16.25	23.38	28.70	32.08	34.45	36.11	38.02	
NOTES															
Shoshone 65-54PT															
BROMIDE, PPM	0.84	0.83	0.44	0.39	0.44	0.62	1.23	0.44	0.42	0.45	0.44	0.38	0.41	0.70	
BR-BGRD, PPM						0.03	0.64	0.00	0.00	0.00	0.00	0.00	0.00	0.12	
BWPD						8	8	8	8	8	8	8	8	8	
# BR PROD.						0.00	0.00	0.00	0.00	0.00	0.00	0.00	0.00	0.00	
CUM # BR PROD.						0.00	0.00	0.00	0.00	0.00	0.00	0.00	0.00	0.00	
% RECOVERY						0.00	0.00	0.00	0.00	0.00	0.00	0.00	0.00	0.00	
NOTES															
Shoshone 65-61PT															
BROMIDE, PPM	0.22	0.11	0.09	0.27	0.24	1.72	0.73	0.12	0.12	0.11	0.12	0.13	0.09	0.60	
BR-BGRD, PPM						1.54	0.54	0.00	0.00	0.00	0.00	0.00	0.00	0.42	
BWPD						308	308	308	308	308	308	308	308	308	
# BR PROD.						0.17	0.08	0.00	0.00	0.00	0.00	0.00	0.00	0.05	
CUM # BR PROD.						0.04	0.11	0.14	0.14	0.14	0.14	0.14	0.14	0.21	
% RECOVERY						0.00	0.00	0.00	0.00	0.00	0.00	0.00	0.00	0.01	
NOTES															
Shoshone 65-67PT															
BROMIDE, PPM	0.21	0.19	0.07	0.22	0.20	0.15	0.42	0.66	0.47	0.68	1.01	1.08	1.19	1.12	
BR-BGRD, PPM						0.00	0.24	0.49	0.29	0.50	0.84	0.90	1.01	0.94	
BWPD						612	612	612	612	612	612	612	612	612	
# BR PROD.						0.00	0.05	0.10	0.06	0.11	0.18	0.19	0.22	0.20	
CUM # BR PROD.						0.00	0.02	0.11	0.27	0.44	0.73	1.10	1.51	2.14	
% RECOVERY						0.00	0.00	0.00	0.01	0.01	0.02	0.03	0.05	0.06	
NOTES															
Shoshone 65-73P															
BROMIDE, PPM	0.09	0.09	0.07	0.22	0.26	0.30	3.57	3.21	3.14	3.11	2.30	2.11	2.25	1.30	
BR-BGRD, PPM						0.16	3.42	3.06	2.99	2.96	2.15	1.96	2.10	1.15	
BWPD						250	250	250	250	250	250	250	250	250	
# BR PROD.						0.01	0.30	0.27	0.26	0.26	0.19	0.17	0.18	0.10	
CUM # BR PROD.						0.00	0.10	0.43	0.96	1.48	1.93	2.29	2.64	3.07	
% RECOVERY						0.00	0.00	0.01	0.03	0.04	0.06	0.07	0.08	0.09	
NOTES															
ALL OFFSETS															
# BR PROD.						385.46	297.86	127.13	112.26	69.28	49.24	34.27	24.50	20.16	
CUM # BR PROD.						88.27	297.03	543.52	782.91	964.45	1082.97	1166.47	1225.24	1292.23	
% RECOVERY						2.64	8.90	16.28	23.45	28.88	32.43	34.93	36.69	38.70	

Table 3-3. Raw data obtained in injection and monitoring wells during the bromide tracer experiment.

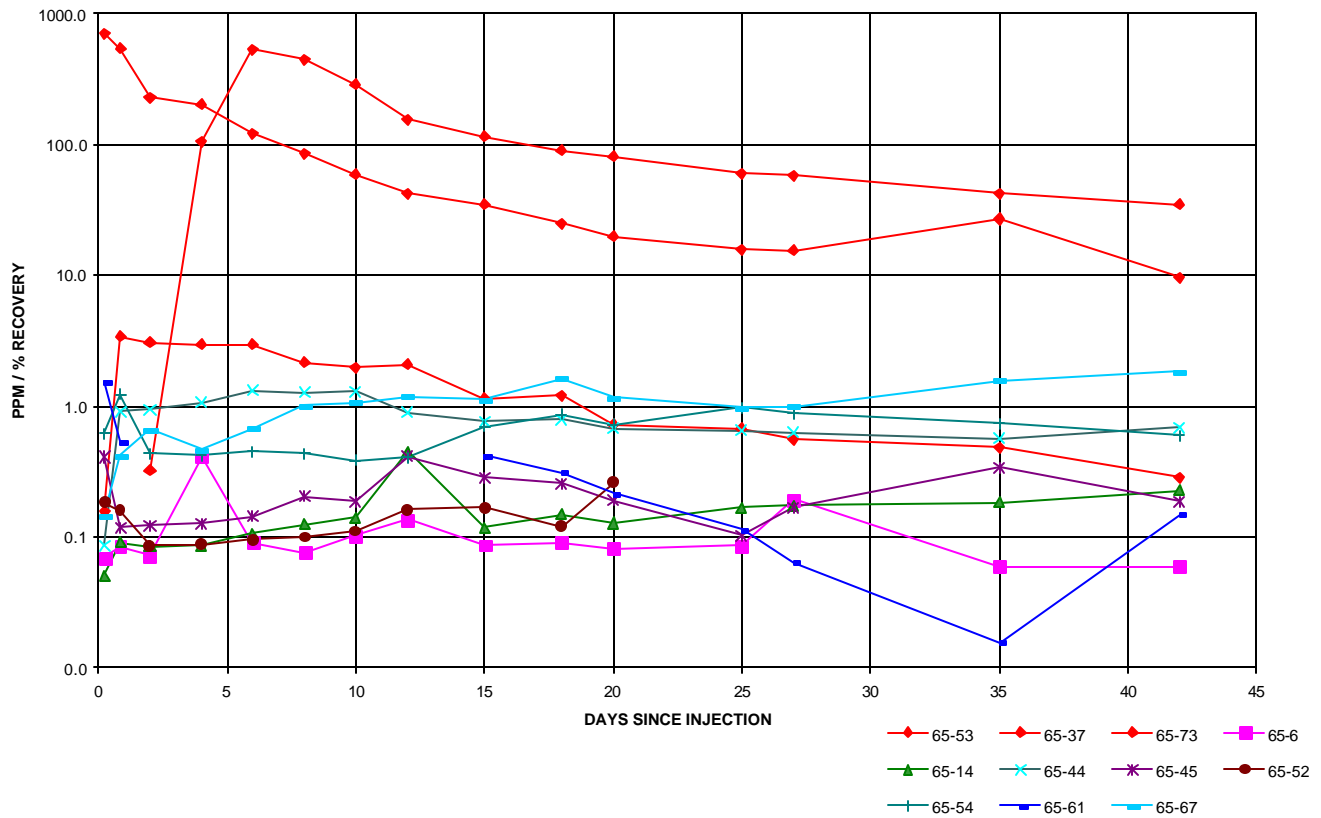


Figure 3-63. Time vs. bromide concentration for the bromide tracer test monitoring wells.

Well	Time (days)	
	Peak	First Break
65-53	Instant	
65-73	0.84	
65-37	4.00	
65-67	2.00	
65-06	4.00	
65-14	12.00	0.84
65-44	0.84	
65-45	12.00	
65-52	12.00	0.18
65-54	15.00	0.84
65-61	15.00	

Table 3-4. Summary of time to maximum measured bromide concentration. Values for wells shaded yellow represent maximum measured concentrations, but do not correspond to obvious breakthroughs, and may be more due to random fluctuations in bromide levels, measurement precision, minor breakthroughs, or some combination of these factors.

Figure 3-64 shows that breakthrough did not occur in the three wells completed in the Tensleep but not the Phosphoria (Shoshone 65-14, 65-44 and 65-52). This may indicate a decoupling of the fracture system in the upper Tensleep and the lower Phosphoria. There is field evidence for this decoupling in outcrops of the upper Tensleep at Zeisman Dome on the west flank of the Bighorn Basin between Manderson and Worland, WY (Figure 3-65). The cliff in the upper portion of this figure shows a number of joints that are subvertical and cut through the entire cross-bedded dune sequence making up most of the visible rock in the photo. A closer examination of the contact between these dunes and the underlying interdune sequence shows how these large, dramatic joints typically terminate against this depositional boundary. Inspection of the contact along the entire exposed sequence boundary revealed no fractures that encompassed both the dune and interdune portions of the Tensleep. While the upper contact with the Phosphoria was not observed the lower termination suggests that the large jointing is very much confined to the dune sequence.

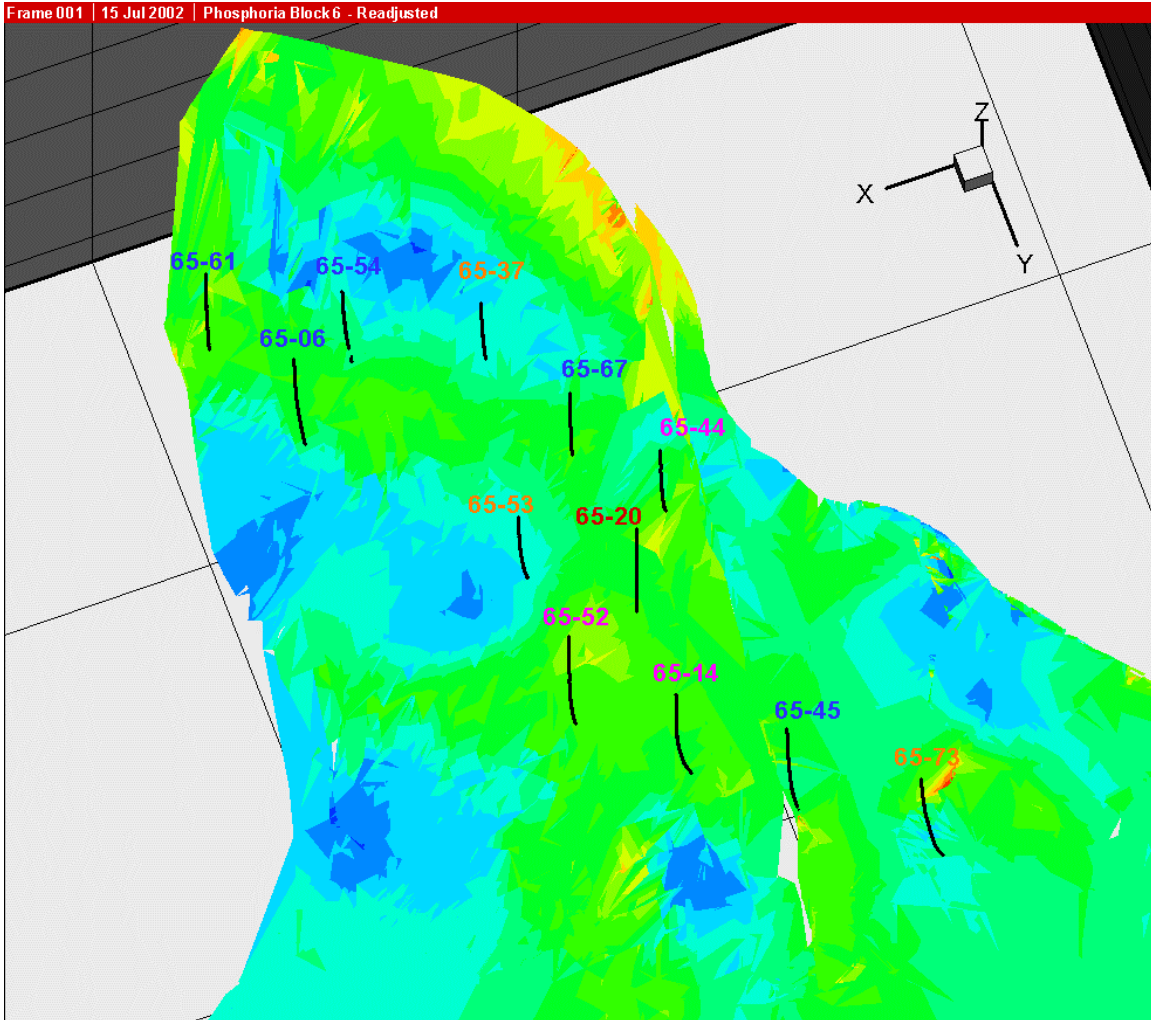
The remaining eight monitoring wells were completed in the Phosphoria and also may have completions in the Tensleep. The strain contours are consistent with many, but not all, of the responses.

Figure 3-66 shows a display of the wells, the strain field and the inferred strike direction of the dominant extensional fracture set that would be expected to develop consistent with the strain field. Under the assumption that fluids would be more likely to follow paths defined by corridors of intense fracturing, and in the direction of the dominant fracture set, this figure explains almost all Phosphoria completion wells except Shoshone 65-44.

Consider first the wells in Fault Block 6, the imbricate lying to the left of the Green Valley Fault in the figure. Shoshone 65-53 showed an almost immediate breakthrough, which is consistent with its close proximity to the injector, its presence in the same high strain region as the injector, and the strike of fractures that would provide a pathway from the injector to the well.

There are several corridors of higher strain that develop in all of the fault blocks, as shown by the green contours in Figure 3-64 and Figure 3-66. All of the Phosphoria wells lie in or near these corridors, however, breakthrough did not occur in all of them.

The explanation for the lack of breakthrough in Shoshone 65-06, Shoshone 65-54 and Shoshone 65-61 may be due to a fracture network "divide", as shown in Figure 3-66. The possible fracture network divide is shown as a red dotted line in the figure. Flow through the fracture system from right to left along this corridor might be inhibited by the orientations of the fractures at the divide: flow would have to occur perpendicular to the prevailing fracture direction. The remaining two wells, Shoshone 65-37 and Shoshone 65-67, lie in the same strain corridor as the injector and on the same side of the divide.



**Figure 3-64. Bromide tracer test breakthrough pattern.** The bromide was injected into Shoshone 65-20 (colored red). Large and nearly instantaneous breakthrough was seen in Shoshone 65-53; other strong breakthroughs were seen in Shoshone 65-37 (4 days) and in Shoshone 65-73 (20 hours). These wells are colored orange. The other wells (purple indicates a Tensleep completion with no Phosphoria completion; blue a Phosphoria completion) were monitored, but no large breakthroughs were seen.

It is possible that this higher permeability zone diverts flow from Block 6 to Block 8. Evidence of this type of behavior has been documented for many faults. Shoshone 65-45 penetrates the Phosphoria near, but still some tens of meters away from the fault. It is possible that the reason for the lack of response is that tracer was diverted along the Green Valley Fault zone, and thus did not reach the well.

The other well, Shoshone 65-73, is in a much larger imbricate separated from Block 8 by the Yellow Flats Fault, and is in a large fracture zone following the footwall of the Yellow Flats Fault. This fault zone seems to be both wider, better connected and more intense than the Green Valley Fault zone, and perhaps explains why Shoshone 65-73 experienced breakthrough in less than a day.

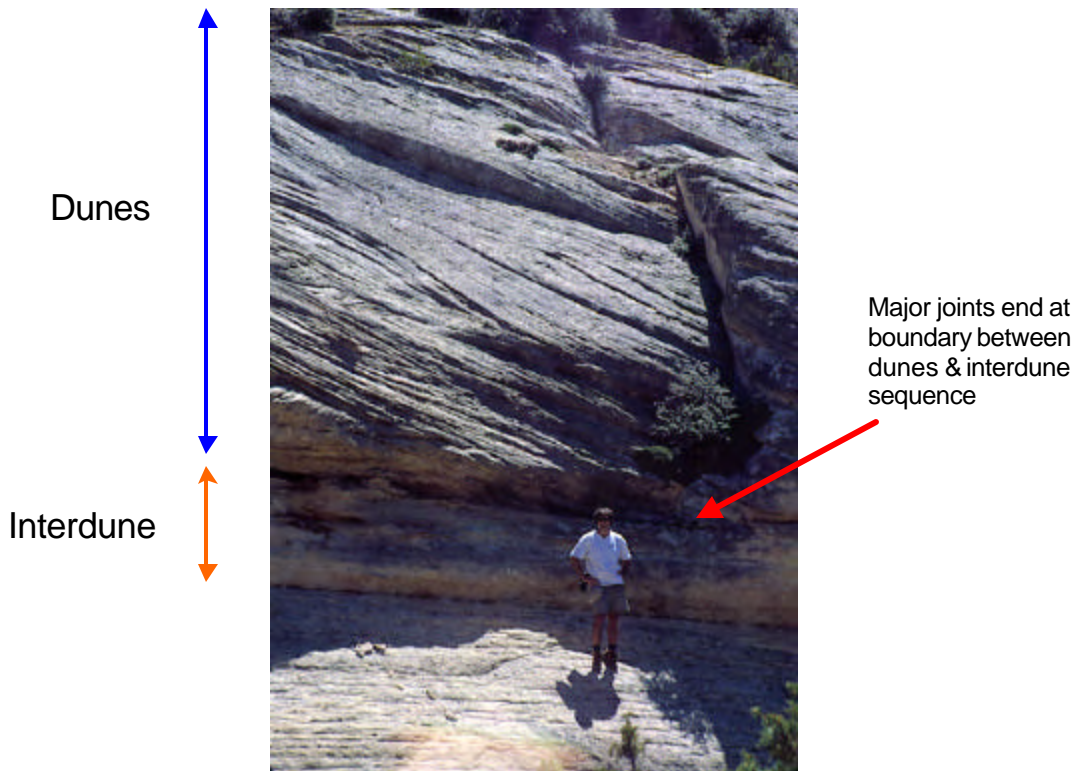
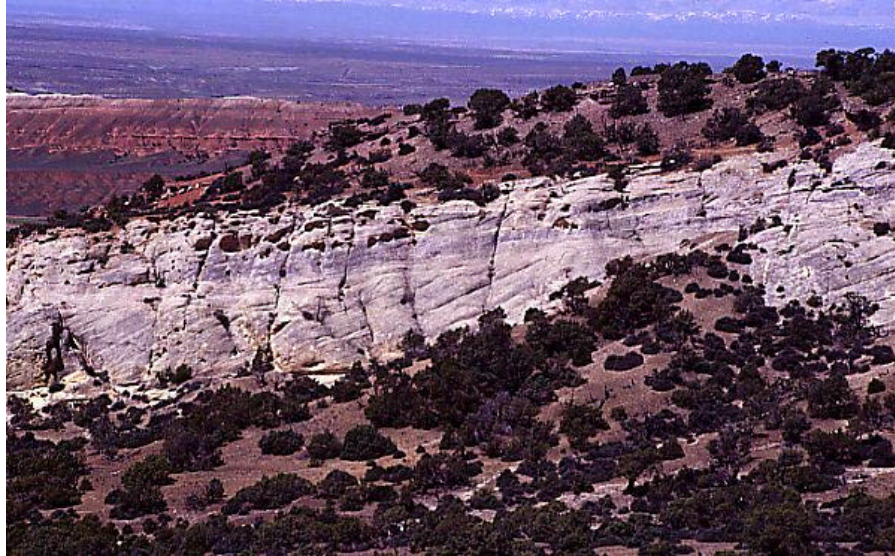


**Figure 3-65. Large-scale fracturing in the upper Tensleep Formation at Zeisman dome. Upper photo shows large joints that extend from the top of the dune sequence to the bottom of the dune sequence, but consistently terminate at the boundaries of the dune sequence (lower photo).**

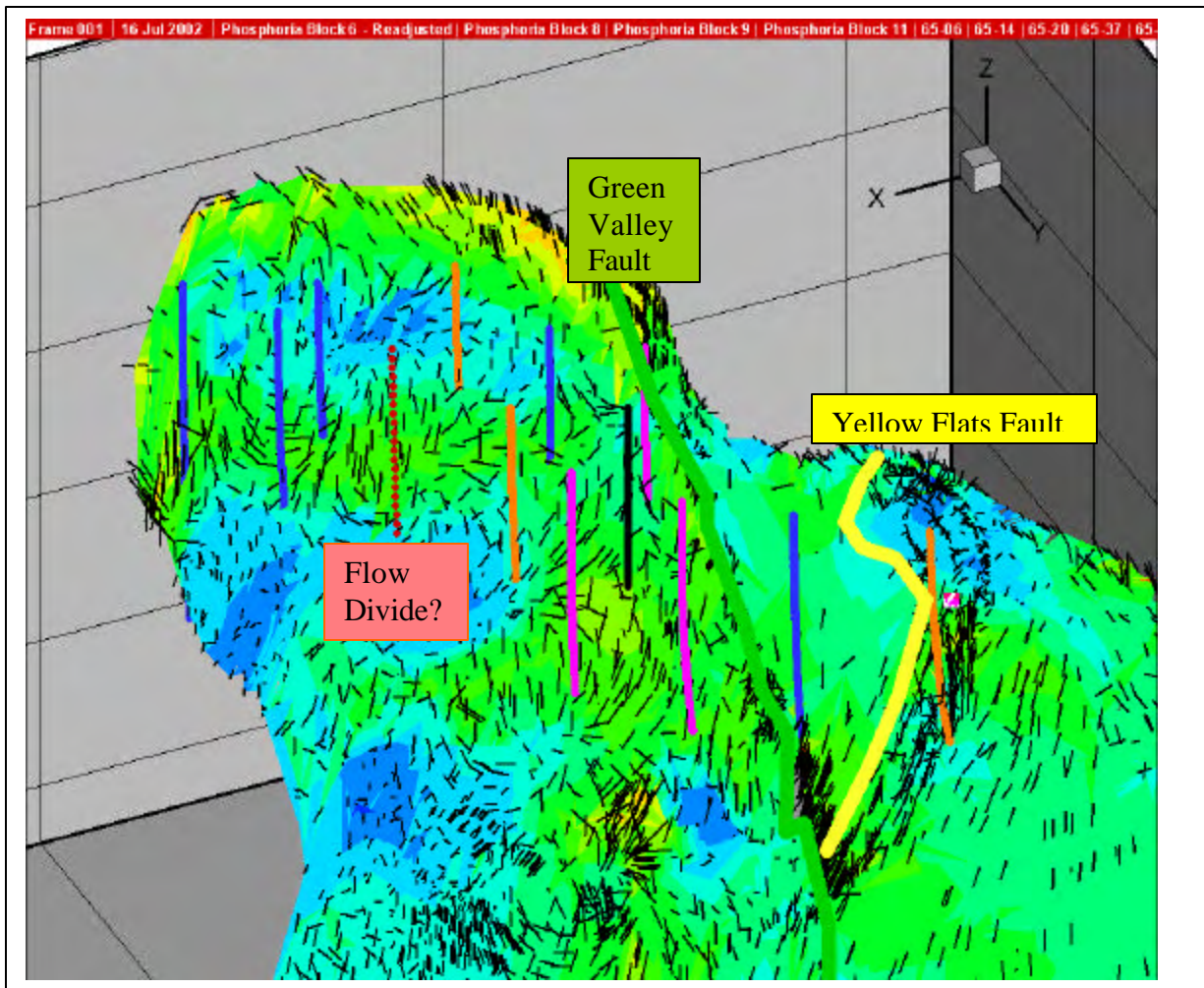


Figure 3-66. Fracture strikes inferred from strain field. Black lines indicate strike of dominant extensional fracture set, while length of line and color of contour indicates the magnitude of extensional strain. Wells are color-coded according to result and completion interval: black = injector; purple = Tensleep but no Phosphoria completion; blue = Phosphoria completion but no response; orange = Phosphoria completion and breakthrough observed.

### 3.5.3.2 Breakthrough Patterns In the Nitrogen Injection Test

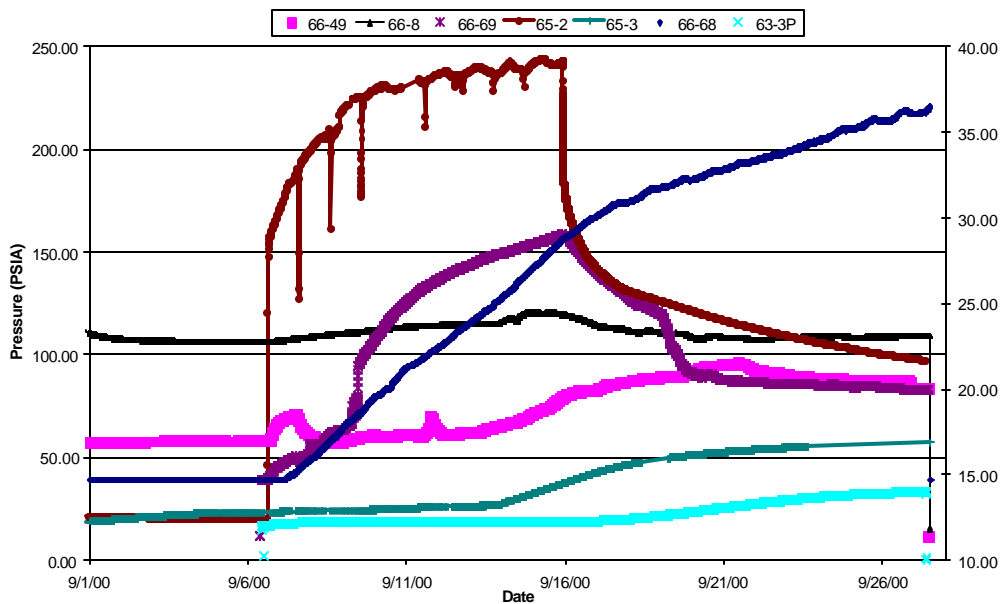
Some of the test parameters for the Nitrogen Injection experiment have been described in Section 2.6.5.1. Table 3-5 shows the injection rates for the test. Figure 3-67 and Figure 3-68 shows the bottom hole and surface pressures measured during the test.

The gas initially broke through down structure to the east at Shoshone 66-69 and 66-40. This breakthrough was along a high directional permeability trend, which had previously been determined from multi-well pressure interference testing. The down structure gas coning occurred prior to gas breakthrough at Shoshone 65-3, an observation well to the

Date	Time	Hours From Start	Instant. Injection Rate (MMCFD)	Instant. Injection Rate (scfm)	Daily Average Injection Rate (MMCFD)	Surface Instant. Injection Pressure (PSI)	Btm. Hole Instant. Injection Pressure (PSIA)	Cumulative Injection (MMCF)
9/6/2000	14:44	0		0	0	3	20	0
9/6/2000	18:00	3.283	1.6530192	1147.93	na	160	160.2	0.225922
9/7/2000	18:00	27.283	1.6790976	1166.04	1.602446	192	195.2	1.828368
9/8/2000	18:00	51.283	1.64683872	1143.638	1.621978	204.5	208.2	3.450346
9/9/2000	18:00	75.283	1.92005424	1333.371	1.864399	223.6	226.1	5.314745
9/10/2000	18:00	99.283	1.88510112	1309.098	1.903202	227.2	229.3	7.217947
9/11/2000	18:00	123.283	2.12548032	1476.028	1.948353	233.6	234.1	9.166301
9/12/2000	18:00	147.283	2.135448	1482.95	2.115795	238.1	236.1	11.2821
9/13/2000	18:00	171.283	2.01242592	1397.518	2.108292	233.3	232.0	13.39039
9/14/2000	18:00	195.283	2.0577096	1428.965	2.06209	237.2	238.3	15.45248
9/15/2000	18:00	219.283	2.04702624	1421.546	2.073576	239.3	241.2	17.52605
9/15/2000	21:53	223.166	2.06718624	1435.546	na	240.4	242.7	17.85791
						Test Rate Ave (MMCFD)		1.920498

Table 3-5. Injection rate data for nitrogen injection test.

Figure 3-67. Bottom-hole pressures measured during nitrogen injection test.



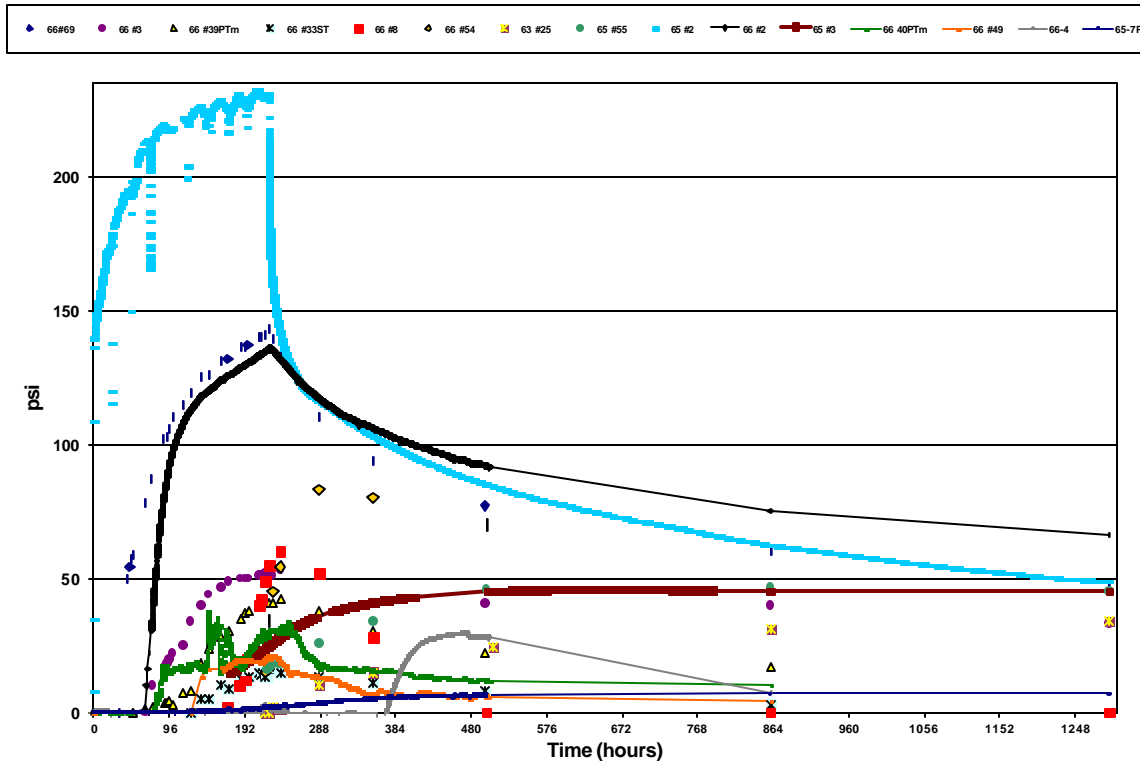


Figure 3-68. Surface pressures measured during the nitrogen injection test.

north. Shoshone 65-3's open hole completion interval included Overthrust Tensleep at approximately the same structural elevation as the nitrogen injector.

Gas breakthrough was noted at over twenty monitor wells during and following gas injection. Times for breakthrough were noted whenever possible. Gas breakthrough occurred in both the Overthrust Tensleep and Overthrust Phosphoria reservoirs. The communication between the Overthrust Tensleep and the Overthrust Phosphoria may have occurred through reservoir pathways or at individual wellbores. .

A block of Overthrust Tensleep with apparently little or no effective fracturing was also highlighted by the nitrogen test. This block surrounds Shoshone 66-68. While liquid pressure response was observed at this well, no gas breakthrough occurred. Shoshone 66-68 is located up structure of other gas breakthrough wells (Shoshone 66-8 and Shoshone 66-55) and down structure of the gas injector, Shoshone 65-2.

As was the case for the bromide tracer test, the areas of high strain in the palinspastic reconstruction generally corresponded to pathways between the injector and wells where breakthrough was measured.

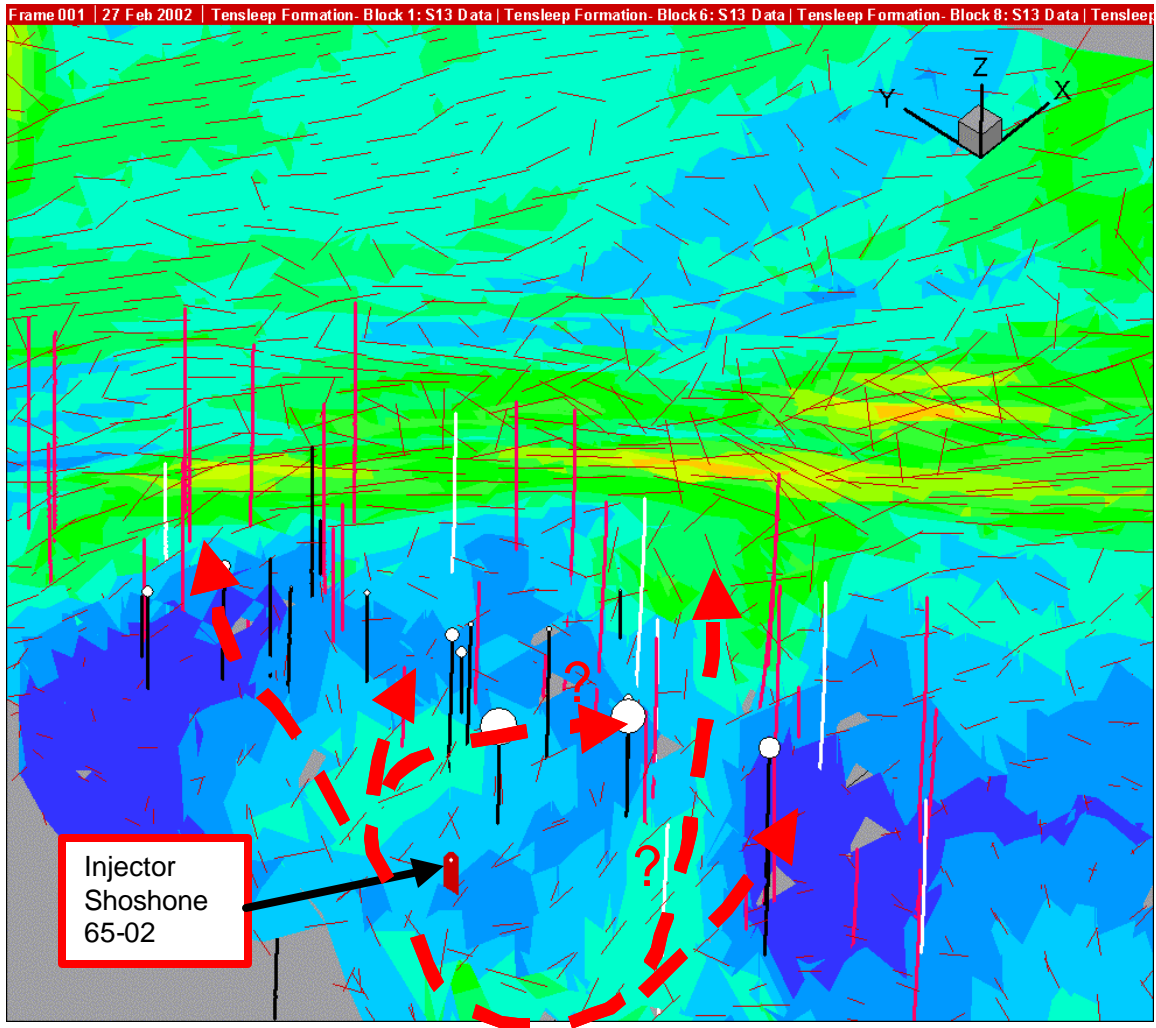


**Figure 3-69. Overview of Nitrogen Injection tests results. The Overthrust Block is viewed looking from southeast to northwest. Contours indicate extensional strain magnitude, red lines indicate strike of fractures in response to extensional strain field. Wells where nitrogen breakthrough was indicated are shown; size of yellow circle at well top indicates the time of breakthrough (large circle indicate slow response; small circles indicate rapid response). Nitrogen test took place in upper portion of the structure where the reservoir tends to flatten.**

Figure 3-69 shows an overview of the nitrogen injection test results. Most of the wells where nitrogen breakthrough was observed are located on the top, flatter portion of the structure. The inferred flexure zones are also shown. A number of wells that were also monitored, but where no nitrogen breakthrough was observed, occurred downdip from the responding wells.

This can be seen a little more clearly in Figure 3-70, which shows the results of the pressure magnitudes. In this figure, the size of the white circle atop the well is proportional to the pressure magnitude observed. Although there were many wells monitored downdip from the injection well, only those wells within the immediate cyan-

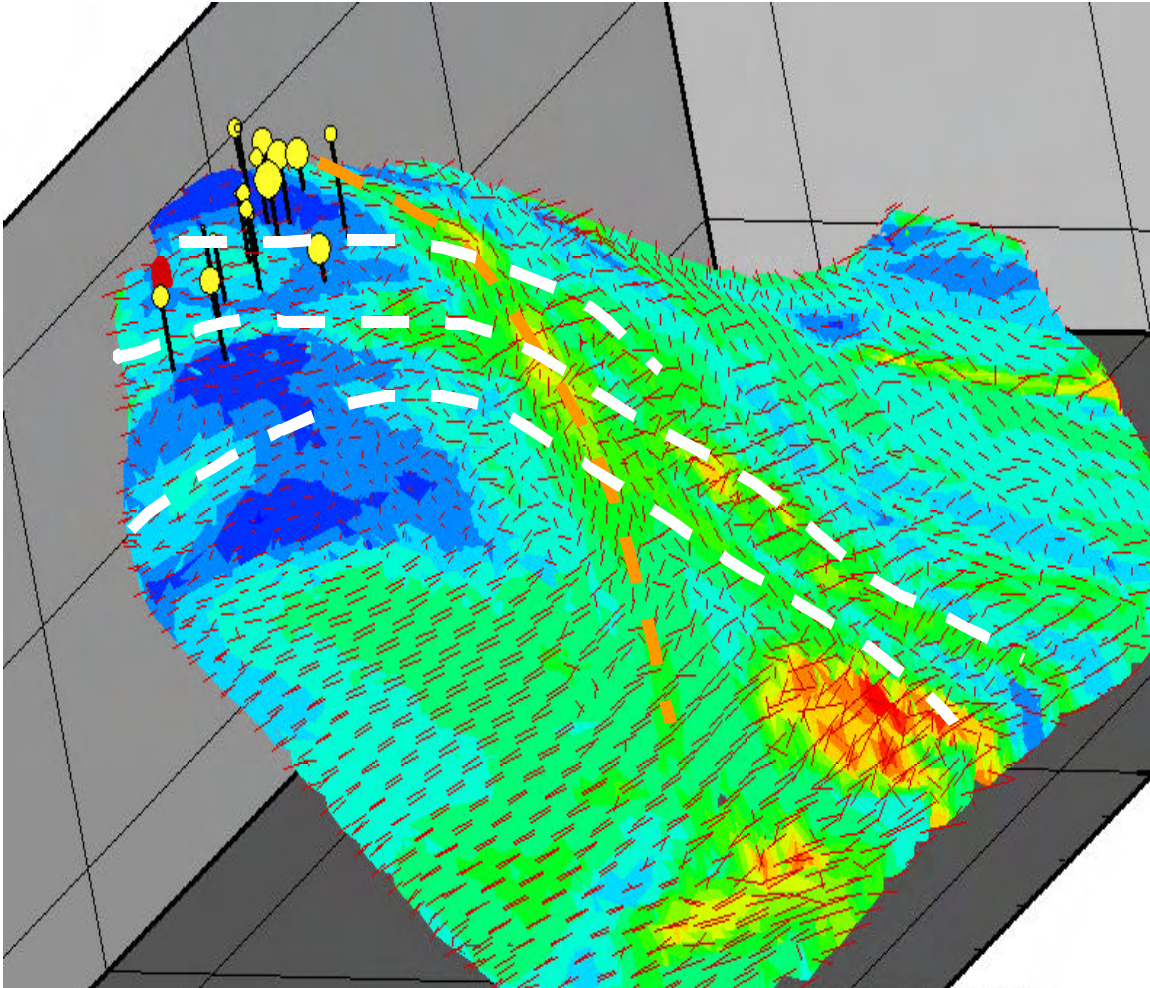


**Figure 3-70. Pressure magnitudes and possible migration pathways for the nitrogen injection test. View is looking down on the structure from the southwest to the northeast. Size of circles indicates magnitude of pressure response. The largest responses were seen in two wells on flexure corridors close to the injector. Most of the responding wells are either in the cyan-colored pod above and left (northwest) of the injector, or along the downdip flexure corridor to the right (southeast) of the injector.**

colored contours (indicative of higher strains) showed pressure response. Figure 3-71 shows a similar migration fairway in terms of time to breakthrough. Wells close in terms of path length along a fracture corridor from the injector tended to experience stronger and more rapid breakthrough. Wells at the distant ends of the corridors experienced slower and smaller magnitude breakthroughs. Monitoring wells separated from the fracture corridors by regions of low strain showed no breakthroughs. Essentially, the responding wells occur in one of two main strain “pods”, or regions of higher strain (Figure 3-72). It is not clear why the monitoring wells down dip in the white-dashed flexure zone experienced no nitrogen breakthrough. It is possible that the portion of the zone where fracture intensity is much lower (shown in figure) may have led to a disconnect in the fracture network connection between the Phosphoria and Tensleep, at

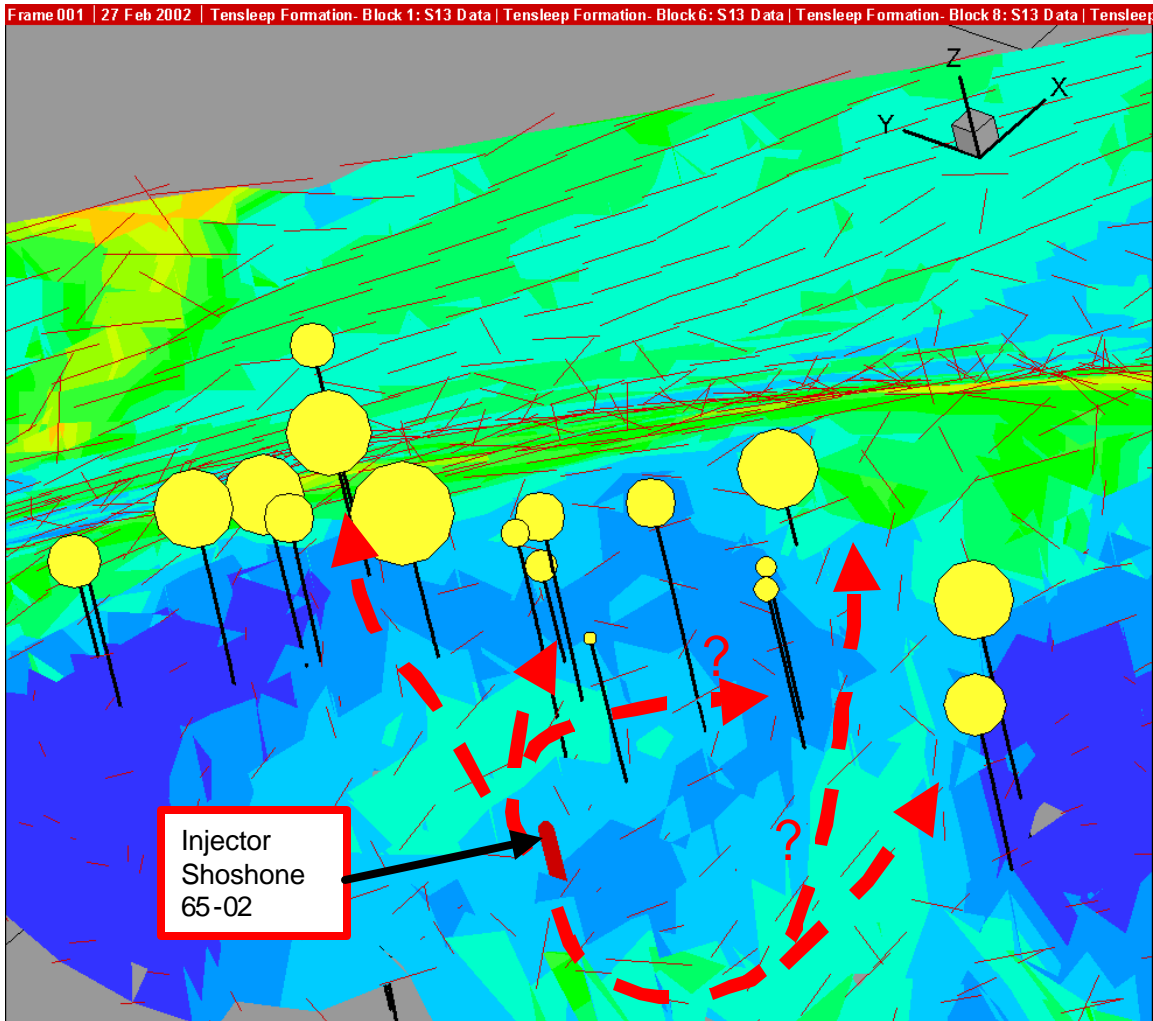


**Figure 3-71. Time to breakthrough for only the wells in which a breakthrough response was observed. Radius of circle is proportional to time of breakthrough, so large circle indicate a longer time to breakthrough than small circles. Note that the responding wells tend to be in the high strain regions around the injector, and that the time to breakthrough is relatively short for the 5 wells in the center of the diagram nearest the injector, and increases along the red-dashed fracture corridors as indicated in the figure.**

least for tracer injected into the Phosphoria and monitored in the Tensleep. The reason for this may be that the large extensional joints that form in the upper dune sequence of the Tensleep may terminate at the top of the sequence boundary, as they do in outcrops elsewhere in the Wind River and Bighorn Basins.

These results suggest that there is no “characteristic” tributary drainage radius from a well. Rather, the drainage area is a function of whether the well is situated in a strain corridor or not, and if it is in a corridor, how extensive and well connected the corridor is. Moreover, corridors should be much more extensive in the northwestern portion of the field where the greater horizontal shortening required more faulting and tighter folding.

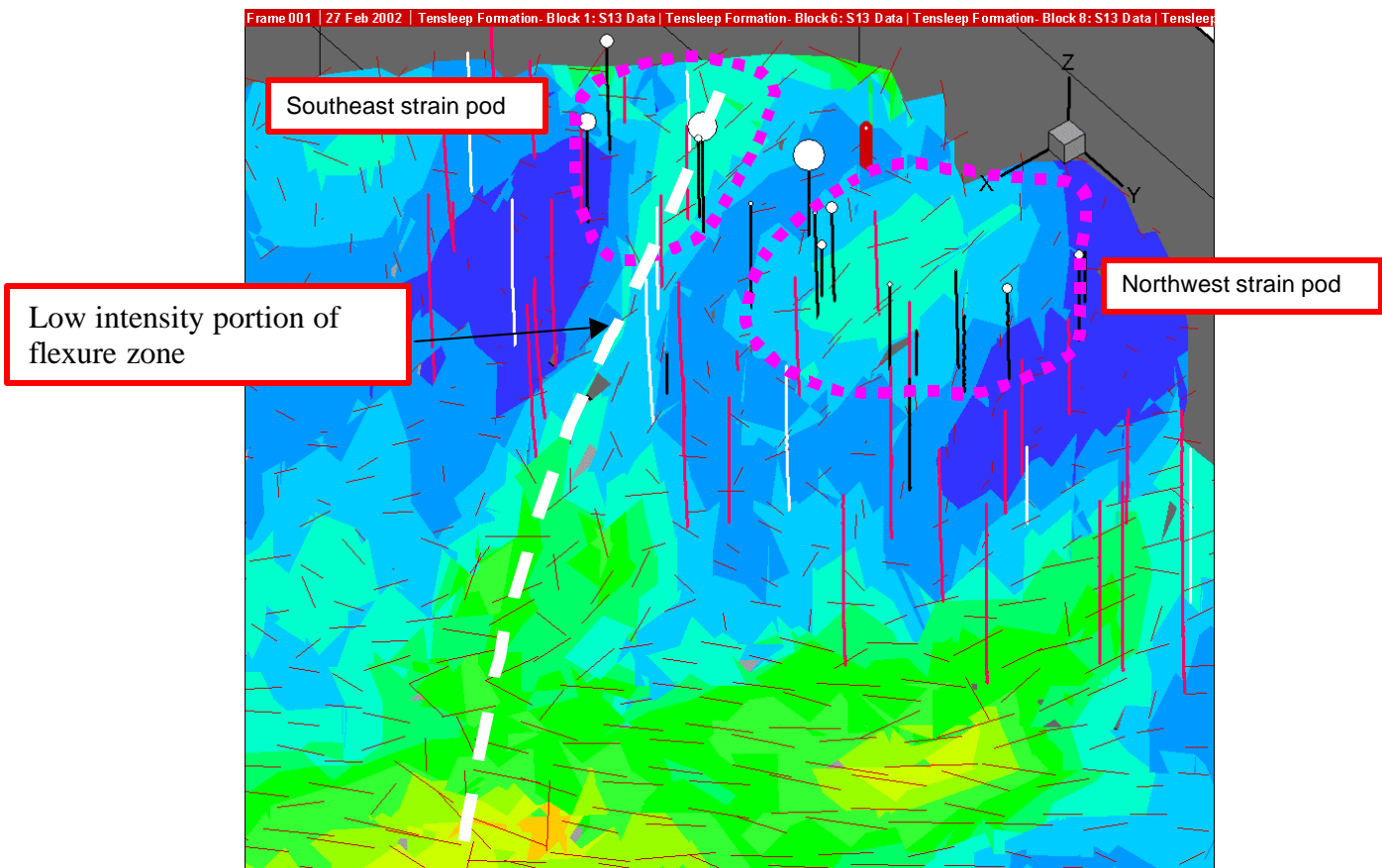


**Figure 3-72. Delineation of strain pods.** Most of the responding wells are in one of two strain “pods”. Non-responding wells are typically not in these pods. They tend to be in low strain zones or in pods separated from the pods connected to the injector pods by areas of low strain. White dashed line indicates a dip-parallel flexure zone.

### 3.5.3.3 Conclusions Regarding the Tributary Drainage/Compartmentalization Characteristics of the Reservoir From The Tracer Experimental Results

The bromide and nitrogen injection tracer test results, combined with the strain patterns developed from the palinspastic reconstruction and comparison to outcrop evidence, suggests that the reservoir may be characterized by linear zones or corridors of high strain/high fracture network permeability. These zones are not randomly located or oriented, but rather occur in sub-horizontal and dip-parallel orientations. The horizontal zones formed during the initial folding of the field, and are features that accommodate the upwarping and downwarping of the field (Figure 3-73). The dip-parallel zones formed to accommodate the horizontal compression in the northwest and southeast portions of the field, particularly in the northwest, where horizontal shortening is much greater. Some of this shortening was taken up by the imbricate faulting, but the formation of the doubly plunging fold also occurred along these flexural hinges that show little or no offset. Field evidence confirms the existence of these two types of zones.

While connectivity within these zones leads to enhanced fluid movement within the Tensleep or Phosphoria Formations, the bromide tracer test results indicate poor connection between the Phosphoria and Tensleep, at least for tracer injected into the Phosphoria and monitored in the Tensleep. The reason for this may be that the large extensional joints that form in the upper dune sequence of the Tensleep may terminate at

the top of the sequence boundary, as they do in outcrops elsewhere in the Wind River and Bighorn Basins.

These results suggest that there is no “characteristic” tributary drainage radius from a well. Rather, the drainage area is a function of whether the well is situated in a strain corridor or not, and if it is in a corridor, how extensive and well connected the corridor is. Moreover, corridors should be much more extensive in the northwestern portion of the field where the greater horizontal shortening required more faulting and tighter folding.

These results also indicate that fracture network permeability is a second order effect compared to fracture network connectivity patterns, and that a stochastic continuum representation of permeability in this reservoir using techniques such as Kriging would produce very different reservoir models than the one generated from the palinspastic reconstruction. Such structured corridors of high permeability are nearly impossible to characterize or simulate using stochastic field representations like Kriging that are commonly applied to matrix properties.

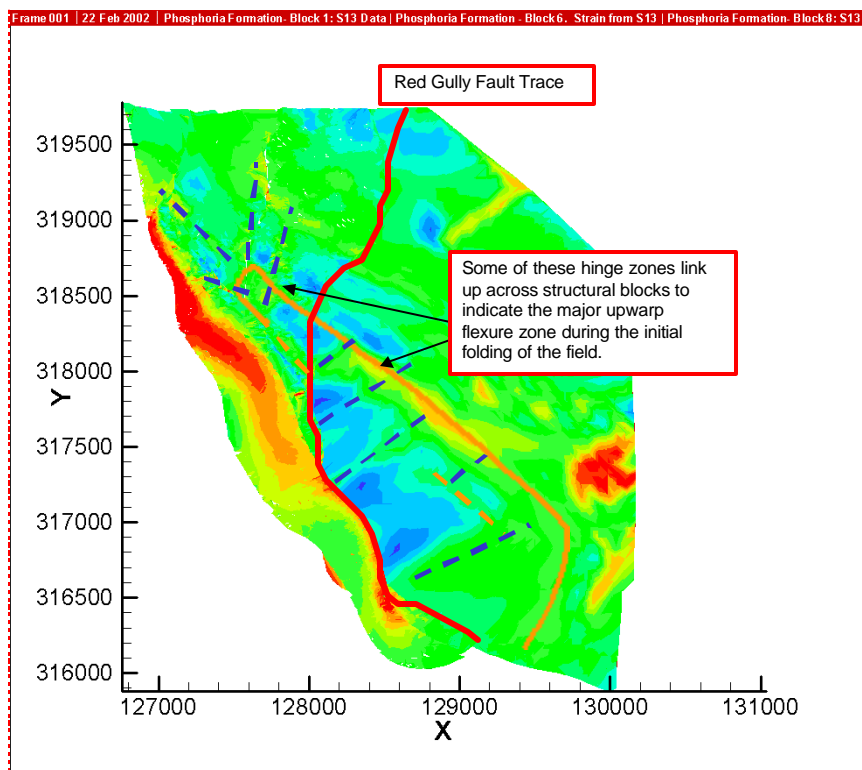


Figure 3-73. Strain pattern and the development of dip-parallel and strike parallel hinge zones.

### 3.6 Development of the Reservoir Scale Fracture Model

The work described in the previous the previous three sections established the geological controls on the development of the fracturing in the Tensleep and Phosphoria Formations. The combination of field work, structural reconstruction, subsurface data and tracer experiments showed that the folding of the reservoir units in the early stages of the structural deformation history probably produced most of the fracturing, and that flexural hinge zones developed that form high-conductivity corridors in the reservoir.

Prior to generating the DFN model, it is necessary to obtain some additional parameter values concerning the flow properties of the fractures and the conductive fracture intensity and size.

#### 3.6.1 CONDUCTIVE FRACTURE INTENSITY

It is common to find in high-resolution flow logging that only a small percentage of open fractures provide most of the production or injectivity of a well. As the goal of this project was in part to derive effective fracture flow properties for the reservoir, it was important to further investigate the relation between the total fracturing and the conductive fracturing. Analysis of Shoshone 66-14 exemplifies what was seen in all three wells.

Shoshone 66-14 is located in the Overthrust Block (Structural Block 1) in the southeastern end of the Circle Ridge Field. The interval logged extended from measured depths of 745 ft (227.08 m) to 1090 ft (332.23 m). This interval begins in the Tensleep Marker portion of the Phosphoria and extends to the base of the Tensleep Formation. The spinner log was run over a measured depth of 580 ft (176.78 m) to 1080 ft (329.18 m).

Figure 3-74 and Figure 3-75 show how fracture and bedding orientations and intensity vary over the logged interval.

Bedding orientation (shown by the purple and dark blue symbols in difference above 840 ft (256.03 m) MD, Figure 3-74) is quite consistent throughout, although there does seem to be a minor difference from the bedding orientation below. Bedding orientations in terms of both dip and dip azimuth are less variable above 840 ft (256.03 m) MD than below, and have a slightly different orientation. Bedding dip azimuths are around 140° to 160° and the bedding dips from 10° to 20° above 840 ft (256.03 m) MD and about ten degrees more below that depth. Bedding dip azimuth also rotates 10° to 20° in a clockwise manner going from the upper zone to the lower zone. Fracture dip azimuths fall largely into one of three orientations: 25° to 30°; 160°; and 340° to 350°. There appear to be no differences between 4-pad fractures and 3-pad fractures in terms of orientations. The 340° orientation is 180° opposite the bedding dip azimuth, and the dip

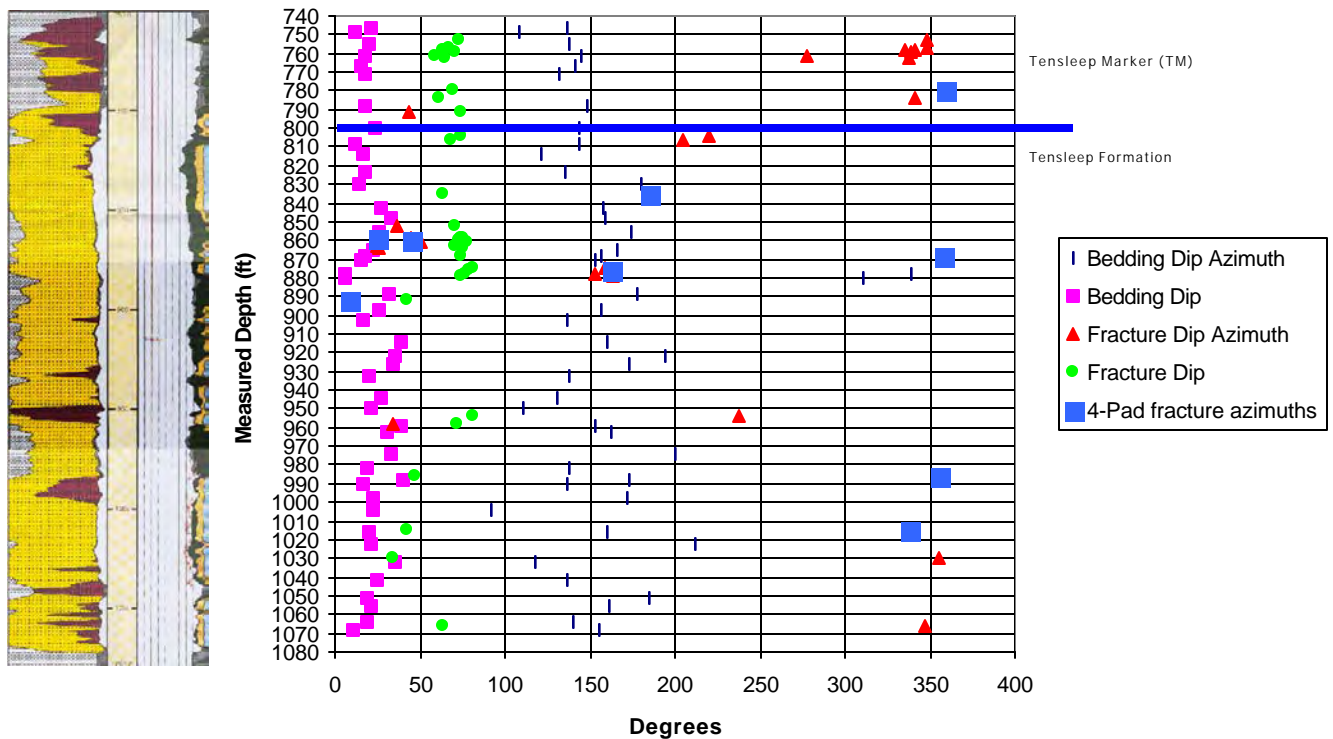


**Figure 3-74. Orientation of fractures and bedding in Shoshone 66-14 interpreted from image logs. The top of the Tensleep Formation is shown by the solid blue line.**

angles are about 90° different. This means that the fractures whose dip azimuth is around the 340° are orthogonal to bedding and parallel or nearly parallel to bedding strike. This is an orientation that would be expected if fractures formed during the folding of the rock. The group of fractures whose azimuths are near 150° also strike parallel to bedding, but dip about 30° more steeply than bedding and in the same direction as bedding dip. The fractures whose dip azimuths are in the 25° to 35° range dip steeply and are about 20° from being subparallel to bedding dip, although they are nearly orthogonal to bedding.

The largest visual change in the pattern of orientations does not appear to correspond to the boundary between the Tensleep Marker and the top of the Tensleep; rather, the most noticeable change, although a small one, occurs at about 840 ft (256.03 m). This is located somewhere in the T2A unit of the Tensleep, and is not a major stratigraphic boundary.

Figure 3-75, which is the plot of the cumulative fracture count, shows a similar break at this point. The slope of the line on this figure is inversely related to fracture intensity: the shallower the slope, the higher the intensity. There appear to be two zones of higher fracture intensity, and two zones of lower intensity. There may be some minor increases in fracture intensity at the top of the Tensleep and at the top of the T3 unit (952 ft or 290.17 m) MD. Within each of the four zones, the fracture intensity (slope) is relatively constant. The major zone boundaries, however, don't necessarily correspond with the stratigraphic unit boundaries, nor do they seem to be consistently associated with particular lithologies. For example, the top of the T3 is associated with a more highly

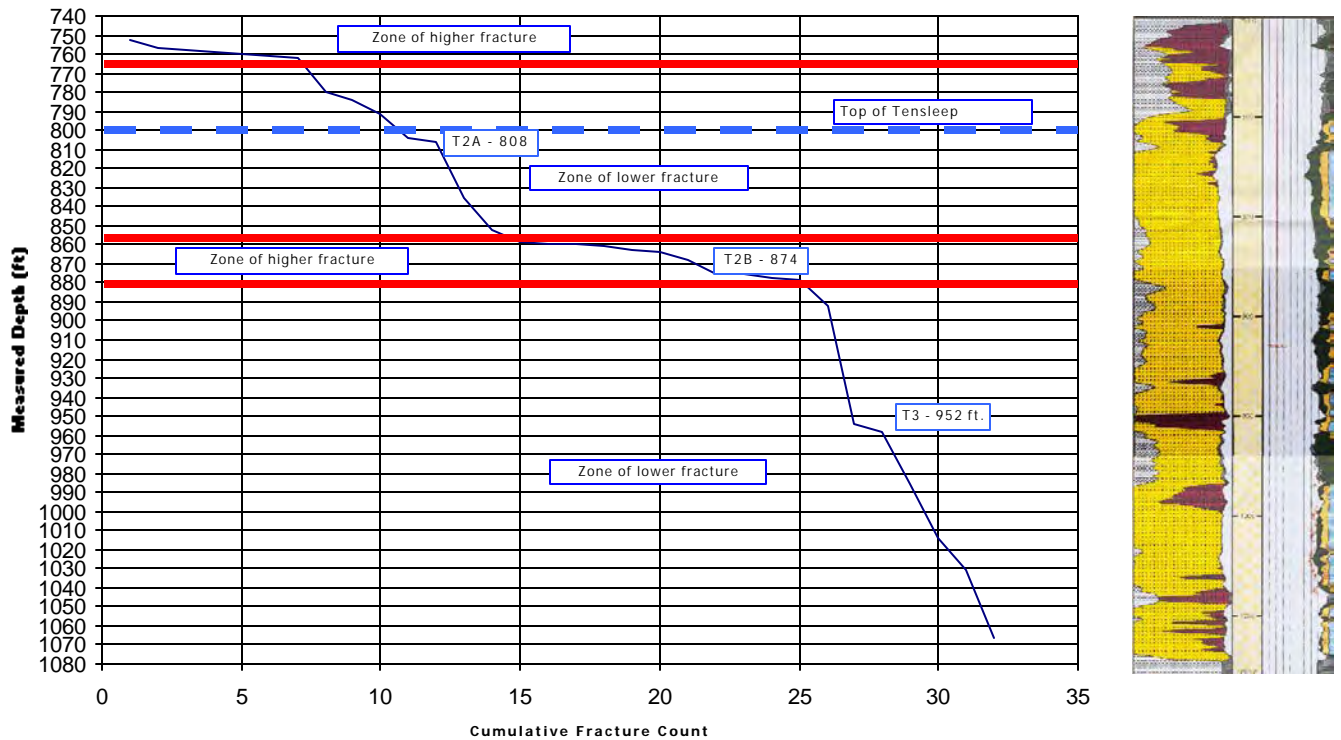


**Figure 3-75. Cumulative fracture count for Shoshone 66-14 for fractures interpreted from image log. Red solid lines indicate alternating zones of higher and lower fracture intensity. Dashed blue line indicates the approximate top of the Tensleep Formation.**

fractured dolomitic unit, as is the top of the T2A unit and the more dolomitic rich portion of the TM above 765 ft (233.17 m). However, the zone of highest fracture intensity from about 855 ft to 880 ft (260.60 m to 268.22 m) is devoid of dolomite. The presence of dolomite below the top of T3 appears to have no relation to increased fracture intensity.

What does cause the variations in fracture intensity with depth? Another possibility is bed thickness. In many layered rocks, fracture spacing is proportional to bed thickness: the thinner the beds, the shorter the fracture spacing of fractures orthogonal to the beds

Figure 3-76 compares bedding intensity with fracture intensity. In this plot, the number of beds or fractures was counted over 15 ft (4.572 m) windows. This figure shows that there does appear to be a visual correspondence between bedding plane intensity and fracture intensity. A Wilcoxon signed-rank test was significant at  $\alpha = 0.06$ , which suggests that bedding thickness does influence fracture intensity. The variations in bedding plane intensity do not show any obvious visual correspondence with variations in the three principal lithologies: sandstone, shale and dolomite (Figure 3-76). It is important to note that the higher intensity does not necessarily indicate that the fractures are larger or that the overall fracture surface area per volume of rock is greater. Thus, the relation between fracture intensity and formation productivity is not resolved until the intensity is compared to productivity.

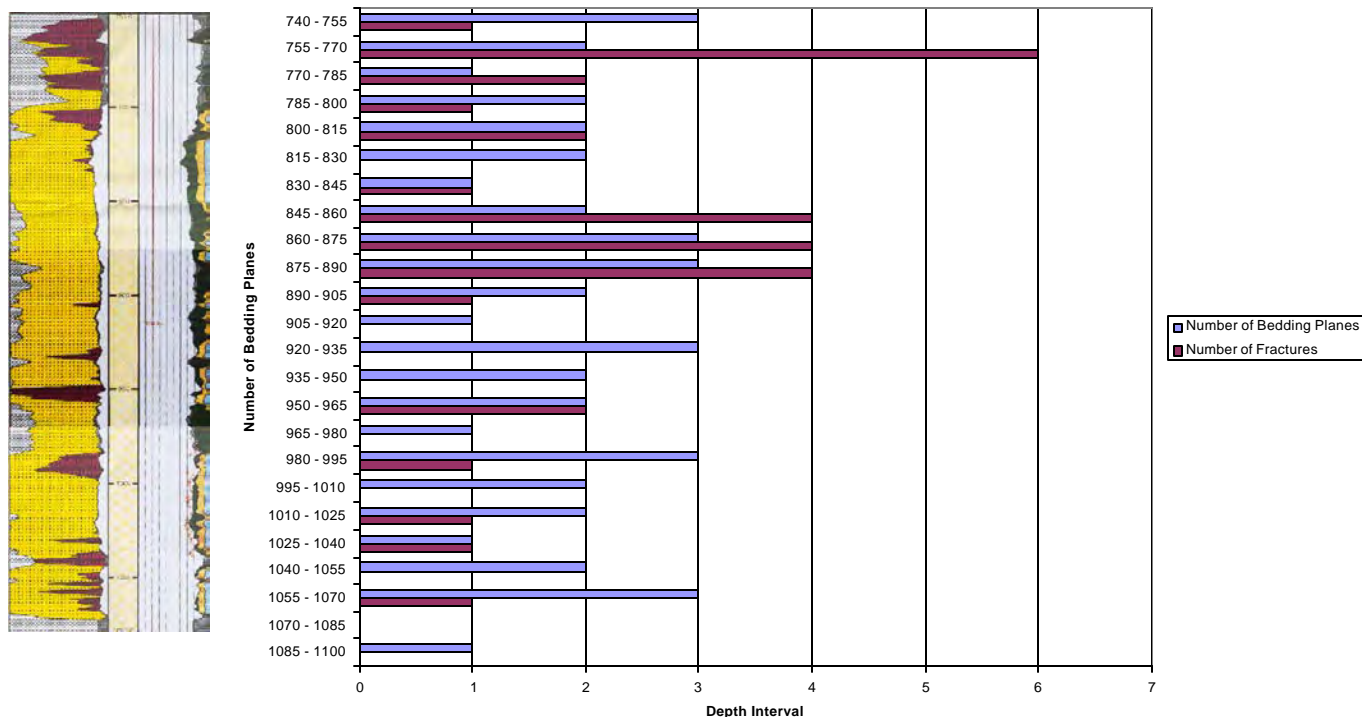


**Figure 3-76. Correspondence of bedding intensity and fracture intensity. Intensity is calculated over 15 ft (4.572 m) non-overlapping windows.**

### 3.6.1.1 Productivity

A spinner log survey was carried out in Shoshone 66-14 on Dec. 12, 2001. The results of the cumulative production are shown in Figure 3-77. As in many, if not most, fractured reservoirs, the majority of major flow anomalies coincide with the location of open fractures, but most of the open fractures do not coincide with major flow anomalies.

It is interesting to plot the cumulative intensity of open fractures and the cumulative production over the same interval (Figure 3-77). The cumulative production and the cumulative fracture intensity have been normalized to a range of 0% to 100% in order to commensurate them.

The comparison of these two cumulative plots shows that the increases in production generally follow increases in open fracture intensity. The flow anomaly at 810 ft (246.89 m) corresponds to the small zone of high fracture intensity at the top of the T2A unit. The anomaly at 802 ft (244.45 m) is close to the top of the T1 unit. The anomalies at 748 ft and 752 ft (227.99 m and 229.21 m) are in the higher fracture intensity zone at the top of the Tensleep Marker zone. The flow anomaly at 788 ft (240.18 m) corresponds to neither a stratigraphic boundary nor to a fracture intensity zone boundary, nor were there

## Production Profile From Flow Log

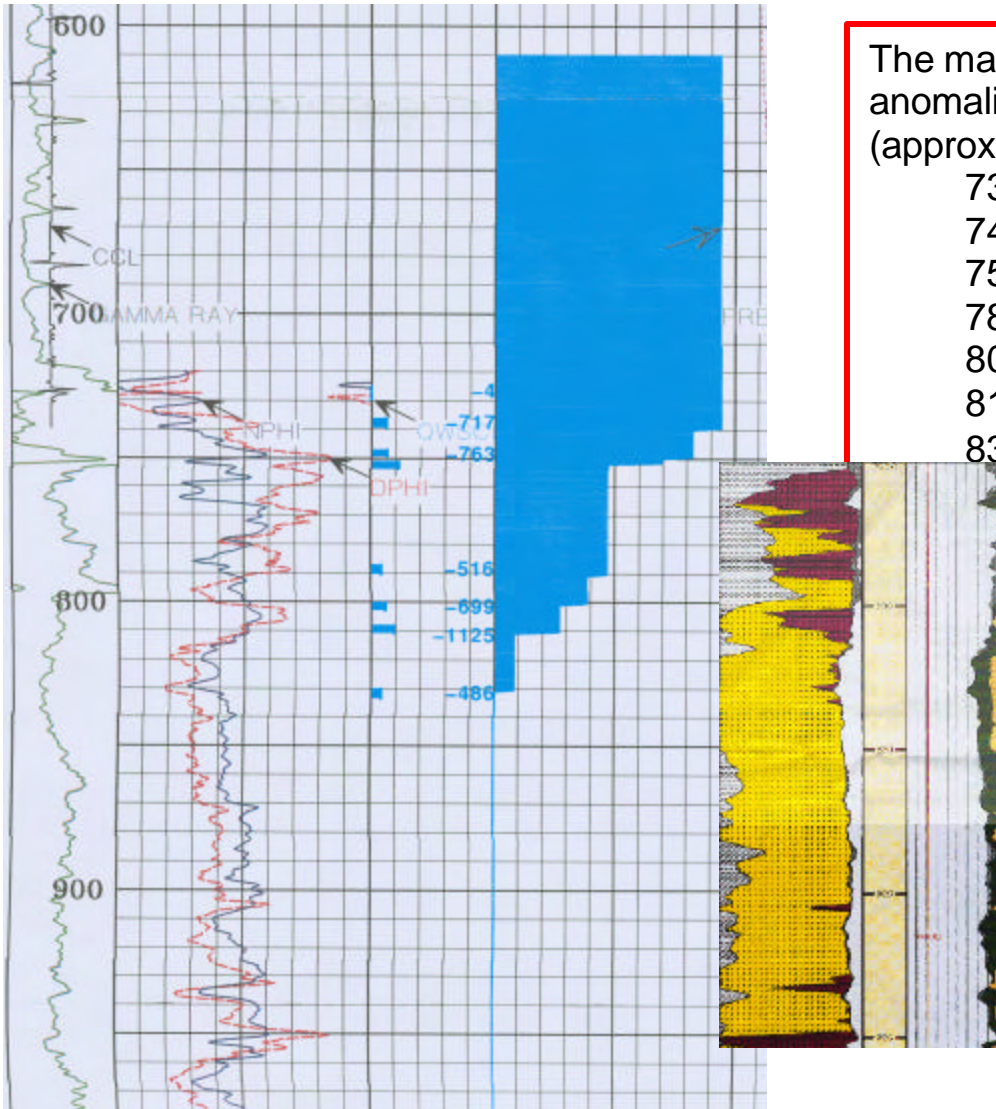


**Figure 3-77. Cumulative production profile for Shoshone 66-14.**

fractures found in that interval. The remainder of the flow anomalies were above the fracture image log, and so their correspondence could not be ascertained.

Figure 3-78 compares the cumulative production to the cumulative fracture intensity normalized to vary from 0% to 100) over the interval that was logged for flow and starting at 0% at the bottom of the flow-logged interval. The cumulative fracture intensity and cumulative production follow one another fairly closely. One interpretation of the fact that flow anomalies generally track open fracture intensity, but may or may not correspond to the presence or absences of individual fractures, is that it is the general strain in the rock that matters, not how that strain is locally connected to the wellbore. If a zone is highly strained, it has a much higher fracture permeability, and whether that

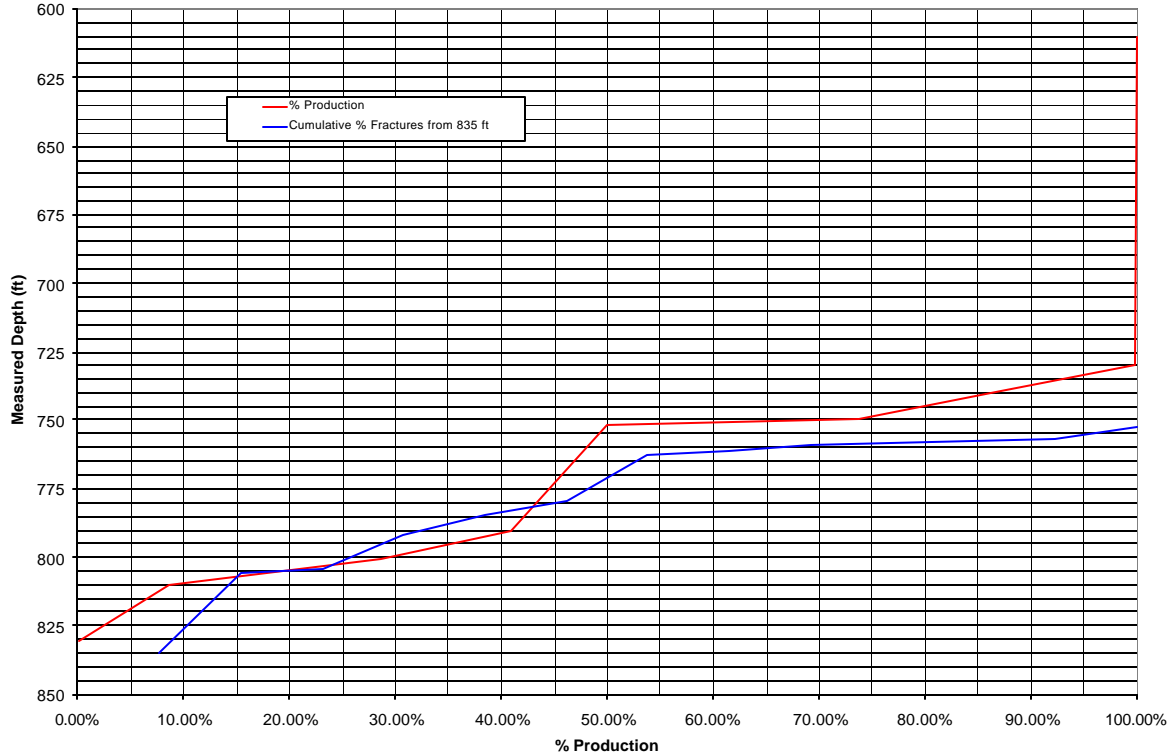


**Figure 3-78. Comparison of cumulative fracture intensity and cumulative production from Shoshone 66-14. The red line is the % production from the spinner survey data. The blue line is the cumulative percent of fractures starting at a depth of 835 ft. (there were not enough 4-pad fractures to plot this component separately).**

permeability is connected to the wellbore by one fracture or some small fractures or by the matrix may be less important. This suggests that the strain anomalies calculated through the palinspastic reconstruction may be good predictors of reservoir-scale subsurface fluid movement, while at the same time not necessarily predicting local scale well behavior with the same level of utility.

### 3.6.2 DERIVATION OF FRACTURE FLOW PARAMETER VALUES FROM WELL TESTS

#### 3.6.2.1 Local model

In order to simulate the single well injection/fall-off test a small DFN model was constructed around well Shoshone 65-02. The locations of key wells are shown in Figure 3-79. Two sub-vertical fracture sets were generated based on the orientation of the strain field in the vicinity of Shoshone 65-02 with one set sub-parallel (L) and one set sub-perpendicular (T) to the regional strain field near this well. Geometric parameters for these two sets are given in Table 3-6. A single 250 m x 260 m x 100m realization of this

fracture network is presented in Figure 3-80. For the local scale simulation both fracture sets are given the same aperture size and permeability in order to calibrate the network and reservoir  $kh$ , while in the following section the relative permeabilities of the two sets is varied to calibrate to the relative breakthrough times of each of the wells.

Parameters for the local scale DFN model were based on the orientation of the strain field in the vicinity of the injection well Shoshone 65-02. Fracture size and fracture intensity were initially chosen to be consistent with reservoir and the expected intensity of major conductive features. The effect of varying length and the relative intensity of the two fracture sets are analyzed in the next section.

The network that results from these input parameters is well-connected network composed primarily of sub-vertical fractures. Six sided fractures are used with an aspect ratio of one, and these fractures are large enough that most reach from the top to the bottom of the reservoir. In order to calibrate the effective network permeability, a constant permeability was applied to each fracture within both the T and L fracture sets. The permeability thickness of the reservoir depends on both the permeability of the

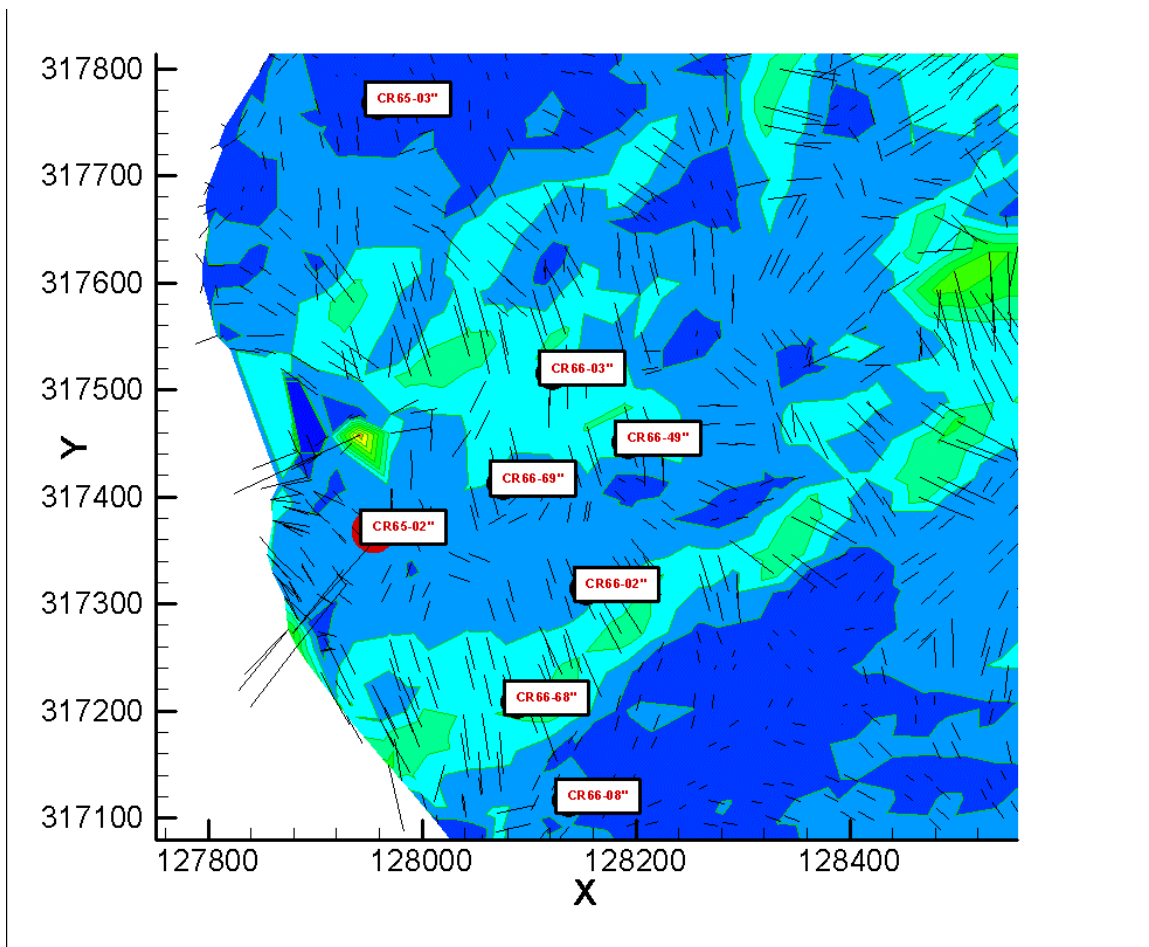


Figure 3-79. Key well locations for nitrogen injection test.

individual fractures within each set, and the overall connectivity of the network. The connectivity of the network for the local model depends on the fracture intensity and fracture length. The effects of applying different permeabilities for each fracture set are discussed further below, and the impact of changing the relative intensities of each of the fractures sets, and the size of the fractures is also examined.

A snapshot of the pressure differential due to nitrogen injection at Shoshone 65-02 is presented in Figure 3-81. Close to the well the pressure distribution is strongly affected by local discrete features. As the pressure field moves away from the injector, the effect of the individual features is averaged out so that an almost circular radius of influence appears. The circular radius of influence is not expected in the field and is likely a consequence of the two fracture sets being assigned equal permeability. The pressure tends to migrate along the T-set direction faster than along the L-set direction because of the higher fracture intensity in the T-set.

A series of simulations were run in which individual fractures were assigned permeabilities averaging from 1 to 1000 millidarcies (Figure 3-82). Each of these pressure curves has a similar response character other than an increase in effective permeability for an increase in fracture permeability. Each derivative shows a positive half-slope at early times indicating a restriction in the immediate vicinity of the well. After this early period the derivative drops off as the pressure field expands out of the “entry feature” and into the fracture network. Once the pressure field expands to the point where it is constrained by the upper and lower boundaries of the reservoir, the derivative goes to a slope of zero, similar to classic radial flow. The value at which the derivative levels off is a function of the permeability of the fracture system, with smaller derivative values consistent with higher reservoir permeabilities. Conversely the derivatives can be plotted as a function of permeability thickness (Figure 3-83), and the value of the calibrated fracture permeability can be determined. There appears to be a linear relationship between assigned fracture permeability and the corresponding effective  $kh$  of the reservoir. Based on this it appears that the average fracture permeability must be approximately 40 mD to obtain a reservoir  $kh$  of 408 mD-m. The 40-mD value can be compared to spinner log data in order to calibrate the model to observed values of flowing features. This value of 40mD is consistent with the order of magnitude of flowing features observed in similar reservoirs. The 40 mD represents an average value for an individual fracture. When a network is formed by a number of fractures, the network permeability is much greater.

Fracture Set	Orientation			Size: Log Normal				Intensity
	Mean Pole	Mean Plunge	Fischer Dispersion	Mean	St.Dev	Min	Max	
Strain Perpendicular	73	0	30	50	30	20	200	P <sub>32</sub> 0.05
Strain Parallel	163	0	30	50	30	20	200	0.03

**Table 3-6. Geometric inputs for local DFN model**

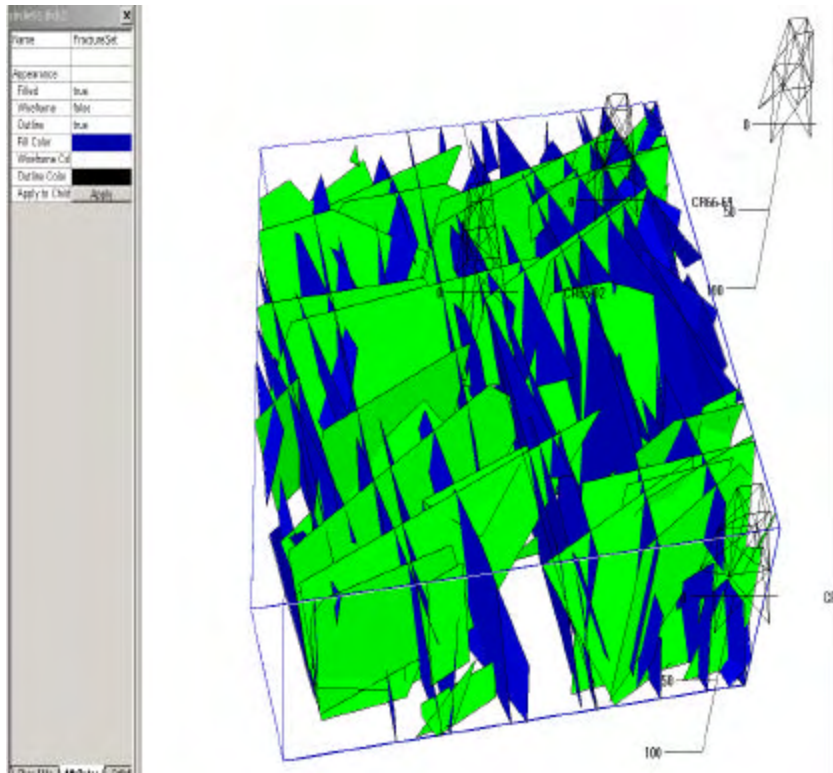


Figure 3-80. Local scale DFN model for Shoshone 65-02.

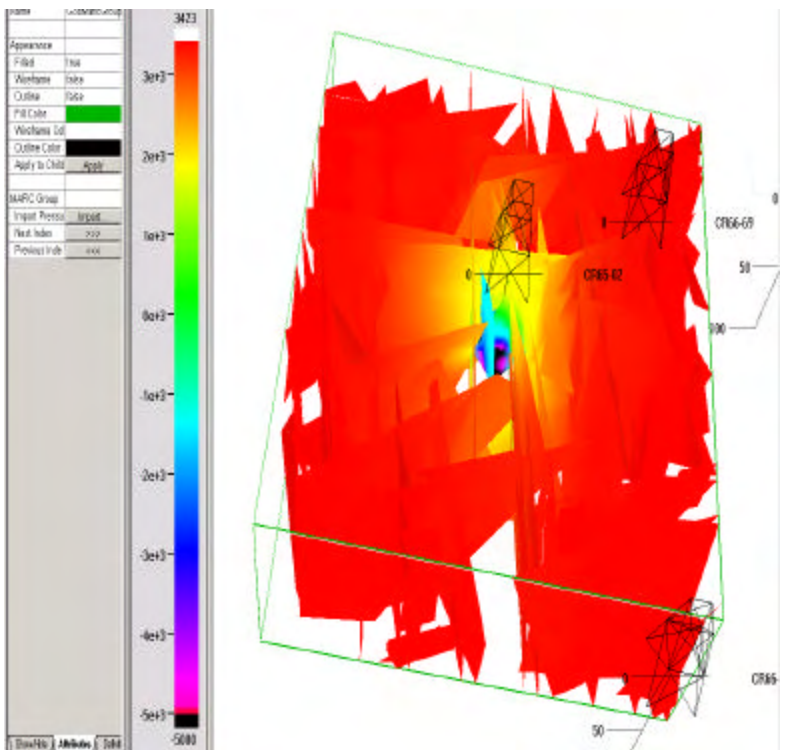


Figure 3-81. Pressure snap shot at 100 hours. Color indicates change from initial reservoir conditions in red.

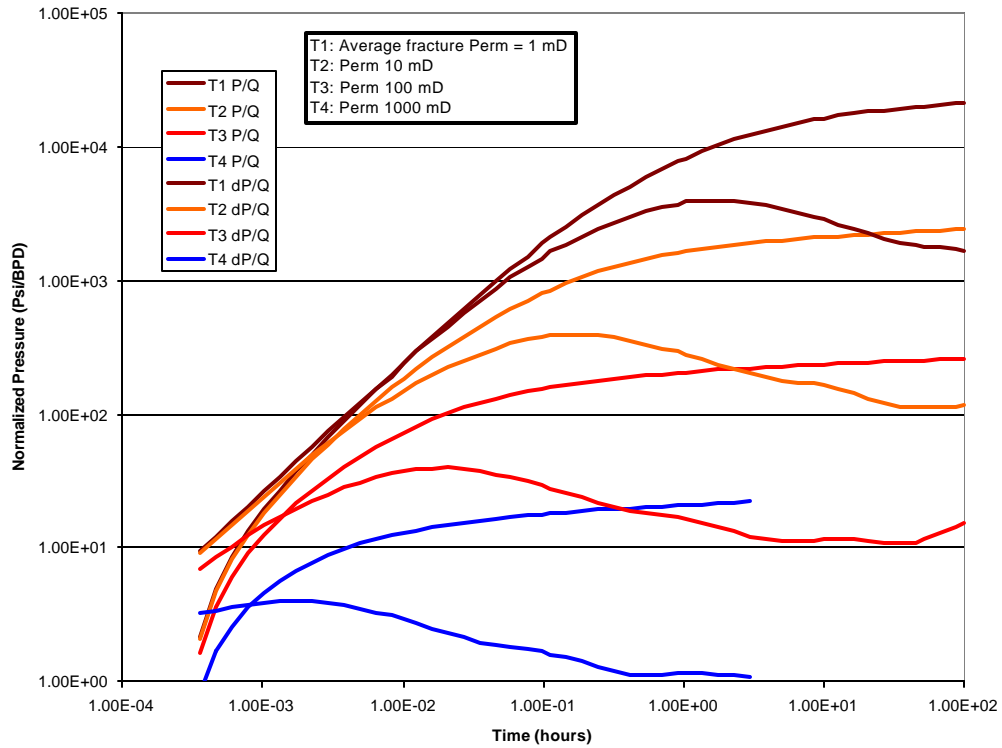


Figure 3-82. Build up test simulations for average fracture permeabilities of 1 to 1000 mD

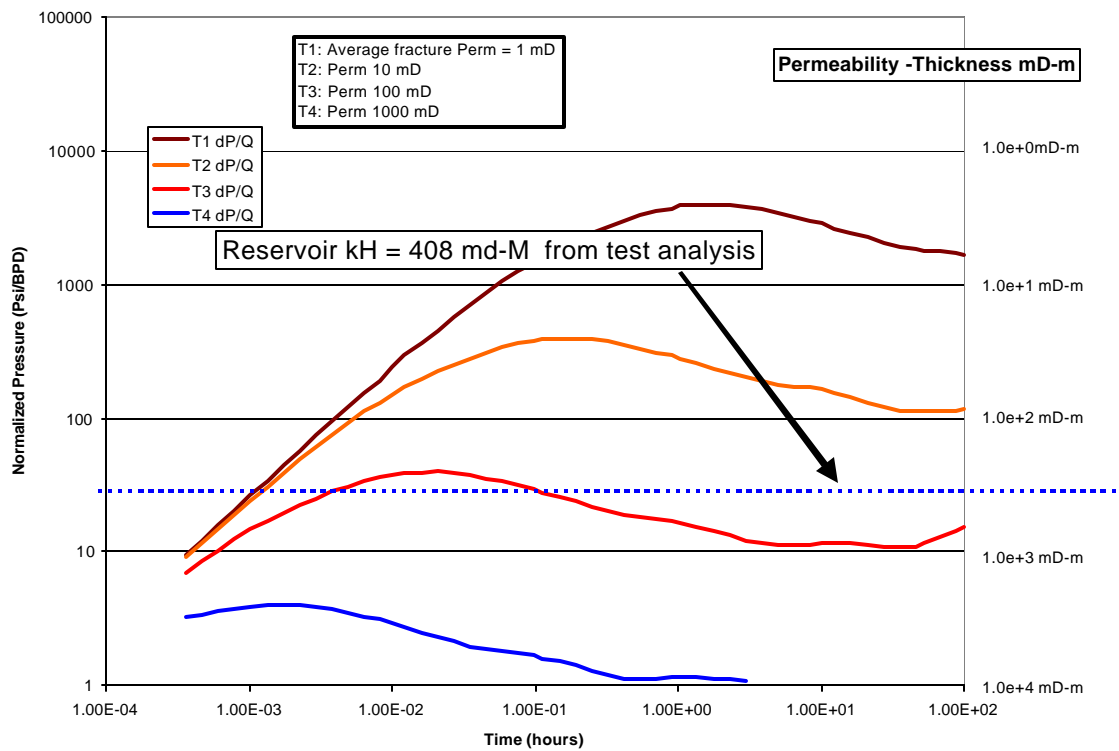


Figure 3-83. Permeability thickness values based on late-time derivative curves

### 3.6.2.2 Breakthrough match

Although the single well simulation will help calibrate the fracture geometry and permeability necessary to match reservoir  $kh$ , simulating pressure response in the pumping wells is necessary to determine the relative permeability of one set to the next. For this reason a regional scale model was simulated using the calibrated parameters from the local scale model (Table 3-6) over the entire test area (Figure 3-79). The underlying control grid geometry is shown in

Figure 3-84. Additionally, the strain field from the palinspastic reconstruction was used to control both fracture intensity and fracture orientation. Two sets were generated: (1) A T-set perpendicular to the local strain field orientation; and (2) an L-set sub-parallel to the local strain field vector. One realization of this network is presented in Figure 3-85. The regional model encompasses a 1 km x 1km region of the strain grid. This includes the test well and 6 production wells in which pressure values were monitored. Fracture intensity varies within the model according to the extensional strain values in each of the grid cells. These strain values were determined during the palinspastic reconstruction work described previously. The extensional strain is summed throughout the grid region, and then a normalized strain is

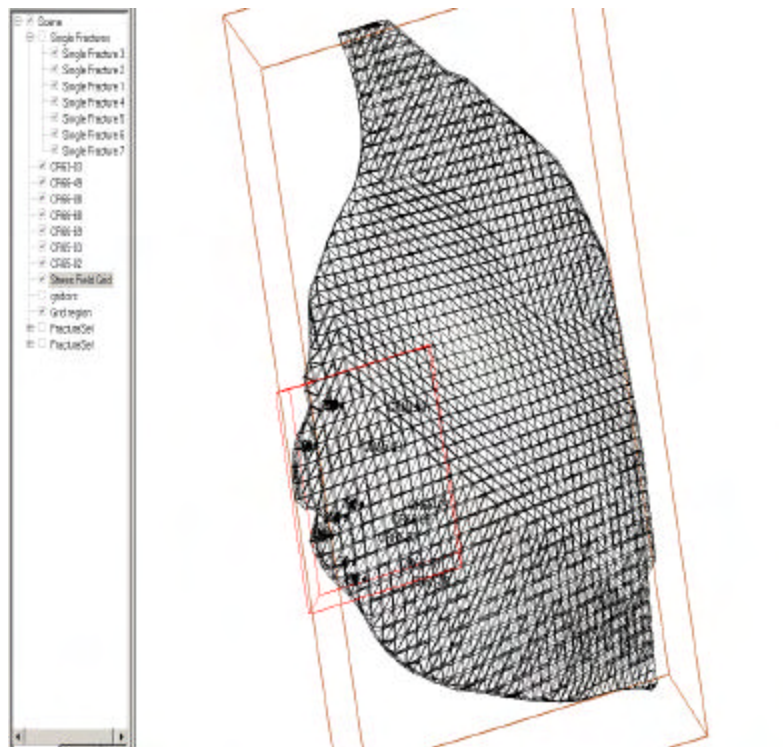
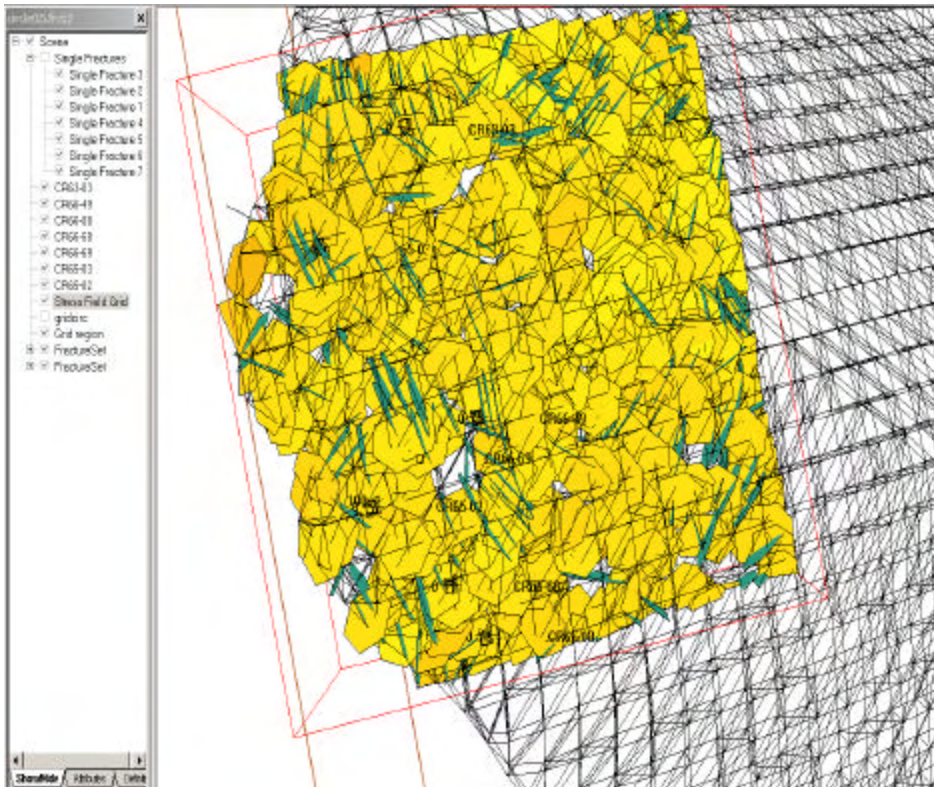


Figure 3-84. Strain grid for development of regional scale model



**Figure 3-85. Regional scale DFN model populated by strain perpendicular and strain parallel fracture sets.**

calculated for each grid cell. An average fracture intensity or  $P_{32}$  is assigned to the fracture system, and then the normalized strain is used to calculate an individual  $P_{32}$  value for each grid cell. In this manner the fracture intensity varies throughout the model domain while the average fracture intensity of each fracture set, averaged over the entire grid, can be scaled up or down.

In addition to the magnitude of the strain field, the orientation is used to determine the orientation of the T and L fracture sets. For the early realizations the T-set is exactly perpendicular to the local strain field and the L set is sub-parallel to the strain field.

In the resulting DFN model the T-set has a 25% higher fracture intensity than the L-set, and tends to dip at shallower angles than the L-set. As a result of the varying strain grid the fracture intensity varies throughout the model.

An average value  $0.09 \text{ m}^2/\text{m}^3$  was used for the fracture intensity, with a linear correlation between strain magnitude and local intensity. A plot of the resulting  $P_{32}$  values is given in Figure 3-86. Fracture intensity in the model region is dominated by cells with a calculated fracture intensity of  $0.1 \text{ m}^2/\text{m}^3$  and slightly higher. A few scattered grid cells

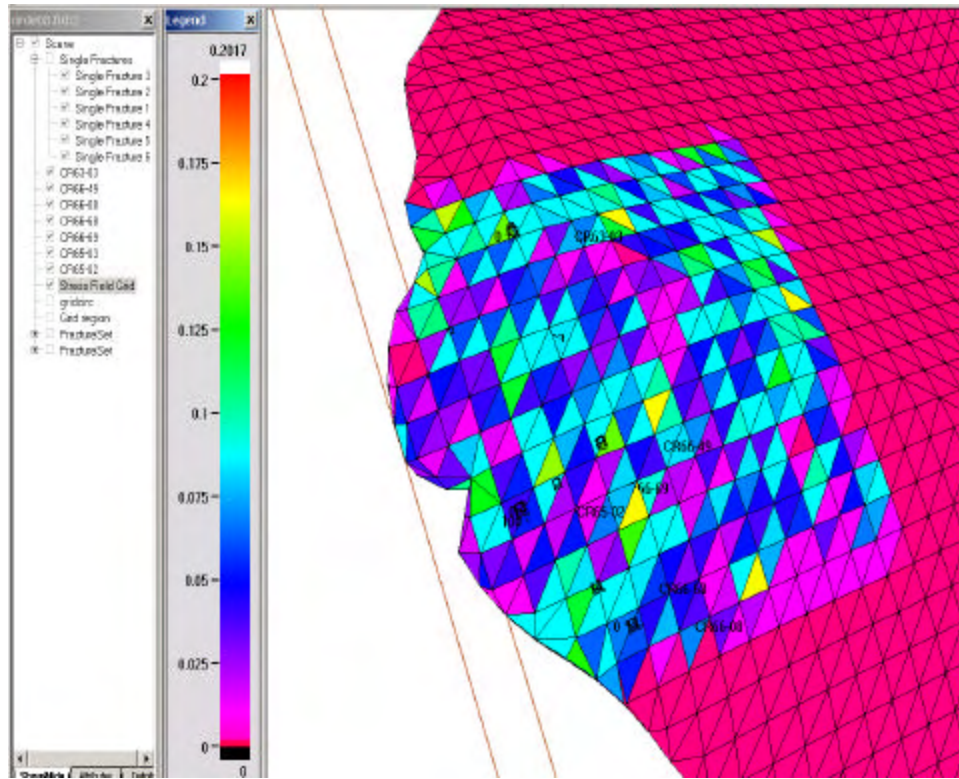


**Figure 3-86. Fracture intensity values ( $P_{32}$ ) resulting from an average  $P_{32}$  value of 0.08**

have  $P_{32}$  values higher than 0.015 m<sup>2</sup>/m<sup>3</sup>. Cells with fracture intensities below 0.025 tend to appear in clusters. One of these low permeability clusters occurs immediately to the north-east of Shoshone 65-02, the injection well. As a result there tend not to be connecting fractures immediately to the north-east of Shoshone 65-02. This becomes important, as this direction has been identified by the nitrogen break-through as a direction of preferential permeability.

As had been seen in the breakthroughs during the nitrogen injection there is some directional trends suggested in the permeability. The time before the pressure field travels from the injector to the producer is a function of both the distance between the two wells, and the direction from one to the other.

Three simulations of the regional model were run, in order to evaluate the relative permeabilities of the T and L- fracture sets. In the first simulation the ratio of the T to L set permeabilities was set to 1, i.e. the permeability assigned to all fractures was identical. In the second simulation the permeability assigned to fractures in the T-set was 10 times that assigned to fractures in the L-set (ratio of 10:1). In the third simulation the ratio was reversed (0.1) with fractures in the L-set assigned a permeability value 10 x the permeability assigned to fractures in the T-set.

One of the key features of the injection experiment was that breakthrough times for well Shoshone 66-49 were earlier than for well Shoshone 66-69, although Shoshone 66-68 is

closer to the injector. The low intensity of the fracture network between the injection well and Shoshone 66-49 suggests that a large permeability difference must occur between the T and L fracture sets. When the permeability ratio is set so that the permeability of the L-set is 10 times the permeability of the T-set the pressure evolve in a north east direction more quickly than in the north-west/south-east direction, consistent with the fast arrival time at Shoshone 66-49.

When the permeability assigned to each of the two sets is equal breakthrough occurs in the following order: well 66-69, 66-68, 66-49, 66-8, 65-03 and finally 63-03. These pressure breakthroughs are generally a function of distance from the injector, notably that 66-68 breaks through before 66-49.

Three pressure snap-shots are presented to illustrate the effect of changing the relative permeabilities of the strain-perpendicular and strain-parallel sets. In Figure 3-87 the regional model is presented with the average fracture permeability in both sets identical (ratio of Set1 k: Set2 k =1). In Figure 3-88, a permeability ratio of 10:1 is presented and a 1:10 ratio is presented in Figure 3-30. As is apparent from these plots the second fracture set must have a lower permeability in order to explain the high NE permeability trend, and the low SE permeability trend.

In Figure 3-90 the change in pressure for wells Shoshone 65-02, Shoshone 65-49 and Shoshone 66-68 is plotted for the regional model where the permeability of each fracture set is equal (i.e. ratio of Set1 k: Set2 k =1). The breakthroughs for Shoshone 65-49 and Shoshone 66-68 occur within minutes of each other, and the closer well (Shoshone 66-68) breaks through earlier.

In Figure 3-91 the same changes are plotted but for the case in which the ratio of Set1 to Set 2 permeabilities is 0.1. The Shoshone 65-49 well now breaks through earlier, consistent with the measured breakthroughs.

### 3.6.2.3 Conclusions

The true relative intensity of the T and L fracture sets is not known, but the ratio of T-set is thought to range between 2 and 5 times the intensity of the L-set. The effect of changing the relative fracture intensity of the two fracture sets, while keeping the overall intensity, and fracture length consistent is shown in Figure 3-92. The input parameters for the fracture intensity for each of the two fracture sets is given in Table 3-8, with the simulations ranging from intensity ratios of 1.25: 1 to 5:1 with the T-set having the higher fracture intensity. Results are varied depending upon the location of the well relative to the injector. For example, for the Shoshone 66-69 well that is closest to the injector, as the T fracture set intensity increases, the breakthrough time decreases. For Shoshone 65-03, the opposite occurs: as the T-fracture set intensity increase, there is an increased delay in the arrival of the pressure field. For the Shoshone 66-49, and Shoshone 66-68, as the T-fracture intensity increases, the breakthrough time decreases for Shoshone 66-49, but increases for Shoshone 66-68. For a fracture intensity ratio of 3.5:1, the pressure

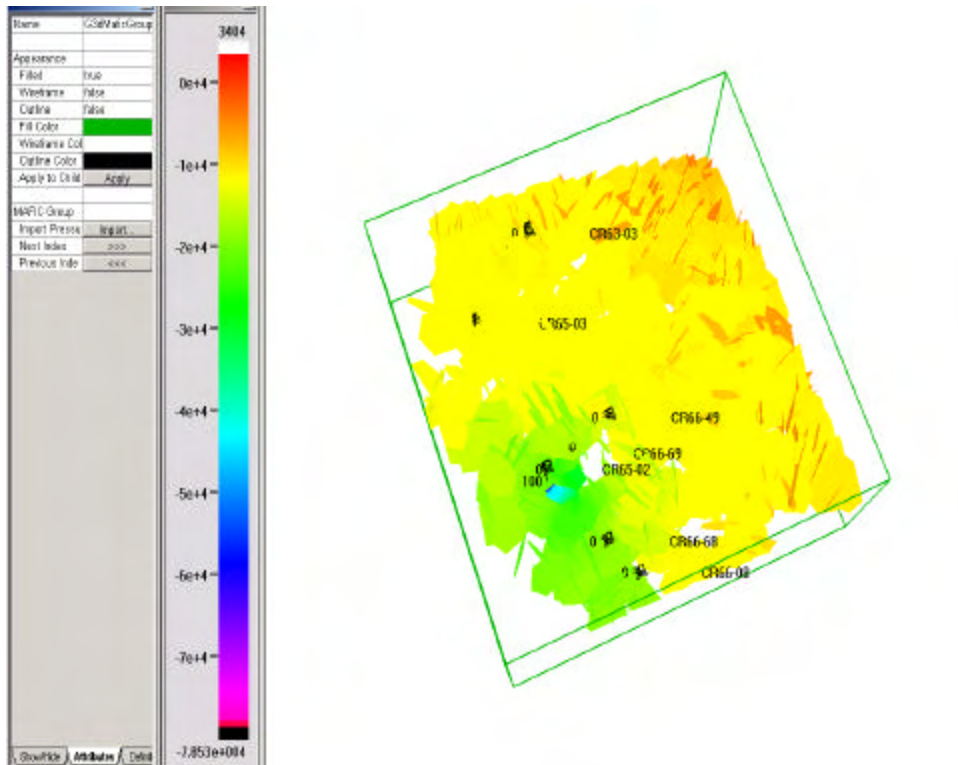


Figure 3-87. Pressure snapshot of injection in regional model with permeability ratio Set1:S

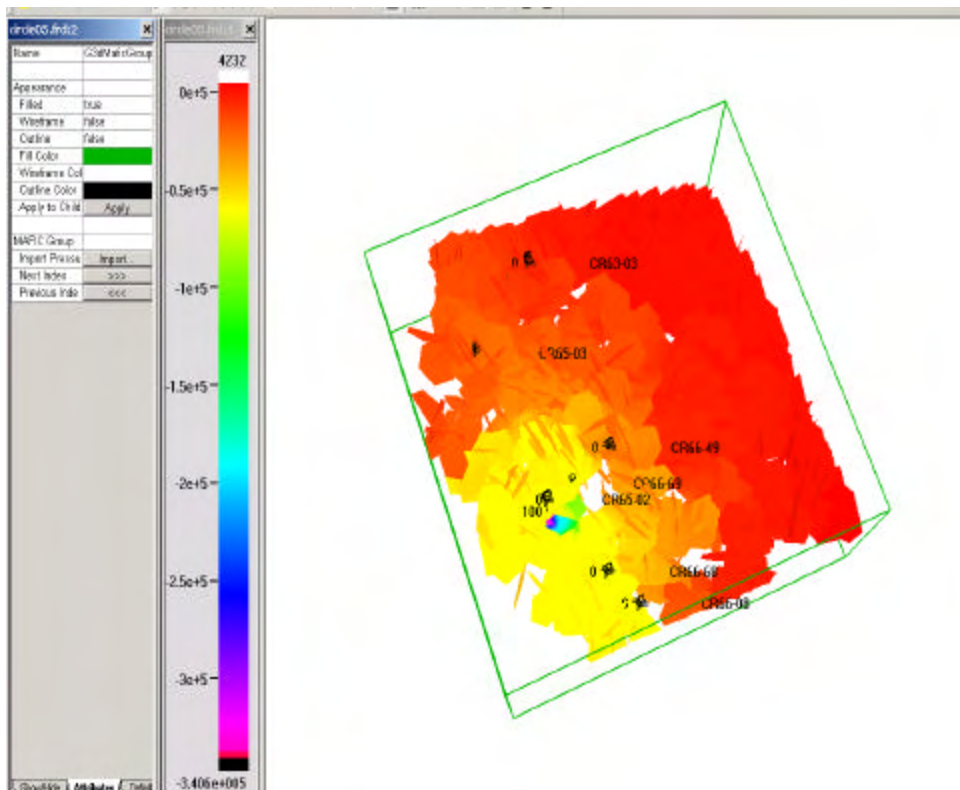


Figure 3-88. Pressure snapshot of injection in regional model permeability ratio Set1:Set2 = 10. This simulation shows earlier pressure breakthrough to the north-west and south-east rather than to the north-east set2 = 1

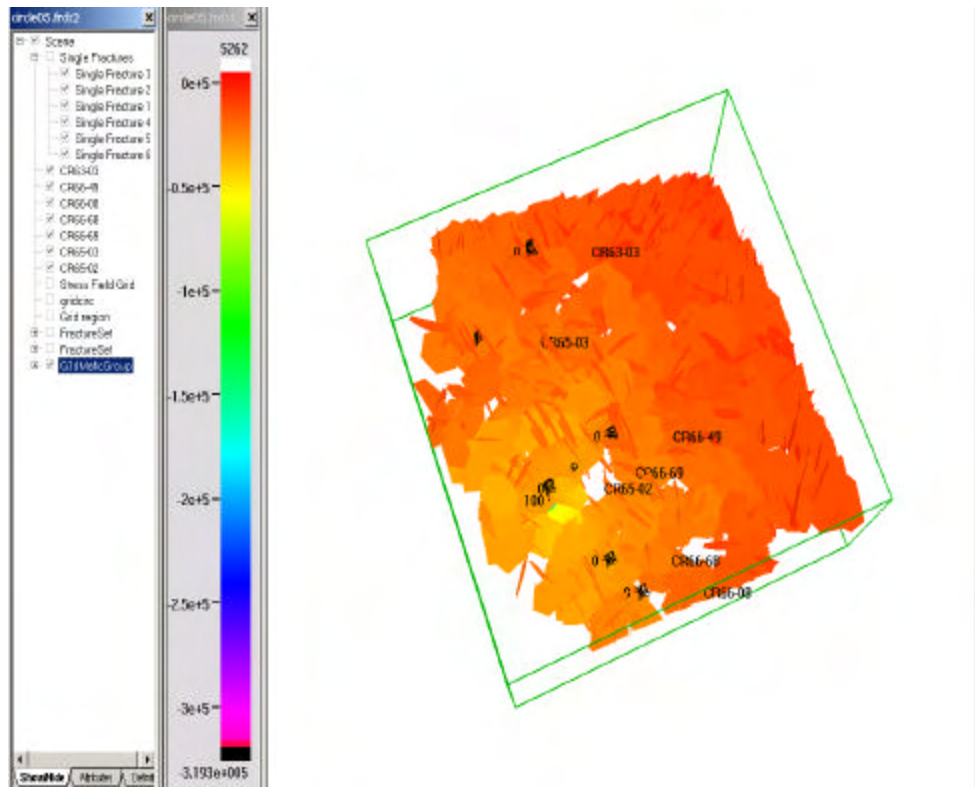


Figure 3-89. Permeability ratio Set1:Set2 = 0.1.

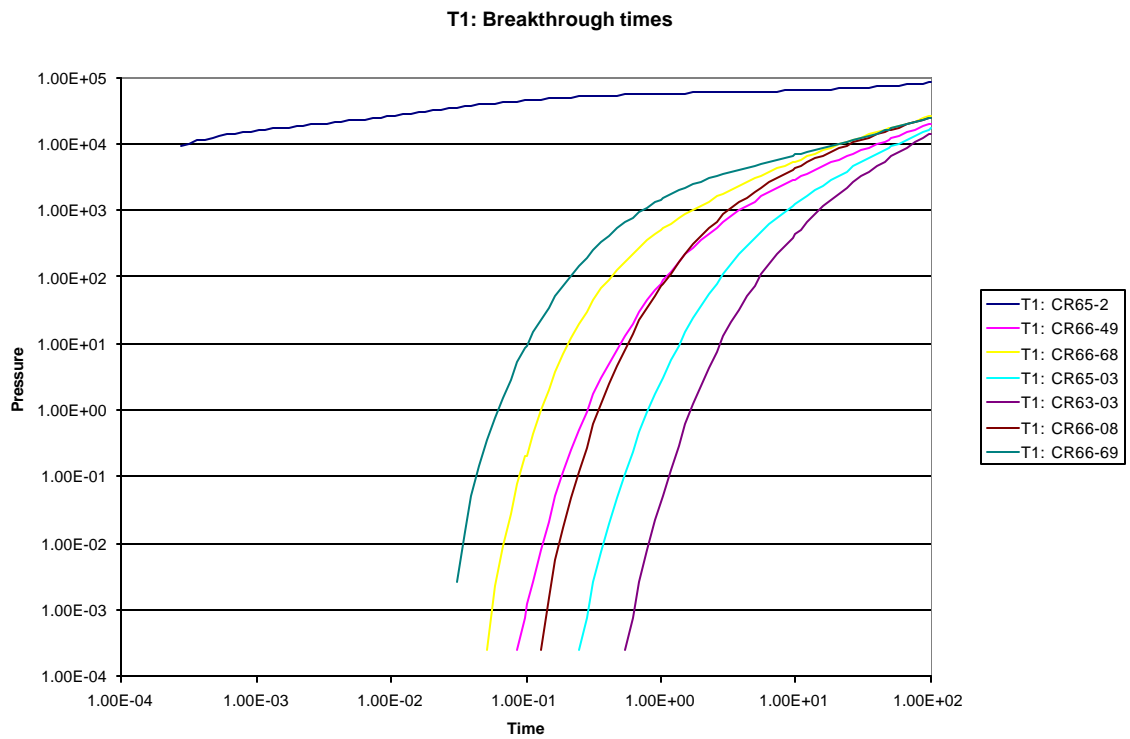


Figure 3-90. Change in pressure for wells 52, 49 and 68. Pressure response is quicker for Shoshone 66-68 because it is closer to the injection in Shoshone 65-2

T2: Breakthrough times

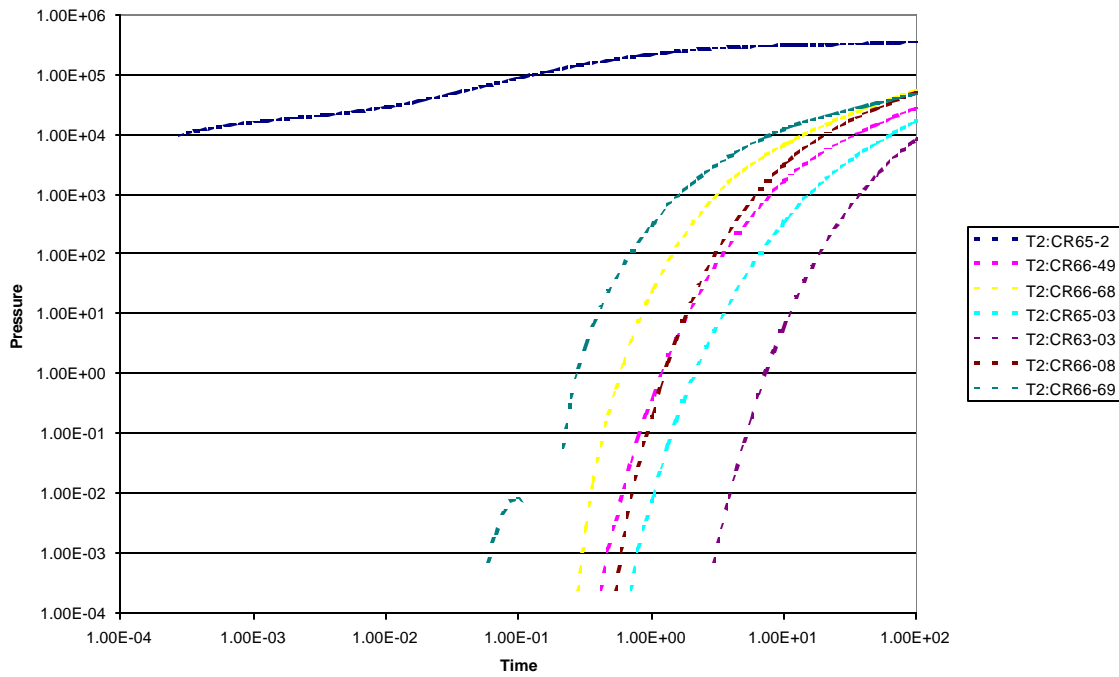


Figure 3-91. Change in pressure for wells 65-52, 66-49 and 66-68. Pressure response is quicker for Shoshone 66-49 although Shoshone 66-68 is closer to the injection in Shoshone 65-2.

Variable Fracture intensity ratios: Breakthrough times

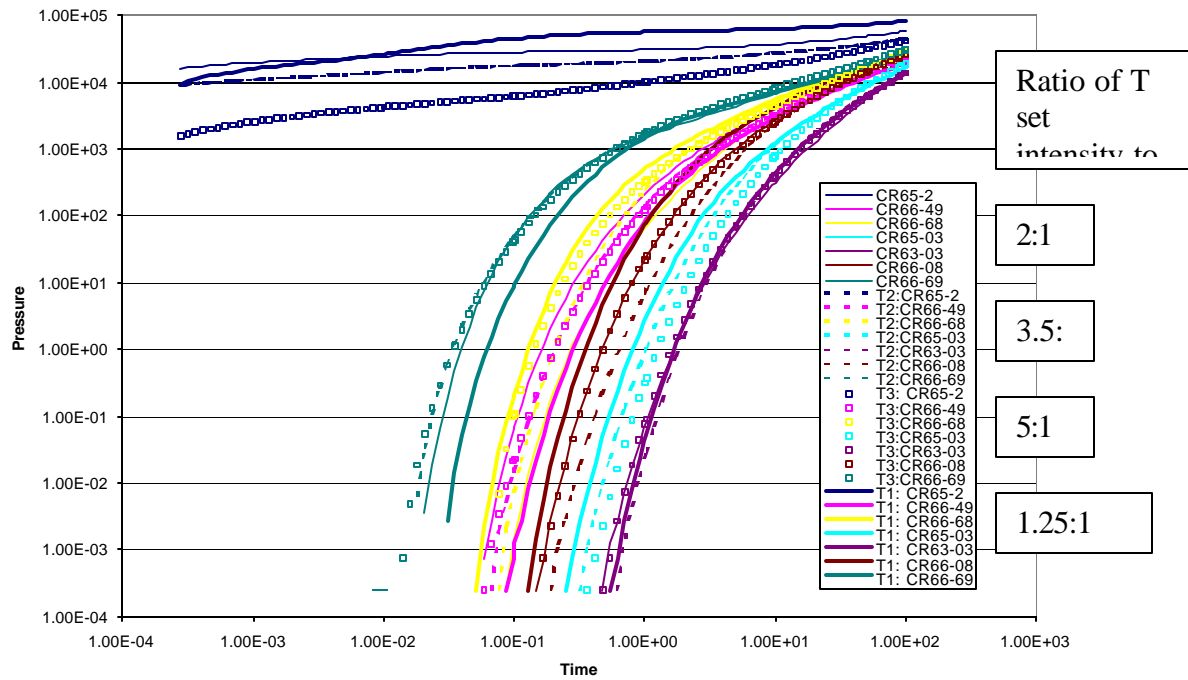


Figure 3-92. Breakthrough curves for all wells for varying the ratio of the fracture intensities between the T and L sets.

Fracture intensity for T and L sets				
Run	T-set	L-set	Ratio	Total
1	0.05	0.04	1.25	0.09
2	0.06	0.03	2	0.09
3	0.07	0.02	3.5	0.09
4	0.075	0.015	5	0.09
5	0.0819	0.0081	10.11111	0.09

Table 3-7. Input parameters for varying fracture intensities in T and L sets

Fracture set intensity ( $P_{32}$ )				
Run	T-set	L-set	Fracture Length	
1	0.06	0.03	50	
2	0.06	0.03	75	
3	0.06	0.03	100	

Table 3-8. Input parameters for breakthrough test with variable fracture length

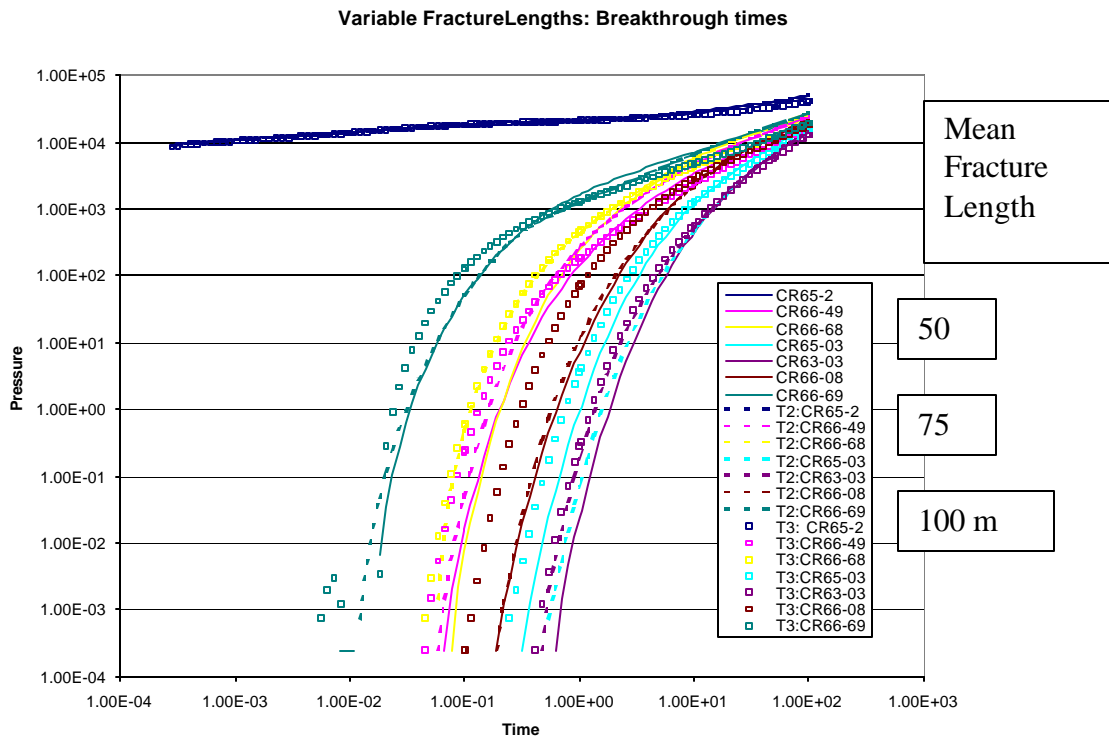


Figure 3-93. Relative breakthrough curves as a function of fracture length.

response is seen earlier in Shoshone 66-49 than in Shoshone 66-68, which is consistent with the field observations.

A second model experiment was to maintain the fracture intensity but vary the equivalent radius of the fractures in both sets. Using a relative fracture intensity of 2:1, the fracture radius was varied from 50 m to 75 m to 100m. The resulting breakthrough curves are shown in Figure 3-93. Generally, as the fracture radius increases the time to breakthrough decrease for almost all wells. However, this is not uniformly true. Interestingly as the fracture radius increase to 75 the breakthrough times for Shoshone 66-49 and Shoshone 66-68 become almost identical. The breakthrough time for well Shoshone 65-08 is unchanged from 50 to 75m, but is substantially reduced for a fracture radius of 100 m. Shoshone 65-03, as there was no consistent correlation between increased fracture length and decreased arrival time.

Pressure transient modeling has demonstrated that the DFN models generated for the Circle Ridge field are consistent with permeability values calculated from fall-off tests. Differences in pressure breakthrough times in the producing wells can also be introduced by the discrete nature of the flow-fields within the DFN model. Calibration has suggested that individual fractures have permeability around 40 mD and a radius on the order of 50 to 75 m. Model results also suggest a 2:1 ratio of T-set to L-set fracture intensities will produce breakthrough times consistent with field observation.

Pressure breakthrough times at production wells are strongly influenced by local heterogeneity in the DFN model, for this fracture intensity.

#### *3.6.2.4 Single Well Pressure Transient Testing*

A 44-hour Subthrust Block 6 Phosphoria falloff test was performed at Shoshone 65-20. This test was matched using commercial software and a uniform flux fractured well model in a radial composite reservoir. Late time data indicated a constant pressure boundary. The inner zone may reflect a region of wellbore damage, or may be due to a situation where only a few fractures are directly connected to the wellbore. As the distance from the wellbore increases, these fractures become part of a more well-connected fracture network, thereby increasing the network permeability. Results from the this test are as follows:

Inner zone kh= 444 millidarcy-ft (k=17.8 md, h=25 ft (7.6 m))  
Fracture half length = 315 feet (96 m)  
Skin=0.1  
Inner/Outer Mobility Ratio= 0.13  
Radius to high mobility zone= 321 feet (97.8 m)  
Constant Pressure Outer Boundary= 210 psi

A plot of the falloff type-curve match is presented in .

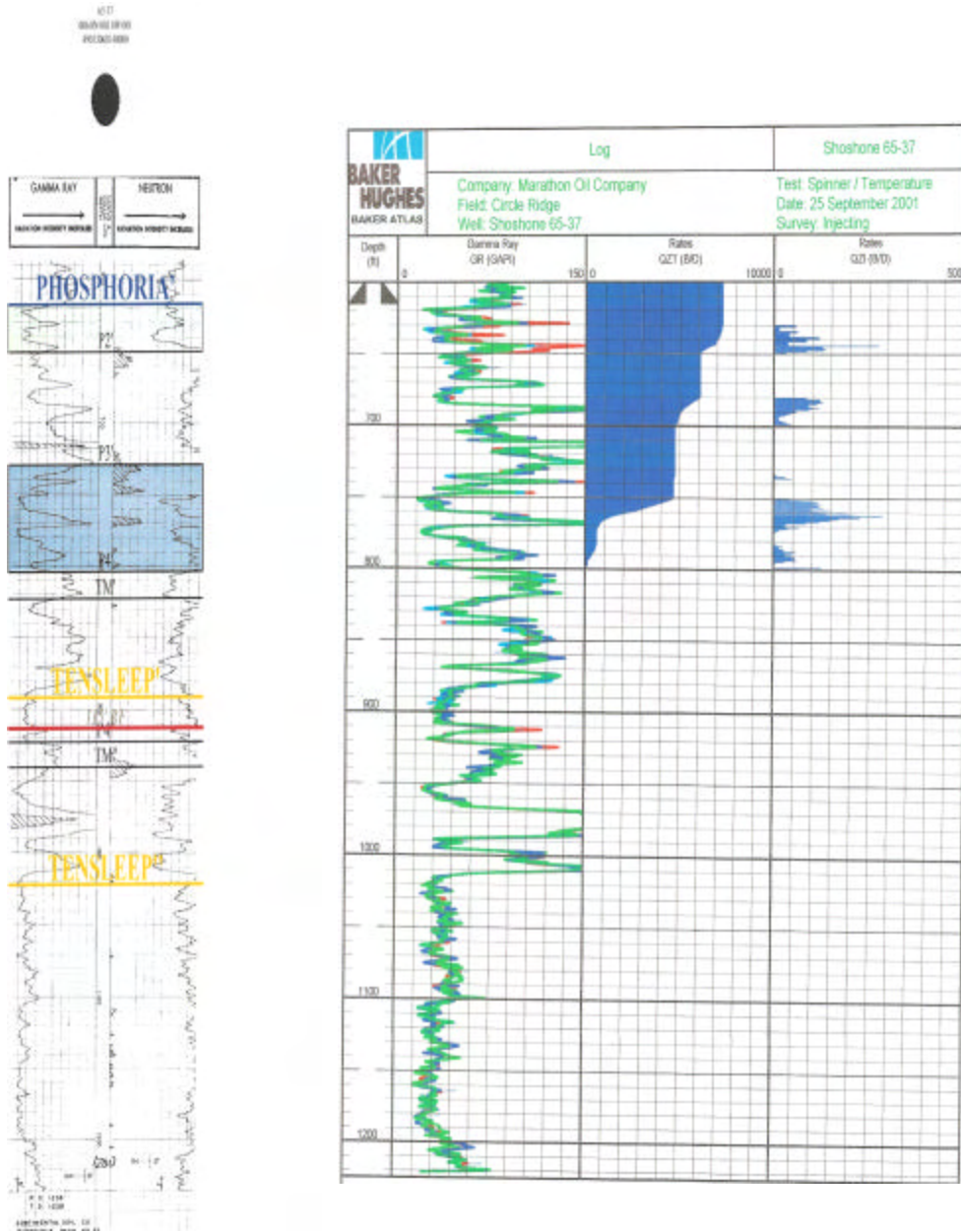
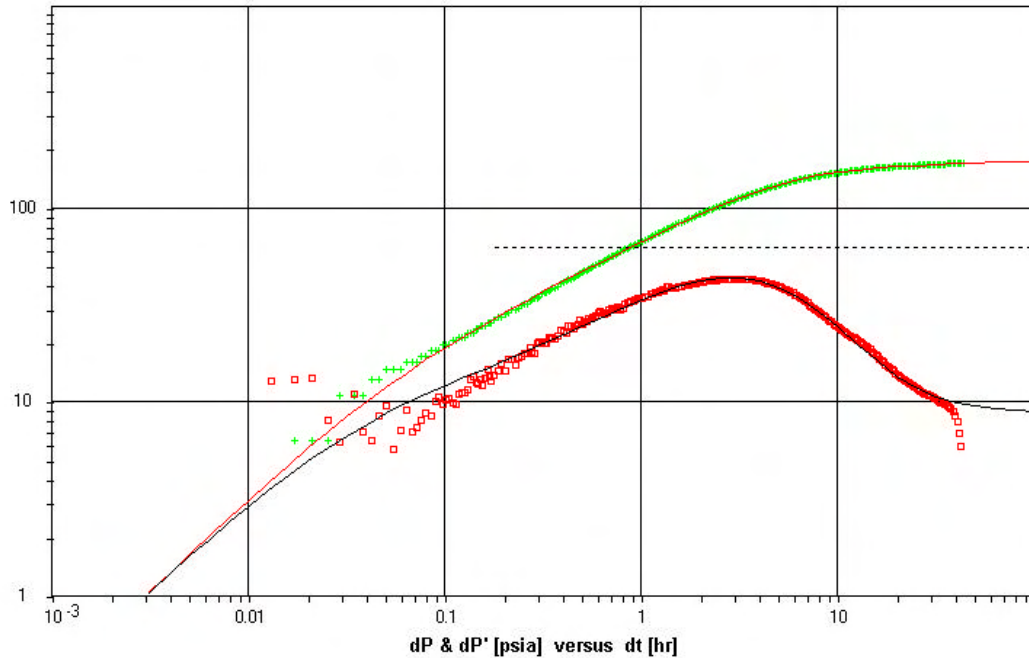


Figure 3-94. High-resolution spinner profile for Shoshone 65-37.



**Figure 3-95. Fall-off curve for Shoshone 65-20.**

### 3.6.3 DFN MODEL PARAMETER SUMMARY

The final DFN model was constructed based on a combination of the outcrop, subsurface image log, palinspastic strain, well test and tracer test data. Table 3-9 shows the parameters used to build the Circle Ridge Field DFN model and from what tests or processes the data values were derived. In addition, Figure 3-97 shows an example of the DFN model generated for the imbricate blocks 6 and 8. Also shown in this figure are the Red Gully, Green Valley and Blue Draw faults. The tops of the DFN model was generated separately for the Tensleep and Phosphoria Formations. Fractures were truncated against these boundaries (and the top of the Amsden at the base of the model).

The field-scale DFN model of fracturing was generated by formation and by block. This led to the creation of 18 individual DFN models (9 blocks, 2 formations) for the entire field.

One final check was carried out to evaluate the qualitative reasonableness of the model. This involved an assessment of the DFN model in light of fracturing seen in outcrop elsewhere in the Wind River Basin region (Figure 3-96). This outcrop shows that the fractures are large – on the order of 31 m, and that typically two sets orthogonal to bedding and to each other are common. This is consistent with the DFN model parameters determined for the Tensleep in Circle Ridge.

Parameter	Value	Where Obtained
No. Fracture Sets	2 dominant	Outcrop, Fracture Image log data
Fracture Set Orientations	Orthogonal to maximum extensional strain and orthogonal to bedding and parallel to maximum extensional strain (T & L sets)	Palinspastic reconstruction of folding and faulting history of field
Fracture Intensity	T Set $P_{32} = 0.06 \text{ m}^{-1}$ L Set $P_{32} = 0.03 \text{ m}^{-1}$	nitrogen injection test modeling
Fracture Size	Lognormal, mean = 50 m radius, 15 m std dev.	nitrogen injection test modeling
Fracture Permeability	mean 40 mD, std dev 40 mD	nitrogen injection test modeling
Kh	135 mD-m	Shoshone 65-20 fall-off test simulation
Fault Surfaces	NA	created from 3DMove palinspastic modeling
Formation tops	NA	created from well intersections and 3DMove palinspastic modeling

**Table 3-9. Table of parameters for DFN models.**

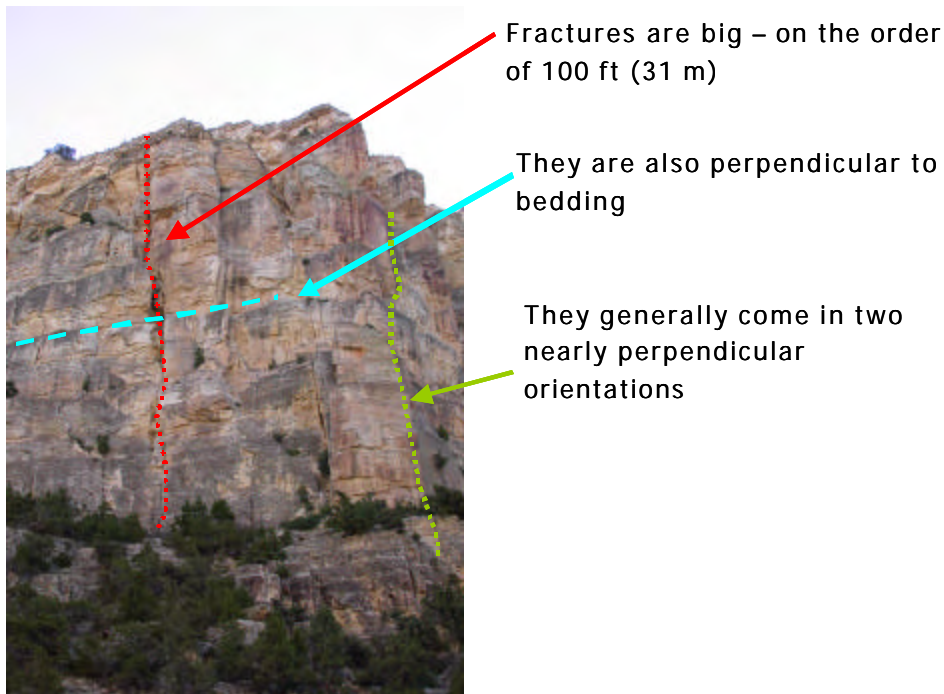


**Figure 3-96. Outcrop of Tensleep Sandstone in the Wind River Canyon.**

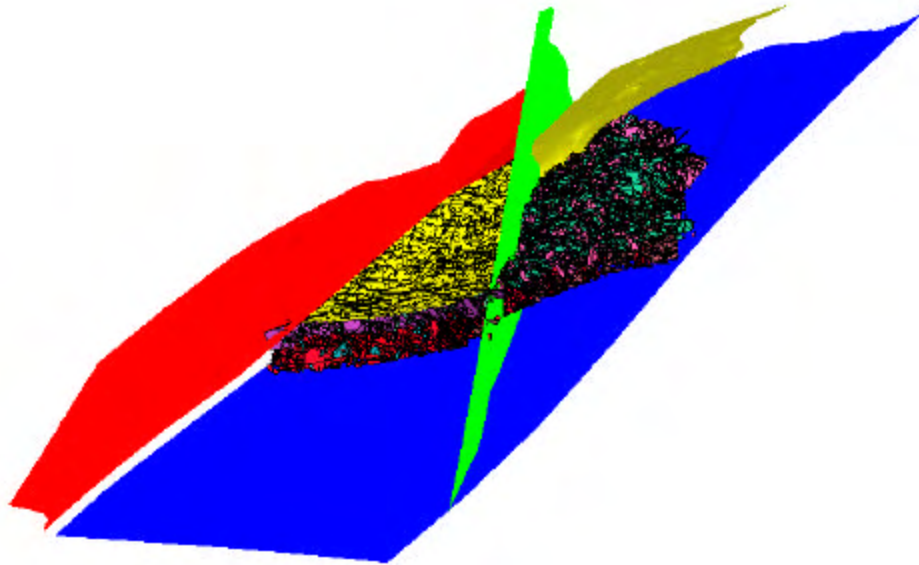


Figure 3-97. Example of the DFN model for imbricate blocks 8 and 9. The major faults (Red Gully, Yellow Flats, Green Valley and Blue Draw) are also shown.

### 3.7 Calculation of Reservoir Engineering Parameters

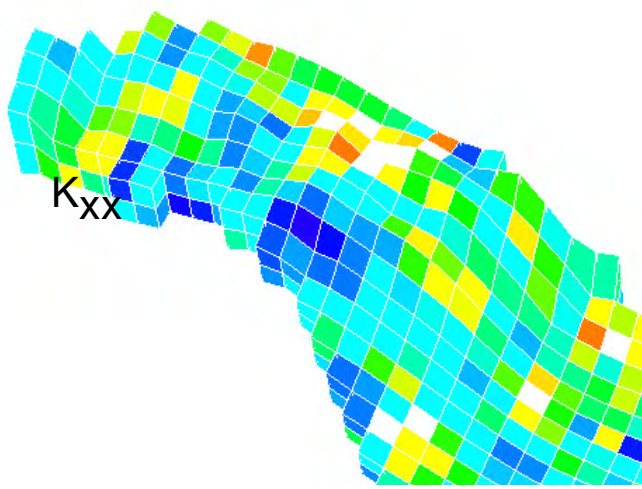
An important step in completing the reservoir model is to compute effective reservoir properties that reflect the porosity and permeability of the fracture system, and way in which fluids may transfer between the matrix and the fracture system.

The calculation of the effective properties is done for each grid cell based upon the fractures found in that grid cell in the model and the properties of the fractures. No upscaling of properties takes place, as is often done for matrix permeability values that have been established at a scale finer than the gridding.

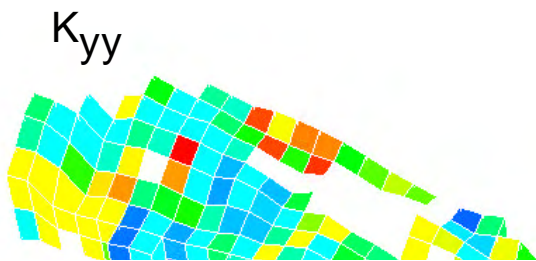
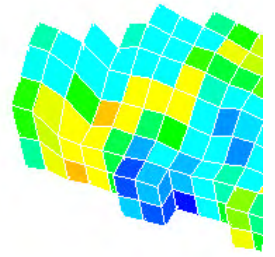
The total number of data sets associated with the calculation of effective properties is large: 6 properties for each of 9 structural blocks for each of 2 formations, or 108 distinct files that were loaded into the final 3D integrated reservoir model (Figure 3-98) shows an example for Block 6, Phosphoria Formation.

The grid architecture has both a layer-parallel and a layer-orthogonal thickness. The six separate variables plotted in this Figure correspond to the six effective fracture parameters incorporated into the final model for all blocks and formations. The actual displays shown below are not from the final model; rather, they are displays of the parameters calculated within the discrete fracture network modeling code.

The patterns of all of these parameters tend to follow the major flexural hinge zones. Figure 3-98 shows the higher values at the upwarp at the base of the structure and the downwarp or flattening at the top. The patterns also show a down-dip flexural hinge as



$P_{32}$



$P_{33}$



$K_{zz}$

Sigma

Figure 3-98. Examples of the calculation of effective reservoir properties for Block 6.

well, which can be seen most clearly in the Sigma Facto plot of the figure as a down-dip cyan colored corridor.

The grid cells for all structural blocks were designed to be approximately 50m by 50 m in the bedding-parallel directions, and 25 m in the layer perpendicular direction. Deviations from these target dimensions occurred if the formations significantly thinned or thickened over the individual structural block.

### 3.8 3D Integrated Reservoir Model

This section shows aspects of the 3D integrated reservoir model using the GoCad™ software. Figure 3-99 shows the distribution of matrix porosity for both the Tensleep and Phosphoria Formations in the Overthrust Block. Wells in which the matrix porosity was calculated from the wireline logging suite are also shown, including wells that are outside of the immediate overthrust block itself. Matrix properties for structural blocks with well control are incorporated into the model. The fence display shown in the Figure is intended to help visualize the three-dimensional distribution of the matrix properties.

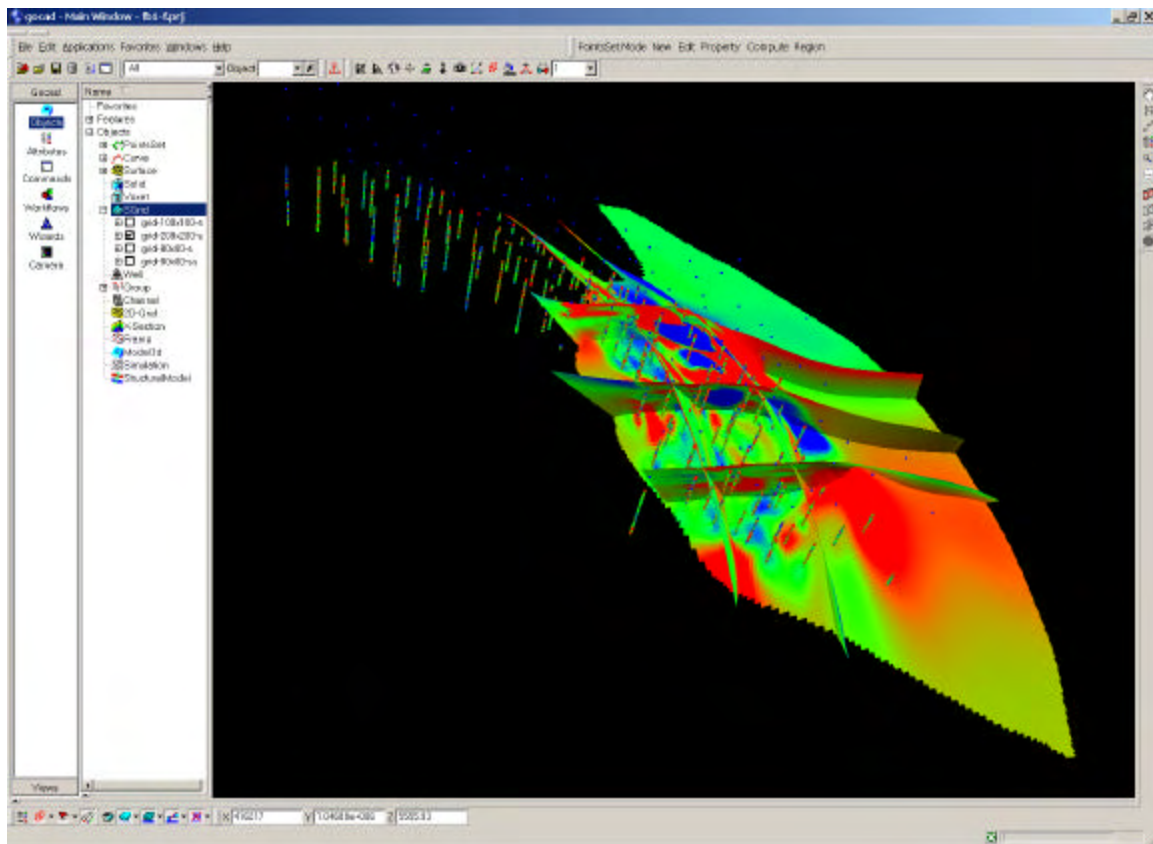


Figure 3-99. Matrix porosity distributed from well data in the Overthrust Block. The colors represent the value of the porosity. The wells used to create the model are also shown, and the colors in these wells indicate the value of matrix porosity calculated from the wireline log suite. The subvertical surfaces shown are not faults, but rather fence displays of the matrix porosity to help visualize the three-dimensional distribution of the data.

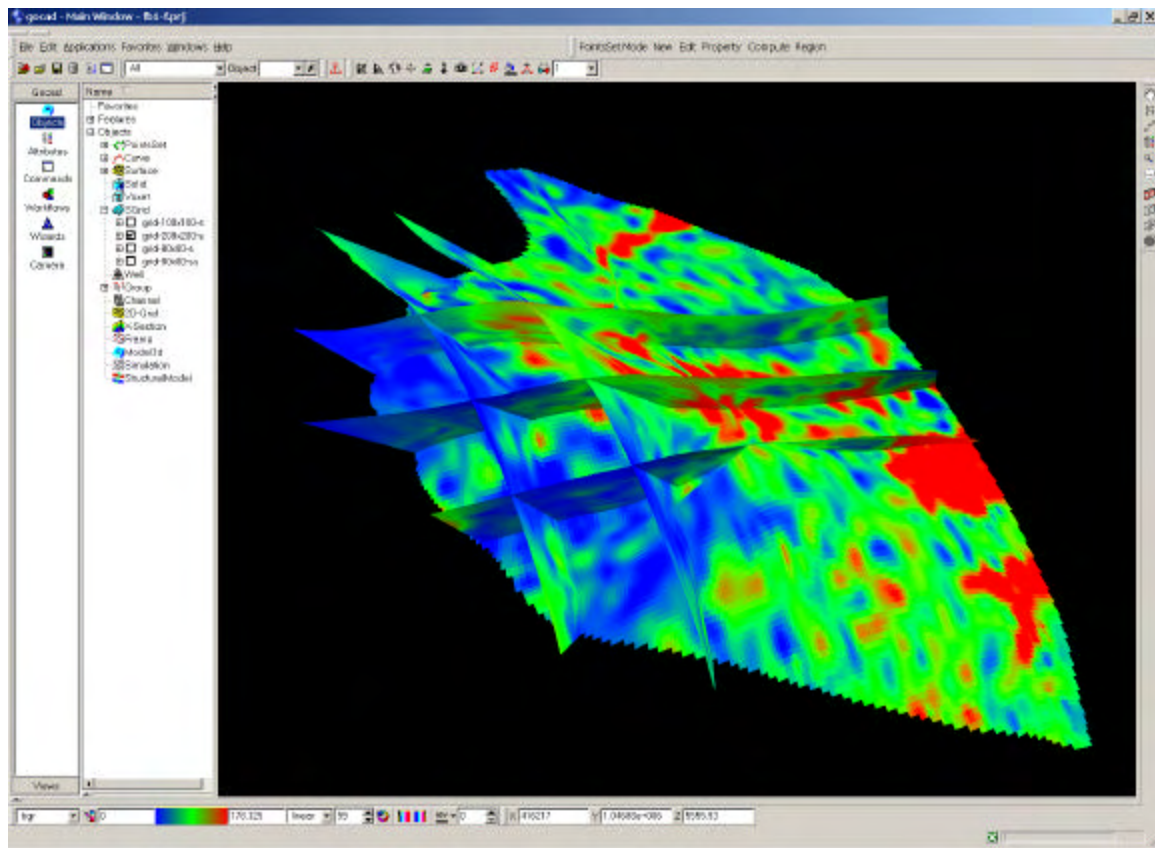


Figure 3-100. Distribution of fracture porosity in the Overthrust Block.

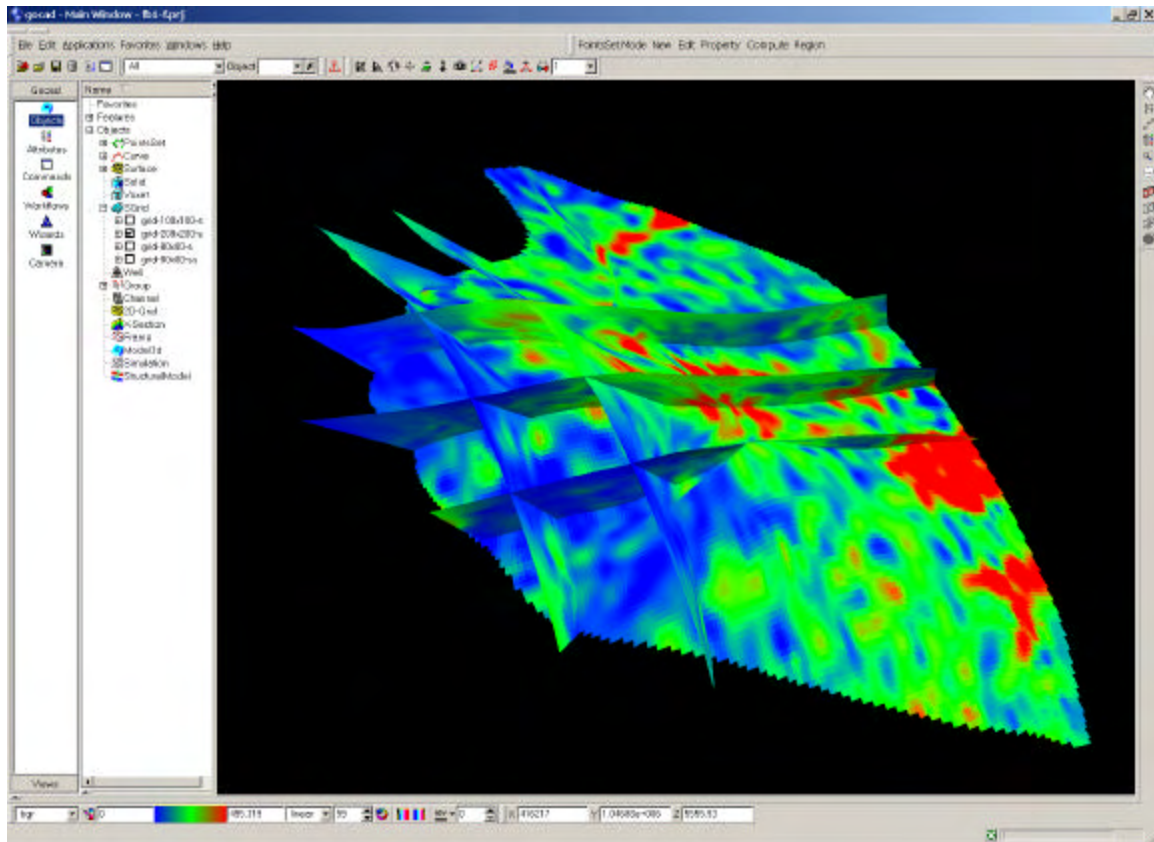


Figure 3-101. Distribution of fracture intensity in the Overthrust Block.

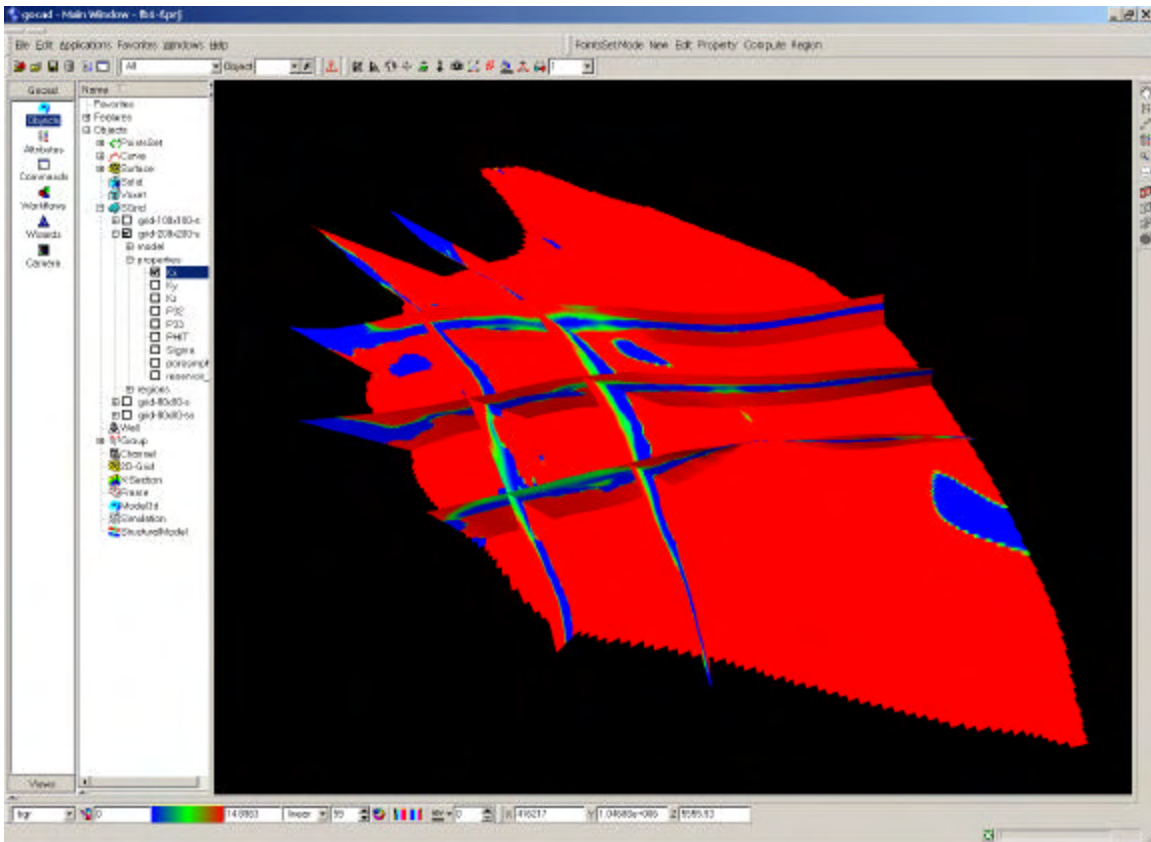


Figure 3-102. Distribution of effective fracture  $K_{xx}$  values in the Overthrust Block

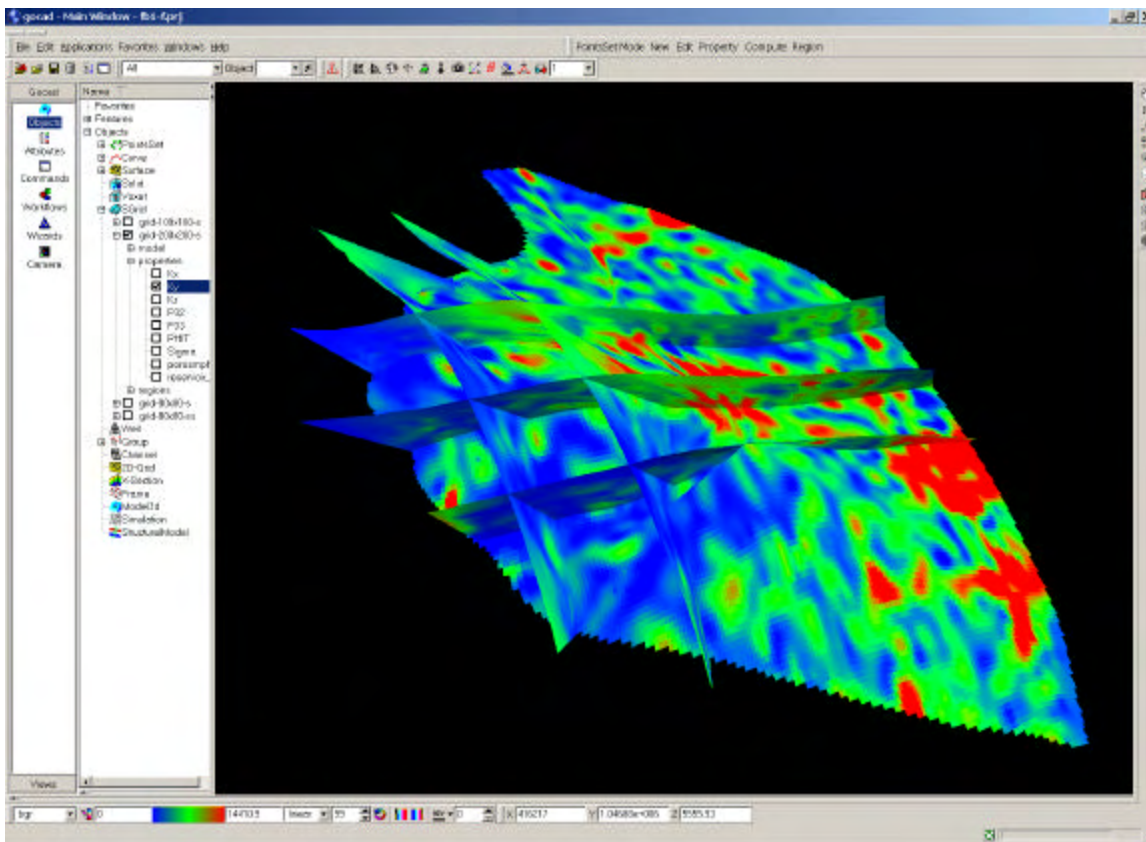
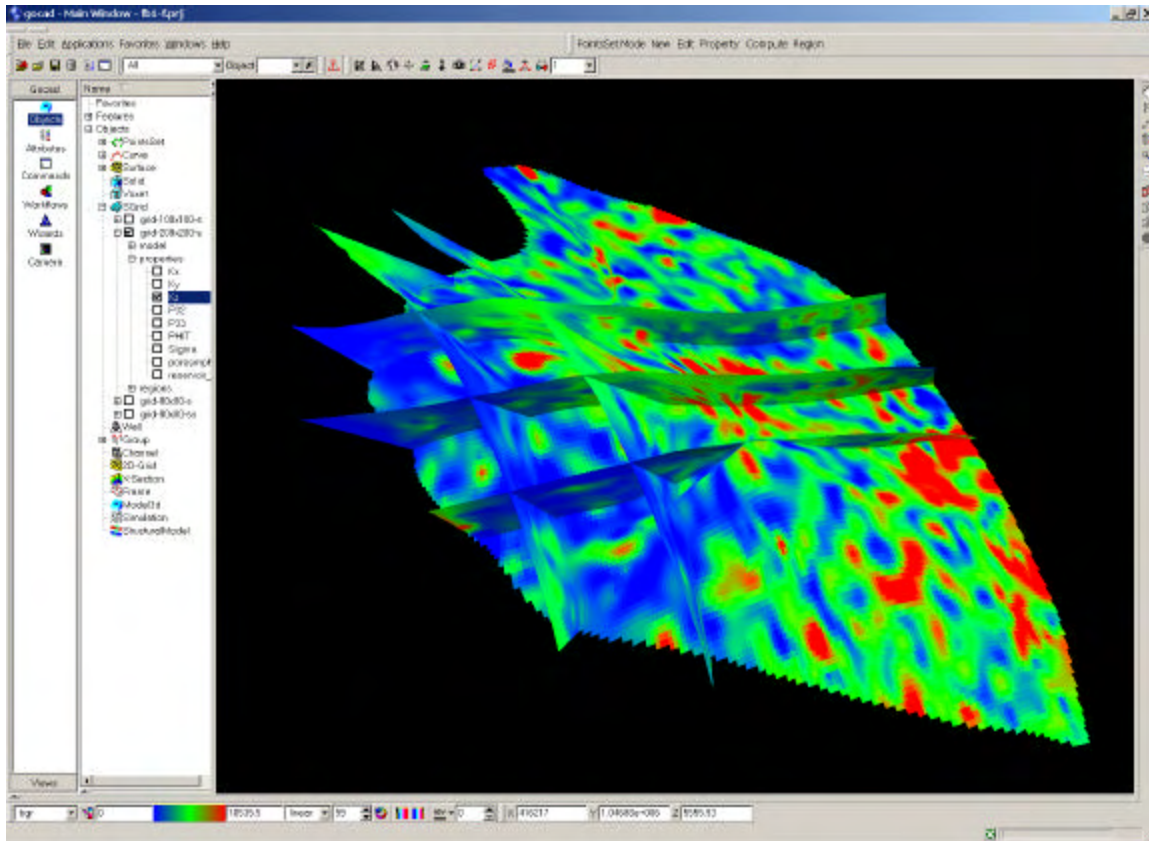


Figure 3-103. Distribution of effective fracture  $K_{yy}$  values in the Overthrust Block



**Figure 3-104. Distribution of effective fracture  $K_{zz}$  values in the Overthrust Block**

Figure 3-100 through Figure 3-104 show displays of the effective fracture properties. These include the directional fracture permeability values, fracture intensity, fracture porosity, and sigma factor for the Overthrust Block (structural block 1).

### **3.9 Evaluation of Reservoir Management Strategies**

Marathon Oil has been actively studying the economics of gas injection to improve the ultimate recovery of oil at Circle Ridge Field. The information contained within the final GoCad™ model is all directly applicable to quantifying the economics of such a project. Marathon plans to high-grade their predictions concerning gas injection using the GoCad™ model information, in conjunction with reservoir simulators and desktop calculations.

Due to the highly fractured nature of the Phosphoria and Tensleep in Circle Ridge, water flooding for secondary recovery operations has proved only marginally effective. In fact, Tensleep and Phosphoria water flooding has been suspended in the overthrust block, the major remaining reserve target for the field. In dual porosity fields like Circle Ridge, the drainage rates of oil from the matrix can be improved by filling the fractures with gas and driving the fracture gas-liquid contact down structure. This gas-oil gravity drainage

mobilization process is described by the following Richardson and Blackwell (1971) equation:

$$\frac{(\Delta Z)_{S_o}}{\Delta t} = \frac{4.4 \times 10^{-5} K_v \Delta \rho}{\mathbf{u}_o \mathbf{q}} \frac{dK_{ro}}{dS_o} \quad \text{Equation 3-1}$$

where:  $K_{ro}$  = relative permeability to oil

$K_v$  = matrix vertical permeability, in millidarcies

$S_o$  = oil saturation, fraction of pore volume

$\Delta t$  = change in time in days

$\Delta \rho$  = difference in density between draining liquid and injected gas, in lb<sub>m</sub>/ft<sup>3</sup>

$\mathbf{u}_o$  = oil viscosity, in centipoises

$\mathbf{q}$  = porosity, fraction of bulk rock volume

$(\Delta Z)_{S_o}$  = vertical distance oil saturation moves in ft

As indicated by this equation, in order to predict the process, both matrix permeability and porosity, as well as current oil saturations, must be known. The petrophysical analysis of Circle Ridge logs performed under this project has allowed Marathon to update these critical components.

Equally as important as understanding these matrix properties, is an understanding of the fracturing in the field. The understanding of fracture porosity, in conjunction with the oil drainage rates and reservoir pressures, allows for the projection of gas requirements for gas-oil gravity drainage projects. This gas injection forecast is critical to the design and economics of the project. Additionally, Marathon's experience with gas injection projects has indicated the importance of fracture understanding in maximizing oil capture efficiency and in limiting the production of gas. Gas production is very undesirable, as it must be recompressed for reinjection or replaced by increased extraneous gas injection. Both of these cases result in higher costs for the project and a lowering of economic viability. The optimum placement of completions within highly productive fractures helps maximize the production of oil per completion, while limiting the potential for gas coning and production. An improved picture of fracture intensity and compartmentalization also aid in the placement of gas injectors. Ideal placement of injectors can help limit the number of injectors required and ensure that unnecessarily high completion pressure drops are not encountered.

In addition to studying the viability of gas injection at Circle Ridge, Marathon is also using information from this DOE project to evaluate the potential for dewatering the fracture system through increased withdrawals. This dewatering can create dual porosity gas-oil gravity drainage even with little or no extraneous gas injection. In conjunction with this dewatering, Marathon plans to investigate the use of horizontal drain holes to aid in the efficient capture of oil. Two Tensleep horizontal drain holes have been proposed for funding in 2003. Information from this project will aid the placement of the horizontal drain holes at or directly below the oil-water contact in the fracture system.

The orientation of the boreholes will be guided by the desire to intersect fractures and to produce areas of undrained oil-filled fractures (Figure 3-105). The red wellbore would be parallel to the dominant fracture orientation, and also be drilled into a region where lower than average fracture intensity is predicted. Alternatively, the yellow wellbore is oriented nearly perpendicular to the main fracture orientation, and into an area where the model predicts higher fracture intensity.

The improved structural visualization available from the GoCad™ model is also expected to aid future recompletion attempts by Marathon oil. This visualization will also help quantify the potential for expanding any improved oil recovery process into the smaller fault blocks.

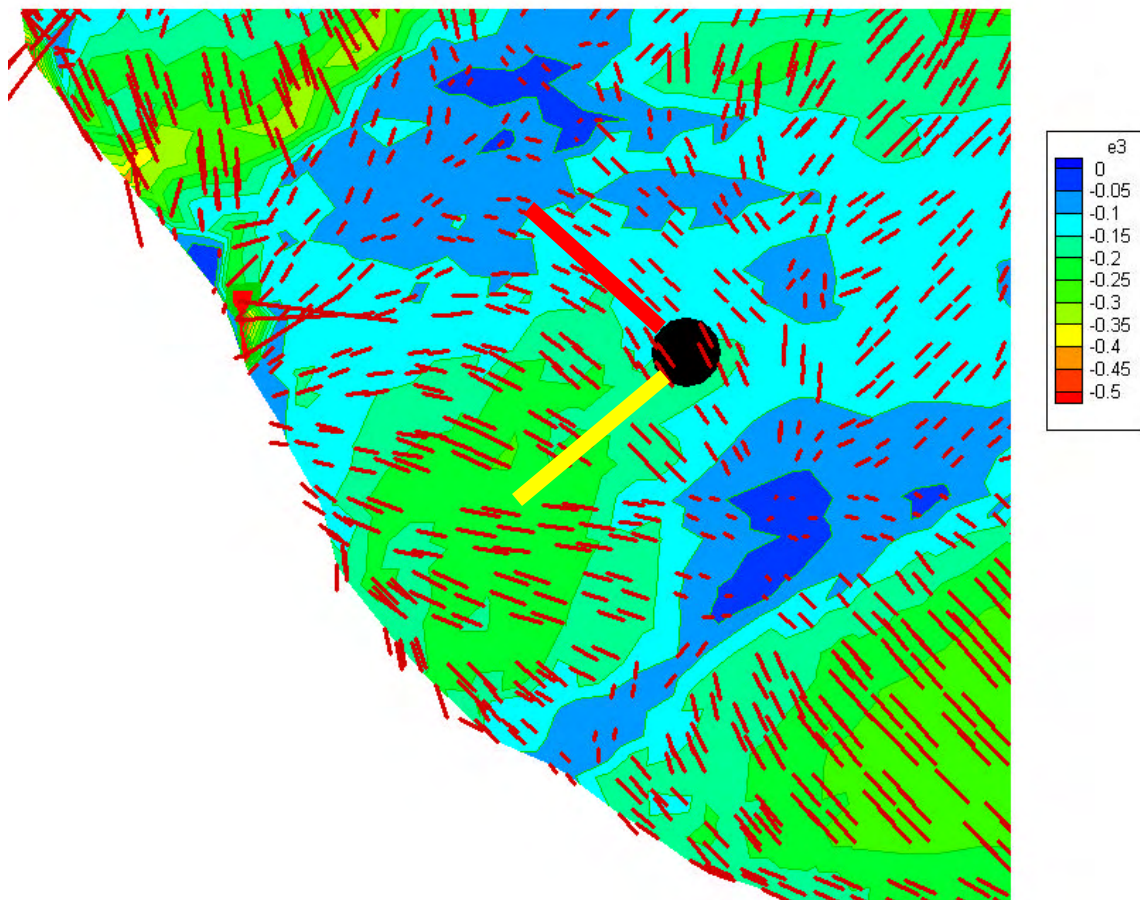


**Figure 3-105. Example of fracture model for use in drainhole planning.**

Another of the many benefits of this project has been the re-interpretation of matrix porosity made possible by the re-calibration of the older logs. Prior to this project, there had been two determinations of matrix pore volume for the Overthrust block. The first was made by Conoco, the original operator of the field. They estimated the total pore volume in the Tensleep and Phosphoria Formations in this block to be 149 MMBbls.

Prior to this project, Marathon made their own estimate of the pore volume from a Stratamodel that they had created for the block. Their estimate was 157 MMBbls, representing an increase of 5.4% over the Conoco estimate. As a result of this project, the knowledge of the matrix properties was greatly expended. The updated Stratamodel for the Overthrust block was estimated, based on the results of this project, to be 182 MMBbls, representing an increase of 22.1% over the original Conoco estimate and a 15.9% increase over the previous Marathon Stratamodel estimate.

Some of this pore volume may be water saturated, and some of the oil may not be producible, so the impact on reserves is not yet known. Reserve calculations are outside of the scope of the present study. However, since some of the is probably both oil saturated and producible, it is likely that the matrix study will add oil reserves to this field, representing increased income potential for the Tribes..

### **3.10 Technology Transfer**

Technology transfer was accomplished in several different ways during the project. These included meetings and presentations with the members of the tribal oil & gas commission and Marathon Oil, publications, additions and maintenance of the project web site, and semiannual progress reports.

#### **3.10.1 MEETINGS AND WORKSHOPS**

Several half-day meetings were held during the course of this project to report progress and discuss and resolve any issues that had arisen. These meetings consisted of principals from Golder, Marathon Oil, the Eastern Shoshone and Northern Arapaho tribes, and subcontractors and representatives from government agencies such as the Bureau of Indian Affairs, the Bureau of Land Management, the Montana Bureau of Mines and the U. S. Department of Energy. Presentations were made by PowerPoint for each of these meetings, and the PowerPoint presentations were posted and are available at the project web site (Section 3.10.3). The dates and locations of the meetings are shown below:

Kick-off meeting – Fort Washakie – June, 2000  
Progress Report – Cody, WY – May, 2001  
Progress Report – Cody, WY – Jan, 2002  
Progress Report – Cody, WY – July, 2002  
Final Report – Cody, WY – Sept., 2002

#### **3.10.2 PUBLICATIONS/CONFERENCE PRESENTATIONS**

Articles and conference proceedings published thus far include:

*La Pointe, P. R., J. Hermanson, M. Dunleavy and R. Parney (2002). New tools for modeling and visualizing fractured reservoirs enhance engineering & reservoir development. Oil & Gas Journal, May 2002.*

*Parney, R. and P. La Pointe (2002). Structural Interpretation of Natural Fracture Patterns in the Wind River Basin Wyoming. Annual Meeting, Canadian Society of Exploration Geophysicists, 6 May – 10 May 2002, Calgary, Canada.*

*La Pointe, P. R. and J. Hermanson (2002). The Prediction of the Orientation and Intensity of Fractures in the Circle Ridge Field, Wind River Basin, WY, through the Geomechanical Reconstruction of the Palinspastic Strain Field. 2002 Oil Rock (SPE/ISRM Rock Mechanics Conference), 20-23 Oct., 2002, Irving, TX.*

Additional manuscripts on various aspects of the project are underway, but have not been submitted.

In addition, various aspects of this project have been presented in effective ways outside of formal publication. During 2001, Dr. La Pointe developed and taught a half-day course for the Society of Petroleum Engineers (SPE) on fractured reservoir characterization and modeling. This course was presented in Washington D. C., San Francisco, Tehran, Iran, Santa Cruz, Bolivia, and The Hague, Netherlands, and featured the generation of fractured reservoir models through 3D palinspastic reconstruction, using the data and examples from the Circle Ridge study. Aspects of the tracer test modeling were also included in some of the later workshops.

### 3.10.3 PROJECT WEB SITE

#### 3.10.3.1 Web Site Development

The purpose of the project web site was to make available most of the data and results obtained in this project, and also to communicate how and why the work flow was the way it was, so that those wishing to carry out similar studies would have a template and an explanation of that template to follow. When the user logs onto to <http://www.fracturedreservoirs.com>, the following index page appears (Figure 3-106).

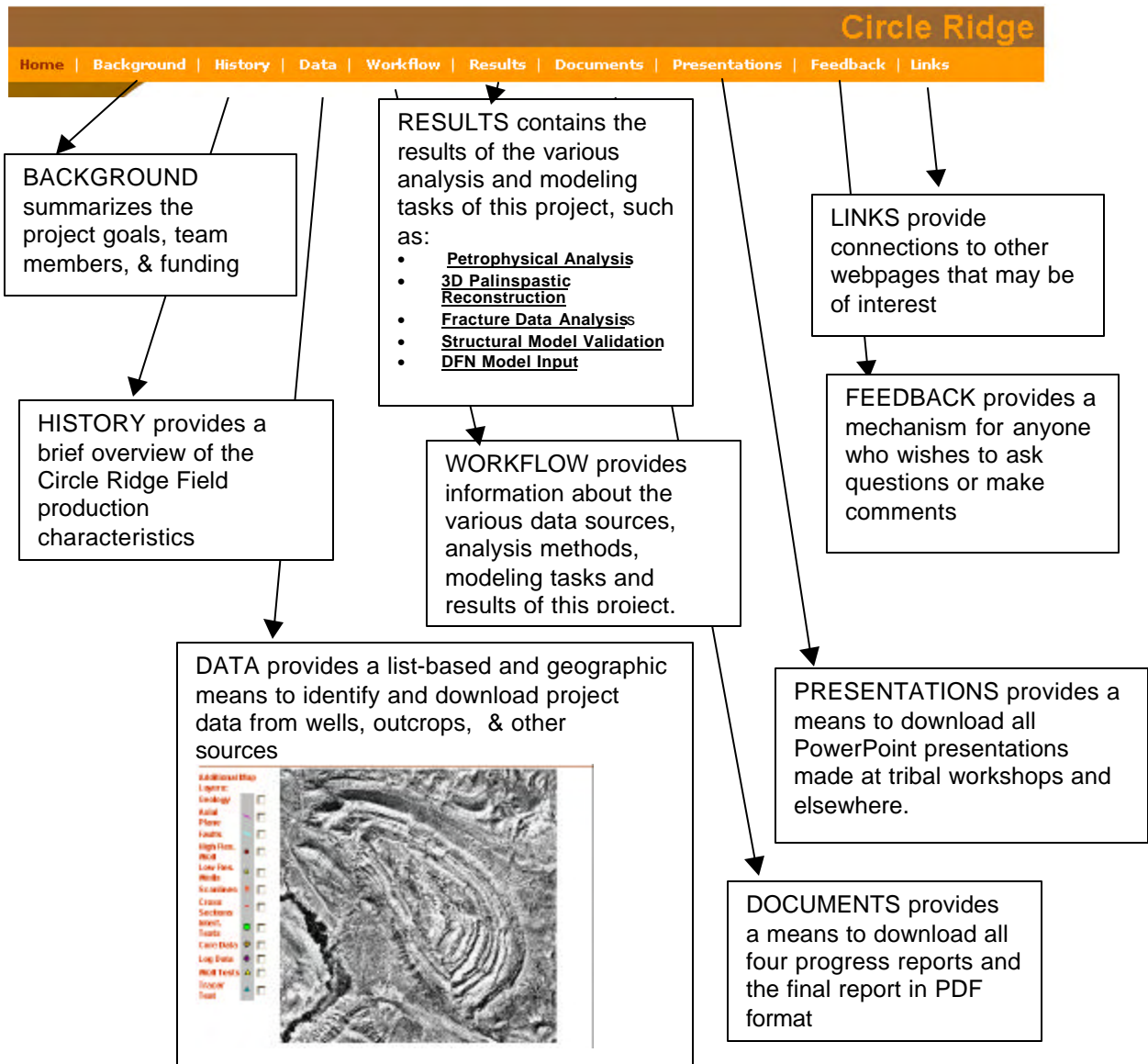


Figure 3-106. Overview of home page for Circle Ridge Project.

The homepage provides the user with a starting point to learn about the project, the production history of the Circle Ridge Field, the geology and tectonics of the Field and surrounding areas, obtain for their own use all data obtained through the project, obtained results derived from this data, to develop an understanding of the workflow, to download or view the various presentations and reports issues by the project, and to provide feedback and comments.

One of the unique features of this project website is the interactive workflow diagram. Figure 3-107 shows the interface for this module. The visitor is able to move the mouse over various portions of the diagram shown in the figure and to activate explanatory pages for most of the objects shown, as well as to go to the data or results that are related. For example, when “Field Reconnaissance” was selected (arrow in the

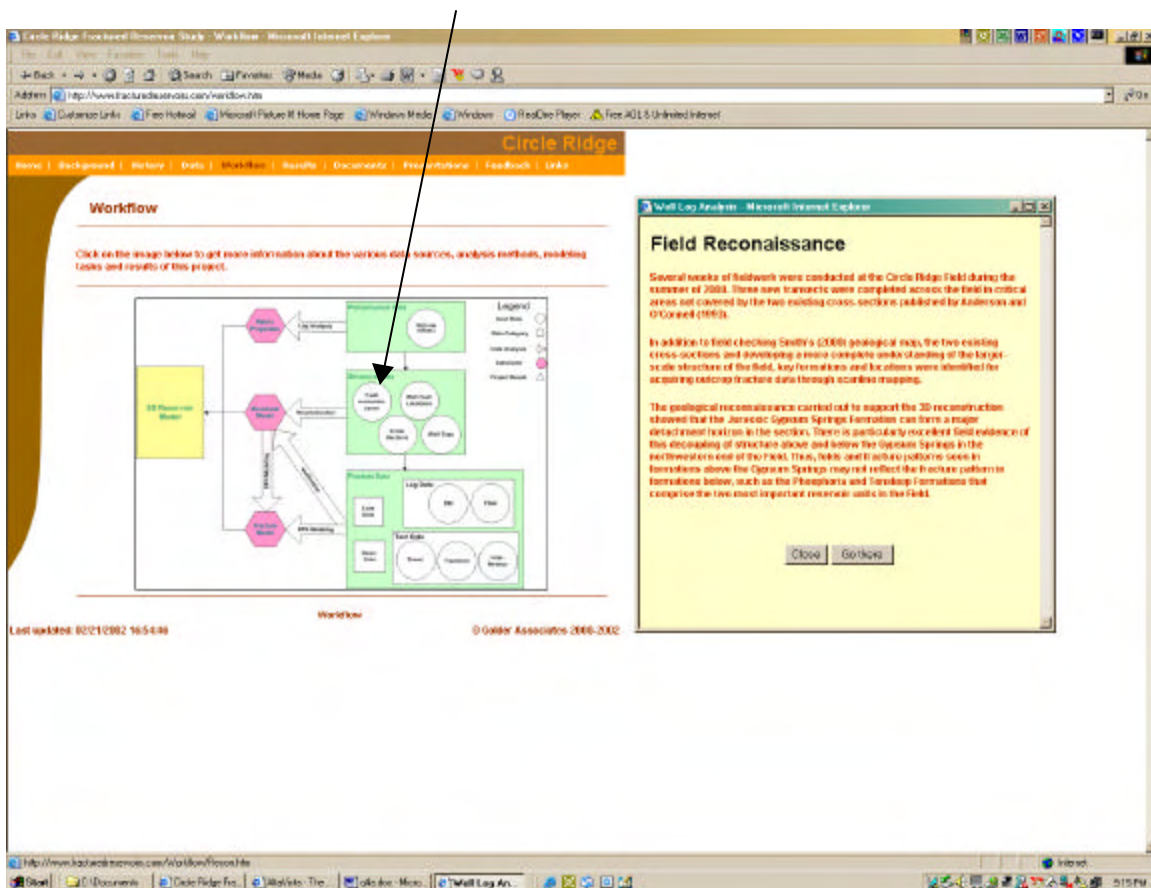


Figure 3-107. Screen grab showing new interface for *WorkFlow* module.

figure), a new frame appears that explains what this data was and how it fits into the overall workflow. If the visitor wishes to learn more, then clicking the “Go There” button takes the visitor to the section of the website containing photographs of the field reconnaissance. This feature helps the visitor to more readily understand why certain data has been collected, how it is analyzed or used, and how it fits into the overall project.

### 3.10.3.2 Web Site Statistics

The project website became operational in August 2000. Individuals visited the web site on the first day it was open to the public. Publication on the web site of the first Semiannual Progress Report at the end of October 2000 coincided with a major increase in visits. The rate of visitation has remained relatively constant throughout the project. Visits average between two and three external visits a day. Figure 3-108 provides an overview of website activity, spanning the period August 17, 2000 through July 31, 2002. This figure shows that the level of website activity has remained nearly constant since late November 2000, the time when the first project report was released.

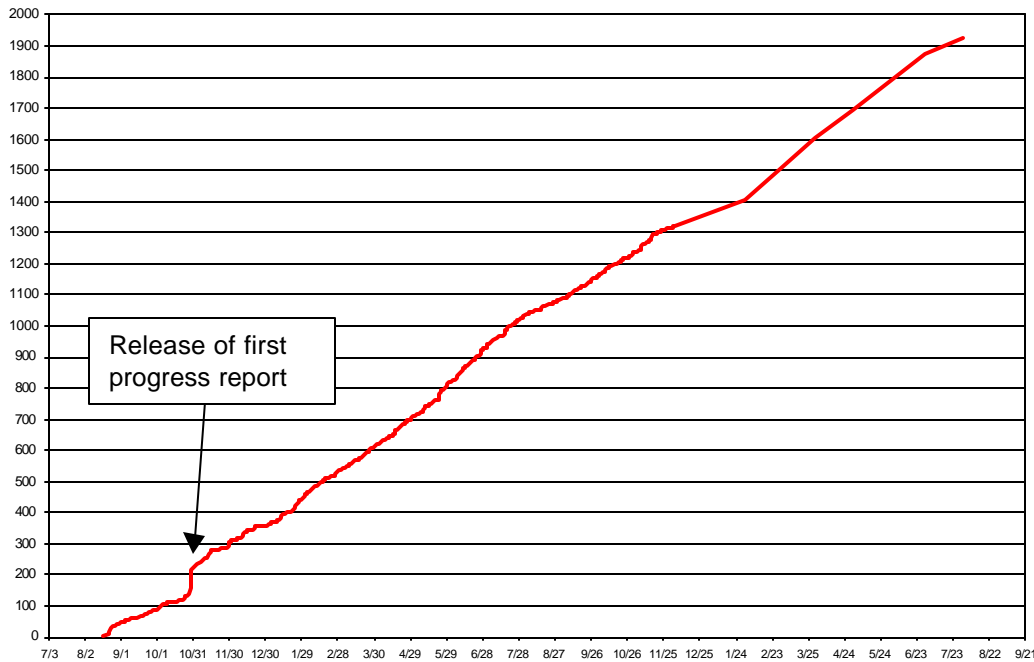


Figure 3-108. Web site activity, August 17, 2000 through July 31, 2002.

## 4 CONCLUSIONS

### 4.1 Overview

This section summarizes the most important accomplishments of the project and their benefit to the Northern Arapaho and Eastern Shoshone tribes through a better understanding of the Circle Ridge field

### 4.2 Improvements in Reservoir Understanding

#### 4.2.1 FAULT BLOCK ARCHITECTURE

Prior to this project, the structural understanding of the Circle Ridge Field was clearly in need of improvement.

One aspect in need of improvement was the large-scale structural block architecture of the Field. The structural model for the field was uncertain, as shown in Figure 4-1.

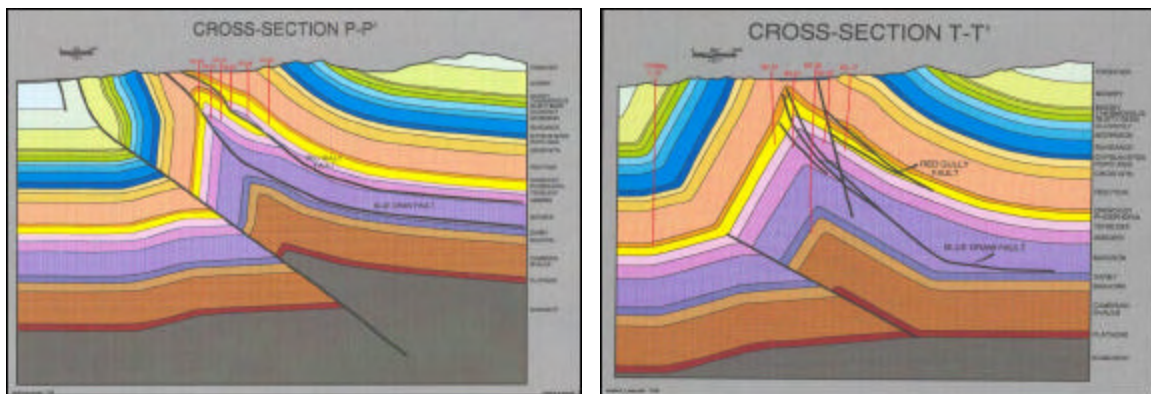


**Figure 4-1. Two of three structural cross-sections prepared by Anderson and O'Connell for the Circle Ridge Field.**

The cross section on the left shows basement involvement; the one on the right shows no basement involvement. Such a radical change in mechanics is possible but unlikely.

Through the 3D palinspastic reconstruction carried out in this project, these inconsistencies were resolved. The three dimensional constraints and the balancing constraints made it possible to derive a much more reliable interpretation of the fault block architecture (Figure 4-2). Not only have the faults been reconstructed in a way that is far more accurate than the old 2D cross-sections, but the fact that they have been imported into modern numerical visualization tools such as GoCad™ make it possible to interactively view and examine any part of these fault blocks. Previous to this project, fault surfaces were viewed as structural contours in different colors (Figure 4-3), a very useful method for a skilled structural geologist, but difficult for many engineers and much less suitable for the types of interactive viewing that can clarify how reservoir development in one block might impact development in other blocks.

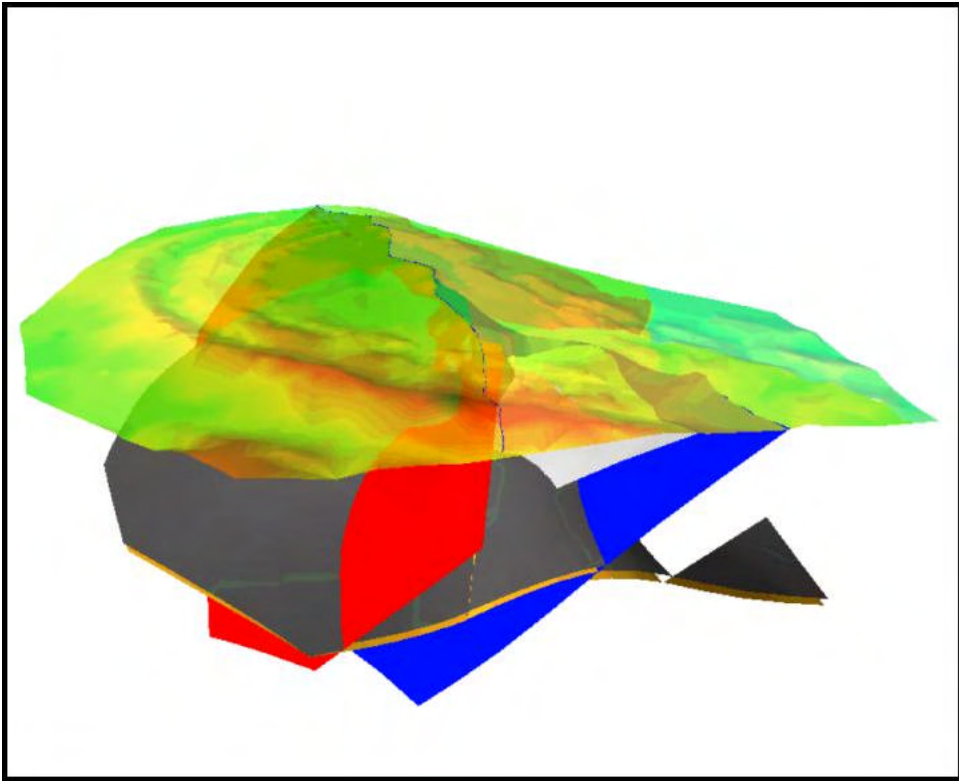


Figure 4-2. 3D visualization of the faults as reconstructed in this project.

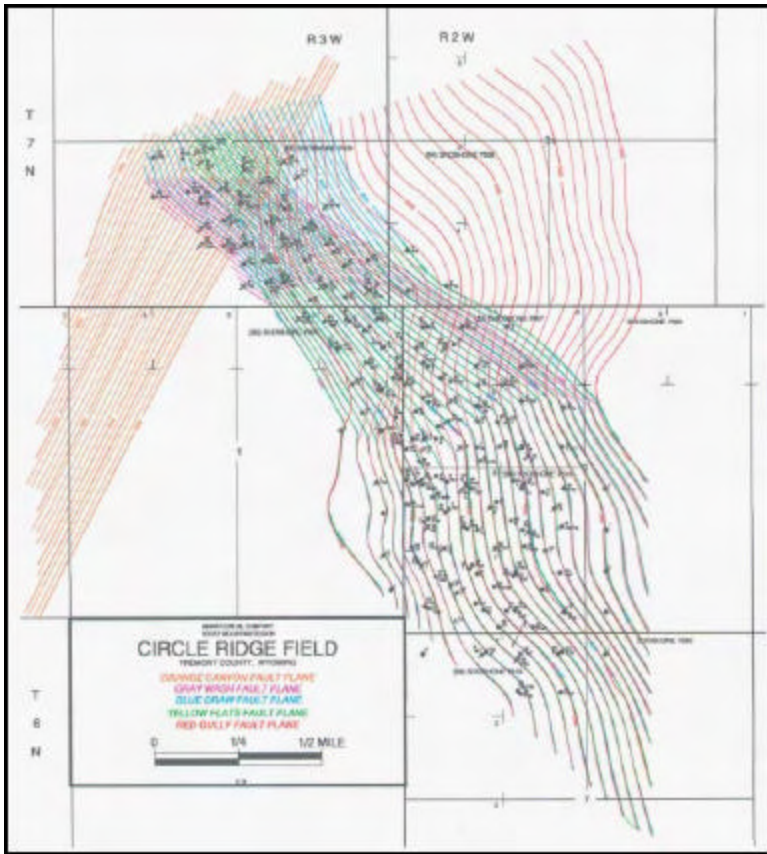


Figure 4-3. Visualization of fault surfaces prior to this project.

#### 4.2.2 MATRIX PROPERTIES

Another key area where this project has greatly improved reservoir understanding is through the improved matrix property characterization through the innovative calibration of older wireline logs.

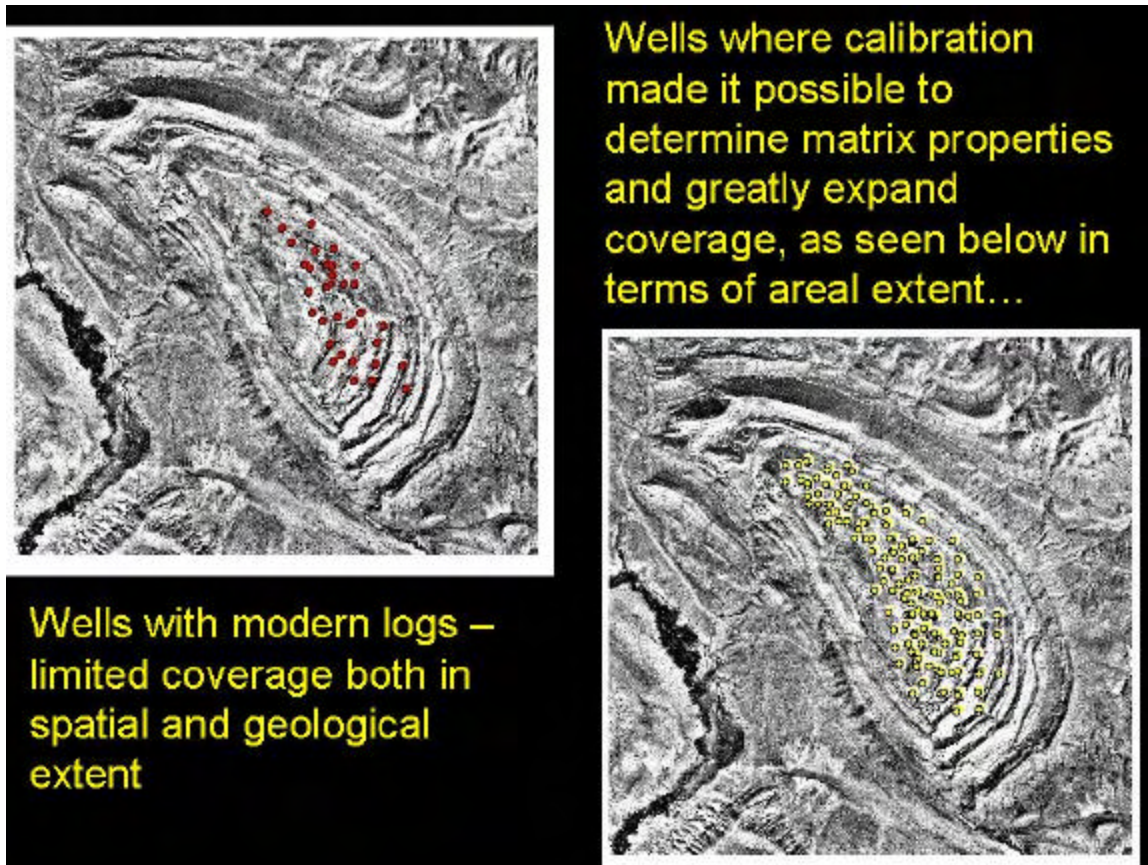


Figure 4-4. Expansion of matrix property knowledge through calibration of older wireline logs.

Figure 4-4 shows the extent of this expanded coverage. The inset diagram in the upper left shows the locations of wells where modern wireline log suites had previously been available for interpreting matrix properties. The total matrix pore volume determined by marathon prior to this study was based on interpretations from these wells. As a result of the recalibration of older logs in this study, the coverage was greatly expended, as shown by the yellow wells in the inset diagram in the lower right-hand corner of the figure. In the overthrust block alone, this additional data identified an additional 25 million barrels of matrix porosity, which should lead to an upward revision of oil reserves in the field and additional revenue projections for the tribes.

### 4.2.3 RESERVOIR SCALE FRACTURING

Prior to this project, the model for fracturing in this field (Marathon Oil Company, unpublished reports) was that there was a dominant fracture set oriented that was vertical or subvertical and had a northeasterly strike (Figure 4-5). A secondary set approximately orthogonal to it was also recognized.

The results of the fieldwork in this project, and the validation of fracture orientations against the palinspastic strain, have shown that this model is in error. Figure 4-6 shows the strikes of the fractures measured at the eleven scanline sites in the Red Peak and Crow Mountain Members. The strikes have been corrected for orientation bias. The dominant fracture directions do not show a single, regional set as previously hypothesized. Rather, the strikes tend to wrap around the structure, which is what would be expected if the fractures occurred during the initial folding of the rock. Work in this project has shown that the fractures probably did occur during the folding, and moreover, that much more highly fractured and permeable corridors developed in areas of high strain that relate to the development of hinge zones.

Thus, the previous model of a dominant northeasterly regional set has been replaced by one in which the strain patterns produced as the rocks were originally folded can be used to predict the orientation and relative intensity of fracturing. This model was validated using the fracture image log from three wells, and by evaluating the breakthrough patterns in the nitrogen injection and bromide tracer experiments.

This new model for reservoir-scale fracturing is important because:

- a. It can be generated throughout the field using the strains from the palinspastic reconstruction;
- b. It predicts the local fracture pattern geometry; and
- c. its connection to the structural formation of the field and verification provide additional confidence in the model.

### 4.2.4 RESERVOIR VISUALIZATION

Prior to this project, there was no integrated 3D visualization of this reservoir. Matrix properties resided within a geocellular model, but his model did not contain fracture properties. Structural visualization was limited to three 3D structural cross sections (Anderson and O'Connell, 1993), or structural contour maps of the fault surfaces (Figure 4-3).

This project built a fully 3D integrated numerical model in GoCad™ that can be used to visualize all of the components of the reservoir, including matrix properties, faults, fracture properties and wells (Figure 4-7).

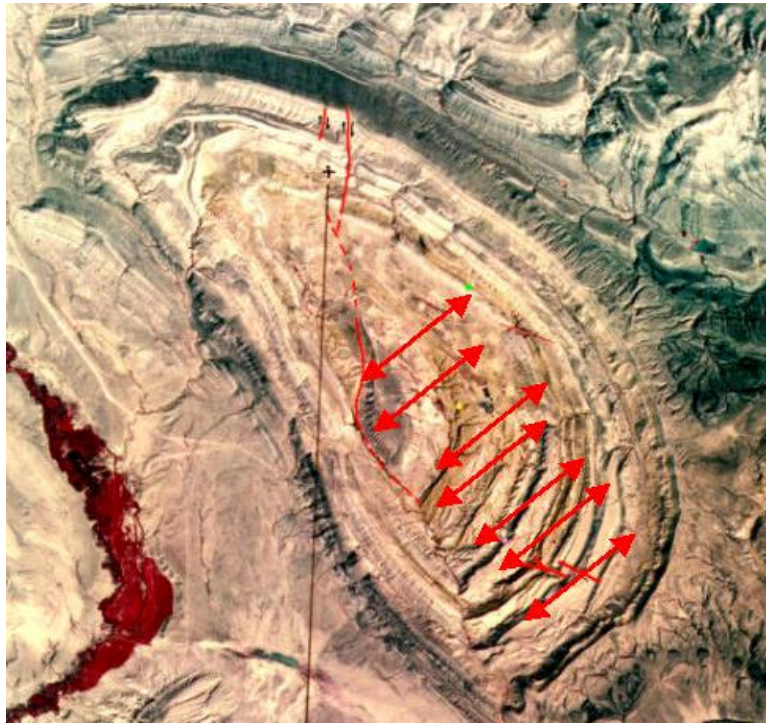


Figure 4-5. Satellite image of Field with perceived regional northeasterly striking fracture set superimposed on photo.

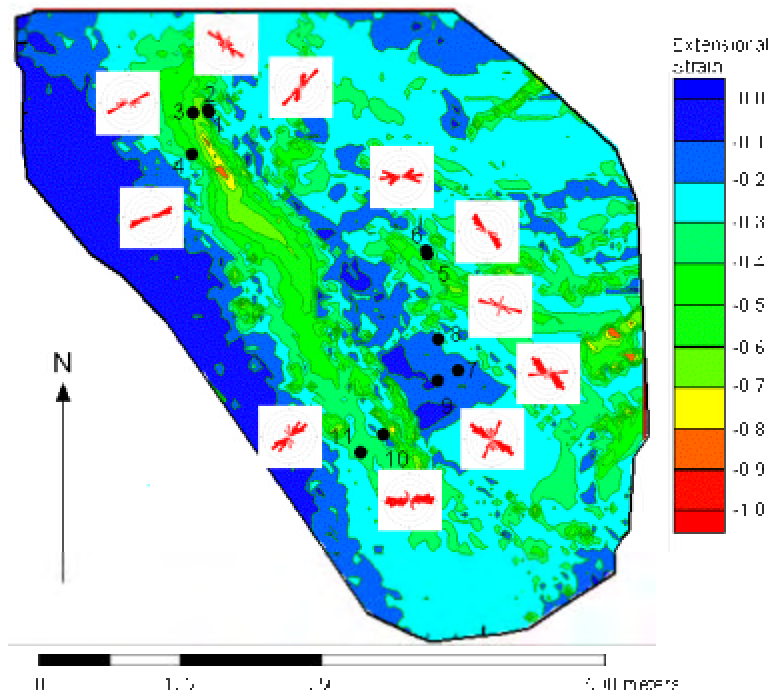


Figure 4-6. Rosette of Terzaghi-corrected fracture strikes at the eleven scanline sites.

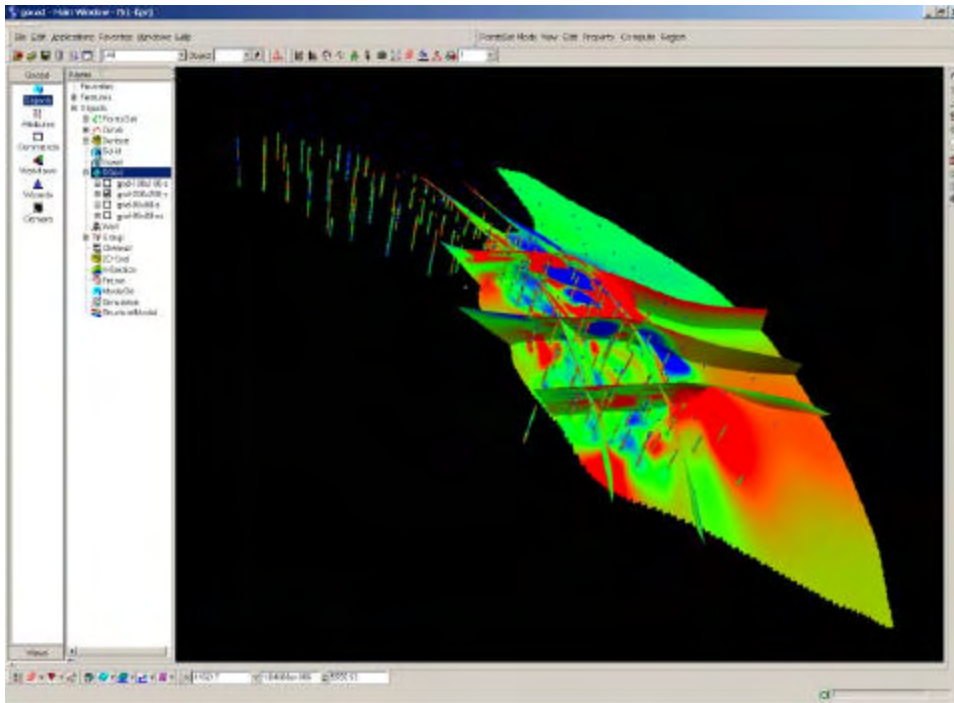


Figure 4-7. Example of 3D visualization of reservoir parameter values and well control.

### 4.3 Development of Reservoir Management Strategies

#### 4.3.1 CALCULATION OF EFFECTIVE FRACTURE PROPERTIES FOR NUMERICAL RESERVOIR SIMULATION

The results from this project have provided two types of information that were not previously available for use in numerical reservoir simulation: effective fracture parameter values throughout the field; and revisions to fault and formation surfaces throughout the field.

The effective fracture properties were calculated from the fracture pattern developed locally under using the folding strain as a control on both fracture orientation and intensity. The fracture pattern was represented as a DFN model. This DFN model was then gridded into cell with target dimensions of 50 m by 50 m parallel to bedding, and 25 m perpendicular to bedding. The following parameter values for each cell were calculated:

- fracture pore volume
- fracture intensity
- sigma factor
- effective directional fracture permeability
- fracture surface area

The entire grid for the Tensleep Formation was composed of 25,967 grid cells, while the grid for the Phosphoria Formation was composed of 11,430 cells.

#### 4.3.2 USE OF PROJECT RESULTS FOR ENHANCED RECOVERY PROCESS SELECTION AND DESIGN

Marathon Oil has identified the following characteristics of the Circle Ridge Field:

- Complex Structure-Multiple Fault Blocks
- Low Recovery: Highly Fractured Reservoirs with Viscous Oil
- Oil Viscosity 55 cp and Reservoir Temperature of 55<sup>0</sup>F
- Recovery less than 20% of OOIP

The daily water production from the field has increased consistently over the last 25 years. Oil rates have remained relatively flat by comparison, peaking in 1997 (Figure 4-8).

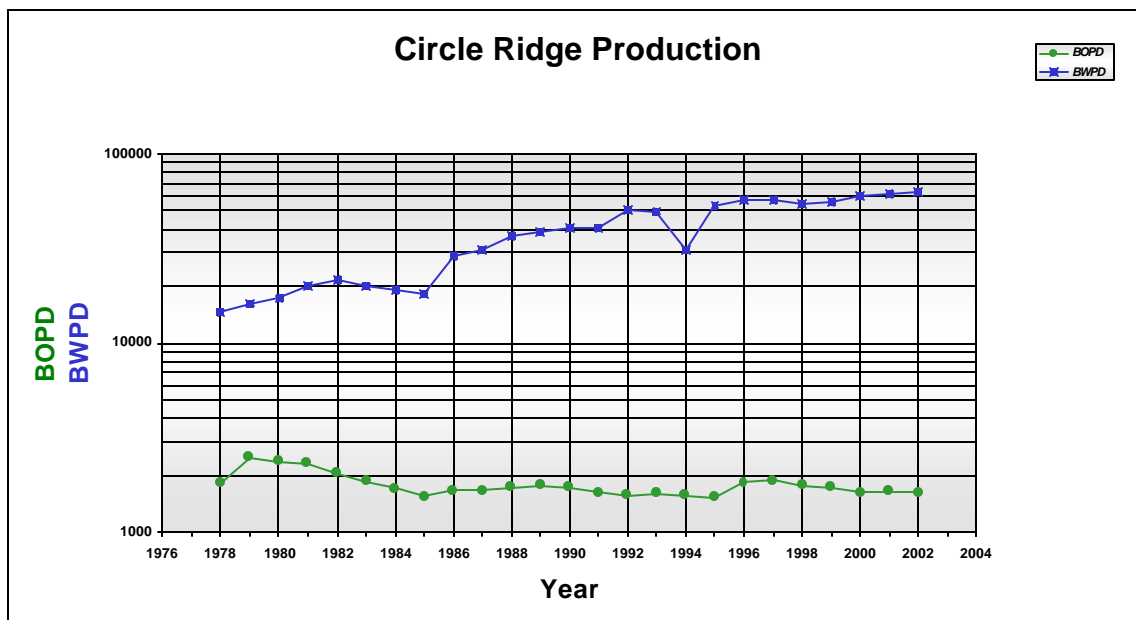


Figure 4-8. Water and oil rates for the Circle Ridge Field, 1978 – present.

These characteristics suggest that the Circle Ridge Field might be a good candidate for various types of gravity drainage recovery processes, including gas injection, de-watering and strategic recompletions. The Richardson and Blackwell equation describes the variables that can impact this process. The oil drainage rate is a function of matrix and fluid properties, such as:

- gas/oil density difference
- matrix vertical permeability
- oil viscosity
- oil relative permeability,  $f(S_w)$

In addition to the matrix and fluid properties listed above, the fracture system is also critical to exploit properly in designing and assessing the economic viability of these recovery processes. The results of this project that show the orientations of the fractures and the changes in fracture intensity can be used for:

- Placement (existing operations) of HDHs and recompletions
- Gaining a more accurate understanding gas injection volume requirements
- Optimizing placement of injectors and producers for gas injection projects based on fracture spacing and connections
- Understanding the linkage between formations
- Forecasting oil drainage rates which also depend upon fracture characteristics (sigma, porosity, intensity) in addition to matrix characteristics.

The results from this project will allow Marathon Oil to increase recovery from this field in at least four ways:

1. OOIP update leading to possible reserve additions;
2. Usage of fracture data in their Eclipse 3D reservoir simulator for reservoir management;
3. Use of 3D simulator/desktop models to evaluate gas/oil gravity drainage
4. Placement of recompletions and horizontals using increased understanding of fracturing.

Two Tensleep horizontal drain holes have been proposed for funding in 2003.

## 5 REFERENCES

- Agaston, R. S., 1952, Tensleep Formation of the Bighorn Basin: Wyoming Geological Association 7th Annual Field Conference Guidebook, southern Bighorn Basin, Wyoming, p. 44-48.
- Anderson, T. C., and O'Connell, P., J., 1993, Structural geology of the Circle Ridge Oilfield, Fremont County Wyoming, in Keefer, W. R., Metzger, W. J., Godwin, L. H. eds., Wyoming Geological Association Special Symposium on Oil and Gas and Other Resources of the Wind River Basin, Wyoming, p. 399-418.
- Andrews, D. A., 1944, Geologic and structure contour map of the Maverick Springs area, Fremont County, Wyoming: U.S. Geological Survey Oil and Gas Investigations Preliminary Map 13.
- Asquith, G. and C. Gibson (1982). Basic Well Log Analysis for Geologists. American Association of Petroleum Geologists, Methods in Exploration Series, Tulsa, OK (4<sup>th</sup> Printing), 216p.
- Barton, C. C. and P. R. La Pointe, 1995. Fractals in the Earth Sciences. Plenum Press, New York. 265p.
- Billings, M. P., 1972. Structural Geology (3<sup>rd</sup> Edition). Prentice Hall, Inc., Englewood Cliffs, New Jersey. 606p.
- Brown, W. G., 1988, Deformational style of Laramide uplifts in the Wyoming foreland: Geological Society of America Memoir 171, p. 1-25.
- Brown W. G., 1993, Structural Style of Laramide basement-cored uplifts and associated folds, in Snoke, A. W., Steidtmann, J. R., and Roberts, S. M., eds., Geology of Wyoming: Geological Survey of Wyoming Memoir no. 5, p. 312-371.
- Burtner, R. L., and Warner, M. A., 1984, Hydrocarbon generation in lower Cretaceous Mowry and Skull Creek Shales in the northern Rocky Mountains area; in Woodward, J., Meissner, F. F., and Clayton, J. L., eds., Hydrocarbon source rocks of the greater Rocky Mountain region: Rocky Mountain Association of Geologists Guidebook, p. 449-467.
- Coney, P. J., 1978, Mesozoic-Cenozoic plate tectonics, Cenozoic tectonics and regional geophysics of western Cordillera: Geological Society of America Memoir no. 152, p. 33-50.
- Curry, W. H., 1962, Depositional environments in central Wyoming during Early Cretaceous: Wyoming Geological Association 17th Annual Field Conference Guidebook, p. 118-123.

Dershowitz, W. S. and H. H. Herda, 1992, Interpretation of fracture spacing and density: *in Proc. 33<sup>rd</sup> U. S. Symposium on Rock Mechanics*, J. R. Tillerson and W. R. Wawersik, eds., A. A. Balkema, Rotterdam, 757-766.

Dershowitz, W., P. La Pointe, T. Eiben and L. Wei (2000). Integration of Discrete Feature Network Methods With Conventional Simulator Approaches. *SPE Reservoir Evaluation & Engineering Journal*, April, 2000

Downs, G. R., 1952, Summary of Mesozoic stratigraphy, Bighorn Basin, Wyoming: Wyoming Geological Association 7th Annual Field Conference Guidebook, southern Bighorn Basin, Wyoming, p. 26-31.

Fanshawe, J. R., 1952, Big Horn Basin Tectonics: Wyoming Geological Association 7th Annual Field Conference Guidebook, southern Bighorn Basin, Wyoming, p. 19- 21.

Flinn, D. (1962). On folding during three dimensional progressive deformation. *Q.J. Geol. Soc. London*, 118, 385 - 433.

Frielinghausen, K. W., 1952, The Phosphoria Formation of southern and southeastern Bighorn Basin, Big Horn, Hot Springs, and Washakie Counties, Wyoming: Wyoming Geological Association 7th Annual Field Conference Guidebook, southern Bighorn Basin, Wyoming, p. 55-57.

Gower, M. A., 1978, Catalog of Paleozoic, Mesozoic, and Cenozoic rock names for the Wind River Basin: Wyoming Geological Association 30th Annual Field Conference Guidebook, Resources of the Wind River Basin, p. 39-45

Horne, R. N., 2000. *Modern Well Test Analysis* (4<sup>th</sup> Printing). Petroway, Inc., Palo Alto, CA. 257p.

Jamison, W. R., 1997. Quantitative evaluation of fractures on Monkshood anticline, a detachment fold in the foothills of western Canada.. *Bulletin of the American Association of Petroleum Geologists*, vol. 81, no. 7, p. 1110-1132

Jaeger, J. C. and N. G. W. Cook, 1976. *Fundamentals of Rock Mechanics* (2<sup>nd</sup> Edition). Chapman and Hall, London. 585p.

Keefer, W. R., 1965, Geologic history of Wind River Basin, central Wyoming: *Bulletin of the American Association of Petroleum Geologists*, vol. 49, no. 495-b, 58p.

Keefer, W. R., 1969, Geology of petroleum in Wind River Basin, central Wyoming: *Bulletin of the American Association of Petroleum Geologists*, vol. 53, no. 9, p. 1839-1865.

Kinsman, D. J., 1969, Modes of formation, sedimentary associations, and diagnostic features of shallow water and supratidal evaporites: *Bulletin of the American Association of Petroleum Geologists*, vol. 53, no. 4, p. 830-840.

La Pointe, P. R. and J. A. Hudson (1985). *Characterization and Interpretation of Rock Mass Joint Patterns*. Geological Society of America, Special Paper 199, 37p.

La Pointe, P. R., P. C. Wallmann and W. S. Dershowitz, 1993. Stochastic estimation of fracture size through simulated sampling. *International Journal of Rock Mechanics, Mining Sciences & Geomechanics Abstracts*, vol. 30, no. 7, 1611-1617.

Love, J. D., 1939, *Geology along southern margin of the Absaroka Range, Wyoming*: Geological Society of America, vol. 53, p. 830-840.

Mandelbrot, B. B., 1983. *The Fractal Geometry of Nature*, W.H. Freeman and Company, New York.

Medwedeff, D. A., 1989, Growth fault-bend folding at southeast Lost Hills, San Joaquin Valley, California: *AAPG Bulletin*, v. 73, p. 54-67.

Midland Valley, 2000, *3DMove User Guide & Online help pages*, Midland Valley Exploration Ltd.

Mills, N. K., 1956, Subsurface stratigraphy of the pre-Niobrara Formations in the Big Horn Basin: *Wyoming Geological Association Nomenclature Committee*, pt. 1, p. 8-22.

Mitra, S., 1986, Duplex structures and imbricate thrust systems: geometry, structural positions and hydrocarbon potential: *AAPG Bulletin* v. 70, p. 1087-1112.

Mitra, S., 1990, Fault-propagation folds: Geometry, kinematic evolution, and hydrocarbon traps: *Bulletin of the American Association of Petroleum Geologists*, vol. 74, no. 6, p. 921-945.

Olson, W. G., 1948, Circle Ridge and Maverick Springs Oil Fields, Fremont County, Wyoming: *Wyoming Geological Association 3rd Annual Field Conference Guidebook*, p. 178-185

Pedry, J. J., 1975, Tensleep fault trap, Cottonwood Creek Field, Washakie County, Wyoming. *Wyoming Geological Association Guidebook, 27<sup>th</sup> Annual Field Conference*, Wyoming, p. 211-219.

Peterson, J. A., 1954, Marine Upper Jurassic, Eastern Wyoming: *Bulletin of the American Association of Petroleum Geologists*, v. 38., p. 463-507.

Picard, M. D., 1978, Stratigraphy of the Triassic rocks in west-central Wyoming. Wyoming Geological Association Guidebook, 30<sup>th</sup> Annual Field Conference, Wind River Basin, Wyoming, p. 101-130.

Reading, H.G., 1980, Characteristics and recognition of strike-slip fault systems, in Ballance, P.F. and Reading, H.G., eds., Sedimentation in oblique-slip mobile zones: International Association of Sedimentologists Special Publication 4, p. 7- 26

Richardson, J.G. and R. J. Blackwell, (1971). Use of simple mathematical models for predicting reservoir behavior, Journal Petrol. Tech. (JPT), Vol 251, 1145-1151.

Riedel, W., 1929. Zur Mechanik geologischer Brucherscheinungen.: Zbl. Miner. Geol. Palaeont., B 354, p. 354-368

Smith, V. (2000). Surface Geologic Map of the Circle Ridge Oil Field, Wyoming. M. S. Thesis, Baylor University, Waco, TX.

Stearns, D. W. and M. Friedman, 1972, Reservoirs in fractured rock: AAPG Memoir 16, Stratigraphic Oil and Gas Fields, American Association of Petroleum Geologists, Tulsa, OK, 82-106.

Stipp, T. F., 1952, Paleozoic formations of the Big Horn Basin, Wyoming. Wyoming Geological Association Guidebook, 7<sup>th</sup> Annual Field Conference, Southern Big Horn Basin, Wyoming, 22-25.

Stock, J. and P. Molnar, 1988: Uncertainties and implications of the Late Cretaceous and Tertiary position of North America relative to the Farallon, Kula & Pacific plates. Tectonics, Washington, 7, 1339-1348.

Suppe, J., 1983, Geometry and kinematics of fault-bend folding: American Journal of Science, v. 283, p. 684-721.

Suppe, J., 1985, Principles of structural geology: Englewood Cliffs, New Jersey, Prentice Hall, 537 p.

Suppe, J., 1989, Rates of fault slip and fold growth (abs): GSA abstracts with programs, v. 21, p. A28.

Suppe, J., Mount, V. S., Hook, S. C., 1990, A forward modeling strategy for balancing cross-sections, AAPG, v. 74 no. 5, p. 521-531.

Terzaghi, R. D., 1965, Sources of error in joint surveys: Geotechnique 15, 287-304.

## 6 APPENDIX

### Loglan program for density-only wells

---

PROGRAM: PHIT\_RHOB Phit estimate from single porosity wells  
with rhob

```
/*-----  
-----  
/*start_doc  
/*Rhob in the Phosphoria\Tensleep to Phit estimate.  
/*end_doc  
/*-----  
-----
```

#### INPUT

```
/*  
/* CONSTANTS -----  
/*  
    GRMT                               /*  
    dpthsw                             /* et boundary  
/*  
/* INTERVALS -----  
/*  
ZONE                                ALPHA*12 /*  
/*  
/* LOGS -----  
/*  
    RHOB                                G/C3    /* Bulk Density  
    GR                                  GAPI    /* Gamma Ray  
    DEPTH                               FEET    /*
```

#### LOCAL

```
    rhomce                             /* for Phosphoria  
    rhomct                             /* for tensleep
```

#### OUTPUT

```
/*  
/* CONSTANTS -----  
/*  
    GRMT                               /*  
                                         /*  
/* LOGS -----  
/*  
    PHIT_DO                            v/v /* Total Porosity
```

START:

```

    rhomce = 2.79
    rhomct = 2.77
dowhile GET_FRAME ()
    if (depth<dpthsw) then          /* if depth is in the
Phosphoria
        phit_do = (2.79 - rhob)/1.79 /* use straight 2.79 for
matrix
    else                            /* now in the Tensleep
        if (rhob > 2.55 & gr < grmt) | gr > 80 then /*check GR
& rhob values
            if rhomct < 2.84 then /*if rhob heavy and gr high
                rhomct = rhomct + .05 /*or low then in dolomite
            endif
        else
            if ( rhomct > 2.67) then /*if we don't meet the above
conditions
                rhomct = rhomct - .05 /*then we're in quartz...
            endif
        endif
        phit_do = (rhomct - rhob)/(rhomct - 1) /* calculate
our porosity
    endif
        phit_do = limit(phit_do, 0, 1) /* limit the
porosity
        call PUT_FRAME ()          /* save the porosity

enddo

```